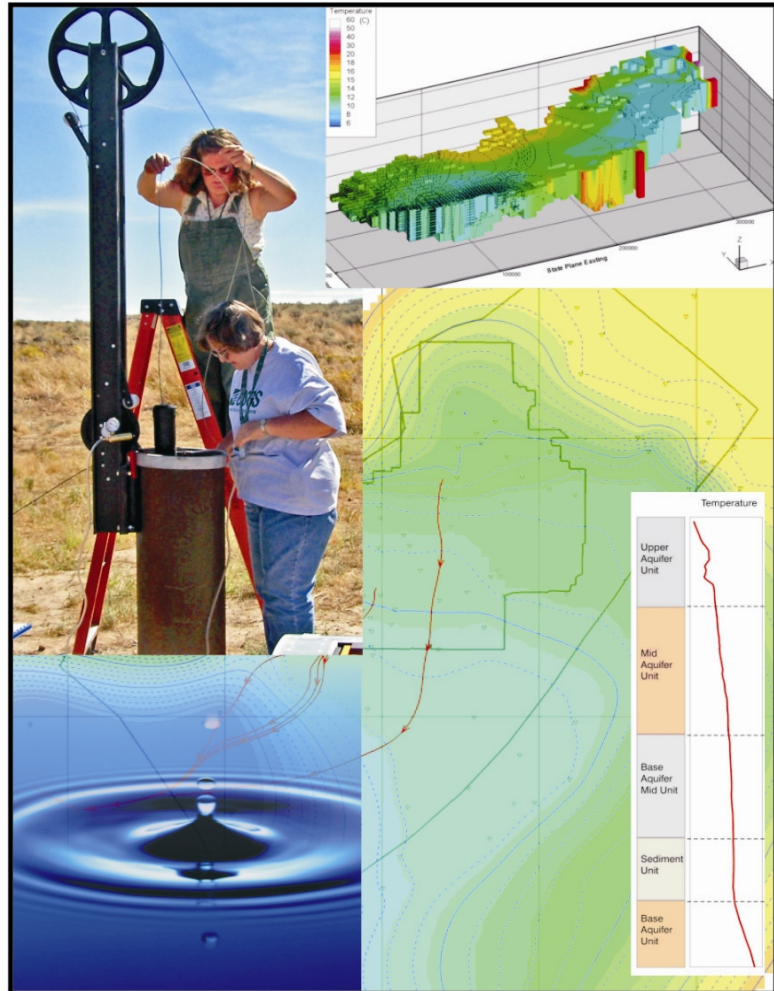


Development Report on the Idaho National Laboratory Sitewide Three-Dimensional Aquifer Model



September 2007



The INL is a U.S. Department of Energy National Laboratory operated by Battelle Energy Alliance

Development Report on the Idaho National Laboratory Sitewide Three-Dimensional Aquifer Model

Thomas R. Wood¹
Catherine M. Helm-Clark⁵
Hai Huang¹
Swen Magnuson¹
Travis McLing¹
Brennon Orr³
Mitchell A. Plummer¹
Robert Podgorney¹
Michael S. Roddy²
Michael J. Rohe⁴
Erik Whitmore³

¹INL

²ICP (CH2M-WG Idaho)

³North Wind, Inc.

⁴MicroH2O

⁵Idaho State University

September 2007

Idaho National Laboratory
Idaho Falls, Idaho 83415

Prepared for the
U.S. Department of Energy
Assistant Secretary for Environmental Management
Under DOE Idaho Operations Office
Contract DE-AC07-05ID14517

ABSTRACT

A sub-regional scale, three-dimensional flow model of the Snake River Plain Aquifer was developed to support remediation decisions for Waste Area Group 10, Operable Unit 10-08 at the Idaho National Laboratory (INL) Site. This model has been calibrated primarily to water levels and secondarily to groundwater velocities interpreted from stable isotope disequilibrium studies and the movement of anthropogenic contaminants in the aquifer from facilities at the INL. The three-dimensional flow model described in this report is one step in the process of constructing a fully three-dimensional groundwater flow and contaminant transport model as prescribed in the Idaho National Engineering and Environmental Laboratory Operable Unit 10-08 Sitewide Groundwater Model Work Plan.

An updated three-dimensional hydrogeologic conceptual model is presented along with the geologic basis for the conceptual model. Sediment-dominated three-dimensional volumes were used to represent the geology and constrain groundwater flow as part of the conceptual model. Hydrological, geochemical, and geological data were summarized and evaluated to infer aquifer behavior. A primary observation from development and evaluation of the conceptual model was that relative to flow on a regional scale, the aquifer can be treated with steady-state conditions. Boundary conditions developed for the three-dimensional flow model are presented along with inverse simulations that estimate parameterization of hydraulic conductivity. Inverse simulations were performed using the pilot-point method to estimate permeability distributions. Thermal modeling at the regional aquifer scale and at the sub-regional scale using the inverted permeabilities is presented to corroborate the results of the flow model.

The results from the flow model show good agreement with simulated and observed water levels almost always within 1 meter. Simulated velocities show generally good agreement with some discrepancies in an interpreted low-velocity region near the toe of the Arco Hills. This discrepancy persisted in each of the aquifer bottom thickness scenarios that were simulated precluding decisions on which aquifer bottom thickness to use in transport simulations. When joint-calibration was performed using both water levels and velocities assigned as calibration targets, the discrepancy was prevented. This result highlighted the need to consider multiple calibration objectives and not rely solely on calibration to water levels.

The next and last step in the process of constructing a fully three-dimensional groundwater flow and contaminant transport model will be calibration directly to transport from facilities. This last step will likely require further modification of the velocity fields resulting from the three-dimensional groundwater flow model presented in this report.

CONTENTS

ABSTRACT.....	iii
ACRONYMS.....	xv
1. INTRODUCTION.....	1-1
1.1 Background	1-1
1.1.1 Regulatory Background	1-2
1.1.2 Previous Modeling Studies	1-3
1.2 Objectives.....	1-3
1.2.1 Overall Project Objective.....	1-3
1.2.2 Three-Dimensional Modeling Objective.....	1-3
1.3 General Modeling Approach.....	1-4
1.4 Document Scope.....	1-5
1.5 Document Overview.....	1-5
1.6 Software Quality Assurance	1-6
1.7 References	1-6
2. CONCEPTUAL MODEL OF THREE-DIMENSIONAL GROUNDWATER FLOW IN THE AREA REPRESENTED BY THE OU 10-08 MODEL DOMAIN.....	2-1
2.1 Hydrogeologic Unit Characterization.....	2-1
2.1.1 Stratigraphic Conceptualization of the Basaltic SRPA in the Area Represented by the OU 10-08 Model.....	2-1
2.1.2 Derivation of Hydrogeologic Units.....	2-12
2.2 Hydrologic Conditions	2-34
2.2.1 Inflows and Outflows to and from the Area Represented by the OU 10-08 Model Domain	2-34
2.2.2 Three-Dimensional Distribution of Regional Underflow into the Modeled Area.....	2-37
2.2.3 Three-Dimensional Water-Level and Temperature Data Sets	2-38
2.2.4 Groundwater Flow Velocity Estimates	2-58
2.2.5 Estimates of Specific Discharge Based on Deep Well Temperature Profiles	2-63
2.3 Key Conceptual Model Issues	2-69
2.4 References	2-70

3.	THREE-DIMENSIONAL FLOW MODEL IMPLEMENTATION	3-1
3.1	Horizontal Domain	3-1
3.2	Vertical Domain	3-2
3.3	Discretization of Three-Dimensional Model Domain	3-4
3.4	Methodology for Assigning Model Parameter Zones	3-7
3.5	Incorporation of WAG-Specific Permeabilities	3-8
3.6	Three-Dimensional Boundary Conditions.....	3-9
3.6.1	Upgradient Boundary (NE) and Vertical Distribution of Inflow Fluxes.....	3-9
3.6.2	Influxes from Tributary Basins and Distribution onto Surface of Model	3-12
3.6.3	No-Flux Boundaries along Mountain Ranges on Northwest	3-13
3.6.4	Lateral No-Flow Boundary on Southeast.....	3-13
3.6.5	Downgradient Boundary on Southwest	3-14
3.6.6	Base of the Active Aquifer: Thick and Thin Scenario	3-14
3.6.7	Aquifer Top: Areal Infiltration and the Big Lost River	3-14
3.7	References	3-16
4.	FLOW MODEL CALIBRATION.....	4-1
4.1	Calibration Approach for the Three-Dimensional Flow Model	4-1
4.2	Calibration Data: Water Levels and Velocity Estimates	4-2
4.2.1	Three-Dimensional Water Level Data	4-2
4.2.2	Velocity Estimates	4-6
4.3	Multi-Objective Calibration Approach and Weighting of Calibration Targets.....	4-6
4.3.1	Overview of Simulations	4-7
4.3.2	Pilot Point Methodology	4-8
4.4	Inverse Simulation Results	4-13
4.4.1	Thick Aquifer Scenario	4-13
4.4.2	Thin Aquifer Scenario.....	4-19
4.4.3	Discussion of Inverse Simulation Results.....	4-31
4.5	Sensitivity Simulations.....	4-34
4.5.1	Model 2 with Reduced Anisotropy	4-34
4.5.2	Joint Inversion with Measured Heads and Velocity Estimates	4-37
4.6	References	4-43

5.	THERMAL MODELING	5-1
5.1	Introduction	5-1
5.2	Two-Dimensional Heat Flow Modeling Studies	5-1
5.2.1	Two-Dimensional Modeling and Evolution of Temperature Profiles along a Flow Line	5-2
5.3	Three-Dimensional Heat Flow Modeling	5-4
5.3.1	Phase 1 - Heat Flow Modeling of the Regional Aquifer	5-4
5.3.2	Phase 2 - INL Subregional Groundwater Flow and Heat Transport Model	5-12
5.4	References	5-24
6.	SUMMARY	6-1
6.1	Northeastern Boundary Flux Assignment Impacts	6-2
6.2	Approach to Assigning Northeastern Boundary Fluxes	6-2
6.3	Approach to Selecting Between Thick and Thin Aquifer Interpretations	6-3
6.4	Conclusion	6-3
6.5	References	6-3
	Appendix A—Software Management Agreement	A-1
	Appendix B—Fiscal Year 2006 Volcanic Stratigraphy Supporting Revision of the Geologic Conceptual Model	B-1
	Appendix C—The Treatment of Volcanic Rifts and Geophysical Data in the Conceptual Model	C-1
	Appendix D—Heat-Flow Implementation Details	D-1
	Appendix E—Error Statistics for Head Mismatches (Simulated – Observed) for Four Base Case Models	E-1

FIGURES

2-1.	Geographical and geological features in the conceptual model study area	2-2
2-2.	The four different eruptive styles seen on the eastern Snake River Plain	2-3
2-3.	Diagram showing how the fractured and vesicular flow top of an underlying flow contacts the fractured and vesicular flow bottom of an overlying flow	2-4
2-4.	Fence diagram oriented from the southwest to northeast across the INL showing the Olduvai lakebeds dipping to the south and intersecting the effective base of the SRPA	2-10

2-5.	Interpreted extent of pluvial Lake Terretton based on modern elevations.....	2-11
2-6.	Simplified diagram of deposition directions on the flood plain of the Big Lost River.....	2-11
2-7.	Numerical model domain with geologic subdomains and aquifer wells identified	2-13
2-8.	Hydrogeologic unit delineation in Well INEL-1. Only the interpreted active thickness of the aquifer is portrayed	2-17
2-9.	Hydrogeologic unit delineation in Well 2-2A. Only the interpreted active thickness of the aquifer is portrayed	2-18
2-10.	Hydrogeologic unit delineation in Well ANL-1. Only the interpreted active thickness of the aquifer is portrayed	2-19
2-11.	Locations of composite cross sections through simulation domain.....	2-21
2-12a.	Hydrogeologic Unit Cross Sections 1–4.....	2-23
2-12b.	Hydrogeologic Unit Cross Sections 5–8.....	2-24
2-13a.	Extrapolated solids for all of the aquifer units looking from the southeast to the northwest.....	2-29
2-13b.	Extrapolated solids for all of the aquifer units looking from the southeast to the northwest, with upper basalt hydrogeological unit removed to show detail of mid- and base-mid basalt units.....	2-30
2-13c.	Extrapolated solids basal aquifer unit looking from the southeast to the northwest.....	2-31
2-13d.	Extrapolated solids for all of the sediment-dominated units looking from the southeast to the northwest.....	2-32
2-14.	Aquifer test information presented against depth below the water table.	2-33
2-15.	Operable Unit 10-08 groundwater modeling domain, INL boundary, and eastern Snake River Plain.....	2-39
2-16.	Well locations used in transient water-level analysis. Also shown are the INL boundary and the OU 10-08 model domain.....	2-40
2-17.	Example hydrographs from aquifer wells completed in the OU 10-08 modeling domain	2-41
2-18.	Application of triangulation method for inferring groundwater flow direction near the southern boundary of the INL.....	2-42
2-19.	Interpolated water level for Calendar Year 2000 using 110 wells.....	2-43
2-20.	Mean water potential gradient direction and standard deviation of flow direction	2-43
2-21.	Location and type of aquifer wells and sources of data used as the calibration set for the OU 10-08 model	2-45

2-22.	Water table contour map developed from June 2004 calibration data set	2-46
2-23.	Locations of wells with nested piezometers or Westbay systems.....	2-47
2-24.	Total hydraulic head and vertical gradients as a function of time for piezometer wells.....	2-48
2-25.	Extent of TCE plume at TAN and some of the many aquifer wells at this facility	2-49
2-26.	Average of calculated vertical gradients and hydrographs	2-50
2-27.	Total hydraulic head and vertical gradients as a function of depth in the aquifer	2-51
2-28.	Seven well pairs used for additional vertical gradient analysis	2-52
2-29.	Locations and results of all available vertical gradient information	2-52
2-30.	Schematic diagram illustrating the two-dimensional distribution of water potential and specific discharge vectors for flow through a hypothetical system of discontinuous blocks of contrasting hydraulic conductivity	2-53
2-31.	Locations of temperature measurements for the entire eastern Snake River Plain from National Water Information System	2-55
2-32.	Mean groundwater temperature in the SRPA, based on interpolation of data from wells in southeastern Idaho	2-56
2-33.	Temperature vertical profiles in deep aquifer wells and a cross section defining the base of the aquifer.....	2-57
2-34.	Interpreted preferential flow paths from stable isotope and thermal signatures	2-59
2-35.	Interpreted groundwater velocities along preferential flow paths.....	2-61
2-36.	Temperature field (contours) and groundwater flow vectors used to calculate temperature gradients in the direction of flow	2-64
2-37.	Magnitude of temperature gradient in the direction of groundwater flow	2-65
2-38.	Temperature data at wells where profiles were used to calculate specific discharge	2-66
2-39.	Temperature profile for Well WO-2, illustrating zones where temperature gradients were used to calculate heat fluxes above and below the aquifer	2-67
3-1.	Operable Unit 10-08 model domain	3-1
3-2.	Model domain base of effective aquifer for the OU 10-08 three-dimensional flow model.....	3-2
3-3.	Simulated thickness for the thick and thin aquifer scenarios.....	3-3
3-4.	Grid structures of each model layer for the thick scenario	3-5
3-5.	Grid structures of each model layer for the thin scenario	3-6

3-6.	Parameter zones for each model layer	3-8
3-7.	Location of boundary conditions for the OU 10-08 model.....	3-9
3-8.	Underflow across the northeastern boundary by model layer for the thick and thin aquifer scenarios	3-10
3-9.	Recharge polygons to represent recharge from the tributary drainage basins	3-13
3-10.	Recharge from percolation of Big Lost River channel streamflow divided into three reaches of river plus spreading areas	3-15
4-1.	Generalized weighting scheme to vertically match observation wells that cross multiple layers of a three-dimensional flow model.....	4-3
4-2.	Numbers of wells, open-screen intervals, and alignment with three-dimensional model layers.....	4-4
4-3.	Layer-specific spatial distribution of hydraulic head calibration targets	4-5
4-4.	Point estimates of groundwater velocity obtained from recent geochemical studies	4-6
4-5.	Pilot point distribution in each layer for inverse solution with pure pilot point calibration approach, three-dimensional flow model, thick aquifer scenario	4-10
4-6.	Spatial distribution of the sediment-controlled polygons	4-12
4-7.	Simulated heads in the top layer of the three-dimensional flow model, thick scenario, pure pilot point calibration (base case model 1)	4-15
4-8.	Head residuals for all model layers, thick scenario, pure pilot point calibration (base case model 1).....	4-16
4-9.	Head residuals for all model layers, thick scenario, pure pilot point calibration (base case model 1) for the southern half of the INL.....	4-16
4-10.	Horizontal hydraulic conductivity distribution for OU 10-08 three-dimensional flow model estimated from inverse solution using pure pilot point approach, thick scenario (base case model 1).....	4-17
4-11.	Confidence bounds of model parameters estimated by PEST for base case model 1	4-18
4-12.	Simulated heads in the top layer of the three-dimensional flow model, thick scenario, calibrated with pilot point approach using sedimentary layer bounds (base case model 2)	4-20
4-13.	Head residuals for all model layers, thick scenario, calibrated with pilot point approach using sedimentary layer bounds (base case model 2)	4-21
4-14.	Conductivity distribution within six model layers for thick aquifer scenario estimated using the pilot point approach with sedimentary layer bounds (base case model 2)	4-22
4-15.	Confidence bounds of model parameters estimated by PEST for base case model 2.....	4-23

4-16.	Simulated heads in the top layer of the three-dimensional flow model, thin scenario, calibrated with the pure pilot point approach (base case model 3)	4-24
4-17.	Head residuals for all model layers, thin scenario, calibrated with the pure pilot point approach (base case model 3)	4-25
4-18.	Conductivity distribution within six model layers for thin aquifer scenario estimated using the pure pilot point inverse solution approach (base case model 3).....	4-26
4-19.	Confidence bounds of model parameters estimated by PEST for base case model 3.....	4-27
4-20.	Simulated heads in the top layer of the three-dimensional flow model, thin scenario, calibrated with pilot point approach using sedimentary layer bounds (base case model 4)	4-28
4-21.	Head residuals for all model layers, thin scenario, calibrated with pilot point approach using sedimentary layer bounds (base case model 4).....	4-29
4-22.	Conductivity distribution within six model layers for thin aquifer scenario estimated using the pilot point inverse solution approach with sedimentary bounds (base case model 4).....	4-30
4-23.	Confidence bounds of model parameters estimated by PEST for base case model 4.....	4-31
4-24.	Simulated groundwater velocity in model layer 1 within the top model layer for models 1 to 4 in order	4-33
4-25.	Simulated heads in the top layer of the three-dimensional flow model, thick scenario, with reduced anisotropy, calibrated with pilot point approach using sedimentary layer bounds (model 2, reduced anisotropy).....	4-35
4-26.	Conductivity distribution within six model layers for the thick aquifer scenario, with reduced anisotropy, estimated using the pilot point inverse solution approach with sedimentary bounds (model 2, reduced anisotropy)	4-36
4-27.	Simulated groundwater velocity in model layer 1 with reduced vertical to horizontal anisotropy.....	4-37
4-28.	Simulated heads in the top layer of the three-dimensional flow model, thick scenario, calibrated jointly with pilot point approach using sedimentary layer bounds and velocity estimates.....	4-38
4-29.	Head residuals for all model layers, thick scenario, calibrated jointly with pilot point approach using sedimentary layer bounds and velocity estimates.....	4-39
4-30.	Conductivity distribution within six model layers for thick aquifer scenario estimated using the joint pilot point inverse solution approach with sedimentary bounds and velocity estimates.....	4-40
4-31.	Simulated groundwater velocity in model layer 1 for joint water level-velocity inverse simulation sensitivity simulation	4-41
4-32.	Combined points from Figure 4-4 used to compare simulated and estimated velocities.....	4-41

5-1.	Evolution of temperature distribution along a flow line in an idealized two-dimensional system.....	5-3
5.2.	Effect of a 10-fold increase in velocity	5-4
5-3.	Horizontal extent and grid dimensions of the SRPA heat flow model	5-6
5-4.	Perspective views of the three-dimensional heat and groundwater flow model grid.....	5-8
5-5.	Recharge distribution, from the IWRRRI model.....	5-9
5-6.	Three-dimensional model grid showing discharge cells and specified head cells of preliminary simulation	5-10
5-7.	Comparison of the potentiometric surface calculated from a preliminary groundwater and heat flow simulation and the water potential map interpolated from aquifer well data.....	5-11
5-8.	Calculated temperature field and contours of total water potential, from preliminary simulation of heat flow in the SRPA	5-12
5-9.	Observed temperature distribution across the OU 10-08 model domain	5-17
5-10.	Observed temperature distribution.....	5-18
5-11.	Simulated groundwater seepage velocity vectors and temperatures.....	5-20
5.12.	Perspective view of the heat flow simulation results.....	5-21
5-13.	Simulated temperatures and observed temperatures at locations of several deep boreholes	5-22
5-14.	Illustration of the effect of different boundary conditions on simulated temperature distribution	5-23

TABLES

2-1.	Operable Unit 10-08 characteristic wells.....	2-14
2-2.	Correlation between hydrogeologic subdomains and hydrogeologic units within the area represented by the OU 10-08 model domain	2-15
2-3.	Inflows to the area represented by the Operable Unit 10-08 model domain.....	2-35
2-4.	Layer thickness and percentage of total flow by layer for the Spinazola five-layer model (1994) and layer thickness and percentage of total flow by layer (initial and revised) for the OU 10-08 six-layer model.....	2-38
2-5.	Summary of horizontal specific discharge magnitudes calculated from analysis of temperature profiles	2-68
3-1.	Layer thicknesses and percentage of total flow by layer for the Spinazola five-layer model (1994) and for the OU 10-08 six-layer model.....	3-10
3-2.	Water flux assigned to the northeastern boundary for the thick aquifer scenario, by horizontal boundary segment and model layer	3-11
3-3.	Water flux assigned to the northeastern boundary for the thin aquifer scenario, by horizontal boundary segment and model layer	3-12
3-4.	Summary of areal recharge polygons representing tributary fluxes	3-13
3-5.	Other sources of recharge across the top boundary of the OU 10-08 flow model.....	3-15
4-1.	Treatment of single and multiple open-interval wells in three-dimensional calibration.....	4-4
4-2.	Summary and numbering of the modeling scenarios carried out to test the various conceptual models on the flow domain.....	4-8
4-3.	Summary of the number of pilot points used in the simulations.....	4-9
4-4.	Initial guesses and maximum values of hydraulic conductivity for the pilot points by model layer	4-11
4-5.	Summary of root mean square error (meters) for four base model cases	4-31
4-6.	Comparison of components of estimated point velocities with results of joint inversion model.....	4-42
5-1.	Hydraulic conductivities in the remainder of the model.....	5-7

ACRONYMS

ARA	Auxiliary Reactor Area
AVH	Axial Volcanic High
bls	below land surface
CERCLA	Comprehensive Environmental Response, Compensation, and Liability Act
CFA	Central Facilities Area
cfs	cubic feet per second
DEQ	Department of Environmental Quality
DOE-ID	U.S. Department of Energy Idaho Operations Office
EPA	U.S. Environmental Protection Agency
GMS	Groundwater Modeling System
INEEL	Idaho National Engineering and Environmental Laboratory (now INL)
INEL	Idaho National Engineering Laboratory (now INL)
INL	Idaho National Laboratory
INTEC	Idaho Nuclear Technology and Engineering Center
ISU	Idaho State University
IWRRI	Idaho Water Resources Research Institute
MFC	Materials and Fuels Complex
MSL	mean sea level
NRF	Naval Reactors Facility
OU	Operable Unit
PEST	Parameter Estimation
RI/FS	Remedial Investigation/Feasibility Study
ROD	Record of Decision
RTC	Reactor Technology Complex
RWMC	Radioactive Waste Management Complex

SRPA	Snake River Plain Aquifer
TAN	Test Area North
TCE	trichloroethylene
TRA	Test Reactor Area
USGS	United States Geological Survey
WAG	Waste Area Group

Operable Unit 10-08 Development Report on the Idaho National Laboratory Sitewide Three-Dimensional Aquifer Flow Model

1. INTRODUCTION

A sub-regional scale, three-dimensional flow model of the Snake River Plain Aquifer (SRPA) has been developed to support Comprehensive Environmental Response, Compensation, and Liability Act (CERCLA) (42 USC § 9601 et seq.) decisions for Waste Area Group (WAG) 10, Operable Unit (OU) 10-08 at the Idaho National Laboratory (INL) Site. This report documents progress made toward development of this three-dimensional flow model. The model has been calibrated primarily to water levels and secondarily to groundwater velocities interpreted from stable isotope disequilibrium studies and the movement of anthropogenic contaminants in the aquifer from facilities at the INL. The three-dimensional flow model described in this report is a step in the process of constructing a fully three-dimensional groundwater flow and contaminant transport model as prescribed in the *Idaho National Engineering and Environmental Laboratory Operable Unit 10-08 Sitewide Groundwater Model Work Plan* (DOE-ID 2004).

The modeling process outlined in the OU 10-08 Groundwater Model Work Plan (DOE-ID 2004) will result in a comprehensive evaluation of environmental impacts to the underlying SRPA from operations at the INL Site. The OU 10-08 groundwater modeling study addresses areas outside the boundaries of the other individual INL WAGs and will be used to estimate the potential for risk created by the commingling of residual plumes left by those WAGs. The cumulative impacts on the SRPA are being evaluated during the OU 10-08 Remedial Investigation/Feasibility Study (RI/FS) process as outlined in the *Waste Area Group 10, Operable Unit 10-08, Remedial Investigation/Feasibility Study Work Plan* (DOE-ID 2002).

The OU 10-08 groundwater modeling study is guided by OU 10-08 Sitewide Groundwater Model Work Plan. That plan was developed in collaboration with and reviewed by the U.S. Department of Energy Idaho Operations Office (DOE-ID), the Idaho Department of Environmental Quality (DEQ), and the U.S. Environmental Protection Agency (EPA) to ensure that the products of the modeling studies match those needed for the OU 10-08 RI/FS process. This approach has significantly expanded the regulatory agencies' involvement in the development of the model by engaging them early and frequently over the course of the project. The overall modeling objective and issues resulting from the collaborative planning effort are documented in the OU 10-08 Sitewide Groundwater Model Work Plan.

To enhance integration with the numerous parties involved in modeling aquifer flow and transport in the region, the project is using a tiered approach to the model design. Previous steps completed include the development of a steady-state two-dimensional flow model (Wood et al. 2005) and a two-dimensional transport model (Appendix C of the WAG 10 OU 10-08 RI/FS Annual Status Report for 2006 [DOE-ID 2007]). This report presents the third step in numerical simulations, i.e., a three-dimensional flow model. The next and final step will be a three-dimensional transport/response surface model report, which will directly support preparation of the OU 10-08 RI/FS.

1.1 Background

A key component of the RI/FS effort and long-term stewardship of the groundwater resources at the INL Site is the development of an INL Sitewide groundwater-flow and contaminant-transport numerical model. This Sitewide groundwater model will support decisions and serve as a tool for

managing, compiling, and synthesizing data regarding the SRPA beneath the INL Site. The three-dimensional model presented in this document represents a step in the development of the Sitewide groundwater model. Currently, several different facility-scale aquifer models are used at the INL Site to satisfy specific program needs. These models are not consistent in some cases and are sometimes redundant in the domains represented. Preparation of the Sitewide groundwater model provides the opportunity to promote consistency in representing the aquifer beneath the INL. In the short term, the Sitewide groundwater model will satisfy requirements for preparation of an OU 10-08 Record of Decision (ROD) and will supplement and support existing aquifer models. Vadose zone transport modeling is the responsibility of individual WAGs, and will not be revisited. Rather, the fluxes to the aquifer at the bottom of the individual facility vadose zone models will be used as input to the Sitewide groundwater model.

The need for the Sitewide groundwater model is also driven by advancements in the understanding of the INL Site subsurface and greatly improved computational capabilities. During the past decade, INL Site contractors, the United States Geological Survey (USGS), and numerous academic institutions have obtained new information that significantly improves our understanding of the subsurface beneath the eastern Snake River Plain. The particulars of these new studies are compiled in Section 2 and in previous OU 10-08 groundwater modeling project reports (Wood et al. 2005). In order to use these new data in determining the risk posed by contaminants from the INL Site, the data must be compiled and used to update conceptual and numerical models of flow and transport.

To the extent possible, the Sitewide groundwater model is structured to integrate with and complement existing groundwater-flow and contaminant-transport models developed by individual WAGs and the USGS. This approach will enhance consistency across the INL Site and help resolve differences raised by different interpretations of subsurface data. Communication, staff integration, and data sharing are the foremost components in the strategy for integrating the Sitewide groundwater model with existing models. Meetings are held at regular intervals for technical and management staff involved with the active development or application of numerical simulations of the subsurface at the INL Site. Additionally, use of the Environmental Data Warehouse to share and store data will ensure that the Sitewide groundwater model is developed and based on a common and consistent set of data.

1.1.1 Regulatory Background

The WAG 10 OU 10-08 RI/FS Work Plan (DOE-ID 2002) describes the enforceable milestone schedule for OU 10-08. The OU 10-08 ROD is expected to be the last major ROD completed at the INL Site, and the deliverable date for the draft is planned for December 2008. The *OU 10-08 Sitewide Groundwater Model Work Plan* describes a phased modeling approach that is being conducted to support development of the OU 10-08 RI/FS.

It is critical that the OU 10-08 RI/FS activities overlap and are consistent with remedial decisions across the INL Site, because all WAGs will eventually be managed under WAG 10 as activities are completed. The overlap with the other WAG groundwater models will ensure a smooth and cost-effective transfer to the long-term stewardship role of WAG 10. A final important need addressed under the current OU 10-08 RI/FS schedule is the ability for managers to consolidate all groundwater concerns into a single internally consistent representation of the aquifer beneath the INL Site for communication to concerned stakeholders. The importance of the Sitewide groundwater model is demonstrated by two important facts: (1) the SRPA is the primary INL-related concern for the population of eastern Idaho, and (2) predicted contaminant levels in the SRPA drive the selection of most remedies for individual WAGs. For the aforementioned reasons, the INL Site management team (including the regulatory agencies) has taken a proactive, technically robust approach for developing the Sitewide groundwater model.

1.1.2 Previous Modeling Studies

Numerical modeling of groundwater flow beneath the INL Site has been ongoing for many years, both at the INL Sitewide scale and for much larger areas of interest. Numerical models for assessment of INL groundwater problems were utilized as early as the mid-1970s (Robertson 1974). The USGS Regional Aquifer-System Analysis program produced several SRPA models at various scales for use as characterization tools dealing with regional water-resource issues (Lindholm 1996; Garabedian 1992; Spinazola 1994). Recent numerical modeling efforts include the State of Idaho Regional Water Resource Model (Cosgrove, Contor, and Johnson 2006) and the ongoing USGS Subregional Model. At the INL Site, remedial investigations mandated under CERCLA have resulted in several facility-scale flow and transport models; these include three different numerical flow and transport models prepared for WAGs 1, 3, and 7.

Historical modeling efforts are important, because they identify documented successes that can be incorporated into the Sitewide groundwater model and because they help to identify issues and problems that can be avoided. Several historical models provide input to the OU 10-08 conceptual model and provide useful summaries of data to be used in the Sitewide groundwater model. Wood et al. (2005) summarized the basic features and applicable results for several regional eastern Snake River Plain and subregional INL Site models and the individual WAG aquifer models.

1.2 Objectives

1.2.1 Overall Project Objective

From the *OU 10-08 Sitewide Groundwater Model Work Plan*, the overall goal for the Sitewide groundwater model project is to

“Develop a Sitewide flow and transport model of the active flow portion of the Snake River Plain Aquifer that can be used to evaluate OU 10-08 remedial action alternatives and to ensure all remedies remain protective of the aquifer. The model will provide credible estimates of contaminant concentrations from sources at the INL over relevant future timeframes.”

This overall goal comes from the *OU 10-08 RI/FS Work Plan* where it was determined that WAG 10 will evaluate the potential overlap of contaminant plumes for cumulative risk assessment to ensure a comprehensive analysis of INL impacts to the aquifer.

1.2.2 Three-Dimensional Modeling Objective

The objective for the model developed in this document is to expand the two-dimensional model presented in Wood et al (2005) into a three-dimensional representation and ideally to obtain a reasonable representation of the velocity field. The primary objective of the flow model calibration is to match velocities. The expansion from two dimensions to three dimensions includes revising the conceptual model to develop three-dimensional volumes of similar hydrologic properties, revising the boundary conditions for influxing water into the simulation domain, and using three-dimensional head measurements in the calibration. The resulting three-dimensional velocity field will be the starting point for the next phase of the overall Sitewide groundwater model project. In the next phase of the modeling project, calibration to transport occurs, which will further modify the velocity field. It should be understood that the three-dimensional flow model will continue to evolve during the transport calibration.

1.3 General Modeling Approach

The approach taken by the OU 10-08 groundwater modeling project to attain the overall Sitewide groundwater model objective is to use multiple sources of information and perform a multi-objective calibration. These multiple sources of information include hydrologic data, stratigraphic data, contaminant data indicative of transport from specific facilities, isotope data to infer groundwater velocities away from those facilities, and thermal data to corroborate the groundwater flow and transport modeling.

This multi-objective approach is consistent with the philosophy presented by Anderson (2005) where she stated that “It is generally recognized that head data alone are not sufficient to calibrate a groundwater flow model, while estimates of groundwater flux and/or information on the movement of solute and/or heat help constrain the calibration.” The three-dimensional flow model presented in this document is calibrated to water levels and inferred groundwater velocities and represents a step in the process of achieving the final goal of a calibrated three-dimensional transport model. The final flow field will undoubtedly be different when joint calibration to both flow and contaminant transport is completed in the next phase of the project.

The domain considered in the model is termed sub-regional because it encompasses a region slightly larger than the INL, but not the entire SRPA. The modeling approach uses the pilot point method to perform automated inverse estimation of distributed hydraulic conductivities that, along with prescribed boundary conditions, result in reasonable matches with the calibration objectives. This approach is in contrast to that more traditionally applied where stratigraphic information is interpolated over a discretized model domain and explicit basalt and sediment hydraulic conductivities are assigned to specific grid block volumes. Given the scale of the sub-regional model, it is not feasible to incorporate small-scale features such as local sedimentary interbeds within the aquifer that locally influence contaminant transport. Evaluating the influence of these features was the purview of the individual WAG modeling efforts. A focus of the OU 10-08 model is evaluating the potential for commingling of contaminant plumes, hence the sub-regional scale. At this sub-regional scale, the influence of sediments can be included through constraints on the allowed range of the pilot point hydraulic conductivities. The selection of which hydrogeologic units receive these constraints is determined through the stratigraphic evaluation described in Section 2. The stratigraphic evaluation also is used in a post-audit of the permeability distribution resulting from the inversion.

While vertically integrated two-dimensional models can be sufficient for representing hydraulic head, transport in the aquifer is inherently three-dimensional. Contaminants enter the aquifer both at the top of the aquifer from sources in the overlying vadose zone and at depth in the aquifer from injection wells. A three-dimensional model is necessary to represent transport. As an example, the monitoring results from Well MIDDLE-2051 show measurable variation vertically in monitored concentrations at distance downgradient from the Reactor Technology Complex and the Idaho Nuclear Technology and Engineering Center. A vertically-integrated two-dimensional model almost certainly would under-predict the concentrations observed at this point. It can be argued, given the limited vertical discretization in the three-dimensional model presented in this report, that the model also falls short in representing such vertically-varying contaminant profiles. However, this model represents a significant step in the correct direction for simulating transport. This three-dimensional transport modeling approach is consistent with the approach used for local-scale aquifer models for WAGs 1, 3, and 7. The individual WAG models all used a three-dimensional approach to represent transport in the aquifer to preclude under-estimating simulated concentrations. Lastly, while a very thin two-dimensional aquifer model could be used to conservatively estimate transport, that approach would not be consistent with the overall objective of obtaining credible estimates of contaminant concentrations.

The calibrated model will be used along with contaminant sources representing final selected remedies to the degree possible for the individual WAGs to result in a comprehensive model that addresses all impacts to the aquifer within the area defined by the model. The modeling approach also emphasizes flexibility to be able to address different scenarios that result from uncertainty in particular aspects of the model, such as effective aquifer thickness or smaller or larger future contaminant sources to the aquifer at INL facilities. Credibility results from being both comprehensive in evaluating all features that might influence flow and transport, and being flexible in evaluating aspects that are uncertain.

The modeling approach is designed to allow phased development of both the two-dimensional and three-dimensional models. This phased approach allows the methodology for simulating flow and transport to be developed and tested in simpler and less computationally intensive two-dimensional models, and then lessons learned may be applied to the more complex and representative three-dimensional models. Another aspect of the OU 10-08 approach is that, ultimately, a model will be abstracted from the final three-dimensional transport model that will be simpler to run but will provide consistent results and will allow easy extension of the three-dimensional model to include additional sources that may be identified over time. This abstracted model is called a Response Surface Model and was previously demonstrated for a proof-of-principle test (Rood 2005).

The specific steps of the approach are to develop the following:

- Two-dimensional flow model (complete)
- Two-dimensional transport model (complete)
- Three-dimensional flow model, including thermal transport (complete, documented in this report)
- Three-dimensional transport model
- Response surface model (to mimic three-dimensional transport model).

1.4 Document Scope

This document presents an updated three-dimensional hydrogeologic conceptual model and the geologic basis for the conceptual model. This geologic basis represents the culmination of several years of concentrated effort and is documented partly in Section 2 of this report and partly in Appendices B and C. This document also presents the development of a three-dimensional numerical flow model for the sub-regional INL area that is constrained by the conceptual model. Boundary conditions for the three-dimensional flow model are presented along with inverse simulations that estimate parameterization of hydraulic conductivity. These inverse simulations primarily use water levels as calibration targets but also show the utility of using velocities estimated from anthropogenic contaminant plume migration and disequilibrium studies of stable isotopes. Thermal modeling is presented to corroborate the suitability and results of the flow model.

1.5 Document Overview

This report contains a description of the updated conceptual model for flow (Section 2). This is followed by a description of the conceptual model implementation into a numerical three-dimensional flow model (Section 3) and calibration of the three-dimensional flow model (Section 4). The corollary development of both a regional and sub-regional three-dimensional thermal transport model is described in Section 5. A summary including implications for the three-dimensional transport model is contained in Section 6.

1.6 Software Quality Assurance

The requirements for software quality assurance for this modeling effort have been jointly agreed to by the performers, the Idaho Cleanup Project OU 10-08 project manager, and the Battelle Energy Alliance Modeling and Measurement Department manager. Appendix A contains the software management agreement. Modeling for the OU 10-08 Sitewide groundwater model is being conducted according to the requirements of the “Research and Development General Software Management Plan,” PLN-1726.

Software used to develop the three-dimensional flow model included the MODFLOW-2000 (Harbaugh et al. 2000) groundwater flow simulation code, the MT3DMS Version 4.0 transport simulation code (Zheng and Wang 1999), the Parameter Estimation (PEST) (Doherty 2005) parameter estimator, and the Groundwater Modeling System Version 6.0 (BYU 2002) pre- and post-processor and data analyzer. MODFLOW is an industry standard groundwater flow simulation code developed by the USGS. MODFLOW-2000 is the latest version and incorporates many new features. MT3DMS solves advective-dispersive transport, and has been used to simulate thermal transport (documented in this report). MT3DMS will also be used to simulate contaminant transport in the next and last phase of this modeling project. PEST is a robust parameter estimator that is designed to automatically adjust the parameters in any model over a series of runs until model-generated results fit a set of observations within a specified error tolerance. PEST also provides information about the sensitivity of the results to changes in the selected parameters, the correlation (a measure of non-uniqueness) among parameters, and the resolution of the parameters. The Groundwater Modeling System is a widely used software package developed for the Army Corps of Engineers. The Groundwater Modeling System integrates and facilitates implementation of the conceptual model, interpretation of the output, and visualization of the results for all of the codes used in this effort. The Groundwater Modeling System also provides a convenient interface to link MODFLOW-2000 and PEST.

1.7 References

42 USC § 9601, Comprehensive Environmental Response, Compensation, and Liability Act of 1980 (CERCLA/Superfund),” *United States Code*, December 11, 1980.

Anderson, M. P., 2005, “Heat as a Ground Water Tracer,” *Ground Water*, Vol. 43 (6), pp. 951–968.

BYU, 2002, “Groundwater Modeling System Software,” Provo, Utah: Environmental Modeling Research Laboratory, Brigham Young University.

Cosgrove, D. M., B. A. Contor, and G. S. Johnson, 2006, *Enhanced Snake Plain Aquifer Model Final Report*, Idaho Water Resources Research Institute, University of Idaho, prepared for the Idaho Department of Water Resources, IWRI Technical Report 06-002, July 2006.

DOE-ID, 2002, *Waste Area Group 10, Operable Unit 10-08, Remedial Investigation/Feasibility Study Work Plan (FINAL)*, DOE/ID-10902, Rev. 0, U.S. Department of Energy Idaho Operations Office, August 2002.

DOE-ID, 2004, *Idaho National Engineering and Environmental Laboratory Operable Unit 10-08 Sitewide Groundwater Model Work Plan*, DOE/NE-ID-11188, Rev. 0, U.S. Department of Energy Idaho Operations Office, December 2004.

- DOE-ID, 2007, *Waste Area Group 10, Operable Unit 10-08, Remedial Investigation/Feasibility Study Annual Status Report*, DOE/ID-11297, Rev. 0, U.S. Department of Energy Idaho Operations Office, May 2007.
- Doherty, J., 2005, *PEST Model-Independent Parameter Estimation, User's Guide*, 5th Edition Watermark Numerical Computing, January 2005.
- Garabedian, S. P., 1992, "Hydrology and Digital Simulation of the Regional Aquifer System, Eastern Snake River Plain, Idaho," U.S. Geological Survey Professional Paper 1408-F.
- Harbaugh, A.W., E. R. Banta, M. C. Hill, and M. G. McDonald, 2000, *Modflow-2000, The US Geological Survey Modular Ground-Water Model-User Guide to Modularization Concepts and the Ground-Water Flow Process*, U.S. Geological Survey Open-File Report 00-92.
- Lindholm, G. F., 1996, "Summary of the Snake River Plain Regional Aquifer-System Analysis in Idaho and Eastern Oregon," U.S. Geological Survey Professional Paper 1408A.
- PLN-1726, "Research and Development General Software Management Plan," Idaho National Engineering and Environmental Laboratory, Idaho Completion Project, September 2004.
- Robertson, J. B., 1974, *Digital Modeling of Radioactive and Chemical Waste Transport in the Snake River Plain Aquifer at the National Reactor Testing Station, Idaho – 1952–1970*, U.S. Geological Survey Open-File Report IDO-22054.
- Rood, A. S., 2005, *Groundwater Transport Modeling Using Response Surface Modeling: Proof of Principle*, ICP/EXT-05-00952, Rev. 0, Idaho National Laboratory, Idaho Cleanup Project, June 2005.
- Spinazola, J. M., 1994, *Geohydrology and Simulation of Flow and Water Levels in the Aquifer System in the Mud Lake Area of the Eastern Snake River Plain, Eastern Idaho*, U.S. Geological Survey Water-Resources Investigations Report 93-4227.
- Wood, T. R., C. M. Helm-Clark, H. Huang, S. Magnuson, T. McLing, B. Orr, M. Roddy, M. J. Rohe, M. A. Plummer, and R. Podgorney, 2005, *Operable Unit 10-08 Summary Report on the Subregional-Scale Two-Dimensional Aquifer Model*, ICP/EXT-05-00979, Rev. 1, Idaho National Laboratory, Idaho Cleanup Project, October 2005.
- Zheng, Chanmiao, and P. P. Wang, 1999, *MT3DMS: A modular three-dimensional multi-species transport model for simulation of advection, dispersion and chemical reactions of contaminants in groundwater systems: Documentation and user's guide*, Contract report SERDP-99-1, Vicksburg, Miss., U.S. Army Engineer Research and Development Center, 169 p.

2. CONCEPTUAL MODEL OF THREE-DIMENSIONAL GROUNDWATER FLOW IN THE AREA REPRESENTED BY THE OU 10-08 MODEL DOMAIN

The conceptual model of groundwater flow in the SRPA within the area represented by the OU 10-08 model domain consists of the characterization of the hydrogeologic framework, including the extent and thickness of stratigraphic units and distribution of hydraulic properties, and the quantification of aquifer recharge and discharge. Elements of the conceptual model for this modeling effort have been presented in the *Operable Unit 10-08 Summary Report on the Subregional-Scale Two-Dimensional Aquifer Model* (Wood et al. 2005). The development of a three-dimensional model of groundwater flow and transport requires additional conceptual model documentation. The additional work was conducted during 2006 and is described in subsequent sections. Section 2.1 presents the three-dimensional characterization of hydrogeologic units. Section 2.2 describes characterization of hydrologic conditions, including three-dimensional regional inflow, three-dimensional characterization of water level and temperature data, and groundwater flow velocity estimates used for model calibration. Section 2.3 presents a discussion of conceptual model limitations.

2.1 Hydrogeologic Unit Characterization

The hydrogeologic framework of the SRPA consists of a complex system of numerous basalt flows, interbedded sediments, and other geologic structures that has resulted in three-dimensional heterogeneity of hydraulic and transport properties. The OU 10-08 groundwater modeling effort requires characterization of this complex system and identification of discrete hydrogeologic units that can be represented as layers in numerical models of groundwater flow and contaminant transport. Section 2.1.1 summarizes current understanding of the three-dimensional stratigraphic architecture of the area represented by the OU 10-08 model domain. Section 2.1.2 utilizes this three-dimensional characterization to delineate discrete hydrogeologic units within the SRPA. This delineation supports development of a layered model with distributed hydraulic properties. Detailed stratigraphic studies conducted during 2006 as part of this hydrogeologic unit delineation are provided in Appendix B.

2.1.1 Stratigraphic Conceptualization of the Basaltic SRPA in the Area Represented by the OU 10-08 Model

The eastern Snake River Plain is a 350-km long, 50-km wide region of lowered elevation and suppressed topography surrounded by elongated basin and range-style mountains and valleys. The OU 10-08 conceptual model study area encompasses the central third of the eastern Snake River Plain: its features include the Axial Volcanic High (AVH), a slightly-elevated constructional feature that is a locus of volcanic vents, eruptive fissures, shield volcanoes and rhyolitic domes (see Figure 2-1). This feature also is a drainage divide separating the Snake River watershed to the southeast from tributary watersheds to the northwest.

Another prominent feature within the study area is the Great Rift of Idaho, consisting of several fissure sets that cross the width of the Plain. The northern portion of the Great Rift is an eruptive Late Pleistocene to Holocene volcanic fissure complex at Craters of the Moon National Monument. South of Craters of the Moon, the Great Rift grades into multiple sets of Quaternary non-eruptive fissures. The southern end of the Great Rift switches back to eruptive fissures and flows which fed the Holocene Kings Bowl and Wapi Lava Fields. The Arco Rift is a second prominent volcanic rift in the study area, extending southeast from the town of Arco past Big Southern and Cedar Buttes. Appendix C describes the treatment of volcanic rifts.

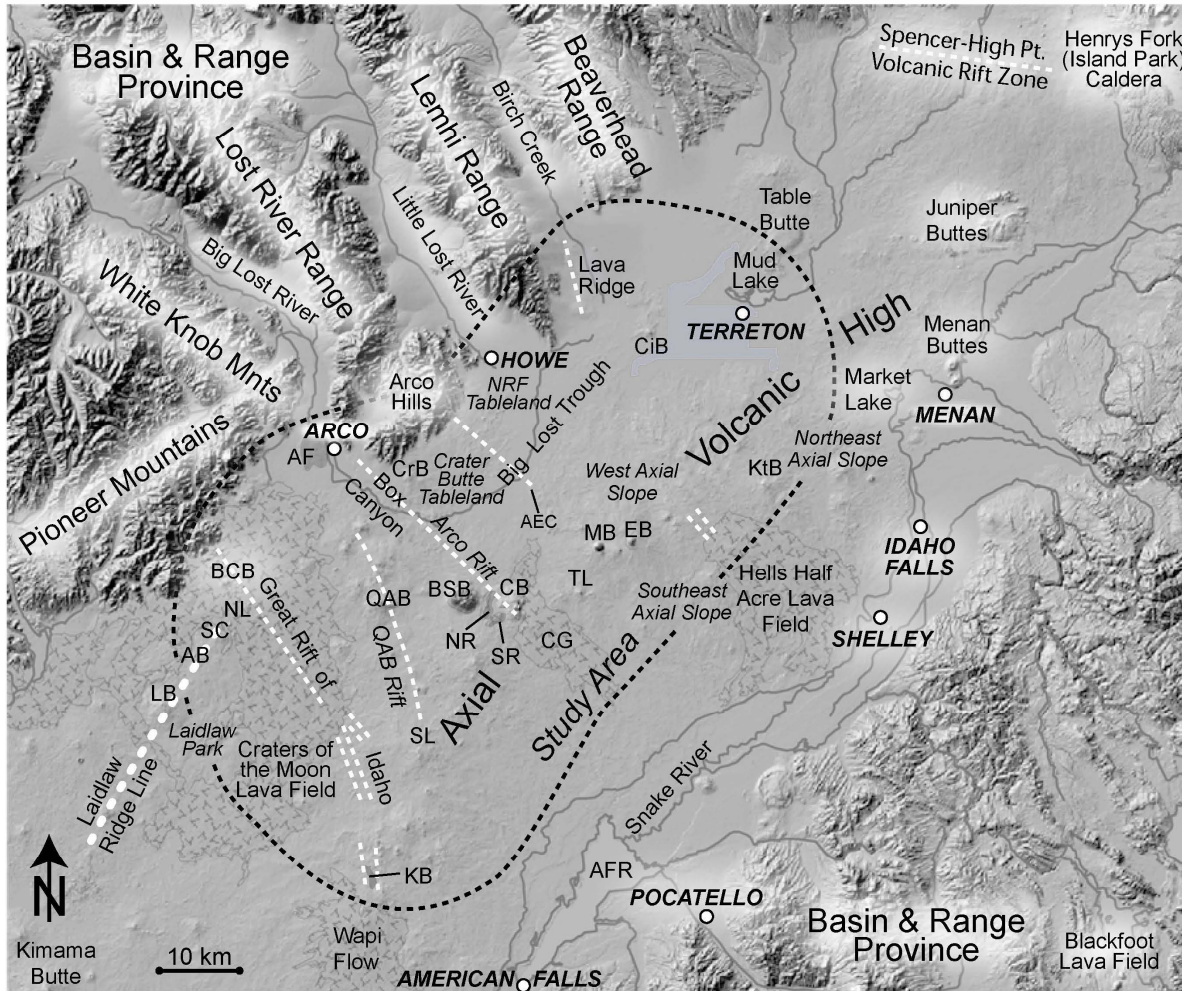


Figure 2-1. Geographical and geological features in the conceptual model study area. Lava fields less than 15,000 years old are denoted by the mottled background pattern. The approximate trends of volcanic rift zones are shown as dashed white lines. Map abbreviations are defined as follows: AB – Ant Butte; AEC - AEC Butte volcanic rift zone; AF – Arco lava flow; AFR – American Falls Reservoir; BCB – Big Cinder Butte; BSB – Big Southern Butte; CB - Cedar Butte; CG – Cerro Grande lava field; CiB - Circular Butte; CrB – Crater Butte; EB – East Butte; KB - Kings Bowl lava field; KtB – Kettle Butte; LB - Laidlaw Butte; MB – Middle Butte; NL – North Laidlaw Butte; NR - North Robbers lava flow; QAB – Quaking Aspen Butte; SC – Snowdrift Crater; SR – South Robbers lava field; TL - Table Legs Butte.

Surface-water features have contributed to sedimentary depositional processes on the eastern Snake River Plain. Tributary basins of the Big Lost River, the Little Lost River and Birch Creek drain onto the eastern Snake River Plain within the study area. The Big Lost River exits the basin and range and flows onto the eastern Snake River Plain at Arco. Because of the elevated topography of the volcanic centers around Quaking Aspen Butte, the Arco Rift, Craters of the Moon and the AVH, the Big Lost River is trapped within the Big Lost Trough, a closed depositional basin on the southern half of the INL. The sinks of both the Big Lost and Little Lost Rivers are also contained within the Big Lost Trough. The sinks of Birch Creek are located at the northern edge of the Big Lost Trough and are separated from the sinks of the Big Lost River and Little Lost River by the southern end of Lava Ridge. Circular Butte and the adjacent Antelope Butte (not shown in figure) separate the sinks of Birch Creek from Mud Lake. The AVH currently separates Mud Lake on the west side of the Plain from the now mostly-drained

Market Lake on the east side of the Plain. Market and Mud Lakes are the remnants of Lake Terretton, a large pluvial lake that extended from Howe to Menan during the last glacial period.

The AVH, volcanic rift zones, and tributary basin drainages have played an important role in the development of major geologic units and hydrogeologic subdomains within the study area. The following subsections describe our current understanding of these geologic units and hydrogeologic subdomains of the OU 10-08 conceptual model.

2.1.1.1 Major Geologic Units and Hydrogeologic Subdomains Composing the Snake River Plain Aquifer within the OU 10-08 Model Domain. Hydrogeologic subdomains are defined here as large-scale geologic features that exert control over groundwater flow by virtue of their intrinsic lithologic and stratigraphic properties. The OU 10-08 study area can be divided into four general hydrogeologic subdomains: volcanic tablelands, volcanic rifts and centers, sedimentary units, and the Big Lost River flood plain. The flood plain subdomain, as used in this report, is defined based on the fluvial and interfluvial geologic units as defined in Kuntz et al. (1994) and is not the same as the 100-year flood plain, which is smaller. The division of the study area into these hydrogeologic subdomains is based on geologic features in three dimensions, some of which have significant dips (for example, the buried lacustrine lake beds in the northern portions of the study area) and some of which are vertical (for example, the fissure and dike complexes of young volcanic rift zones like the Great Rift at Craters of the Moon at the southwest corner of the study area).

2.1.1.1.1 Volcanic Tablelands—The eastern Snake River Plain is an area of young volcanism. More than 98% of the SRPA is hosted in Pliocene to Holocene pahoehoe-type basalt flows erupted from low-shield volcanoes, lava tubes, and fissures (Figure 2-2). Once erupted, these basalts can travel anywhere from 0.1 km to more than 30 km from their eruptive vents as pahoehoe flows. No mapped basalt flow on the eastern Snake River Plain has traveled more than 90 kilometers from its vent; the average length of eastern Snake River Plain pahoehoe flows is approximately 12 km (C. Helm-Clark, unpubl. data, 2006^a; Jenks 1984) and the average thickness is 7 m (Knutson et al. 1992).

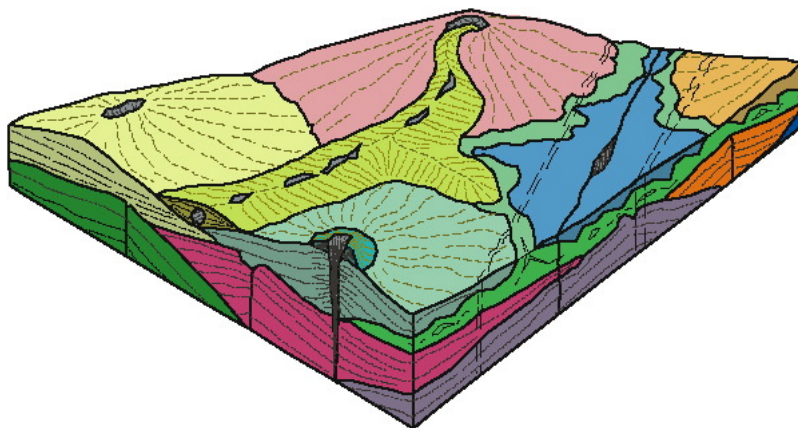


Figure 2-2. The four different eruptive styles seen on the eastern Snake River Plain: from the summit cone of a shield volcano, from the summit crater of a shield volcano, from a fissure, and from a lavatube. The eruptive fissure shown here is flanked by paired sets of non-eruptive fissures, a pattern sometimes observed for basalts on the eastern Snake River Plain and at other igneous provinces. This figure is modified from Greeley (1982).

a. Helm-Clark, C. M., INL, unpublished data, 2006.

The flow direction of lava is downhill away from vent areas. Flows stop traveling either because their source vents stop feeding magma or flows become trapped within topographic lows like the Big Lost Trough. The accumulation of basalt flows between elevated volcanic centers and topographic lows creates broad, mostly flat volcanic tablelands characterized by gradual topographic gradients. Because of their limited lateral extent, the basalts of the eastern Snake River Plain are not flood basalts and do not form the layer cake stratigraphy occurring in large flood basalt provinces like the Columbia River Plateau. Instead, the subsurface stratigraphy is dominated by coalescing low-angle shield volcanoes, lava tube-fed flows and fissure flows, all of limited size in an unordered stack.

Groundwater flow in these basalts occurs mainly in interflow zones. Interflow zones occur at the contact between the flow tops of underlying flows and the flow bottoms of overlying flows (Figure 2-3). Since flow tops and bottoms are typically vesicular and fractured, permeability in interflow zones is high. In contrast, the interiors of flows are dense, mostly unfractured and without vesicles. In comparison to interflow zones, the massive interiors of basalt flows are relatively impermeable. The sandwiching of high-permeability interflow zones and low permeability massive flow interiors results in a large ratio of horizontal to vertical hydraulic conductivity. This anisotropic groundwater flow system within the disordered stacking of coalescing flows results in large heterogeneity of horizontal and vertical groundwater flow. Because this stratigraphic pattern applies to over 98% of the rocks hosting the aquifer, it is safe to say that the character and distribution of interflow zones control groundwater flow. Anything that affects the interflow zones, for example, the deposition of sediments in interbeds between flow tops and bottoms, will also affect groundwater flow.

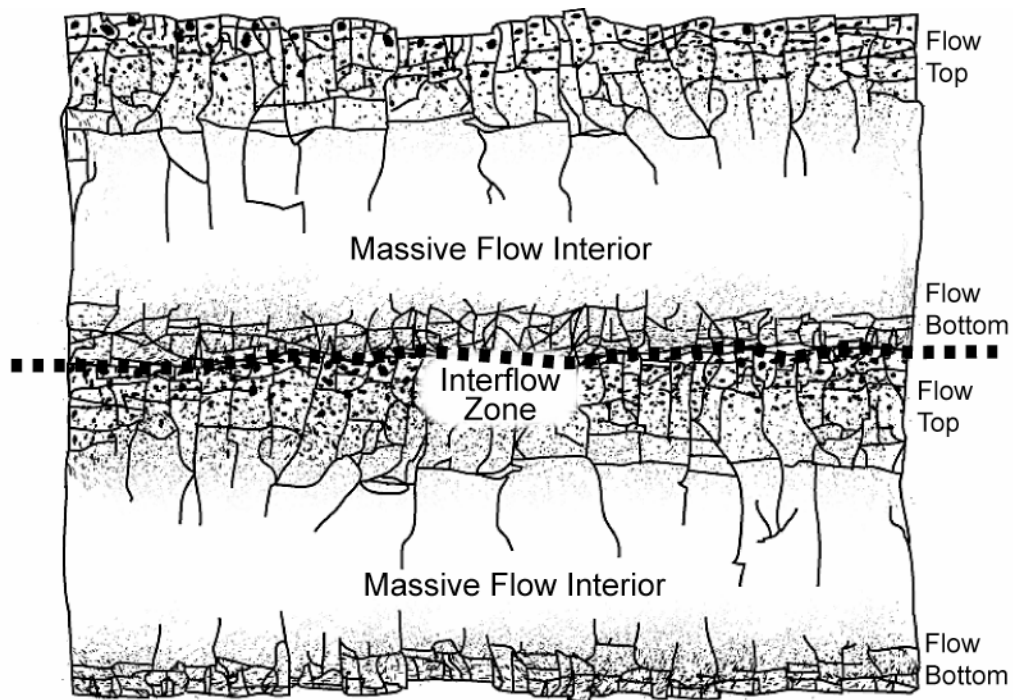


Figure 2-3. Diagram showing how the fractured and vesicular flow top of an underlying flow contacts the fractured and vesicular flow bottom of an overlying flow to form a permeable interflow zone that becomes the preferential pathway through the laterally and vertically heterogeneous stack of basalt flows.

The occurrence of sediments between flows is the most important variable in the permeability of the interflow zones. Volcanic tablelands are less favorable environments for sediment deposition than those of river beds, flood plains, and sinks, though they may include up to approximately 15% by volume of sedimentary materials, mostly as interbedded eolian loess. The volcanic tablelands subdomain includes terrain located in the vicinity of Table Butte, West Axial Slope, Crater Butte, Naval Reactors Facility, Quaking Aspen Butte, and the Southeast and Northeast Axial Slope as described below.

Table Butte Volcanic Tableland—This tableland, comprised of Table Butte and its surroundings is the most northerly area in the conceptual model study area (see Figure 2-1). Table Butte and neighboring volcanoes rise above the pluvial lakebeds in the northernmost part of the study area. These basalts are all older than 700 ka, and the vents of this tableland appear to be on the elevated circular plateau formed by these buttes. This tableland is north of the area represented by the boundary of the OU 10-08 numerical model.

West Axial Slope—This volcanic tableland was fed from vents along the AVH, with a small amount of basalt on its southern end originating from the Arco Rift. The subsurface of this tableland also hosts thick, south-dipping sequences of mixed lacustrine sediments and basalt, which are treated as geologic units in their own right and are discussed in more detail as sedimentary subdomains in Section 2.3.

Crater Butte Volcanic Tableland—The basalts of this tableland originated from Crater Butte and other Arco Rift vents or from the now-inactive and mostly-buried AEC Butte Rift. Along its western boundary, the basalts of this tableland interfinger with ancestral flood plain deposits of the Big Lost River. A thick sequence of sediments occurs deep in the subsurface of this subdomain, but this sequence lies below the base of the aquifer and does not affect groundwater flow in the SRPA.

Naval Reactors Facility Volcanic Tableland—The basalts of this tableland originated from vents along the AEC Butte Rift or from unidentified vents to the north and northeast. The deepest borehole to date on the eastern Snake River Plain (geothermal exploration well INEL-1) is located on this tableland. Well INEL-1, which was drilled to 10,000 ft below land surface, completely penetrated the SRPA, the Plio-Pleistocene basalt cover, a thick sequence of rhyolitic tuffs and bottomed in rhyolite (Doherty, McBroome, and Kuntz 1979). The subsurface of this tableland hosts a thick, south-dipping sequence of sediments that is treated as a hydrogeologic unit in its own right and is discussed in the subsequent section on sedimentary subdomains.

Quaking Aspen Butte Volcanic Tableland—This subdomain includes all of the tableland basalts between the Great Rift and the Arco Rift. The postulated Quaking Aspen Butte rift feature runs through the center of this tableland. Because it lies within the loci of three active or recent rift features, this tableland is higher than all other volcanic tablelands on the eastern Snake River Plain. Its elevation leaves it more exposed to wind and wildfire, the two processes that act together to strip vegetation and retard soil formation and sediment accumulation. As a result, the sediment-to-basalt ratio is lower here compared to other tablelands, less than 10% versus less than 15% elsewhere. Because of its proximity to three volcanic rifts, the amount of cinder and ash in the subsurface is higher here than elsewhere in the conceptual model study domain.

Southeast and Northeast Axial Slope—The volcanic tablelands east of the AVH receive more precipitation than the volcanic tablelands west of the AVH, which are in the rain shadow of the mountains to the northwest of the study area. Volcanic tablelands on the east side of the eastern Snake River Plain are also within the watershed of the Snake River, which provides more water and deposits more sediment than the rivers that feed the Big Lost Trough. The volcanic tablelands on the east side of the eastern Snake River Plain may, therefore, have more interbedded sediment of coarser character in the subsurface as one

approaches the Snake River. The tableland of the east slope of the AVH is divided into two areas, where the dividing line coincides with the non-eruptive fissures and the elongated vent of the Hell's Half Acre lava field and rift feature. Basalts north of this line originate from the AVH or from the nexus of volcanic vents centered on Butterfly and Kettle Buttes west of Idaho Falls, just outside of the study area. Tableland basalts south of the Hell's Half Acre line originate from the AVH or from off-axis vents like Taber Butte. Because the southeast boundary of the conceptual model is closer to the AVH than to the Snake River, Axial Slope tablelands in those areas should contain less than 15% sediments.

2.1.1.1.2 Volcanic Rifts and Centers—Volcanic rifts within the area of the OU 10-08 model domain are defined as linear arrays of volcanic landforms and structures, including non-eruptive fissures, faults, and grabens. These volcanic rifts are oriented NW-SE, perpendicular to the direction of groundwater flow and are characterized by extensional tectonics, elevated heat flux and geothermal features, linear trends with volcanic vents, faults and cracks associated with the motion and emplacement of volcanic dikes that may or may not reach the surface.

Increased hydraulic gradients and reduced hydraulic conductivity occur in proximity to some rift zones. These hydraulic effects have been attributed to the occurrence of dikes within the SRPA. However, because little evidence exists to verify existence of dikes cutting the SRPA, other explanations may be viable. The OU 10-08 geologic conceptual model restricts itself to rift features whose existence are beyond doubt or rift features that are known or suspected to have an influence on groundwater flow. Rifts may restrict groundwater flow through emplacement of a mass of coalescent adjacent dikes along a rift, clogging of non-eruptive fissures through sediment infiltration, concentration of relatively low-permeability near-vent rocks like cinder and ash, or by any combination of these. A few isolated dikes likely are insufficient barriers to groundwater flow by themselves. Indeed, certain rift features may instead represent increased permeability for groundwater flow, particularly through the creation of open fractures, faults and non-eruptive fissures.

The AVH, although not defined as a volcanic rift, is a volcanic center oriented N-S along the axis of the eastern Snake River Plain. The AVH is characterized by several geologic features similar to those of rifts. Volcanic rifts and the AVH affect the distribution of hydraulic properties and groundwater flow at local and subregional scales. These features, shown on Figure 2-1, and their effect on groundwater flow, are described in subsequent sections.

The Great Rift of Idaho—The Great Rift of Idaho is the largest active volcanic rift on the eastern Snake River Plain. It is formed by four major overlapping fissure sets. The northern and southern fissure sets are eruptive. The southern portion of the rift shows paired non-eruptive fissures flanking a central eruptive fissure at the low-volume King's Bowl lava field. The vents of the larger Wapi lava field to the south are in line with the King's Bowl eruptive fissure. Both the Wapi and King's Bowl lava fields are among the youngest flows on the eastern Snake River Plain, at 2.3 and 2.2 ka respectively (Kuntz et al. 1986). The fissures on the southern portion of the Great Rift trend approximately N10W.

The eruptive northern portion of the rift is the source of the Craters of the Moon lava field, the largest mapped lava field on the eastern Snake River Plain. It consists of paired discontinuous segments of eruptive fissures and overlying cinder and spatter cones through which almost all of the flows of the Craters of the Moon lava field have erupted. Dated flows of the Craters of the Moon field span ages of 15 to 2 ka, so the 42 Craters of the Moon eruptions have been fed from the same fissure complex over thousands of years (Kuntz et al. 1988; Kuntz et al. 2004). If any rift on the Plain were to fit the model of multiple coalescing feeder dikes in the subsurface that could both impede groundwater flow and have sufficient cumulative thickness to display a positive magnetic potential anomaly, it is the northern eruptive portion of the Great Rift at Craters of the Moon. The northern Craters of the Moon fissure set trends approximately N35W.

Between the eruptive northern and southern portions of the Great Rift, are the two central fissure sets, the Minidoka and New Butte sets. The Minidoka set appears to be a non-eruptive extension of the Craters of the Moon eruptive fissure complex and has the same N45W trend. The almost-overlapping New Butte set immediately to the south trends approximately N25W. Both of these sets display the paired non-eruptive fissure patterns indicative of dike intrusion at depth.

The northern and southern portions of the Great Rift may present barriers to groundwater flow while the two central non-eruptive fissure sets should pose no impediment to flow on the assumption that the dikes at depth do not penetrate into the aquifer and that the non-eruptive fissures of the open crack sets may actually improve hydraulic conductivity. The Great Rift of Idaho also forms the southwest boundary of the groundwater model domain.

The Arco Rift—The Arco Rift is a northwest-oriented feature that is approximately 4 km wide. Its active portion is between the 49 ka Arco flow (Olig et al. 1997) west of the town of Arco,^b and the vents of the 13.4-ka Cerro Grand Lava Field south of Atomic City. The oldest dated feature along the Arco Rift is Cedar Butte at approximately 400 ka. Between the 12-ka North and South Robbers flows and the Arco flow are several non-eruptive Quaternary fissures and vertical normal faults, two of which control the path of the Big Lost River as it cuts across the Arco Rift through Box Canyon (Kuntz et al. 1994). The northernmost portion of the Arco Rift hosts two fissure-and-graben features that may be indicative of dike emplacement at depth. The base of the aquifer is also shallower under the Arco Rift, comparable to the shallow aquifer base under the AVH between East and Middle Butte.

Quaking Aspen Butte—The Quaking Aspen Butte Rift is a northwest-oriented linear feature made up of several shield volcanoes, whose center line is located somewhat equidistant between the Great Rift at Craters of the Moon and the Arco Rift. Many prior descriptions of eastern Snake River Plain geology usually include the features of the Quaking Aspen Butte rift as part of the Arco Rift. It is treated as distinct from the Arco Rift in the conceptual model for morphometric reasons. A broad NNW-SSE trending topographic swell extends southeastward from the northwest edge of the plain near Arco to intersect with the AVH between Rock Corral and Mosby Buttes. The Arco Rift and Great Rift of Idaho are located on the flanks of this swell and the shield volcanoes of the Quaking Aspen Butte rift feature occur on the swell's central crest. This feature is considered as recently inactive since the ages of many of the shield volcanoes along this trend date from the Late Pleistocene between 40 and 64 ka (Kuntz et al. 2004). They form a linear elevated trend of coalescing shield volcanoes which extends from Wildhorse Butte on its north end to Packsaddle Butte in the south. The Quaking Aspen Butte rift might account for the possible low-transmissivity feature responsible for the sudden head drop at the Site-2 well in the Quaking Aspen Butte volcanic tableland between the Arco and Great Rifts.

Lava Ridge—Lava Ridge is an inactive rift formed by a 8-km (5-mi) -long line of coalesced shield volcanoes with ages between approximately 800 ka and approximately 1 Ma (Kuntz et al. 1994; Hughes, McCurry, and Geist 2002). This rift feature appears to influence the local flow of groundwater northeast of Test Area North (TAN). The trend of vents associated with Lava Ridge is approximately N15W.

Hell's Half Acre Flow—The Hell's Half Acre lava field is a 400 km² Holocene field of pahoehoe basalt dated at 5.1 ka (Kuntz et al. 1994). The Hell's Half Acre vents and fissure set are located on the north end of the lava field, on the east flank of the AVH. Along the northwest edge of the flow, paired non-eruptive fissures trending approximately N50W disrupt a thin loess cover and underlying approximately 350-ka basalts, extending from the edge of the lava field northwestward toward Route 20 over a distance of 4 km. Approximately 6 km to the southeast and in line with the fissure set is the 0.9-km-long linear crater which is the main eruptive edifice of the Hell's Half Acre lava field, followed

b. Forman, S., unpublished data provided to R. P. Smith, 1997.

by a further 1-km-long “tail” of cinder and spatter cones along the same trend as the elongated crater vent (Karlo 1977). From the most southeastern cinder cone to the northwestern terminus of the paired fissure is a distance of 12 km, which is the minimum length of the feeder dike responsible for the fissure-and-vent complex of the Hell’s Half Acre flow. As Kuntz et al. (2002) have pointed out, the lengths of the feeder dikes for the volcanic rift zones on the Plain typically are 20 to 40 km long.

As a Holocene feature, the Hell’s Half Acre fissure-and-vent complex should be classified as an active rift. As the data and analysis supporting the conceptual model have been refined, some doubt has arisen about classifying this feature as a rift. A correlation between modern magnetic anomaly data (Mankinen et al. 2004) and the vent-and-fissure set of Hell’s Half Acre may exist but it is not unambivalent. There also appear to be no marked hydraulic gradient changes, though well coverage is admittedly sparse in this area. The Hell’s Half Acre fissure-and-vent complex may be a case of one fissure, one dike, one eruption—too thin to have magnetic contrast or to impede groundwater flow.

AEC Butte Rift—The surface expression of the AEC Butte Rift is a northwest-oriented line of three volcanic vents, including the 626-ka AEC Butte (Kuntz et al. 1994) immediately northwest of the Reactor Technology Complex. The rift extends across the flood plain of the Big Lost River to the Idaho Nuclear Technology and Engineering Center (INTEC), where scoria and other near vent facies occur at approximately 90 m below land surface at the INTEC tank farm. The thickness and dip of flows at the Reactor Technology Complex also indicate that a vent or vents existed to the east of the flood plain between 640 and 350 ka (Helm-Clark et al. 2005). This rift feature might be the cause of lower transmissivity zones in the aquifer at INTEC and north of the Reactor Technology Complex (Anderson, Kuntz, and Davis 1999).

Axial Volcanic High—The AVH is the largest, highest, and longest feature on the eastern Snake River Plain, extending from the northeast to the southwest along the axis of the plain. It is not an active volcanic rift *per se*, though it shares many of the same characteristics of active rifts, namely relatively elevated topography plus many volcanic vents and shield volcanoes coalescing to form one long linear feature. In contrast to rifts like the Great Rift of Idaho, however, the AVH is a volcanic center that is aligned approximately parallel to the general direction of groundwater flow in the SRPA. The AVH lacks the alignment of elongated vents and fissures that define a volcanic rift for Kuntz, Covington, and Schorr (1992), though there are a small number of aligned vents on the AVH sub-parallel to the axis of the Plain in the vicinity of Rock Corral Butte. In terms of stratigraphy, the eruptive rocks of the AVH are derived from small basaltic vents and from large rhyolitic laccoliths like Big Southern Butte. The off-axis rocks on the flanks of the AVH are mostly volcanic tableland basalts with one difference: heat flow is larger under the AVH, especially between East and Middle Buttes. The AVH within the study area has a higher heat flux than its surroundings, resulting in a thicker transition between the aquifer and underlying low-permeability rocks and a shallower depth to the base of the aquifer in places.

Sedimentary Units—The OU 10-08 groundwater model study area includes several areas where the volcanic rocks are mantled or interbedded with thick sequences of fine-grained sediments. The occurrence of these sedimentary sequences within the SRPA likely reduces hydraulic conductivity of the aquifer. These sedimentary sequences, consisting of deep lacustrine sediments, Lake Terreton and other pluvial sediments, and ponded river sediments, are described in subsequent sections. Since it is impractical to segregate every sediment unit as a separate entity in the numerical model, some of the hydrogeologic units chosen as input to the numerical model are composite basalt+sediment sequences whose hydrologic conductivity is presumed to be controlled by the sediments.

Deep Lacustrine Sediments—The subsurface of the West Axial Slope tableland hosts a thick sequence of sediments named the Olduvai Lake bed (Bestland et al. 2002; Blair and Link 2000) because its age corresponds to the Olduvai normal polarity subchron of the paleomagnetic time scale, dated

between 1.77 and 1.95 Ma (Cande and Kent 1995). In the extreme northern portion of the OU 10-08 study area, the Olduvai Lake sediments are shallow and lie above the SRPA stratigraphically. Like most of the other deep sedimentary strata in the study area, these beds dip gradually to the south. Under TAN, the Olduvai beds intersect the SRPA. In the subsurface at Well 2-2A, the Olduvai beds are sandwiched between tableland basalts in the middle of the aquifer. Under INTEC to the south, these beds have dipped beneath the SRPA, as shown in Figure 2-4.

Other lacustrine sequences occur in the subsurface including the Pillow lakebed (Blair 2002) but this particular lakebed is parallel and in close proximity to the Olduvai beds; the Pillow lake sediments behave like the Olduvai beds, dipping south through the aquifer and into the sub-aquifer zone.

Lake Terreton and Other Pluvial Lakebeds—During glacial periods, pluvial lakes formed on the relatively flat eastern Snake River Plain, leading to widespread deposition of lacustrine sediments on top of basalt (see Figure 2-5). In the northern half of the study area, the playa deposits of Birch Creek, the Big Lost and Little Lost River sinks, and the modern Mud and Market lakes are remnants of the most recent pluvial lake known as Lake Terreton (Stearns, Crandall, and Stewart 1938). Pluvial lakebeds are also present in the shallow subsurface stretching from Howe in the west, the Birch Creek Diversion Channel in the north, and Terreton in the east. These deposits form a thick mantle of lacustrine sediments on top of volcanic tableland basalts in much of the northern half of the study area. The base of the Lemhi Range and adjacent shield volcanoes west of TAN divide the pluvial lakebeds and the modern sinks into northern and southern sections. The northern section includes Mud Lake and the sinks of Birch Creek. The southern section includes the pluvial lake beds in the subsurface between TAN and the Naval Reactors Facility and the sinks of the Big Lost and Little Lost Rivers. More than one episode of Pleistocene glaciation occurred as evidenced by a second shallow pluvial sequence in the West Axial Slope subsurface in the center of the INL, which is penetrated by Well Site-14.

Ponded River Sediments—Rivers flowing onto the eastern Snake River Plain from the neighboring intermountain valleys often become trapped at the mouths of those valleys when their river channels are dammed by lava flows. When rivers are trapped this way, the trapped ponded sediments interfinger with eastern Snake River Plain basalt flows. These sediments are mostly fine-grained but do include some coarser sands and gravels. A distinctive feature of these ponded sediments is their extension outward onto the eastern Snake River Plain. Within the area represented by the OU 10-08 model domain, these ponded sediments occur at the mouths of the tributary valleys of the Big Lost River, Little Lost River, and Birch Creek. The most extensive of these ponded sediment beds occurs at the mouth of the Big Lost River valley, extending 12 km into the eastern Snake River Plain subsurface south of Arco where it is observed as far south as the Site-1 well of Section 22, Range 26 East, Township 2 North.

The recognition and subsurface mapping of these ponded sediments is based on the stratigraphic analysis of drillers' and geologists' logs from 157 wells in the Arco area and 149 wells in the Howe area. Additionally, gravity data indicates that a tongue of lower density material appears to extend southward and then southwestward from the valley of the Little Lost River onto the eastern Snake River Plain. The extent of these ponded sediment sequences is clear in the Arco area; however, given the current data set for the Howe area, it is sometimes not possible to distinguish between ponded river sediments spreading out onto the Plain from pluvial lakebed sediments spreading toward Howe and into the valley of the Little Lost River.

The process of ponding river sediments behind a lava dam is not unique to the three tributary rivers of the study area. Similar sediment sequences occur along the southeast border of the eastern Snake River Plain; these sequences formed when the Snake River was trapped by lava dams, and include the Raft River Formation and American Falls lake beds (Houser 1992).

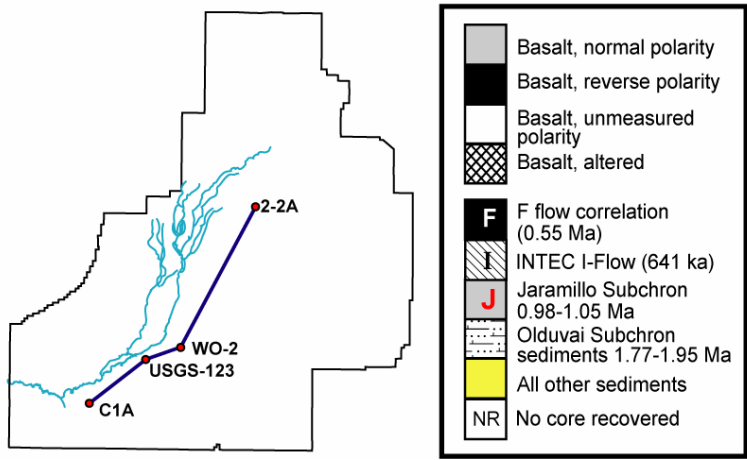
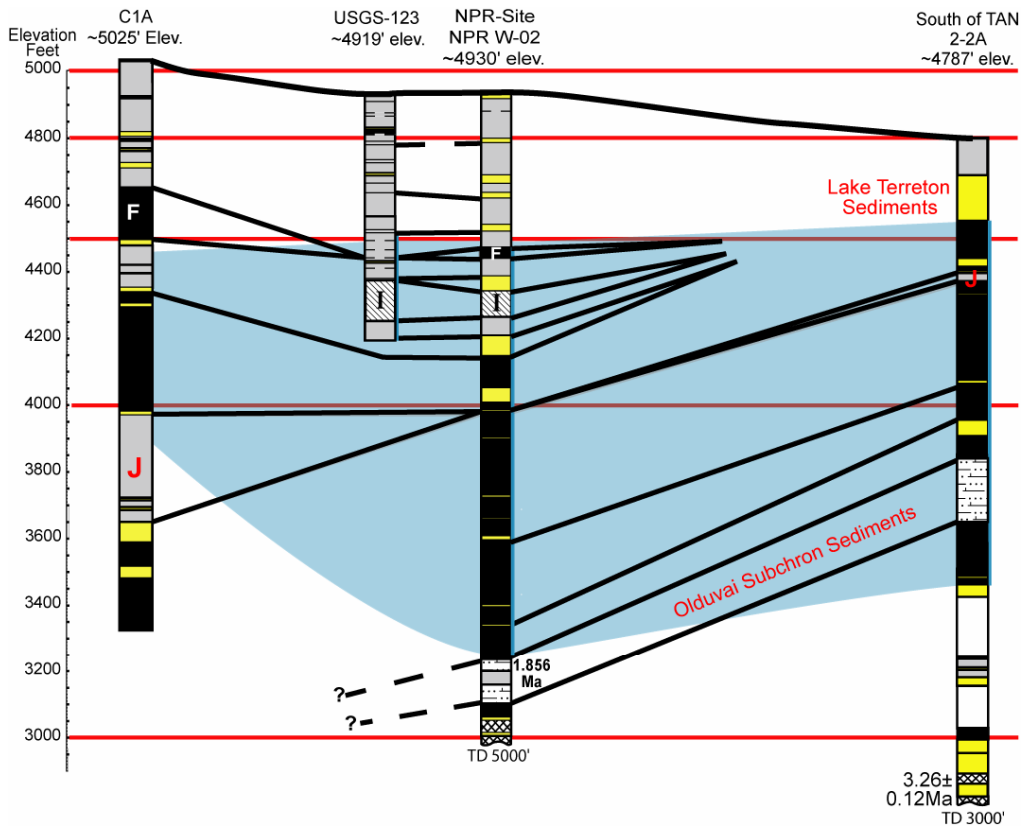


Figure 2-4. Fence diagram oriented from the southwest to northeast across the INL showing the Olduvai lakebeds dipping to the south and intersecting the effective base of the SRPA. Dipping sediment packages like this one are potential agents of groundwater flow path refraction which in turn might be the causative mechanism for the observed differential head measurements in the northeast portion of the INL, where the head at the base of the aquifer is greater than the head at the top of the aquifer. On this figure, grey intervals have normal polarity paleomagnetic remanence; black intervals have reverse polarity, and white intervals are unmeasured due to lack of core recovery. The letter F denotes the position of the F flow marker bed and the I denotes the position of the INTEC I flow (Anderson et al. 1996). J denotes the interval interpreted by Helm-Clark and Rodgers (2004) as belonging to the Jaramillo normal-polarity Subchron. The blue shading shows the profile of the aquifer.

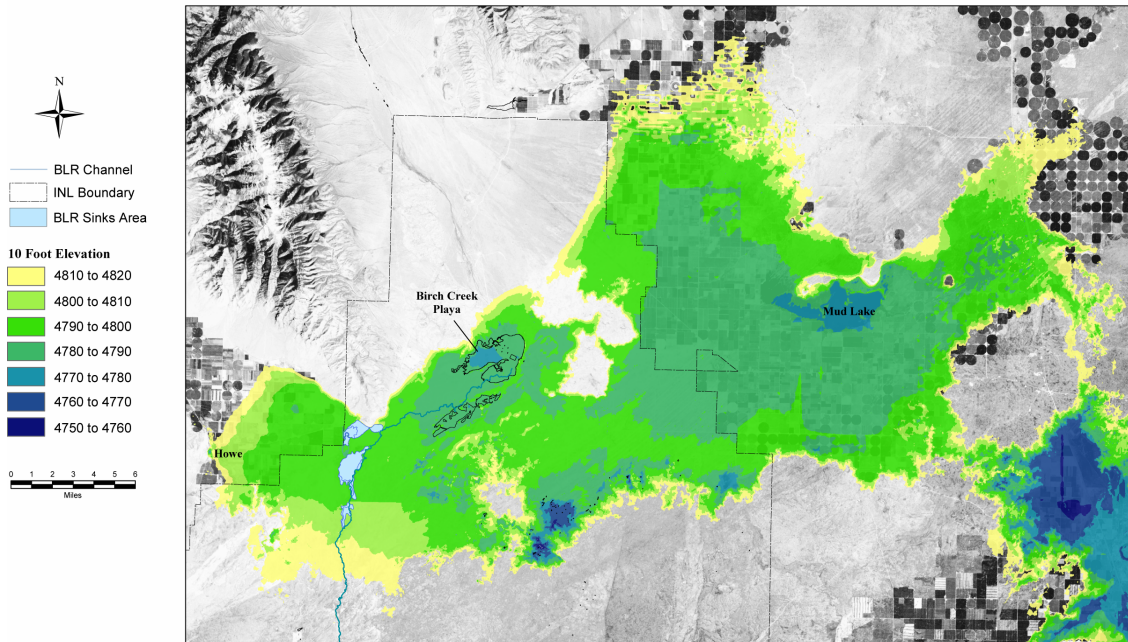


Figure 2-5. Interpreted extent of pluvial Lake Terreton based on modern elevations.

2.1.1.1.3 Big Lost River Flood Plain—Geologically, the flood plain of the Big Lost River is the most complex portion of the study area, where meandering braided fluvium interfingers with pahoehoe basalts originating from several different volcanic centers surrounding the Big Lost Trough. Sediments and basalt flows have deposited in the flood plain coming from three different directions (Figure 2-6), making a very complex stratigraphic column in the subsurface under the path of the river. An additional complication is the fact that basalt flows that entered the flood plain area from the west and southwest are 61 to 122 m (200 to 400 ft) higher in elevation than flows of equivalent age that entered the flood plain area from the AVH to the east and southeast. This stratigraphic disparity is discussed in detail in Appendix B.

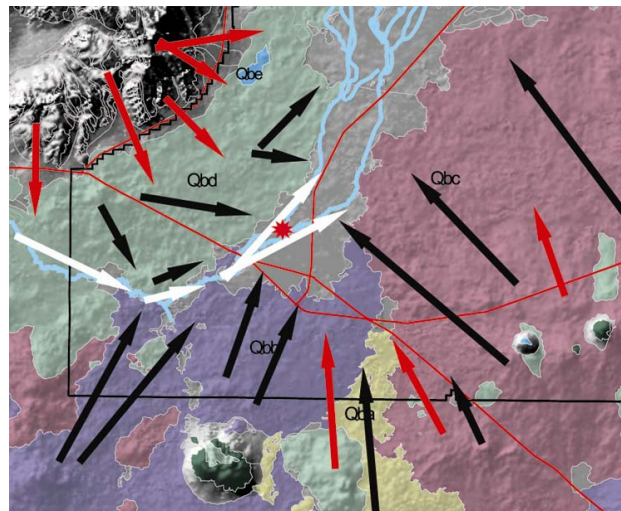


Figure 2-6. Simplified diagram of deposition directions for lavas (black arrows), slope wash alluvium (red arrows), and fluvium (white arrows) on the flood plain of the Big Lost River. Blue lines are river channels. Red lines are roads. The black line is the southwest boundary of the INL. This figure was modified from Helm-Clark et al. (2005). The flood plain is based on the geologic units defined in Kuntz et al (1994).

2.1.2 Derivation of Hydrogeologic Units

Conceptual and numerical models of three-dimensional groundwater flow and contaminant transport within the SRPA at the INL require identification of large-scale effective hydrogeologic units. A hydrogeologic unit is defined here as a body of geologic material that can be characterized by a specified range of hydraulic properties and that constitutes a distinct hydrologic subsystem within the SRPA. Identification of these units is a challenging task because of the complex nature of the basaltic aquifer, comprised of an intercalated sequence of basalt flows, interflow zones, and sedimentary interbeds, all of which exhibit a high degree of variability in their hydraulic properties and distribution both spatially and vertically. The architecture of basalt-flow sequences, presence or absence of sediments, and local structural features exert significant control over groundwater flow. Subsequent sections describe the methodology used to identify hydrogeologic units in support of the OU 10-08 three-dimensional groundwater and contaminant transport modeling study.

Identification of hydrogeologic units began with selection of characteristic wells that represented the general character of the subsurface in the vicinity of the well. The vertical sequence of hydrogeologic units was delineated in individual wells and these delineations were used to generate a series of cross sections within the area represented by the OU 10-08 model domain. Cross sections were then extrapolated to construct three-dimensional “solids” that characterized the entire aquifer volume within the area. These solids in turn were used to develop the vertical and areal distribution of the numerical grid and to assist in the initial distribution and range of hydraulic properties. Subsequent sections discuss the identification of hydrogeologic units in characteristic wells, development of hydrogeologic cross sections, construction of three-dimensional solids representing hydrogeologic units throughout the model domain, and assignment of ranges of hydraulic properties to the solids to be used in inverse modeling runs.

2.1.2.1 Hydrogeologic Unit Identification in Characteristic Wells. A total of 41 wells, located as shown on Figure 2-7, were selected as characteristic wells. The criteria for selection included well penetration of at least 50 percent or more of the active aquifer (based on the estimated aquifer thickness as described in Wood et al. [2005]) and existence of a reasonable set of geologic, hydrologic, and geophysical data that could be used to delineate discrete hydrogeologic units. Table 2-1 lists these characteristic wells and provides general information on their location and depth in relation to the active aquifer thickness.

Delineation of hydrogeologic units within characteristic wells was based upon analysis of geophysical logs and core lithologic data collected throughout the active portion of the aquifer. Geophysical logs that provided substantial stratigraphic information included the natural gamma log (to identify areas with high amounts of sediments), gamma-gamma log (density), neutron log (to identify interflow zones and dense basalts), and temperature logs (to provide an indication of alteration in the basalt and/or changes in water flow velocity or mixing).

Up to four basalt-dominated hydrogeologic units and up to six sediment-dominated hydrogeologic units were identified in the 41 characteristic wells. The basalt-dominated hydrogeologic units were identified as the Upper Aquifer Unit (UP_AQ), Mid-Aquifer Unit (MID_AQ), Base Mid-Aquifer Unit (BS_MID_AQ), and Basal Aquifer Unit (BS_AQ). The BS_AQ was further subdivided into upper and lower parts in order to aid with subsequent delineation of aquifer solids within the Groundwater Modeling System (GMS) program. These hydrogeologic units comprise much of the transmissive section of the aquifer. They are laterally continuous over large areas but may not be present in all locations and in all wells. The six sediment-dominated hydrogeologic units are located in the vicinity of the Big Lost Trough. These six hydrogeologic units exhibit only limited lateral continuity. Table 2-2 presents a correlation of hydrogeologic units to the four hydrogeologic subdomains identified within the OU 10-08 model domain.

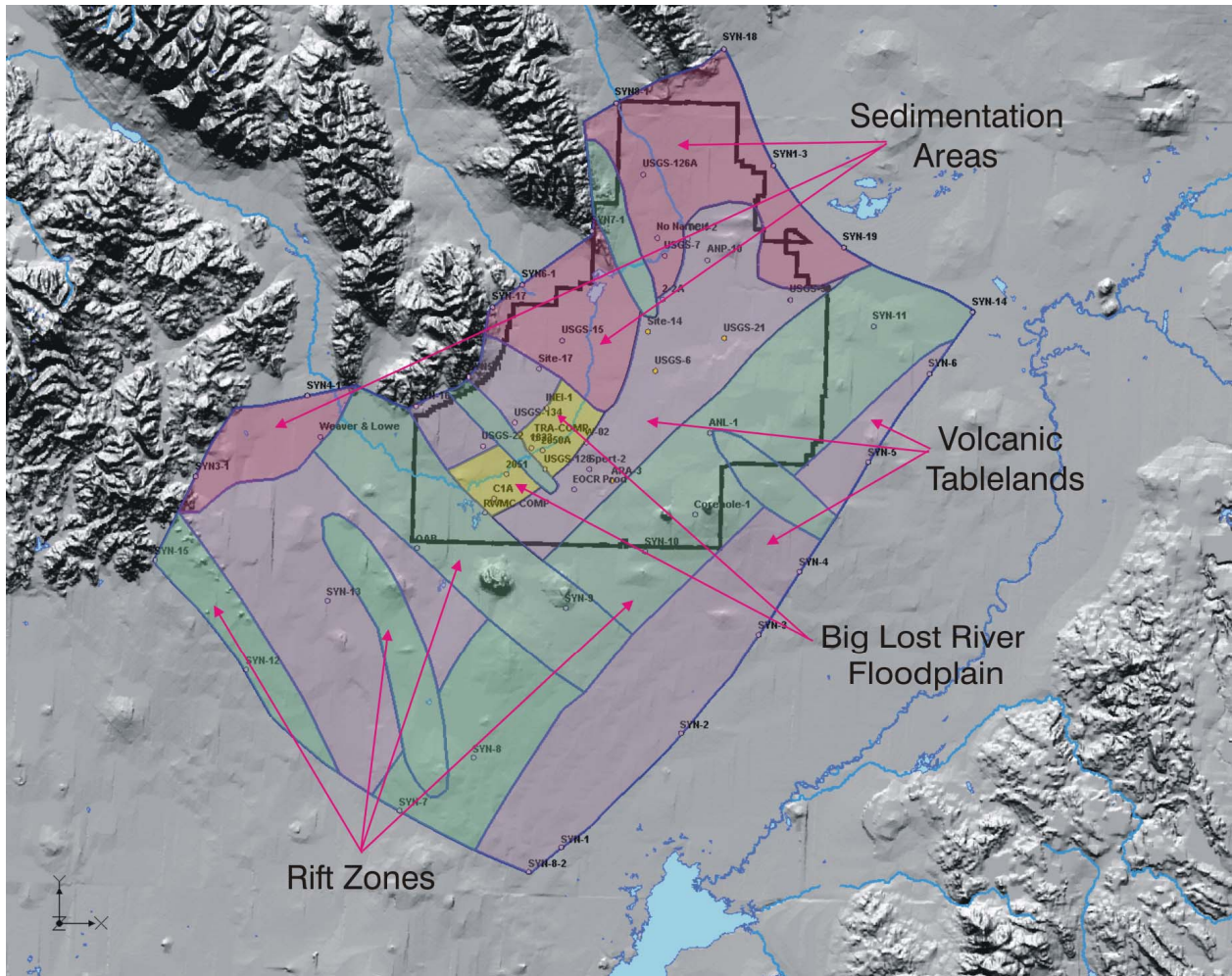


Figure 2-7. Numerical model domain with geologic subdomains and aquifer wells identified.

Table 2-1. Operable Unit 10-08 characteristic wells.

Well Name	Maximum Well Depth (m)	Aquifer Bottom Elev (m)	Water Table Elev (m)	Land Surface Elev (m)	Well Bottom Elev (m)	Penetration Thickness (m)	Aquifer Thickness (m)	Percent Exposed
INEL-1	3149.3	1243.0	1361.0	1495.0	-1664.2	3025.2	118.0	2563.70%
NPR-W-02	1523.9	998.0	1359.0	1498.0	-21.2	1380.2	361.0	382.34%
USGS-015	456.3	1230.0	1368.0	1473.0	1010.5	357.5	138.0	259.06%
C1A	550.1	1202.0	1348.0	1538.0	981.5	366.5	146.0	251.05%
COREHOLE 2A	914.4	1045.0	1379.0	1464.0	544.7	834.3	334.0	249.79%
NRF-S5G	408.4	1213.0	1362.0	1485.0	1069.5	292.5	149.0	196.31%
USGS-134	280.4	1297.0	1357.0	1528.0	1247.6	109.4	60.0	182.34%
COREHOLE 1	610.2	1161.0	1356.0	1651.0	1026.5	329.5	195.0	168.96%
TRA DISPOSAL	388.6	1200.0	1356.0	1503.0	1111.9	244.1	156.0	156.49%
MIDDLE-2051	359.3	1223.0	1351.0	1524.0	1164.7	186.3	128.0	145.59%
USGS-132	377.3	1205.0	1347.0	1539.2	1161.8	185.2	142.0	130.39%
Middle-2050A	434.9	1113.0	1356.0	1504.0	1067.1	288.9	243.0	118.91%
TRA-04	294.1	1218.0	1357.0	1503.0	1203.4	153.6	139.0	110.48%
SITE-19	263.6	1246.0	1356.0	1507.0	1237.8	118.2	110.0	107.42%
USGS-007	365.7	1054.0	1390.0	1460.0	1094.0	296.0	336.0	88.10%
ANL-OBS-A-001	528.5	979.0	1363.0	1562.0	1032.3	330.7	384.0	86.12%
RWMC-MON-A-066	300.5	1214.0	1347.0	1542.0	1236.7	110.3	133.0	82.91%
TCH-2	337.6	1061.0	1392.0	1460.0	1122.5	269.5	331.0	81.41%
EBR-1	327.6	1154.0	1349.0	1529.0	1203.6	145.4	195.0	74.55%
USGS-012	210.9	1221.0	1365.0	1478.0	1258.0	107.0	144.0	74.29%
TRA-02	235.3	1221.0	1356.0	1504.0	1262.7	93.3	135.0	69.14%
WEAVER AND LOWE	312.4	1264.0	1392.0	1641.0	1306.5	85.5	128.0	66.80%
USGS-030	306.8	1036.0	1376.0	1461.0	1154.6	221.4	340.0	65.11%
USGS-OBS-A-126A	190.2	1290.0	1396.0	1527.0	1330.3	65.7	106.0	61.99%
QAB	339.8	1180.0	1338.0	1586.0	1242.0	96.0	158.0	60.76%
SITE-17	182.9	1265.0	1363.0	1493.0	1304.6	58.4	98.0	59.56%
USGS-133	249.3	1156.0	1359.0	1490.4	1241.1	117.9	203.0	58.09%
EOCR PROD WELL	377.0	965.0	1352.0	1503.0	1128.6	223.4	387.0	57.73%
SPERT-2	370.9	959.0	1354.0	1494.0	1129.8	224.2	395.0	56.77%
ARA-3	408.4	961.0	1353.0	1521.0	1131.3	221.7	392.0	56.55%
USGS-079	214.0	1235.0	1356.0	1508.0	1289.0	67.0	121.0	55.40%
M4D	255.4	1217.0	1347.0	1541.0	1275.4	71.6	130.0	55.09%
HIGHWAY-3	228.6	1234.0	1352.0	1521.0	1289.7	62.3	118.0	52.77%
SITE-09	347.5	959.0	1352.0	1497.0	1153.9	198.1	393.0	50.40%
SITE-14	218.4	1063.0	1373.0	1476.0	1242.7	130.3	310.0	42.04%
ANP-10	207.6	1053.0	1390.0	1464.0	1251.2	138.8	337.0	41.19%
OMRE	287.3	964.0	1352.0	1503.0	1217.2	134.8	388.0	34.73%
NO NAME 01	167.6	1071.0	1393.0	1467.0	1290.6	102.4	322.0	31.79%
TAN-22A	162.6	1059.0	1392.0	1460.0	1296.4	95.6	333.0	28.71%
Middle-1823	219.4	1195.0	1355.0	1510.0	1286.0	69.0	160.0	43.13%
USGS-022	200.2	1293.0	1352.0	1553.0	1338.5	13.5	59.0	22.82%

Table 2-2. Correlation between hydrogeologic subdomains and hydrogeologic units within the area represented by the OU 10-08 model domain.

Hydrogeologic Subdomain		Hydrogeologic Unit	Identifier
Basalt-dominated subdomains	Volcanic tablelands (widely distributed basalt flows characterized by small percentage of sedimentary interbeds)	Upper Aquifer Unit	UP_AQ
		Mid-Aquifer Unit	MID-AQ
		Base Mid-Aquifer Unit	BAS_MID_AQ
		Upper Basal Aquifer Unit	BS_AQ_upper
		Lower Basal Aquifer Unit	BS_AQ_lower
	Volcanic rift zones (basalts distributed in areas of active and inactive rifting)	Upper Aquifer Unit	UP_AQ
		Mid-Aquifer Unit	MID-AQ
		Base Mid-Aquifer Unit	BAS_MID_AQ
		Upper Basal Aquifer Unit	BS_AQ_upper
		Lower Basal Aquifer Unit	BS_AQ_lower
Basalt and sediment subdomains	Big Lost River floodplain (basalts from three volcanic centers interfingering with fluvial sediments derived from the Big Lost River)	Upper Aquifer Unit	UP_AQ
		Mid-Aquifer Unit	MID-AQ
		Base Mid-Aquifer Unit	BAS_MID_AQ
		Upper Basal Aquifer Unit	BS_AQ_upper
		Lower Basal Aquifer Unit	BS_AQ_lower
		Sedimentary Unit 3	sed3
Sediment-dominated subdomains	Pluvial sediments (Lake Terretton) in the northern part of the OU 10-08 model domain		Top sed3
	Thick, locally distributed south-dipping sequences of mixed lacustrine sed3 and basalt; Older pluvial sediments in the north central INL subsurface	Sedimentary Unit 1	Sed1
	Thick lacustrine and fluvial sediments interbedded with basalt north of Naval Reactors Facility and south of Howe	Sedimentary Unit 2	sed2
	Deep (>300 m) lacustrine sediments in the southern INL subsurface	Sedimentary Unit 3	sed3
	Both thick and thin fluvial and lacustrine sediments interbedded with basalt in the south central INL subsurface	Sedimentary Unit 4	sed4
	Deep lacustrine sediments (thick south-dipping sequences of lacustrine sediments that occur within the active aquifer in the north-central part of the area represented by the OU 10-08 model domain)	Olduvai Lake	old_lake

2.1.2.1.1 Hydrogeologic Unit Delineation Methodology—Characteristic wells INEL-1, 2-2A, ANL-1, and Corehole-1 exhibit sequences of hydrogeologic units typical of different hydrogeologic subdomains. The following sections describe delineation of specific hydrogeologic units within the stratigraphic columns penetrated by these selected characteristic wells and illustrate the methodology employed for each of the 41 characteristic wells.

Well INEL-1—Well INEL-1 is a characteristic well located near the boundary between the present day Big Lost River flood plain and volcanic tablelands subdomains. This well fully penetrates the SRPA. The sequence of hydrogeologic units penetrated by this well is typical of the volcanic tablelands. Figure 2-8 shows the hydrogeologic units penetrated in Well INEL-1 and selected geophysical logs that were collected from Well INEL-1 over the active thickness of the aquifer.

Three hydrogeologic units were identified within this well. The UP_AQ extends downward from the water table to an elevation of approximately 1,332 m and corresponds to a volcanic tableland subdomain, is generally basalt dominated, and contains a sequence of basalt flows and associated interflow zones with minor amounts of sedimentary materials.

The contact between the UP_AQ and the underlying MID_AQ in Well INEL-1 is identified by the sharp kick in the density log and an inflection in the temperature log (and resulting change in the temperature gradient). The MID_AQ is also considered to be a volcanic tableland subdomain, with the boundary between the MID_AQ and the UP_AQ indicating a likely inhibition to vertical flow and somewhat different effective aquifer properties.

A thin sediment unit was identified in Well INEL-1 underlying the MID_AQ by readily identified peaks in the natural gamma logs and an inflection in the temperature log. This sediment unit, although identifiable in the geophysical logs, could not be correlated to any adjacent wells, and was incorporated into the underlying unit. The BS_MID_AQ unit was identified between the MID_AQ and the base of the active aquifer from an inflection in the temperature log.

Geophysical log analyses from Well INEL-1 provided an example of the overall delineation process, and specifically for the volcanic tablelands. The technique used to identify units in Well INEL-1 varied slightly from well to well because of differences in available data. However, each boundary was identified by at least two of the geophysical logs mentioned above, and, if possible, was supported by other data (i.e., core, video, other geophysical, or driller/geologist logs).

Well 2-2A—Well 2-2A is located near the boundary between a sedimentation area and a volcanic tableland subdomain. Figure 2-9 shows the hydrogeologic units penetrated in Well 2-2A. The stratigraphic section penetrated in this well is strikingly similar to the section for a volcanic tableland presented on Figure 2-8 but includes one or more thin-sediment or sediment controlled units. This sequence is typical for most wells located within the sedimentation areas. In Well 2-2A, a thick sequence of sediments, corresponding to the Olduavi Lake beds, is present at depth. Several other sediment sequences, all thin and not aerially extensive, are also present in this well, as evidenced in the geophysical logs. Several of these units in the upper portion of the column consist of coarse sediments incorporated into the UP_AQ and MID_AQ units.

Wells ANL-1 and Corehole-1—Wells ANL-1 and Corehole-1 are located on the AVH, are exposed to a large portion of the aquifer (334 and 327 m, respectively), and have a fairly complete set of well logs and lithologic information. Based upon evaluation of the data, both wells were strikingly similar in the interpreted vertical hydrogeologic section. The stratigraphic column penetrated by both wells generally lacked sedimentary units and two basalt-dominated hydrogeologic units, the Upper Aquifer Unit (UP_AQ) and the Basal Mid-Aquifer Unit (BS_MID_AQ). Figure 2-10 shows the interpreted hydrogeologic section in Well ANL-1. The inflection in the temperature profile, the spikes in the density log, and natural gamma logs were used to identify the break between the UP_AQ and the BS_MID_AQ.

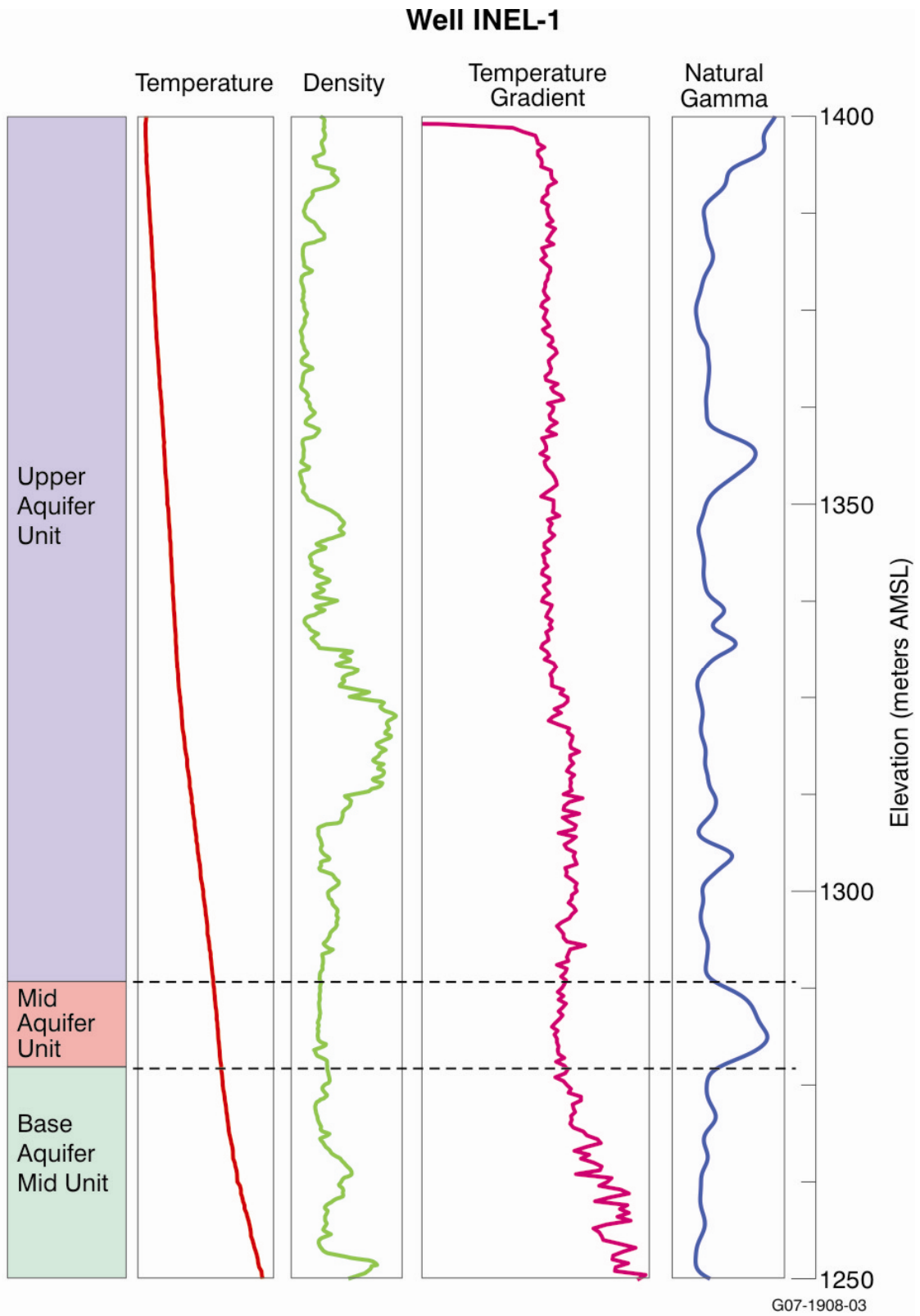


Figure 2-8. Hydrogeologic unit delineation in Well INEL-1. Only the interpreted active thickness of the aquifer is portrayed.

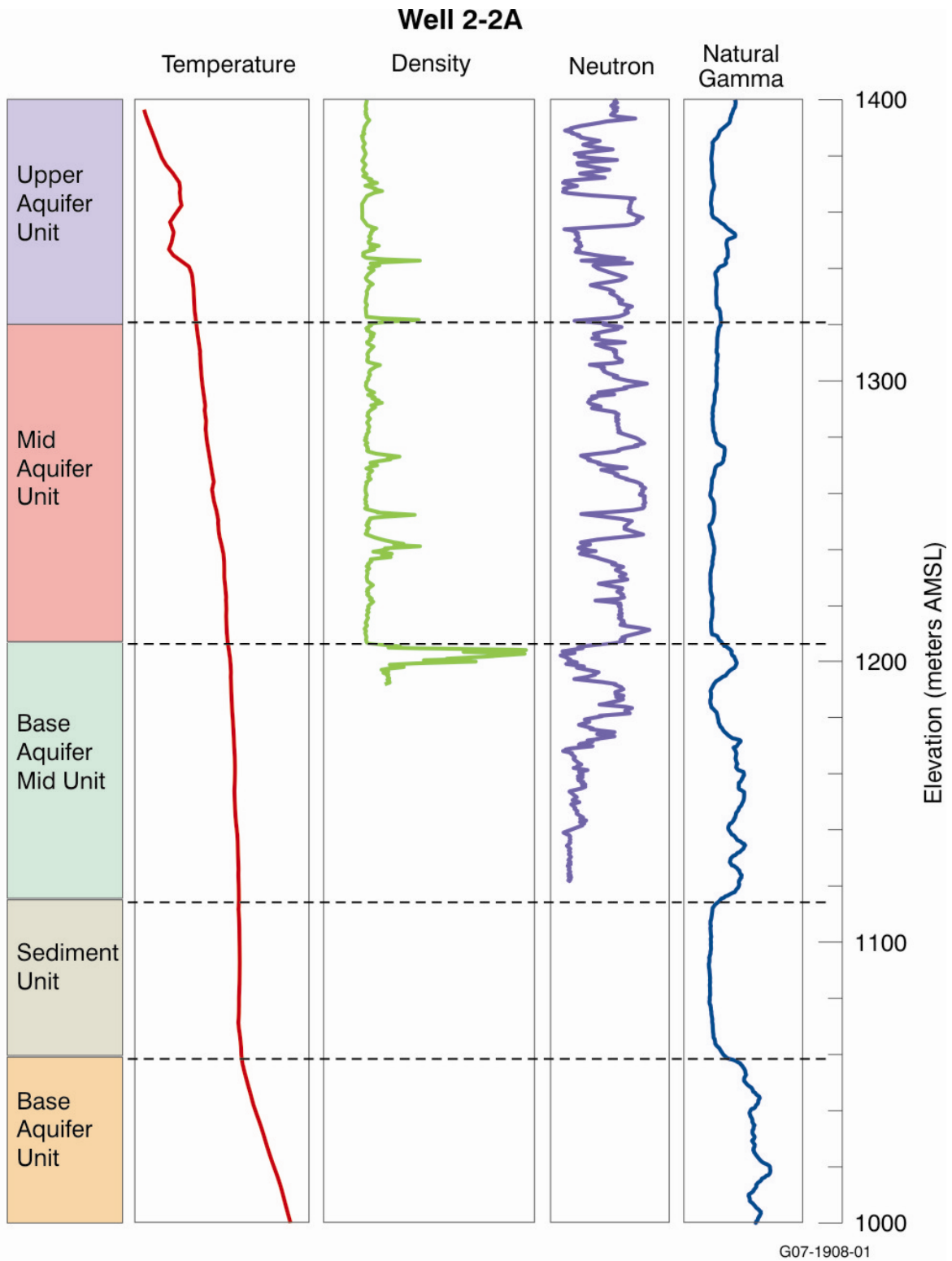


Figure 2-9. Hydrogeologic unit delineation in Well 2-2A. Only the interpreted active thickness of the aquifer is portrayed.

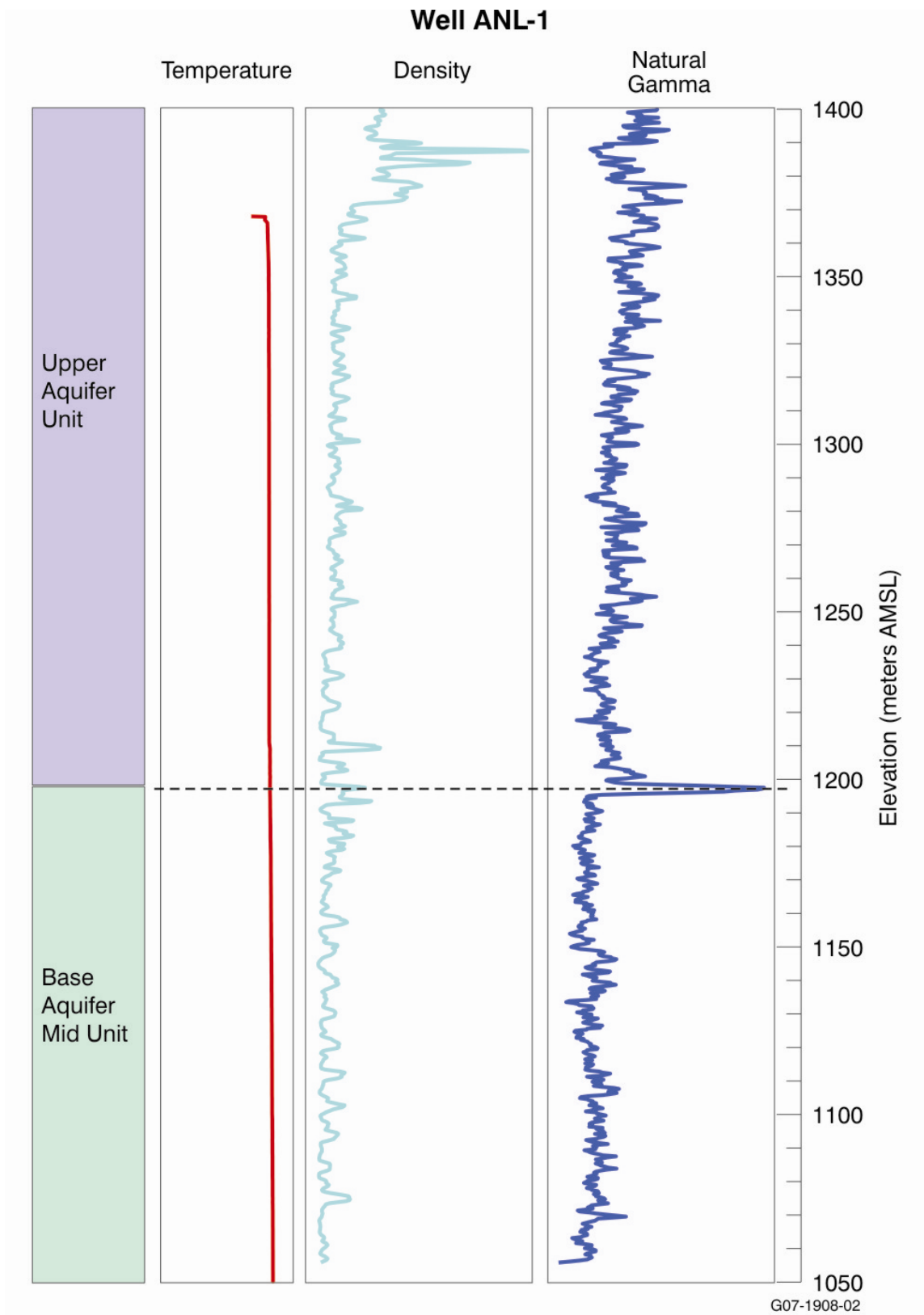


Figure 2-10. Hydrogeologic unit delineation in Well ANL-1. Only the interpreted active thickness of the aquifer is portrayed.

2.1.2.1.2 Composite Hydrogeologic Sequences from Clustered Wells—In several areas adjacent to INL facilities, geologic, hydrologic, and geophysical data were available for numerous clustered wells. In those areas, composite hydrogeologic sequences were constructed from these data to reflect the density of data and localized stratigraphic complexity.

2.1.2.1.3 Generalized Hydrogeologic Unit Columns—Limited distribution of wells in certain locations precluded accurate characterization in those locations. For example, no deeply penetrating wells are located south of the southern INL boundary. In these areas, characterization was dependent on the use of wells with shallower penetration and on the use of synthetic wells and generalized hydrogeologic unit columns.

As previously described, four types of hydrogeologic subdomains were identified within the OU 10-08 area. These include (1) volcanic tablelands, (2) sedimentation areas, (3) rift zones and volcanic centers, and (4) the Big Lost River flood plain. It is important to note that these subdomains represent their surficial expression and that their spatial distributions and boundaries vary with depth in the subsurface due to the evolution of geologic processes acting on the Snake River Plain over the last several million years. Generalized hydrogeologic unit columns were developed for synthetic wells in each of these subdomains from stratigraphic sequences defined in closest characteristic wells that were located within those subdomains. These generalized columns are referred to as synthetic wells (or SYN-##) on the maps and cross sections that follow.

For example, generalized hydrogeologic unit columns for volcanic tablelands subdomains consisted of four hydrogeologic units, all of which were basalt dominated. Thickness of the UP_AQ and MID_AQ units generally varied between 60–120 m for most generalized hydrogeologic unit columns in this subdomain. The BS_MID_AQ and BS_AQ units were generally thinner and in some cases were not present in the sections because the overall aquifer thickness was small enough that they were not required. Generalized hydrogeologic unit columns for volcanic tablelands were primarily required in two distinct areas, to the west of the AVH and south of the Great Rift of Idaho.

Generalized hydrogeologic columns for rift-zone subdomains consisted of only two basalt-dominated aquifer units, the UP_AQ and the BS_MID_AQ. The MID_AQ unit was omitted from this subdomain to accommodate the conceptual understanding of the subdomain, where the volcanic rift zones were considered topographic highs at the time of emplacement and basalt flows originating from the volcanic tablelands terminated at the volcanic rift zones. The thickness of the UP_AQ unit was kept to approximately 100 m in the generalized hydrogeologic column, with the remainder from the base of the UP_AQ to the base of the effective aquifer consisting of BS_MID_AQ. In some locations where the aquifer was especially thick, the BS_AQ unit was also assumed to be present.

2.1.2.2 Hydrogeologic Unit Cross Sections. After a sequence of hydrogeologic units was delineated for each characteristic well, these sequences and composite sequences from clustered wells were projected across the area of the model domain on a series of hydrogeologic cross sections (Figure 2-11). For cross sections in areas of limited well information, generalized hydrogeologic unit columns were constructed and utilized as identified on Figure 2-11 with the identifier “syn”. The cross sections were first completed in GMS using an automated routine to connect adjacent wells and fit the top and bottom of the cross sections to the water table and aquifer bottom (thick scenario), respectively. Cross sections between characteristic wells were used to identify a total of eight composite cross sections that traverse the entire model domain and capture the general nature and variability of the aquifer. The composite cross sections were located to intersect as many of the deeply penetrating wells available in the domain as possible.

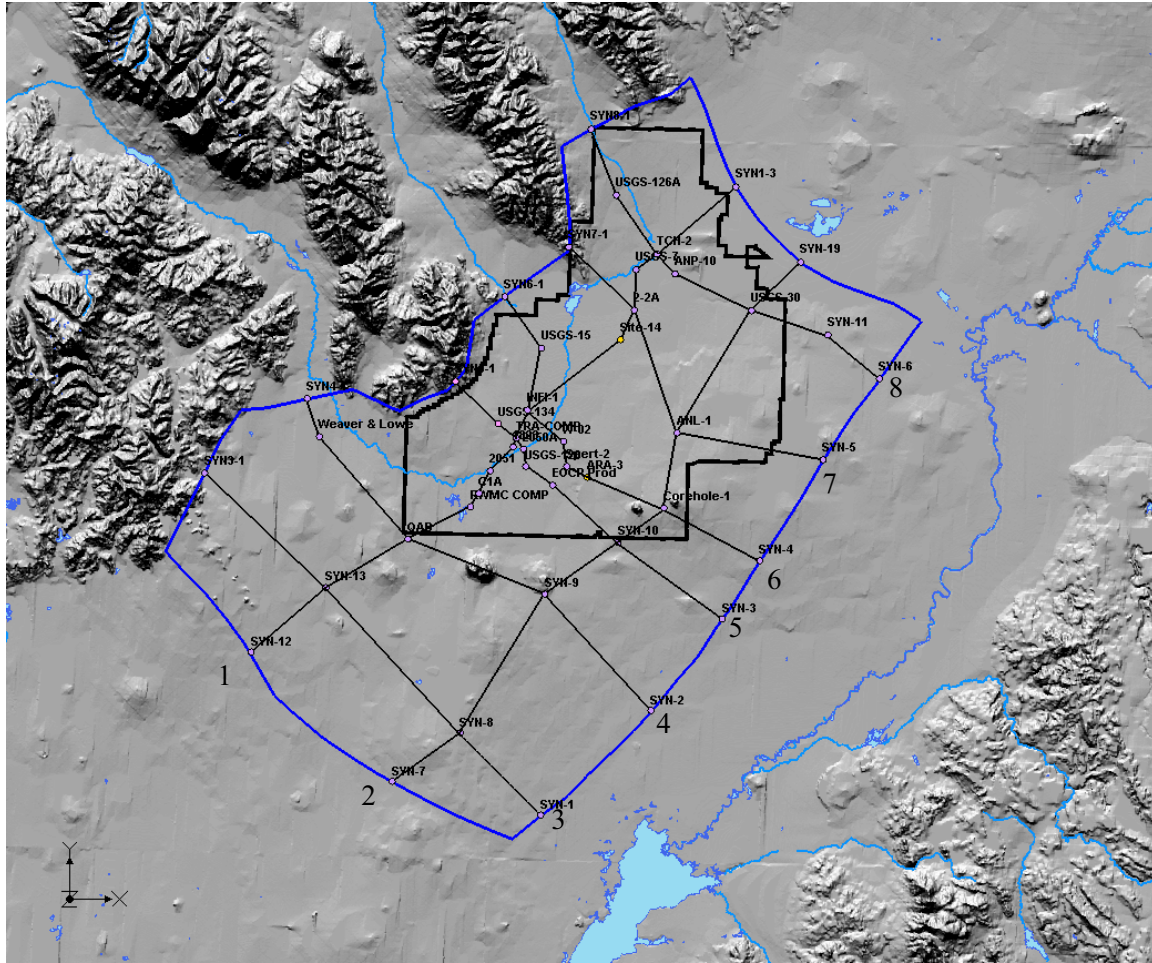


Figure 2-11. Locations of composite cross sections through simulation domain.

2.1.2.2.1 Composite Cross Section 1—Composite cross section 1 runs NE-SW through the model domain, intersecting several rift zones and portions of the Big Lost Trough. A total of 14 wells/data points were used along the cross section, identified from north to the south below:

North

1. Generalized hydrologic unit column (SYN1-3)
2. TCH-2
3. USGS-07
4. 2-2A
5. Site-14
6. INEL-1
7. Composite of TRA-02, TRA-04, TRA-DISP, USGS-79, and Site-19 (TRA-COMP)^c
8. Middle-1823
9. Highway-3
10. MIDDLE-2051

c. The Reactor Technology Complex was formerly known as the Test Reactor Area (TRA).

11. C1A
12. Composite of USGS-132, OW-2, and M4D (RWMC-COMP)
13. Quaking Aspen Butte
14. Generalized hydrologic unit column (SYN 13)
15. Generalized hydrologic unit column (SYN 12)

South

Data from most of the wells identified above were examined and interpreted for use in the hydrogeologic cross section, shown on Figure 2-12a. Seven hydrogeologic units were preliminarily identified on this line, with a significant amount of variability evident in the northern portion of the section, in the vicinity of Site 14 and 2-2A. This area is near the junction/ boundary of a rift zone, sedimentation area, and volcanic tablelands.

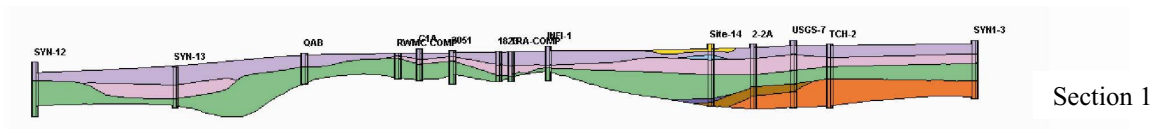
2.1.2.2.2 Composite Cross Section 2—Composite cross section 2 runs NE-SW through the model domain along the AVH, intersecting several additional volcanic rift zones with E-W orientations (e.g., the Arco Rift). A total of eight wells/data points were used along the cross section, identified from north to the south below:

North

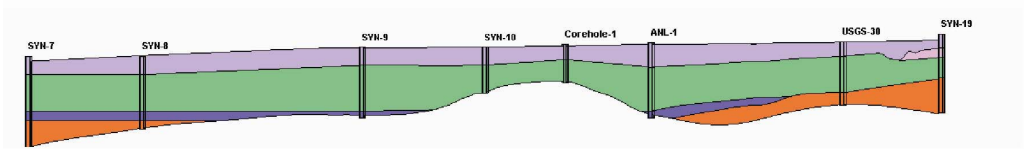
1. Generalized hydrogeologic column (SYN 19)
2. USGS-30
3. ANL-1
4. CH-1
5. Generalized hydrogeologic column (SYN 10)
6. Generalized hydrologic unit column (SYN 9)
7. Generalized hydrologic unit column (SYN 8)
8. Generalized hydrologic unit column (SYN 7)

South

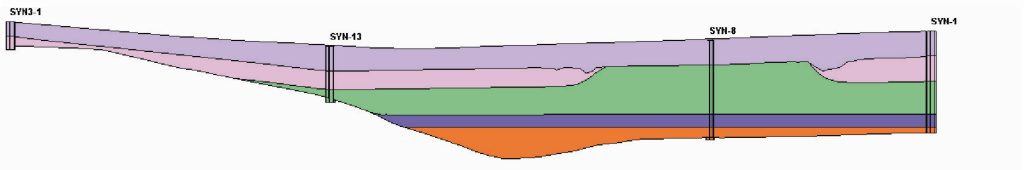
Data from all of the wells identified above were examined and interpreted for use in the composite cross section, shown on Figure 2-12a. Four hydrogeologic units were identified. The stratigraphic sequence in many of the wells was primarily basalt dominated, with only minor sediments being observed. Multiple low-permeability massive basalt units were identified in USGS-30, while only several massive basalt units were identified in ANL-1 and CH-1. This cross section primarily runs down the AVH, a linear volcanic center where sediments are not expected to accumulate in significant thicknesses. Although this cross section runs along the AVH, where generally only two hydrogeologic units were primarily defined, thick portions of the aquifer required that the BS_AQ unit be present along portions of the bottom of this cross section. This was necessary for extrapolation purposes between the adjacent volcanic tablelands to the east and west. Also, constraints with the GMS program required splitting the BS_AQ into upper and lower units. This split was only for convenience with the GMS program and was not related to the hydrogeologic structure.



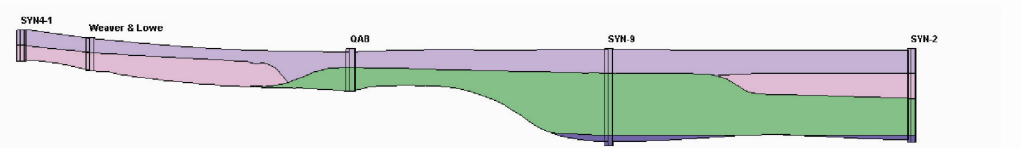
Section 1



Section 2



Section 3



Section 4

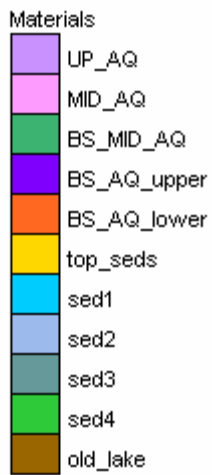


Figure 2-12a. Hydrogeologic Unit Cross Sections 1–4 (Sections 1 and 2 oriented northeast to southwest, with northeast to the right of the figure. Sections 3 and 4 oriented east to west, with west to the right of the figure). Vertical exaggeration of the sections approximately 35X.

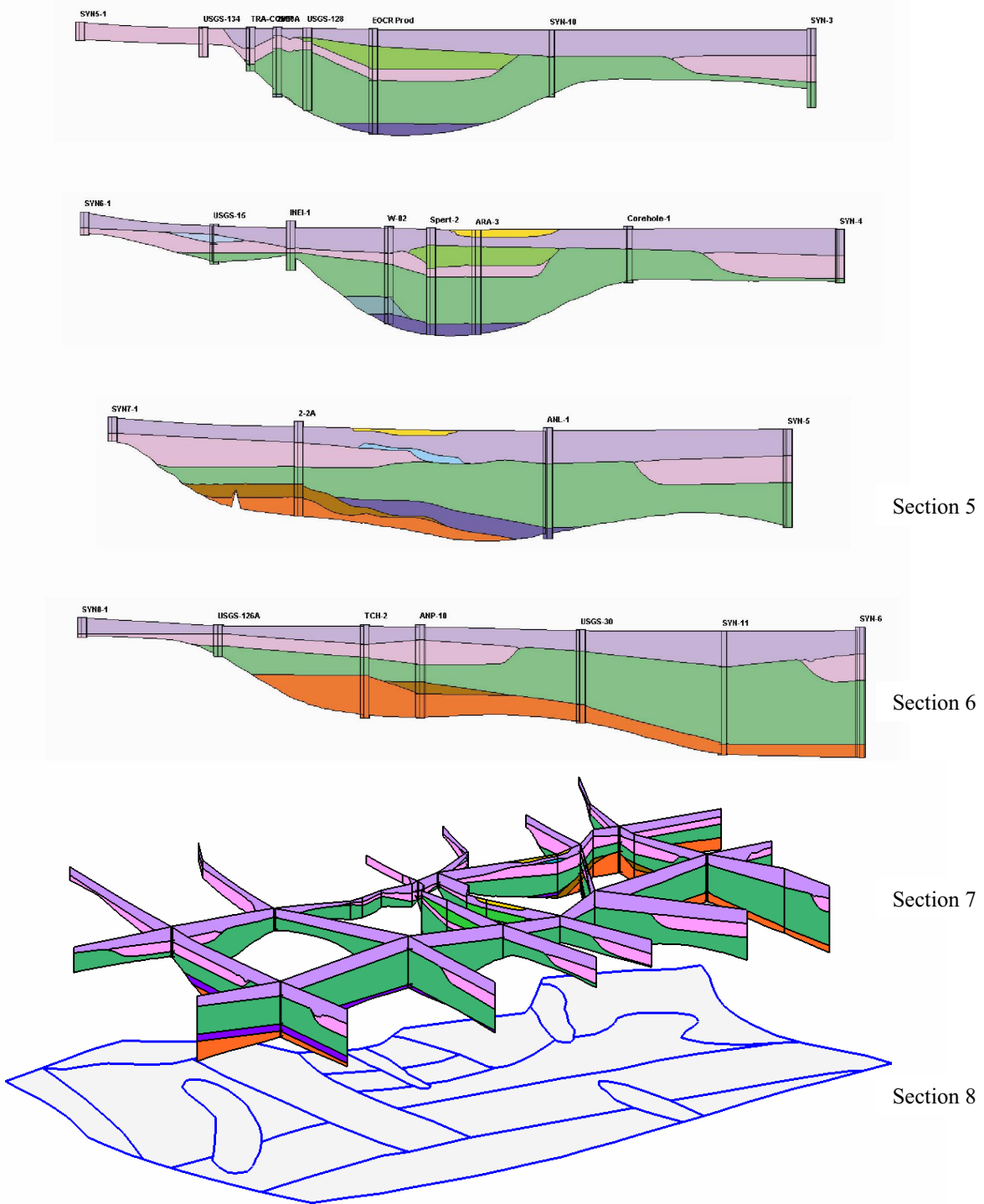


Figure 2-12b. Hydrogeologic Unit Cross Sections 5–8 oriented east to west, with west to the right of the figure) and a fence diagram overlying the outline of hydrogeologic subdomains. Vertical exaggeration of the sections approximately 35X.

2.1.2.2.3 Composite Cross Section 3—Composite cross section 3, shown on Figure 2-12a, runs generally E-W near the southern boundary of the model domain. Data were very sparse in this area, because no wells penetrate significant aquifer thicknesses. All of the data points along the cross section were derived from generalized hydrogeologic columns, with the data points intersecting composite cross sections 1 and 2. Hydrogeologic subdomains occurring in this area consisted primarily of volcanic rift zones and volcanic tablelands.

2.1.2.2.4 Composite Cross Section 4—Composite cross section 4 runs E-W through the model domain primarily along the Arco Rift, and includes the sedimentation area at the mouth of the Big Lost River Valley. A total of five wells/data points were used along the cross section, identified from east to west below:

East

1. Generalized hydrologic unit column (SYN 2)
2. Generalized hydrologic unit column (SYN 9)
3. Quaking Aspen Butte
4. Weaver and Lowe
5. Generalized hydrologic unit column (SYN 4-1)

West

Data from all of the wells identified above were examined and interpreted for use in the composite cross section, shown on Figure 2-12a. Two to three hydrogeologic units were identified. The stratigraphic sequence in many of the wells was primarily dominated by basalt, with only minimal occurrence of sediments. This cross section primarily runs along a volcanic rift zone, through an area where significant thicknesses of sediments are not expected to accumulate. The area at the mouth of the Big Lost River valley consists of a transition zone between the Basin and Range Province and the Snake River Plain, and requires additional interpretation.

2.1.2.2.5 Composite Cross Section 5—Composite cross section 5 runs E-W through the model domain, intersecting the Big Lost River and the AVH. A total of seven wells/data points were used along the cross section, identified from east to west below:

East

1. Generalized hydrologic unit column (SYN 3)
2. Generalized hydrologic unit column (SYN 10)
3. Composite of Site-9, OMRE, and EOCR Production
4. USGS-128
5. MIDDLE-2050A
6. Composite of TRA-02, TRA-04, TRA-DISP, USGS-79, and Site-19 (TRA-COMP)
7. USGS-134
8. Generalized hydrologic unit column (SYN 5-1)

West

The definition of hydrogeologic units proved to be difficult along this cross section, shown on Figure 2-12b. Difficulties included working out composite hydrogeologic unit sequences using data from clustered wells Site-9, OMRE, and EOCR Production and from clustered wells TRA-02, TRA-04, TRA-DISP, USGS-79, and Site-19. The variability in this section was quite dramatic. At the Site-9, OMRE, and EOCR Production composite data point, an 85-m-thick sediment unit began approximately 70 m below the water table and likely exhibited a significant control on groundwater flow; however, this unit did not appear to be spatially extensive, and was only correlated to Well USGS-128.

2.1.2.2.6 Composite Cross Section 6—Composite cross section 6 runs E-W through the model domain, intersecting the AVH, volcanic tablelands, the Big Lost River and the pluvial Lake Terretton beds as it moves from east to west. A total of eight wells/data points were used along the cross section, identified from east to west below:

East

1. Generalized hydrologic unit column (SYN 4)
2. CH-1
3. ARA-3
4. SPERT-2
5. W-02
6. INEL-1
7. USGS-15
8. Generalized hydrologic unit column (SYN 6-1)

West

Many sedimentary units were present along the cross section, as shown on Figure 2-12b. The figure also illustrates the pinch out of the MID_AQ unit as it approaches the AVH in the vicinity of CH-1.

2.1.2.2.7 Composite Cross Section 7—Composite cross section 7 runs E-W through the model domain, intersecting volcanic tablelands, the AVH, pluvial Lake Terretton beds/sedimentation areas, and returning to volcanic tablelands to the west of the model domain. A total of four wells/data points were used along the cross section, identified from east to west below:

East

1. Generalized hydrologic unit column (SYN 5)
2. ANL-1
3. 2-2A
4. Generalized hydrologic unit column (SYN 7-1)

West

Data from the two wells identified above were examined and interpreted for use in the composite cross section, shown on Figure 2-12b. Seven hydrogeologic units were identified on this cross section, with a significant amount of variability evident in the vicinity of 2-2A. This area is near the junction/boundary of a volcanic rift zone, sedimentation area, and volcanic tablelands. Interpretation of the transition between hydrogeologic subdomains was somewhat less of a challenge on this section than it was for other sections previously discussed, as the sediments penetrated in 2-2A pinched out as they approached the AVH.

2.1.2.2.8 Composite Cross Section 8—Composite cross section 8 runs E-W near the northern boundary of the model domain, intersecting the AVH, pluvial Lake Terretion beds/sedimentation areas, and the AVH to the west of the model domain. A total of seven wells/data points were used along the cross section, identified from east to west below:

East

1. Generalized hydrologic unit column (SYN 6)
2. Generalized hydrologic unit column (SYN 11)
3. USGS-30
4. ANP-10
5. TCH-2
6. USGS-126A
7. Generalized hydrologic unit column (SYN 8-1)

West

Data from the wells identified above were examined and interpreted for use in the composite cross section, shown on Figure 2-12b. A total of 5 hydrogeologic units were identified on this cross section, with (primarily) basalt and minor amounts of sediments occurring in the stratigraphic sequence. The Olduvai Lake sediments were present in the basal portions of ANP-10, but were not apparent in adjacent wells.

2.1.2.2.9 Composite Cross Section Summary—The eight composite cross sections discussed above and the 146 individual cross sections constructed in GMS captured the conceptual understanding of the SRPA in the vicinity of the INL and represented the first step in transferring this conceptual understanding into the numerical flow model. While all-encompassing generalizations were difficult to reach, several conclusions were made regarding the distribution of hydrogeologic units. These conclusions included the following: (1) sediment or sediment-dominated hydrogeologic units are localized and have limited horizontal and vertical extent; (2) basalt-dominated hydrogeologic units are generally related to the presence of interflow zones and are not distinctly related to age or stratigraphic position; and (3) hydrogeologic unit boundaries are based on localized inhibitors of vertical communication in the flow system (massive basalt or sedimentary interbed) and cannot be based on bulk aquifer properties. Figure 2-12b includes a fence diagram of the eight composite cross sections discussed in the previous sections.

2.1.2.3 Construction of Three-Dimensional Solids. Data and interpretations from the hydrogeologic cross sections were entered into the GMS program after all of the section line interpretations were completed. The borehole and cross section modules in the GMS code were used to enter the data into the modeling software, and the solids module was used to extrapolate the hydrogeologic units throughout the entire model domain. All of the extrapolations required verification to ensure consistency with the hydrogeologic subdomain conceptual model.

Several steps were taken within the GMS program to better constrain the extrapolation in the GMS code. These steps included: (1) extrapolation of all boreholes to the total aquifer thickness; (2) definition of “horizons” in GMS, which were essentially the maximum spatial extent of aquifer unit extrapolation; (3) specification of the nodal spacing for extrapolation along all of the cross sections and boundaries between the aquifer units, and along the horizon extents and model domain boundaries; (4) specification of the extrapolation method used to build the solids; and (5) refinement of the TIN nodal spacing in areas of high complexity.

The GMS program commonly crashed when performing the solids extrapolation. Extension of all of the boreholes to the aquifer bottom, definition of the horizons within each well on a vertical basis, and definition of the horizontal horizon extents significantly increased the stability of GMS during the solids extrapolation. Even after this was completed, the extrapolation process still produced results that were inconsistent and sometimes problematic. Spurious spikes in the contacts between aquifer sub-units existed with the domain, especially in the area where the Olduvai Lake beds were present. The spikes were generally present where units pinched out or where beds dipped significantly. To overcome these problems, the nodal spacings along the cross-section aquifer sub-units were refined to between 10–50 m, with the density of the overall extrapolation TIN surface increased to a uniform 200 or less throughout the entire model domain. In areas where spikes in the extrapolated surfaces were prevalent, local TIN refinement was used to minimize the problems.

Figure 2-13a shows the extrapolated solids for all of the aquifer units looking from the southeast to the northwest. The general layering scheme of the volcanic tablelands can be observed along the eastern edge of the model domain, with 3 to 4 hydrogeologic units exposed, depending on the thickness of the aquifer. Along the southern boundary, the hydrogeologic units were representative of a volcanic rift zone, as this boundary lies primarily along the Great Rift of Idaho. The BS_AQ unit was also present in the thickest portion along the southern boundary below at an altitude of approximately 900 m above mean sea level. Figure 2-13b presents the same view of the model domain with the UP_AQ unit removed. This figure clearly demonstrates the location of the prominent volcanic rifts and volcanic centers in the model domain, with the AVH, the Arco Rift, and the Great Rift evident by the lack of aquifer sub-unit MID_AQ.

The basal aquifer unit is shown on Figure 2-13c. The BS_AQ generally filled in the deepest portions of the active aquifer. As stated earlier, the BS_AQ was subdivided into upper and lower portions for convenience with the GMS program. This was primarily necessitated by the presence of the Olduvai Lake sediments, which projected through the basal aquifer unit to the aquifer bottom in the vicinity of the TAN facility (and shown on the figure where the orange and purple solids meet). Figure 2-13d shows only the sediment and sediment-controlled units in the upper portion of the flow system. These aquifer sub-unit solids were primarily located in the vicinity of the Big Lost River and in areas to the east and north, which was consistent with the interpreted evolution of the Big Lost River channel.

2.1.2.4 Constraint of Hydrogeologic Unit Hydraulic Properties. This steady-state phase of the three-dimensional representation of groundwater flow requires characterization of the distribution of horizontal and vertical hydraulic conductivity throughout the area represented by the OU 10-08 model domain. Heterogeneities derived from the basalt architecture (high-permeability interflow zones separated by low-permeability basalt-flow interiors) likely result in a large ratio of horizontal to vertical hydraulic conductivity. Characterization of the storage coefficient is not required for this steady-state representation; subsequent transient models will require estimates of the storage coefficient.

An inverse numerical modeling technique was used to approximate the areal and vertical distribution of the horizontal hydraulic conductivity within the model domain as described in the model implementation section of this report. This inverse technique required specification of ranges of hydraulic conductivity for defined hydrogeologic units.

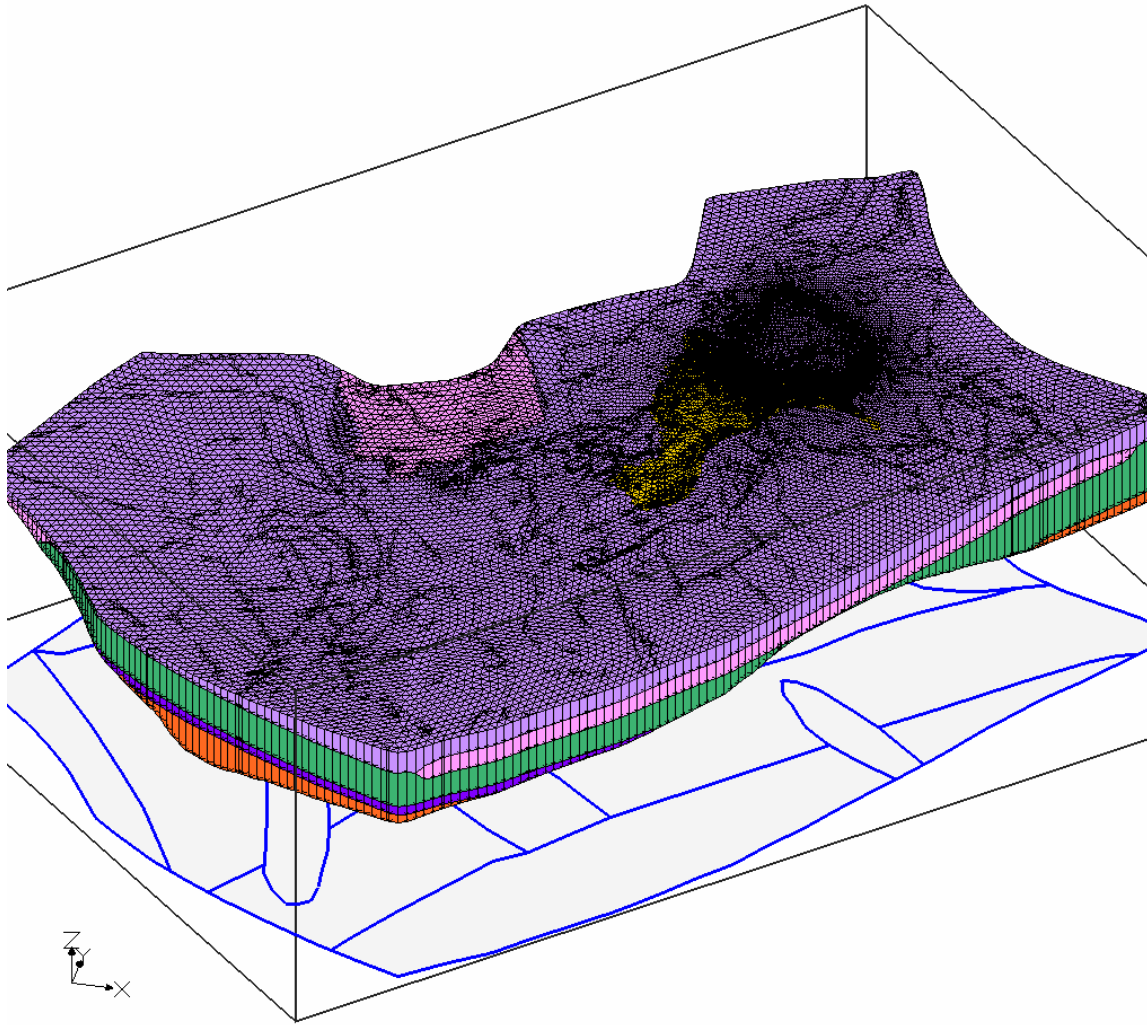


Figure 2-13a. Extrapolated solids for all of the aquifer units looking from the southeast to the northwest.

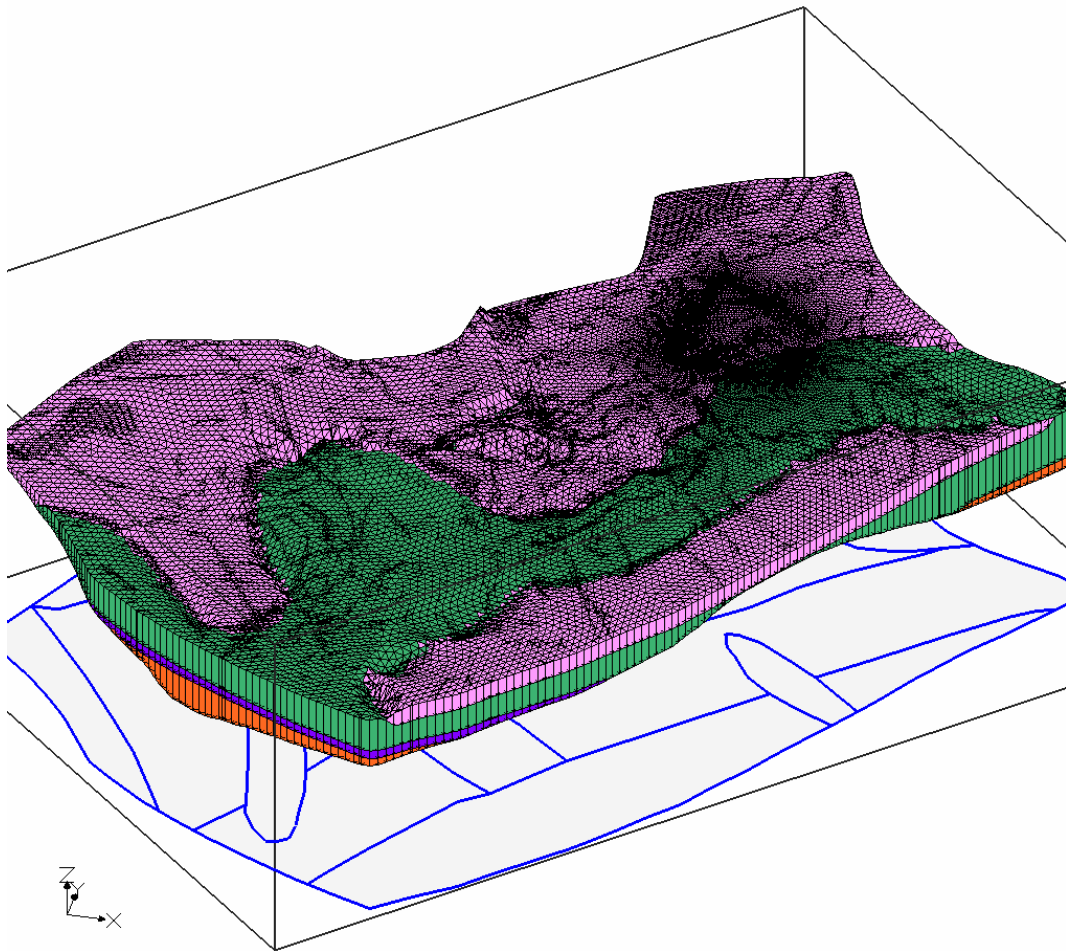
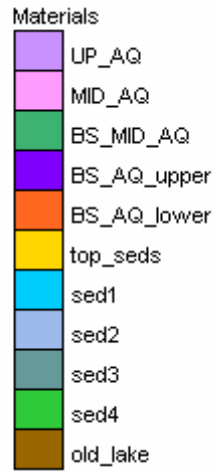


Figure 2-13b. Extrapolated solids for all of the aquifer units looking from the southeast to the northwest, with upper basalt hydrogeological unit removed to show detail of mid- and base-mid basalt units.

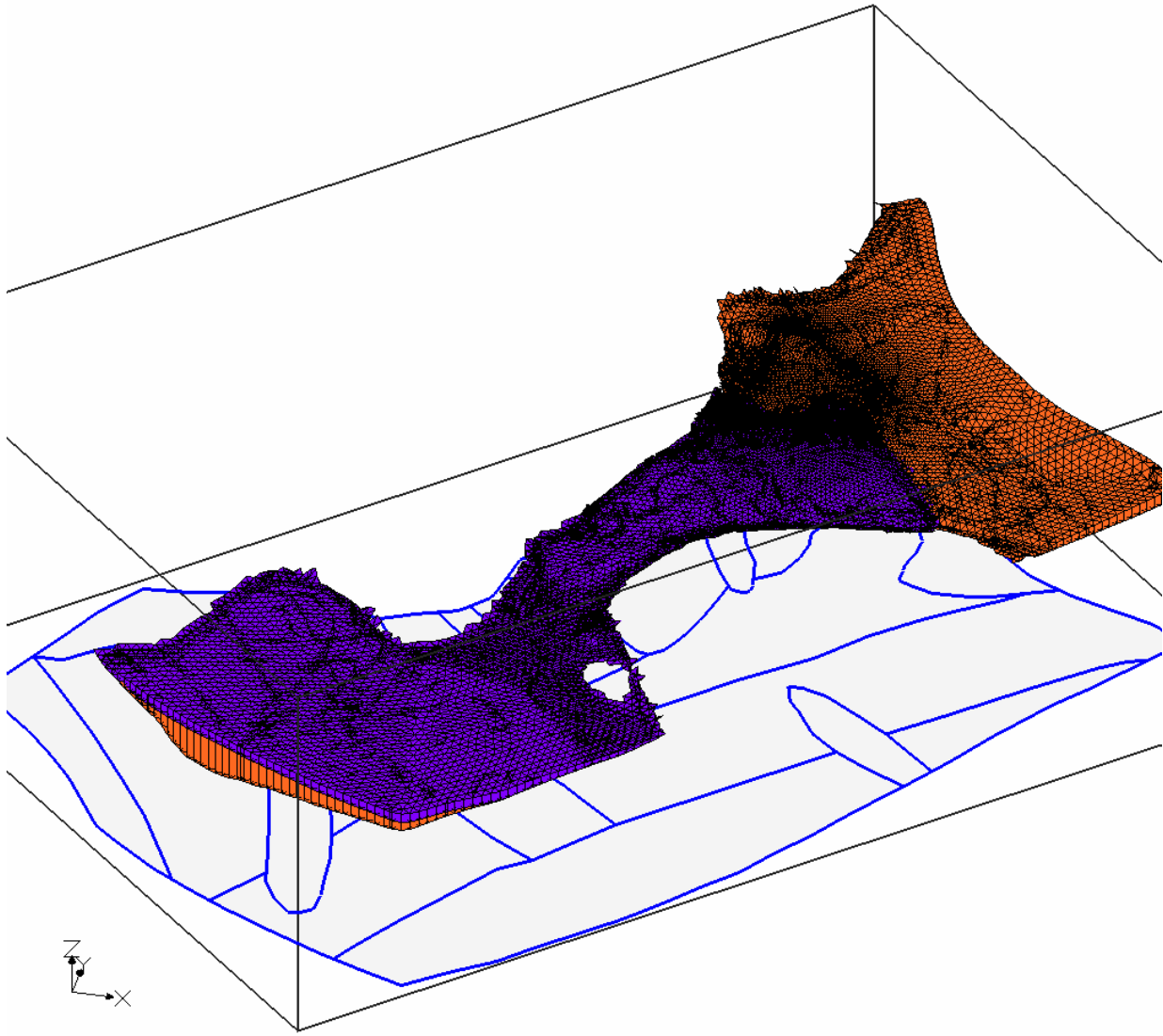


Figure 2-13c. Extrapolated solids basal aquifer unit looking from the southeast to the northwest.

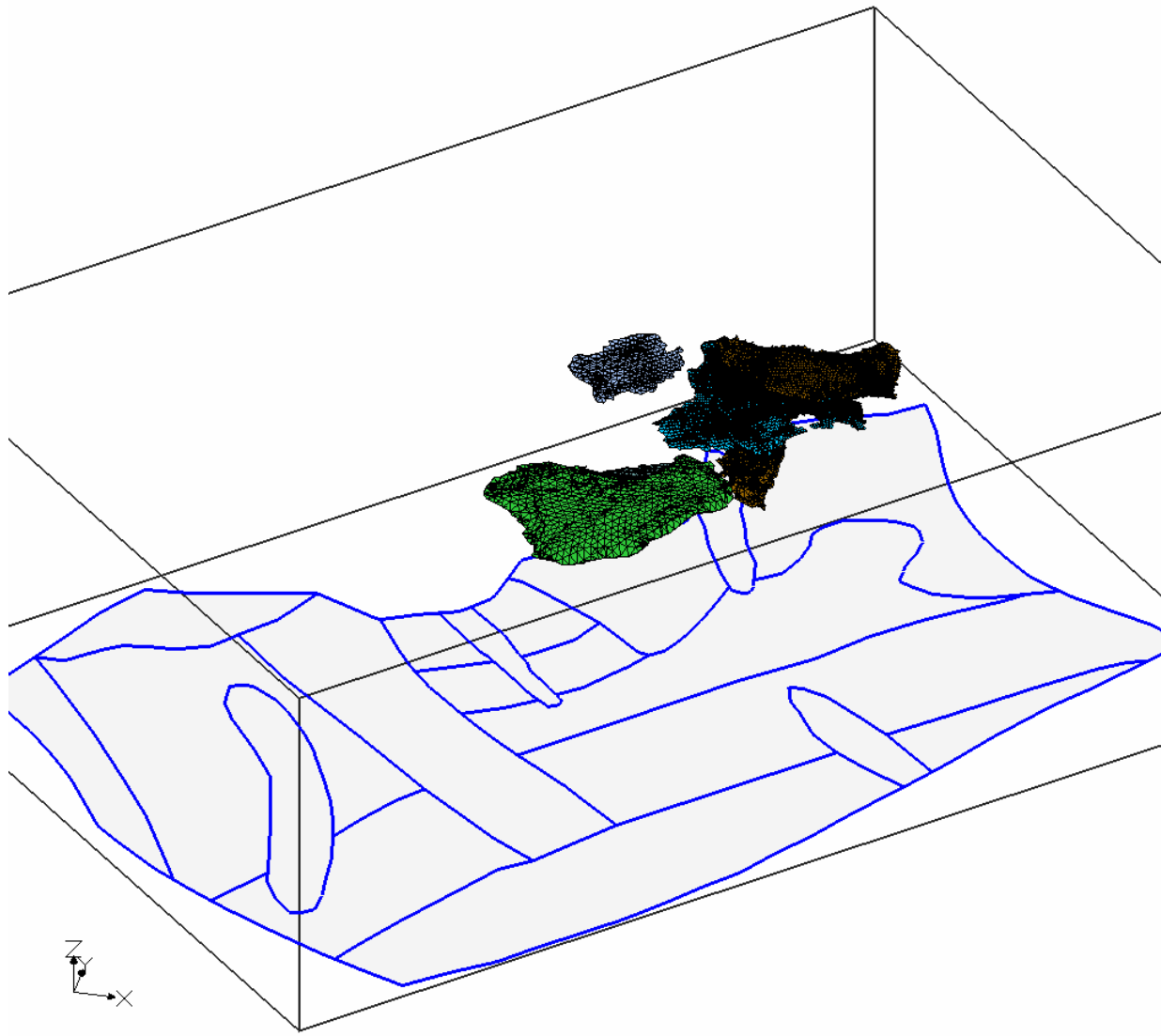


Figure 2-13d. Extrapolated solids for all of the sediment-dominated units looking from the southeast to the northwest.

Most of the aquifer-test data were obtained from wells completed near the water table, but, as seen on Figure 2-14, some of the aquifer tests were conducted in wells with deeper completion intervals. Aquifer-test data were analyzed to identify trends in the hydraulic conductivity with depth below the water table. The hydraulic conductivity estimates were analyzed by binning estimates into 10-ft-thick bins and assuming that all of the aquifer section exposed to the well contributed equally to the production of water in the well. Hydraulic conductivities for all wells completed over the 10-ft bins were then summed and harmonically averaged. The effect of binning the data and assuming equal hydraulic contribution was to decrease the overall hydraulic conductivity for each interval, but was still illustrative for gaining insight into the property distribution with depth. This analysis, presented on Figure 2-14, shows that hydraulic conductivity generally decreases with depth in most areas. The mean value of hydraulic conductivity near the top of the aquifer is approximately 300 ft/day. The range in the data, prior to binning and averaging, was approximately 10^{-2} to 10^5 ft/day.

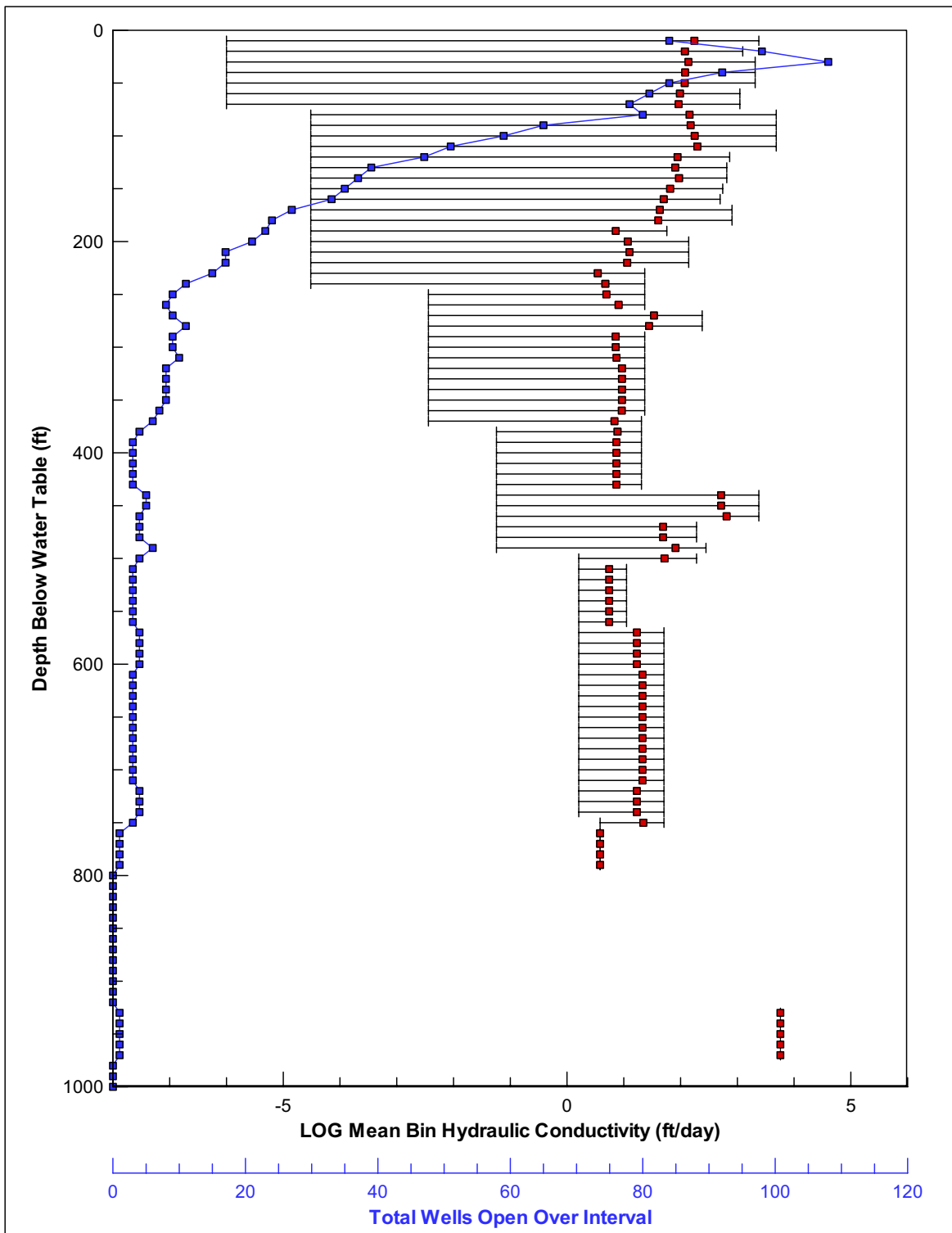


Figure 2-14. Aquifer test information presented against depth below the water table. Aquifer test data from all wells were binned on 10-ft-depth intervals and averaged, with the average values shown by red dots. The range of the binned data is presented with horizontal bars, and the number of tests within the bin are illustrated with a blue line and points.

2.2 Hydrologic Conditions

Previous OU 10-08 two-dimensional numerical models utilized a cross-sectional estimate of inflow across the northeastern boundary of the area represented by the model domain. Because these models were two-dimensional, inflow estimates were not distributed vertically across the active thickness of the aquifer. However, assignment of layered inflows to the fully three-dimensional representation requires characterization of the vertical distribution of regional underflow. Additionally, three-dimensional model calibration will be based on vertically discrete head measurements and on flow velocity estimates. Subsequent sections describe inflows to be represented in the three-dimensional numerical model (and in particular, the vertical distribution of regional underflow), the three-dimensional head data set, and flow velocity estimates required for model calibration.

2.2.1 Inflows and Outflows to and from the Area Represented by the OU 10-08 Model Domain

Major inflows to the area represented by the OU 10-08 model domain consist of (a) regional underflow across the northeast model-domain boundary, (b) tributary basin inflows as tributary aquifer underflow and as infiltrating streamflow, and (c) recharge from areal precipitation. These inflows are summarized in the following section and are tabulated in Table 2-3. Expanded discussion about the characterization of the magnitude and point of recharge to the SRPA is presented in Wood et al. (2005).

2.2.1.1 Regional Underflow Across the Northeastern Model Domain Boundary. Regional underflow in the Mud Lake area was estimated from a numerical modeling study of the Mud Lake area (Spinazola 1994) to be approximately 800,000 acre-ft/year (Wood et al. 2005). The magnitude of this regional underflow estimate was consistent with underflow estimates derived from the USGS Regional Aquifer System Analysis model (Garabedian 1992) and the Idaho Water Resources Research Institute model (Cosgrove, Contor, and Johnson 2006).

The two-dimensional flow model constructed in 2005 (Wood et al. 2005) represented regional underflow from the northeast using a specified-head boundary. However, the flows simulated across this specified-head boundary were significantly smaller than those simulated by the Spinazola, Garabedian, and Idaho Water Resources Research Institute models. Further analysis of the Spinazola model results provided a refined underflow estimate of 833,000 acre-ft/year across the northeast boundary of the OU 10-08 model domain (Table 2-3). This refined underflow estimate was required to support revision of the modeled boundary as a specified flux boundary to provide a better representation of transmissivity, groundwater flow, and contaminant transport throughout the model domain.

The two OU 10-08 aquifer thickness scenarios (Smith 2002) indicate that the SRPA thickens to the southeast along the northeast model-domain boundary. The rate of underflow is considered to increase with increasing thickness. This increase in underflow was estimated by apportioning the total estimated underflow along the northeast boundary with respect to thickness and percentage of flow with depth, as determined from the Spinazola numerical model. For a detailed discussion of the method by which flow was apportioned, see Appendix C-A in Wood et al. (2005).

The Spinazola numerical model represented the SRPA with five layers and overlapped the OU 10-08 model domain. Based on Spinazola's modeling results, approximately 70% of the groundwater flow may occur in the upper 150 ft of the aquifer in the area of the northeast boundary of the OU 10-08 model domain. These flows likely do not fluctuate greatly and are considered to be reasonably stable over time.

Table 2-3. Inflows to the area represented by the Operable Unit 10-08 model domain.

Inflow			Point of Recharge	Rate of Inflow	Source of Information
Regional underflow across the northeast boundary			Flow distributed horizontally across the active thickness of the SRPA	833,000 acre-ft/year (2,815,400 m ³ /day) variably distributed with depth	Spinazola (1994) five-layer numerical model
Tributary inflow	Birch Creek	Underflow	Top of aquifer in transition zone at mouth of Birch Creek Valley	78,200 acre-ft/year (264,300 m ³ /day)	Kjelstrom (1986)
	Little Lost River	Underflow	Top of aquifer in transition zone at mouth of Little Lost River Valley	155,000 acre-ft/year (523,900 m ³ /day)	Kjelstrom (1986)
	Big Lost River	Underflow	Top of aquifer in transition zone at mouth of Big Lost River Valley	295,400 acre-ft/year (998,400 m ³ /day)	Kjelstrom (1986)
		Stream flow	Top of aquifer in stream reach from Arco to the Big Lost River playa	70,200 acre-ft/year (237,200 m ³ /day)	USGS stream-gaging data, 1985–2003 (USGS Surface Water Data for Idaho) http://nwis.waterdata.usgs.gov/id/nwis/annual/calendar_year?search_criteria=station_nm&submitted_form=introduction
Direct precipitation			Distributed uniformly over the model domain and applied to the top of the aquifer	25,600 to 64,000 acre-ft/year (86,500 to 216,300 m ³ /day) – average is 44,800 acre-ft/year (151,400 m ³ /day)	Cecil et al. (1992)

 SRPA = Snake River Plain Aquifer

2.2.1.2 Tributary Inflows. Tributary inflows to the area represented by the OU 10-08 model domain and used in the three-dimensional flow model were derived from the Birch Creek, Little Lost River, and Big Lost River drainage basins. These inflows occur in the form of underflow from tributary basin aquifers and from infiltration of stream flows.

Underflows into the SRPA from the Birch Creek and Little Lost River basins are estimated from Kjelstrom (1986) to be 78,200 acre-ft/year (264,300 m³/day) and 155,000 acre-ft/year (523,900 m³/day), respectively. These underflows represent the basin contributions to tributary basin inflow, and include infiltrating surface-water flows near the mouths of the drainage basins. Underflow from the Big Lost River basin is estimated to be 295,400 acre-ft/year (998,400 m³/day). Underflows from all three tributary basins are considered to be reasonably stable over time, based on long-term stream-gaging data. Underflows are considered to enter the SRPA as vertical leakage to the top of the aquifer from transitional zones at the mouths of tributary basins. These transitional zones are comprised of fluvial deposits derived from the tributary drainages interfingering with basalts of the eastern Snake River Plain.

In contrast, stream flows from the Big Lost River are highly variable. These flows are transported along the Big Lost River, infiltrating along the river channel, in the INL spreading areas, and the Big Lost River Sinks. These episodic flows provide an average recharge to the top of the SRPA of 70,200 acre-ft/year (237,200 m³/day). For an expanded discussion of this episodic source of recharge, see Wood et al. (2005).

2.2.1.3 Recharge from Precipitation. The average precipitation over the OU 10-08 model domain is 8 in. (20 cm) per year. Recharge from precipitation within this area has been estimated to range from 2 to 5% of precipitation. Recharge over the 2,500 mi² model domain is estimated to be 44,800 acre-ft/year (151,400 m³/day) (Table 2-3). This corresponds to an infiltration flux rate of 0.85 cm/year.

Regional groundwater studies (Garabedian 1992; Contor 2004) developed regional distributions of recharge from precipitation based on the amount of precipitation, soil thickness, and infiltration capacity of the soil cover. Based on sensitivity tests using the OU 10-08 two-dimensional flow model, variable recharge with respect to these factors did not significantly affect groundwater flow (Wood et al. 2005).

2.2.1.4 Regional Underflow Out of the OU 10-08 Model Domain. No direct measurements of underflow out the area represented by the OU 10-08 model domain can be made. However, the outflow can be estimated from the accumulated inflows to the area. The estimated outflow across the southwestern boundary of the model domain is estimated to be approximately 1,476,600 acre-ft/year (4,990,600 m³/day).

2.2.1.5 Discussion of Steady-State Flow versus Transient Flow in Context of Transport. Based on the conceptual model of groundwater flow within the OU 10-08 model domain, inflows from regional underflow, tributary underflow, and recharge from precipitation are stable and can be represented using long-term averages. However, recharge from the Big Lost River is highly episodic, with long periods of no recharge interspersed with periods of rapid local recharge along the stream channel, to the INL spreading areas, and to the Big Lost River Sinks. This episodic recharge, while only a small percentage of the total water budget, occurs in the vicinity of known INL contaminant sources and has been considered as causing transient changes in flow directions in these regions (Goode and Konikow 1990). These transient flow directions likely affect contaminant transport and therefore should be considered when simulating three-dimensional transport.

2.2.2 Three-Dimensional Distribution of Regional Underflow into the Modeled Area

Regional underflow derived from the Yellowstone Plateau moves to the southwest across the northeastern boundary of the area represented by the OU 10-08 model domain. Cross-sectional underflow across this boundary was derived for the two-dimensional flow model from Spinazola's numerical modeling results (Spinazola 1994). This flux was estimated to be approximately 833,000 acre-ft/year (2,820,000 m³/day).

The northeastern model domain boundary is characterized by increasing aquifer thickness to the southeast. To accommodate this increasing aquifer thickness in the OU 10-08 two-dimensional model, the specified flux boundary was subdivided into 18 segments that approximated increasing aquifer thickness to the southeast. Two-dimensional flow was apportioned to each segment based on a compilation of Spinazola's layered fluxes.

The OU 10-08 three-dimensional numerical modeling effort required that this underflow be further subdivided over six layers that represent the vertical dimension of flow through the Snake River Plain Aquifer. This subdivision was derived for each of the 18 segments based on the vertical distribution of flow as simulated in the Spinazola model.

The Spinazola model consisted of five layers. Table 2-4 presents the thickness and percentage of total flow for each layer. The upper two layers each were uniformly 31.5 m thick. Layer 3 was uniformly 92 m thick. Layers 4 and 5 were of variable thickness.

Table 2-4 also presents the thickness and initial percentage of flow assigned to each layer of the OU 10-08 numerical model. Percentage assignments to the OU 10-08 model layers 1 and 2 were the same percentages of total flow as those determined in the Spinazola model because their thicknesses were similar. Layers 3 and 4 were each assigned 12.7 percent of total flow to represent the vertical subdivision of the upper 70 m of Spinazola's layer 3. Layer 5 was assigned 25.4 percent of total flow to represent subdivided flows from the bottom section of Spinazola's layer 3 and top of layer 4. Layer 6 was assigned 17.6 percent to represent subdivided flows from the bottom of Spinazola's layer 4 and layer 5.

Layered flows were further apportioned to represent the effect of variable aquifer thicknesses along the boundary. This apportionment was made by assigning layered flows to each of the 18 segments originally identified in the two-dimensional model. For those layers characterized by uniform thickness, segment flows were determined by multiplying the total flow within the layer by a simple ratio of segment length to total boundary length. For those layers with variable thickness and layer truncation, the apportionment was determined by multiplying total flow in the layer by a ratio of segment area to total layer cross-sectional area. This process was conducted for both the thick aquifer and thin aquifer scenarios.

Inverse numerical model runs were made using the initial distribution of inflows to estimate the layered distribution of hydraulic properties. These runs required hydraulic conductivity distributions within the lower layers that were larger than expected to accommodate the large percentage of regional underflows into those layers. The distribution of regional underflows subsequently was revised to better represent decreasing hydraulic conductivity with depth as defined by the conceptual model. This revised distribution consisted of reduction of inflow to layers 5 and 6. Estimated flow reductions were derived from a geometric ratio of the area of the thinnest aquifer cross section to the area of the cross section at the northeast boundary. This revision resulted in a decrease for layers 5 and 6 from 30.3 percent to 18.4 percent of the total underflow (Table 2-4). Underflow percentages for the upper layers subsequently were increased to maintain the total underflow of 833,000 acre-ft/yr (2,820,000 m³/day).

Table 2-4. Layer thickness and percentage of total flow by layer for the Spinazola five-layer model (1994) and layer thickness and percentage of total flow by layer (initial and revised) for the OU 10-08 six-layer model.

Spinazola Model Layer	Thickness (meters)	Percent of Total Flow by Layer	OU 10-08 Model Layer	Thickness (meters)	Percent of Total Flow by Layer	
					Initial	Revised
1	31.5	16.3	1	35	16.3	23.3
2	31.5	15.3	2	35	15.3	21.9
3	92	38.1	3	35	12.7	18.2
4	Variable (<500)	24.0	4	35	12.7	18.2
5	Variable (<1,00)	6.3	5	70	25.4	12.4
			6	Variable	17.6	6.0

2.2.3 Three-Dimensional Water-Level and Temperature Data Sets

Understanding groundwater movement in the SRPA beneath the INL is essential to evaluating potential impacts from anthropogenic activities. This section evaluates historical information on aquifer water levels and temperatures to guide development of the OU 10-08 subregional aquifer flow and transport model. The section is separated into two primary subsections: water level data and temperature data.

2.2.3.1 Water Level Data Evaluation. Contaminant transport in groundwater is primarily controlled by the groundwater flow field, so understanding that flow field is paramount to development of a robust contaminant transport model. An objective of this evaluation is determining impacts of transient water levels since groundwater flow models solve either a transient flow equation or a steady-state flow equation. The former accounts for water levels and flow directions that may change with time, in response to changing water fluxes or other conditions. The latter assumes that such transients have a negligible impact on the variable of interest, and thereby defines a flow field that is constant over time. Determination of which is appropriate for a particular problem is generally based on some knowledge of the flow field, the relative magnitude of the transient fluxes, or other observations of the system.

For the OU 10-08 model, potentially significant transient effects can occur at timescales ranging from one to many years. Transient effects may also occur at different length scales, from very local influences, like pumping, to regional-scale influences such as large-scale changes in vertical recharge. At the INL, local transient fluxes primarily result from ephemeral flow of the Big Lost River. Regional scale transients at the INL include variations in underflow into the study area from either the upgradient area to the northeast or from tributary basins northwest of the INL Site.

Transient influences on groundwater flow have been considered, in varying detail, in several previous studies. The Idaho Water Resources Research Institute groundwater model of the SRPA (Cosgrove et al. 2006) considered transient effects in great detail because one of its primary goals was improved understanding of the water balance of the aquifer. Focusing on groundwater resources, that effort did not address contaminant transport. Goode and Konikow (1990) examined the influence of the Big Lost River on contaminant transport in an unsuccessful effort to explain large dispersivities required in previous contaminant transport models near INTEC. The ongoing USGS modeling effort also incorporates transient recharge from the Big Lost River. Based on those studies and other observations,

the OU 10-08 modeling project assumes that substantial interannual variations in Big Lost River discharge will have to be included in any robust contaminant transport model. Due to the potential importance of Big Lost River flows and their affect on groundwater flow directions at the Site, a separate study, involving installation and high-resolution monitoring of water levels with an increased data collection density around the river, was initiated in 2006 with initial reporting to occur in FY 2007.

The focus of the transient evaluation in this section is on regional-scale transient behavior. Historical time-series water level data from in and around the OU 10-08 modeling domain (Figure 2-15) were examined to assess how and where changes in water levels appear to most significantly influence groundwater flow.

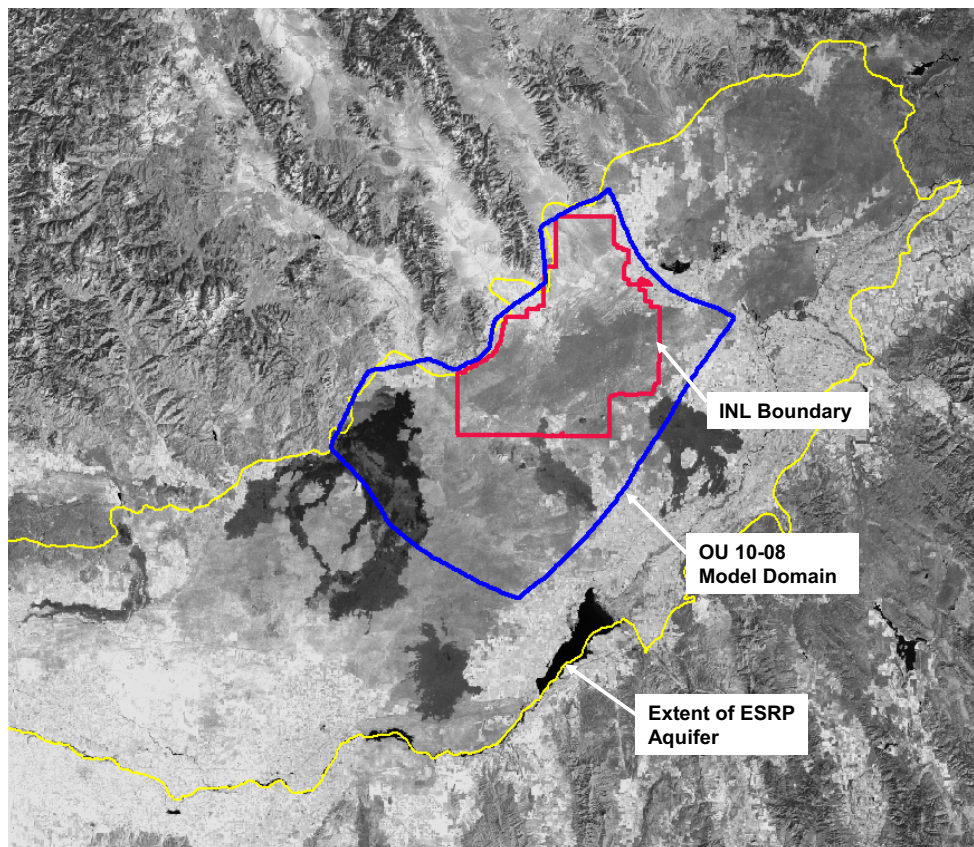


Figure 2-15. Operable Unit 10-08 groundwater modeling domain, INL boundary, and eastern Snake River Plain.

2.2.3.1.1 Water Level Data Sources—Water level data for this study were obtained from two sources. Time-series data were primarily obtained from the on-line National Water Information System database of the U.S. Geological Survey (USGS 2005). Higher spatial density water level data were obtained from the year 2004 and 2005 water level monitoring campaigns of the OU 10-08 project team, using conventional field equipment. The latter data are now available in the Environmental Data Warehouse. The majority of the water level data is from within the OU 10-08 model domain but some data external to the OU 10-08 model domain are used to improve mapping along the domain edges.

2.2.3.1.2 Transient Water Level Data—To examine the magnitude and spatial and temporal variability of transients in the groundwater flow field in the SRPA, long-term water level records were compiled from 110 wells (Figure 2-16) in the SRPA for the period between 1980 and 2005. The wells selected were those with hydrographs sufficient to describe both seasonal and long-term variations.

Examination of hydrographs from selected wells suggests that, in general, water levels across most of the model domain behave similarly (Figure 2-17). At the longest timescale, there is a general decline that has been tied to changes in aquifer recharge resulting from changes in irrigation practices (Kjelstrom 1986). Superimposed on that trend are strong multi-year cycles that likely reflect changes in recharge associated with interannual-scale climatic swings. Finally, many of the wells display at least some seasonal water level changes, resulting from a combination of seasonal variations in natural recharge and seasonal water management practices.

Comparing responses at different locations indicates that the seasonal variations are stronger nearer to irrigated areas (south of Mud Lake, for example) and along the margins of the aquifer. The strongest apparent response to multi-year climatic effects, like changes in tributary discharge, is generally evident nearer to those recharge areas, and away from large irrigated tracts, where anthropogenic controls likely mask some of the climatically induced changes in recharge to the aquifer. For example, a multi-year increase in water levels arrives at a peak around 1984 in the southern part of the Site while water levels in the northern part of the Site continue to rise until 1988. A similar multi-year peak occurs again in 1999 in the south with the northern wells again lagging behind.

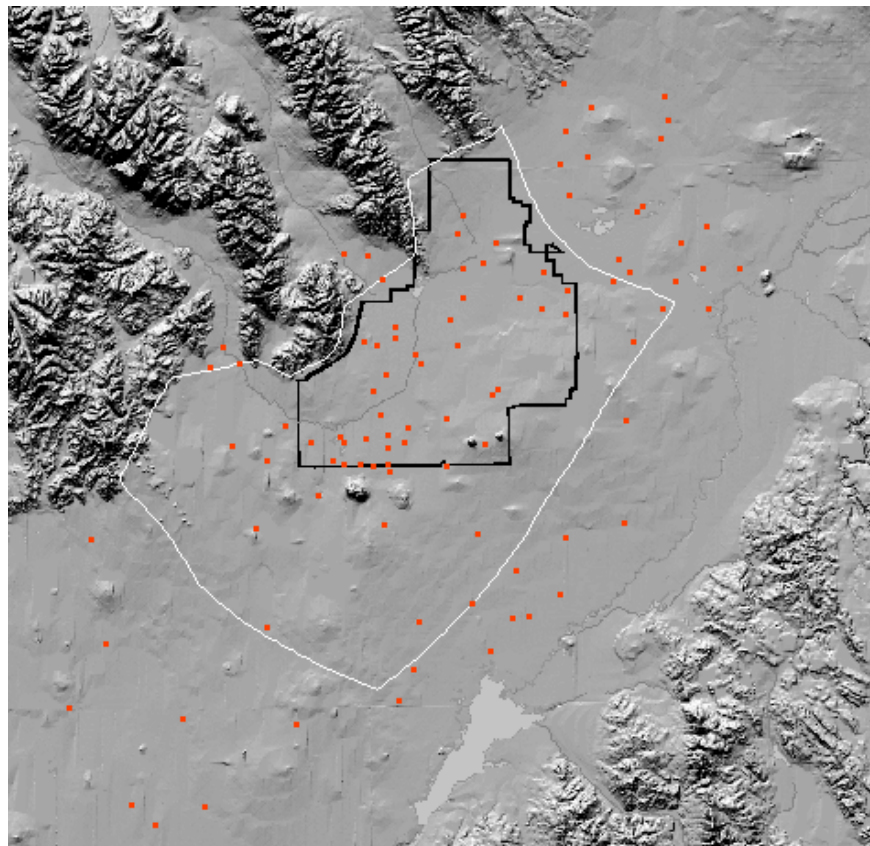


Figure 2-16. Well locations used in transient water-level analysis. Also shown are the INL boundary and the OU 10-08 model domain.

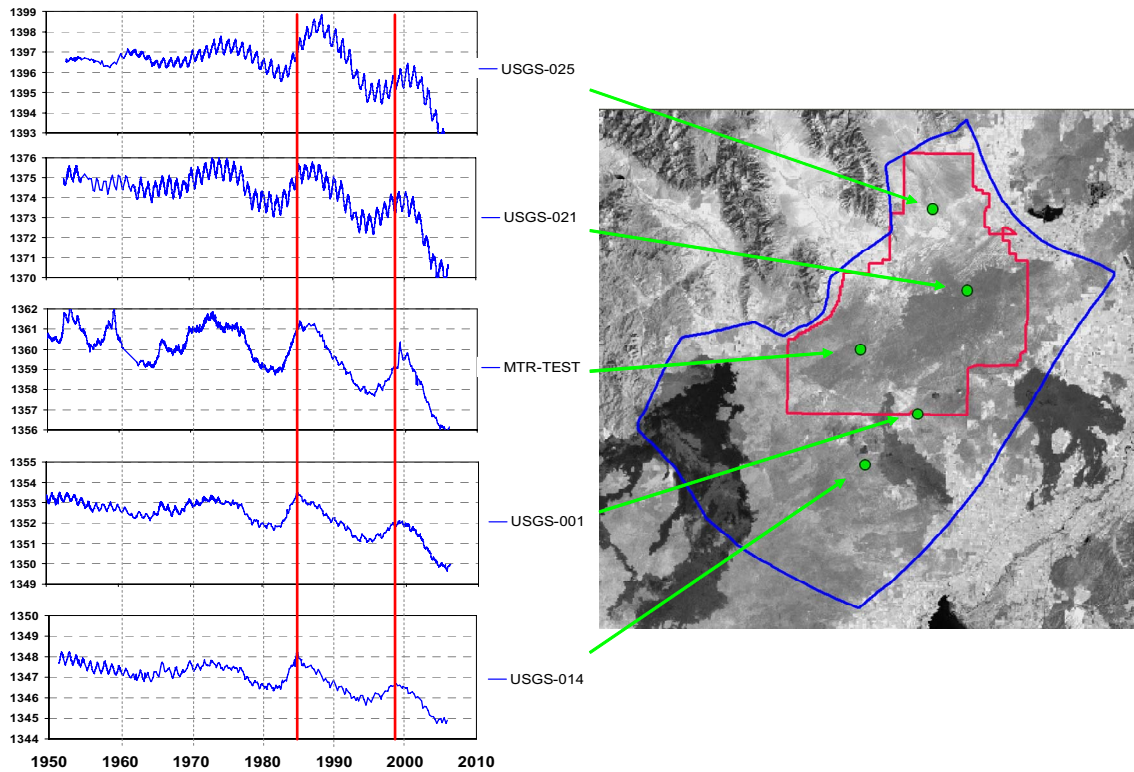


Figure 2-17. Example hydrographs from aquifer wells completed in the OU 10-08 modeling domain.

2.2.3.1.2.1 Time Series Analyses of Horizontal Gradient Data—

Assuming isotropic and homogeneous conditions, the direction and magnitude of the groundwater flow can be inferred from the local hydraulic gradient. The local gradient can be calculated directly by triangulation between appropriate sets of wells or indirectly by interpolation between many wells. Both methods are used in this section. Although these approaches to estimating horizontal gradients would give erroneous results where strong vertical gradients exist, there is little evidence of strong vertical gradients at the INL. There is only a small number of locations (discussed in Section 2.2.3.1.3.1) with information available to determine vertical gradients.

Gradients directly from water level data

Figure 2-18 illustrates application of the triangulation approach to water level time series data for a set of three wells near the southern boundary of the INL. The transient gradient direction calculated from water levels in these three wells varies by less than 10 degrees over the 50-year period of record, indicating only minor changes in flow direction. If enough locations show this behavior of only minor changes in flow direction, it would be reasonable to conclude that water table variations likely have minimal impact on transport directions, and would suggest that a steady state flow model can be used to simulate the system. Performing these three-point calculations for the triangulation approach over the entire OU 10-08 model domain for this purpose would be arduous. Instead, an indirect analysis using interpreted water levels is performed instead.

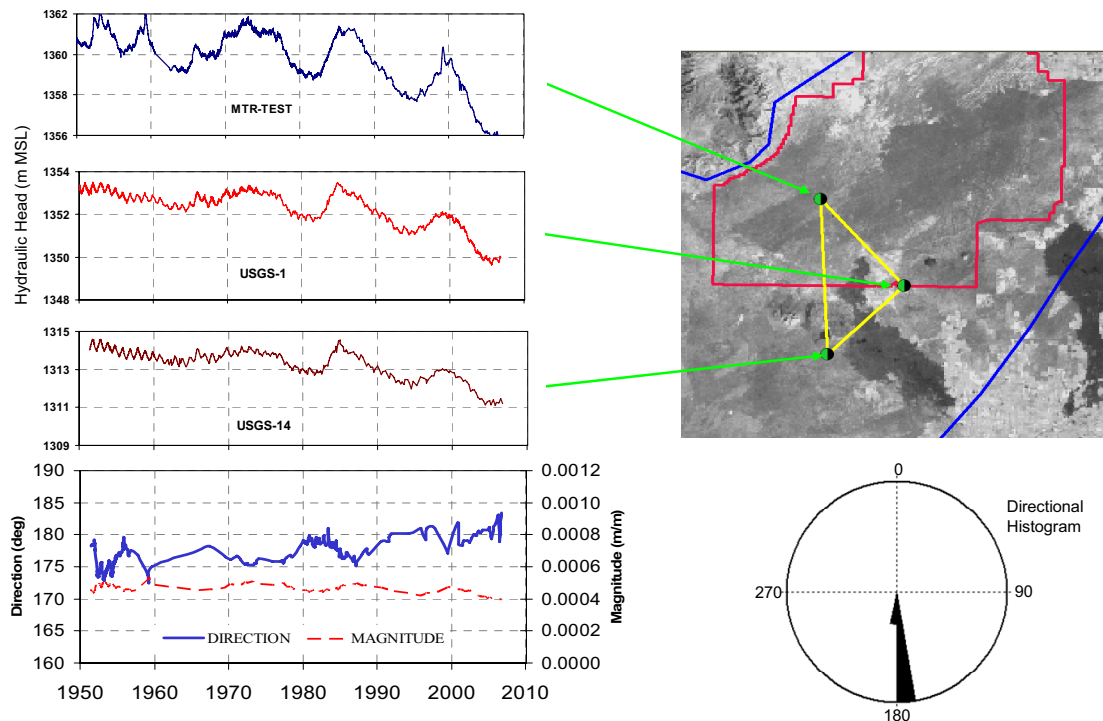


Figure 2-18. Application of triangulation method for inferring groundwater flow direction near the southern boundary of the INL.

Gradients indirectly from interpolated water levels

To examine temporal variations of the water potential gradient across the Site, long-term water level records from 1980 to 2005 for 110 wells in the SRPA were used to calculate long-term trends in water levels and in water potential gradients across the Site. The water level records were first interpolated onto a common temporal time series of approximately 100 time slices. Total water potential data from each time slice were then spatially interpolated, using TECPLOT Version 10, onto a uniform grid using the same Kriging algorithm used for creating reference water table maps for the OU 10-08 project. An example, showing the interpolated water levels for CY 2000 and calculated streamlines from primary INL facilities, is shown as Figure 2-19.^d Water potential gradients were then calculated at each grid location for each time slice and those data were statistically analyzed to determine the average and standard deviation of the flow directions inferred from the gradients (Figure 2-20).

The results of this analysis (Figure 2-20) show that for most of the OU 10-08 model domain there are only minor changes in estimated water potential gradients over the 25-year record analyzed. The standard deviation of the gradient is almost exclusively less than 10 degrees, indicating that flow directions are relatively constant while the water table rises and falls. While the water table may have changed as much as 20 to 25 ft at many locations, with few exceptions the changes in apparent flow directions are minimal.

d. The sequence of resulting water potential maps has been assembled to produce an animation describing water level changes over time in the study area. That animation, including calculated streamlines from primary INL facilities, is stored electronically in OU 10-08 project files.

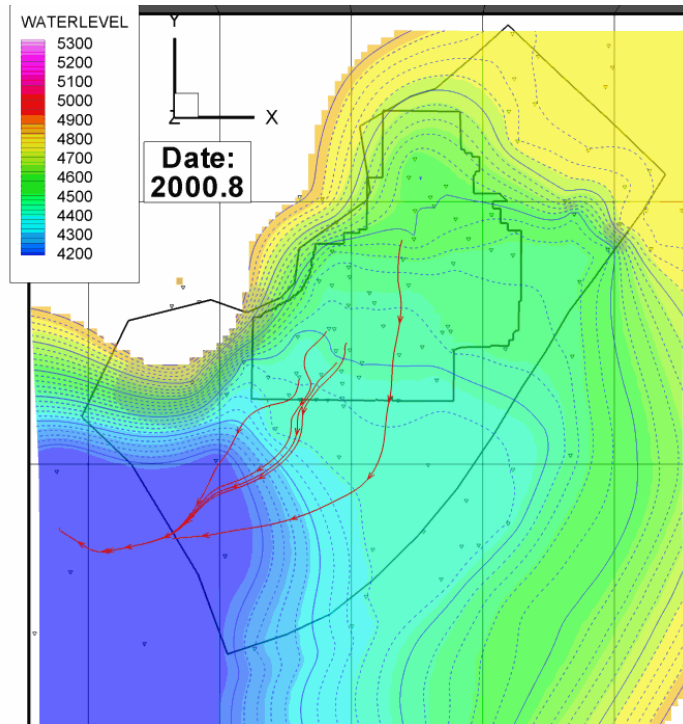


Figure 2-19. Interpolated water level for Calendar Year 2000 using 110 wells. Streamlines are from INL facilities assuming flow directions remain constant and the aquifer is homogeneous and isotropic.

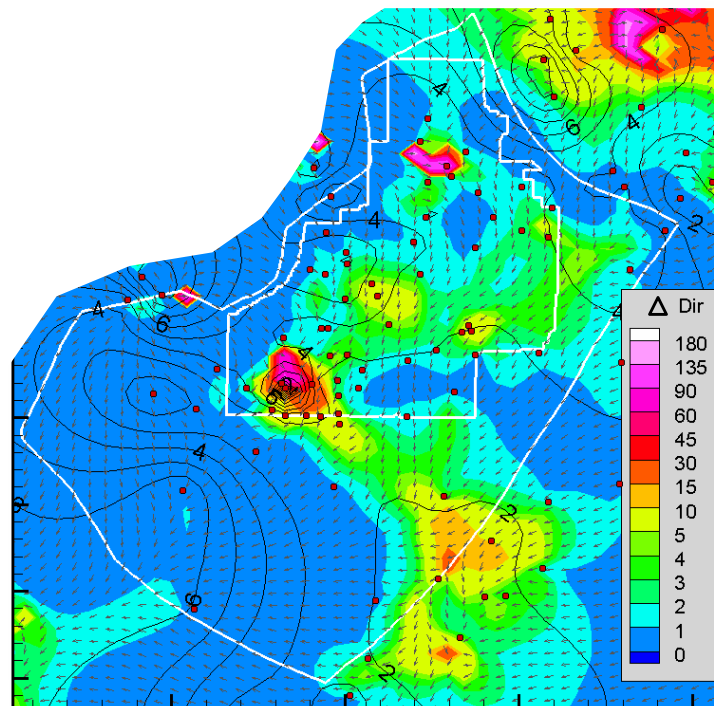


Figure 2-20. Mean water potential gradient direction (arrows) and standard deviation of flow direction (color contouring) from 25-year water level records at 110 wells, interpolated onto a regular grid. Black contour lines show standard deviation of interpolated water level for the 25-year period and red circles show the well locations.

Exceptions that are easily discerned are at the spreading areas south of the Radioactive Waste Management Complex, in the vicinity of TAN, and northeast of the OU 10-08 boundary near Mud Lake. The variation in flow direction at the spreading area is due to the large volumes of water that occasionally are discharged from the Big Lost River. In particular, Well USGS-88, located between spreading areas A and B shows an 18-m rise during the 1980s in response to spreading area diversions of Big Lost River flows. The rise in this one well is several times the response in surrounding wells. This represents an approximate 13% change in the overall saturated thickness of the aquifer at this location. Since these data were included in the analysis, this well likely accounts for the large variation near the Radioactive Waste Management Complex in Figure 2-20.

The variation in flow direction at TAN may be due to the extreme flatness of the water table and resultant elevated sensitivity of the flow direction to slight changes in water level. To the east of TAN, a water-level change of 8 m observed in USGS-30's deepest piezometer between a high in May 1986 and a low in September 2004 represents only a 2–3% change in the estimated overall saturated thickness of the aquifer, and indicates that changes in regional underflow are not significant.

In conclusion, relative to steady-state versus transient simulation, the minor changes in flow directions for the majority of the OU 10-08 model domain suggest that the regional flow system can be represented as a steady-state flow system and, thus, that boundary fluxes and/or heads can be represented using long-term average values. The large variations in apparent flow direction around the Big Lost River, however, support previous assumptions that groundwater flow in that area should incorporate the effect of the transient flow regime on contaminant transport.

2.2.3.1.3 Selection of Water Level Calibration Data—Based on the conclusion that steady state conditions could be used to represent the flow system, a decision was made to use a single-point in time that had the most water level data. This time chosen was Calendar Year 2004 when an extensive groundwater level monitoring campaign was conducted by the OU 10-08 project. All totaled, there are over 300 active aquifer wells in the area covered by the OU 10-08 model domain (6,475 km²). Over 200 wells were measured during a single week in June 2004 by the OU 10-08 field team. Of these, 207 wells were selected because they were mostly contained within or near the INL boundaries (2,305 km²). The remaining area (4170 km²) in the OU 10-08 model domain that is outside INL boundary contains more than 100 aquifer wells. Of these active wells, 17 were selected to supplement the calibration data set. Figure 2-21 shows the locations for the 224 wells that were used for calibration of the three-dimensional flow model.

Ten of the seventeen supplemental wells were chosen because they were measured by the USGS multiple times during the 2004 year and a meaningful average water level could be determined. Seven wells with single water levels measured by the USGS were chosen because they were important for areal coverage or replaced unusable data from the INL set. The ten supplemental wells with time-averaged water levels are along the edges of the modeling domain sufficiently far enough from the major facilities at the INL that use of an average 2004 water level is appropriate.

There are a total of 224 water level observations that were used to calibrate the three-dimensional flow model. This total includes 189 wells with single open intervals in the saturated zone and 35 wells with multiple open intervals below the water table, including two Westbay wells (MIDDLE-2050A and MIDDLE-2051). The implementation of this well set into the calibration set for the three-dimensional flow model is discussed in the three-dimensional flow model implementation (see Section 3).

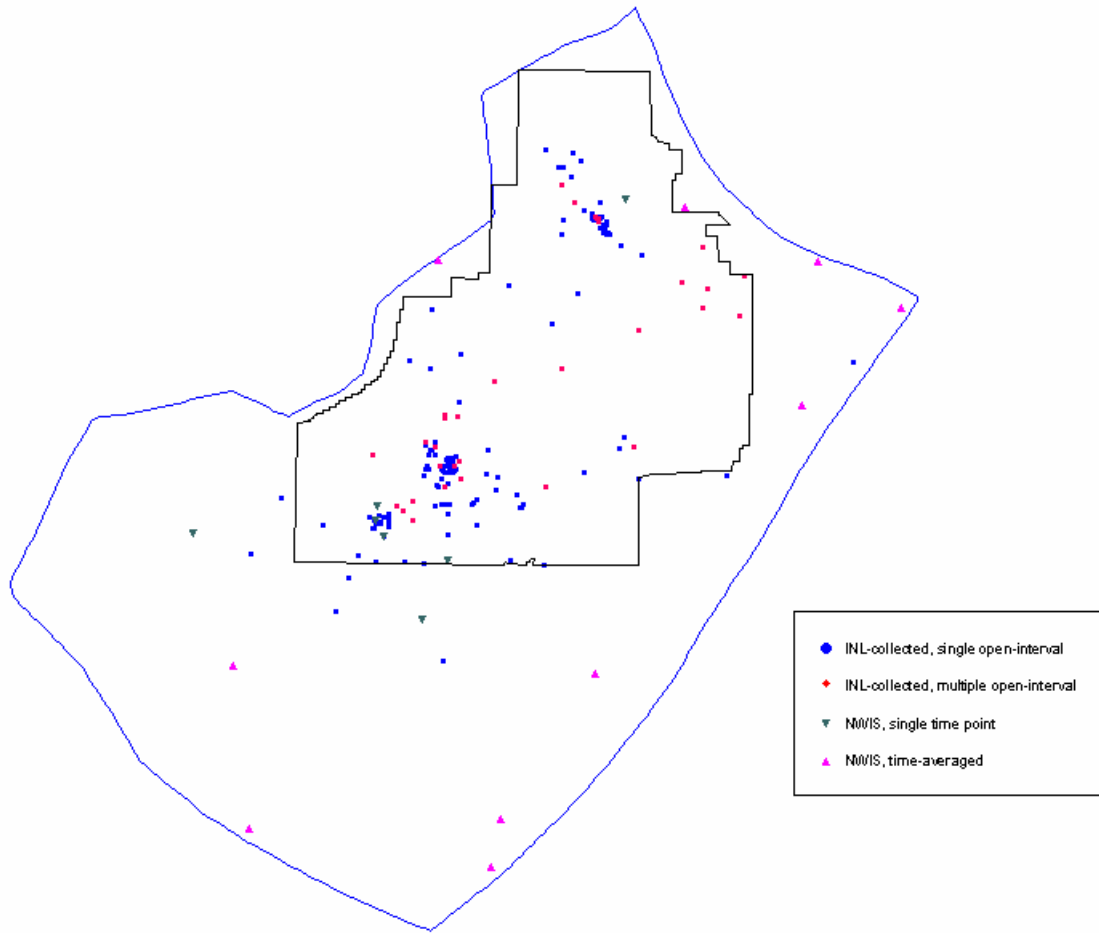


Figure 2-21. Location and type of aquifer wells and sources of data used as the calibration set for the OU 10-08 model.

The Westbay multi-level monitoring wells were constructed after 2004. Pressure readings for each of the five sampling ports per well were available for two periods in 2005 and were backwards extrapolated for 2004 as follows. The 2005 pressure readings were converted to total hydraulic head in terms of elevation above mean sea level (National Geodetic Vertical Datum 1929). The local average annual water table decline for each well was estimated from water levels measured during the 2004 and 2005 monitoring campaigns in surrounding wells. This resulted in an average decline of 0.51 m near MIDDLE-2050A and 0.49 m near MIDDLE-2051. These declines were used to adjust the Westbay equivalent water levels to represent the June 2004 timeframe.

The June 2004 sampling event coupled with supplemental National Water Information System water levels yielded sufficient data to develop a detailed water table contour map (Figure 2-22). The equivalent water pressures provide one of the primary calibration targets for the three-dimensional flow model. Wells with multiple intervals used the pressure from the shallowest interval in this contour map. Additional locations outside the model domain (indicated with “+” symbols) are used to constrain the interpolation. Steady-state head values were extrapolated from this interpolated water table for model boundary conditions along the southwest boundary of the OU 10-08 flow model.

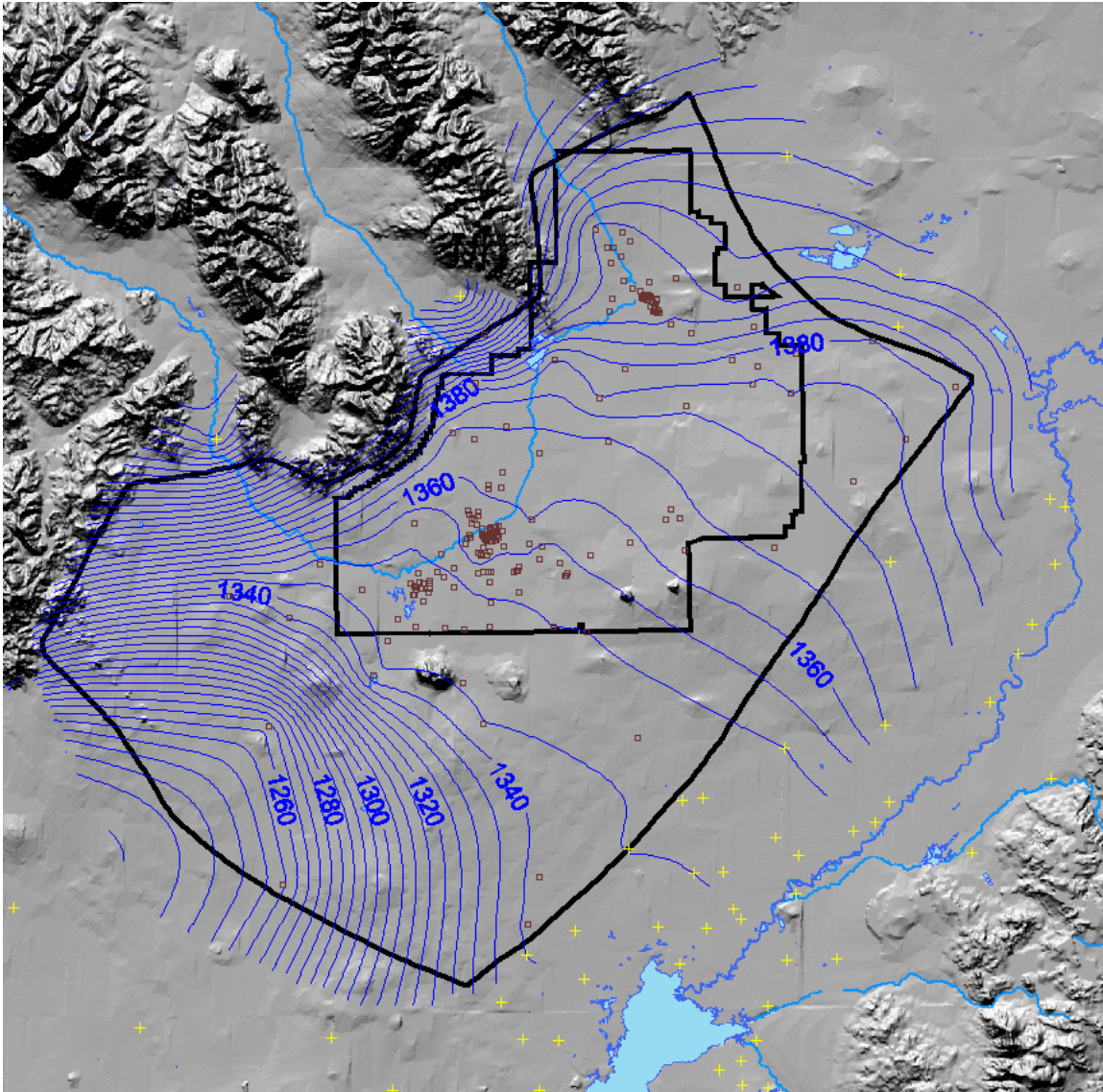


Figure 2-22. Water table contour map developed from June 2004 calibration data set (contours are meters above mean sea level; interval is 5 m). Squares represent locations used for calibration inside the OU 10-08 model domain. Additional measurement locations outside the model domain help constrain interpolation (yellow '+' symbols).

2.2.3.1.3.1 Vertical Gradient Analysis—The potential for vertical flow at a point within an aquifer is defined by the vertical gradient of water potential, which is determined from measurements of water potential at different elevations at the same location. In the OU 10-08 study area, vertical gradient data are limited because most of the aquifer wells interrogate only the upper portion of the aquifer. Locations where vertical gradients have been calculated include wells where nested piezometers or other multi-level sampling systems (e.g., Westbay systems at MIDDLE-2050A and MIDDLE-2051) have been installed and sites where horizontal distances between wells are less than the vertical distance between their screened depths. While the available data indicate, in some cases, sufficient gradients to drive vertical flow, groundwater flow is a function of both gradient and hydraulic conductivity, so even where sufficient gradients exist, there may be little or no vertical flow if the vertical hydraulic conductivity is low. Note that the potential gradient is defined in this section as the change in

head in the direction of increasing elevation, and flow occurs in the direction opposite the gradient. A positive gradient is thus a downward driving force for flow and gradients are hereinafter referred to by the implied potential flow direction (e.g., a negative gradient results in upward flow).

There are six true piezometer clusters on the INL within the OU 10-08 model domain from which vertical head gradients can be determined (Figure 2-23). Two nested piezometers, a corehole near TAN named TCH-2 (two piezometers) and USGS-30 (three piezometers), are located in the northern portion of the model domain. Westbay sampling systems, which provide multiple independent aquifer access points through a single access tube, have been installed at four locations, Wells MIDDLE-2050A, MIDDLE-2051, USGS-132, and USGS-134. Each of the Westbay wells has multiple measuring ports that serve as piezometers.

Figure 2-24 shows hydraulic head hydrographs for the two nested piezometers in the northern part of the INL and the resulting vertical gradient time series. The highest heads in USGS-30 come from the lowest piezometer resulting in upward gradients ranging from approximately -0.025 m/m to -0.030 m/m over the course of 40 years. Much fewer data are available for TCH-2, and, additionally, there appears to be an error with the data. The upper piezometer head is nearly static over time while the lower piezometer shows a downward trend and fairly strong annual fluctuations; this results in a calculated vertical gradient time series that mirrors the lower piezometer hydrograph.

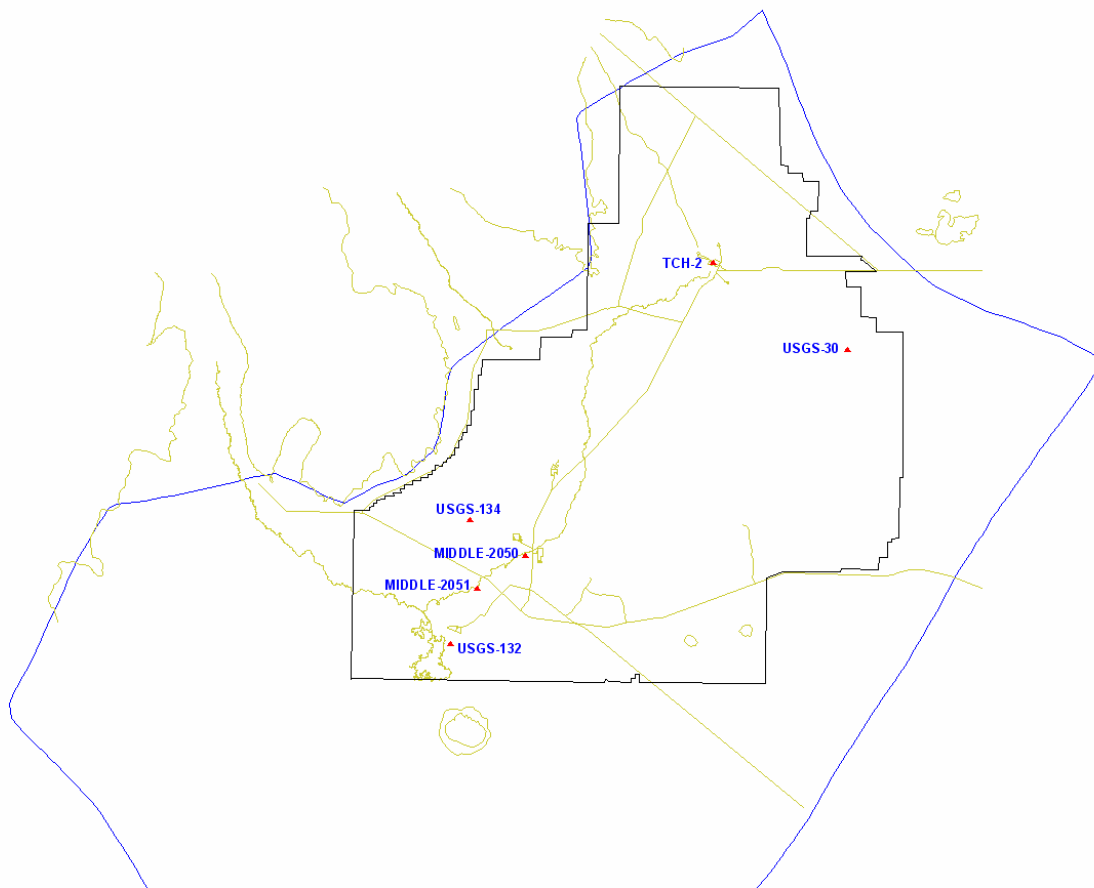
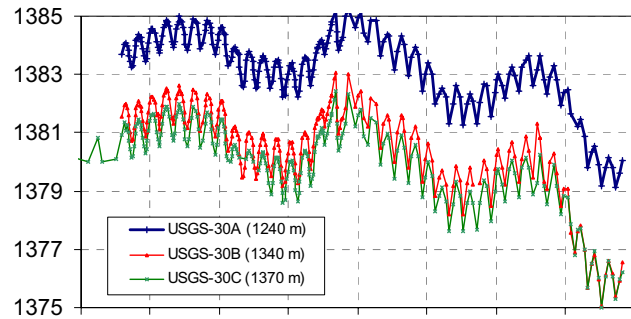


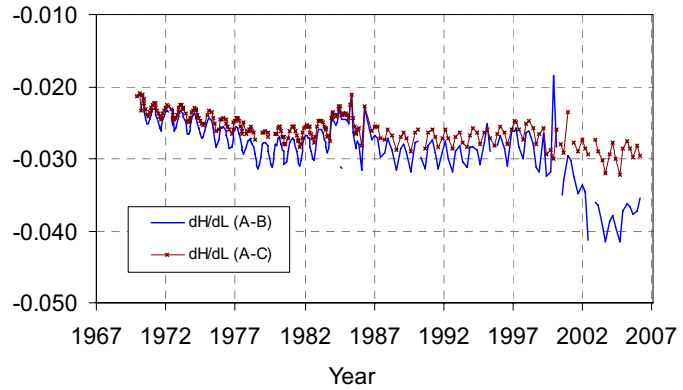
Figure 2-23. Locations of wells with nested piezometers or Westbay systems.

USGS-30 (A,B,C)

Hydraulic head (m)

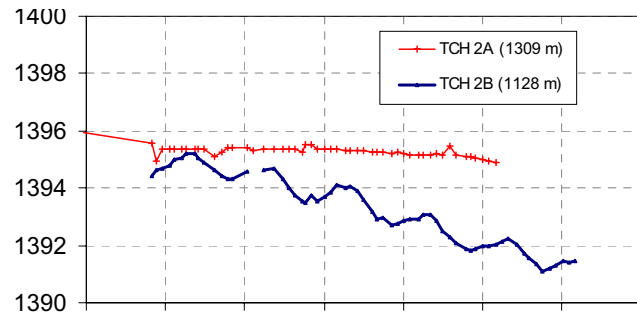


Vertical gradient (m/m)



TCH-2 (A,B)

Hydraulic head (m)



Vertical gradient (m/m)

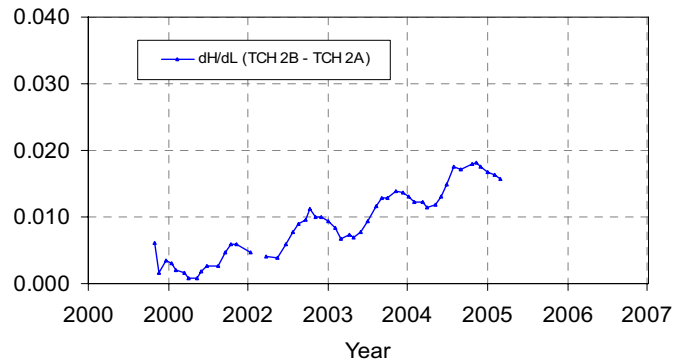


Figure 2-24. Total hydraulic head and vertical gradients as a function of time for piezometer wells USGS-30 (top) and TCH-2 (bottom). Head graph legends include elevation of the opening of each piezometer.

The abundance of aquifer wells in the TAN vicinity provides an opportunity to replace the upper TCH-2 piezometer data in the vertical gradient analysis. Figure 2-25 is an excerpt of an illustration that shows the measured extent of the TAN trichloroethylene (TCE) plume. Very near TCH-2, at distances of 15 and 22 m, respectively, from TCH-2, are two additional aquifer wells, TAN-08 and TAN-17. These two wells are open in the aquifer much higher (1,387 m for TAN-08 and 1,359 m for TAN-17, above mean sea level) than the lower piezometer in TCH-2 (at 1,128 m above mean sea level). Relative to TCH-2, the close horizontal spacing and diverse vertical spacing of these two wells indicates they are suitable for determining vertical hydraulic gradients and may provide better results than were obtained using TCH-2A.

Figure 2-26 shows hydrographs of these three wells compared to a hydrograph for USGS-25, a well located approximately 6.6 km northwest of TCH-2 that is open 257 m higher in the aquifer than the deep piezometer TCH-2B. The hydrographs of USGS-25 and TCH-2B are very similar in seasonal patterns and longer-term trends. Figure 2-26 also compares the deeper TCH-2B hydrograph with the only two available water levels from TAN-08 and TAN-07. Though their records are not extensive like USGS-25, the measurements appear to mimic the same regional downward trend, which is not seen in TCH-2A, the upper piezometer.

Figure 2-26 also shows the averaged results of comparing the June 2004 and June 2005 water levels among the three closely-spaced wells. It appears there may be small negative gradients (upward flow) between the two shallower wells but positive (downward flow) gradients when compared to the deep piezometer.

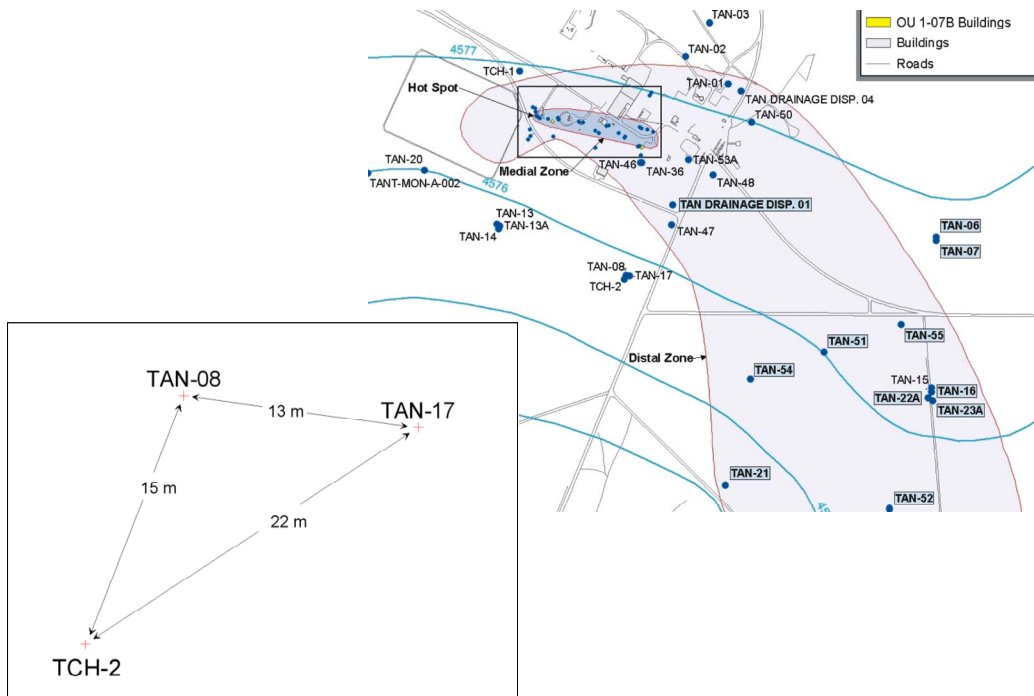


Figure 2-25. Extent of TCE plume at TAN and some of the many aquifer wells at this facility. Inset shows horizontal spacing of two proximal wells (TAN-08 and TAN-17) that are ideal for replacing the upper TCH-2 piezometer in this vertical gradient analysis.

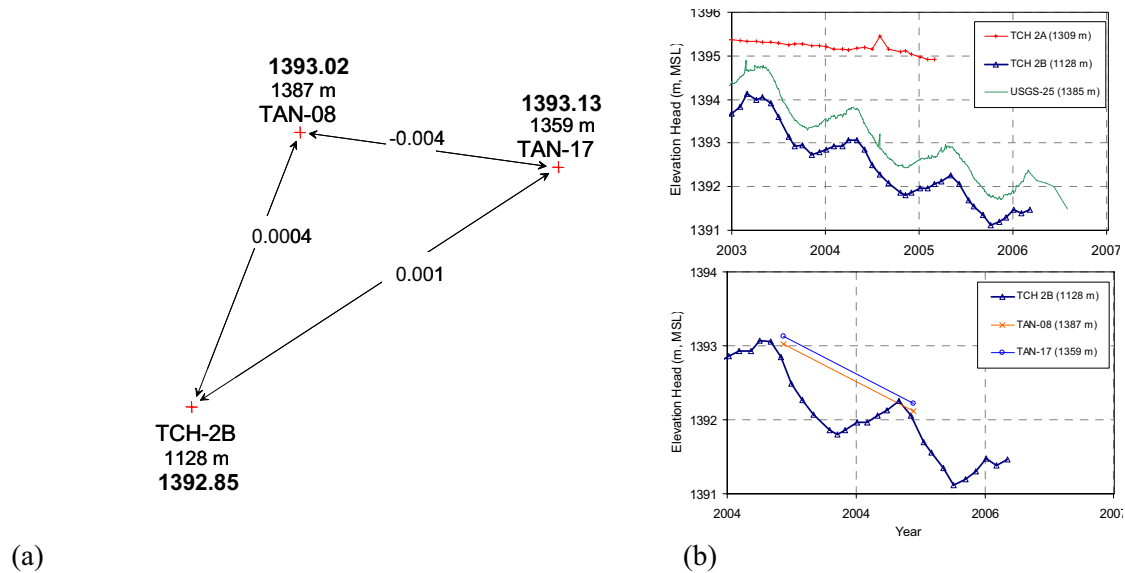


Figure 2-26. (a) Average of calculated vertical gradients (m/m) for June 2004 and 2005 for two shallow wells and the deep piezometer in TCH-2 (bold font shows head value in meters above mean sea level; number closest to name is the open interval midpoint elevation). (b) Hydrographs of upper and lower TCH-2 piezometers compared to USGS-25 (top hydrograph) and TAN-08 and TAN-17 compared to TCH-2 lower piezometer (bottom hydrograph).

The other piezometers with available data include the four Westbay systems installed in MIDDLE-2050A, MIDDLE-2051, USGS-132, and USGS-134. The hydrographs of total hydraulic head and calculated vertical gradient time-series for each are shown with common scale ranges in Figure 2-27. It can be observed that the head in both MIDDLE-2050A and MIDDLE-2051 initially decreases with increasing depth and then reverses sharply before continuing to decrease with depth. The calculated gradients in MIDDLE-2050A range from approximately -0.10 to approximately 0.02 m/m. They range from approximately -0.02 to 0.18 m/m in MIDDLE-2051. These two wells both show a mix of upward and downward gradients. The change in head with depth in the other two Westbay systems, USGS-132 and USGS-134, is more subtle with calculated vertical gradients ranging from -0.01 to 0.02 in both wells.

Similar to the replacement wells for the upper piezometer in TCH-2, wells that are closely-spaced horizontally but that have large differences in open interval depths can be used together to determine vertical gradients. Potential well pairs were examined using criteria such as horizontal separation distances on the order of 50 m or less and vertical separation distances of 100 m or more. Seven well pairs were found and are shown in Figure 2-28. For five of these pairs, horizontal separations ranged from 19 to 34 m. Wells ANP-09 and ANP-10 are horizontally 420 m apart and USGS-18 and CH-2A are 1,020 m apart. Vertical separation (distance between midpoints of open intervals) ranged from 20 to 1,450 m.

Vertical gradients were calculated using data from the June 2004 campaign with the exception of the pairing of USGS-18 and CH-2A, which used data from October 2005.

The absolute values of the magnitudes of the vertical gradients from the two most northern and southern pairs are small (<0.01 m/m) and, with the exception of the USGS-065:TRA-06A pair, significant gradients are only evident where differences in screened interval depth are very large.

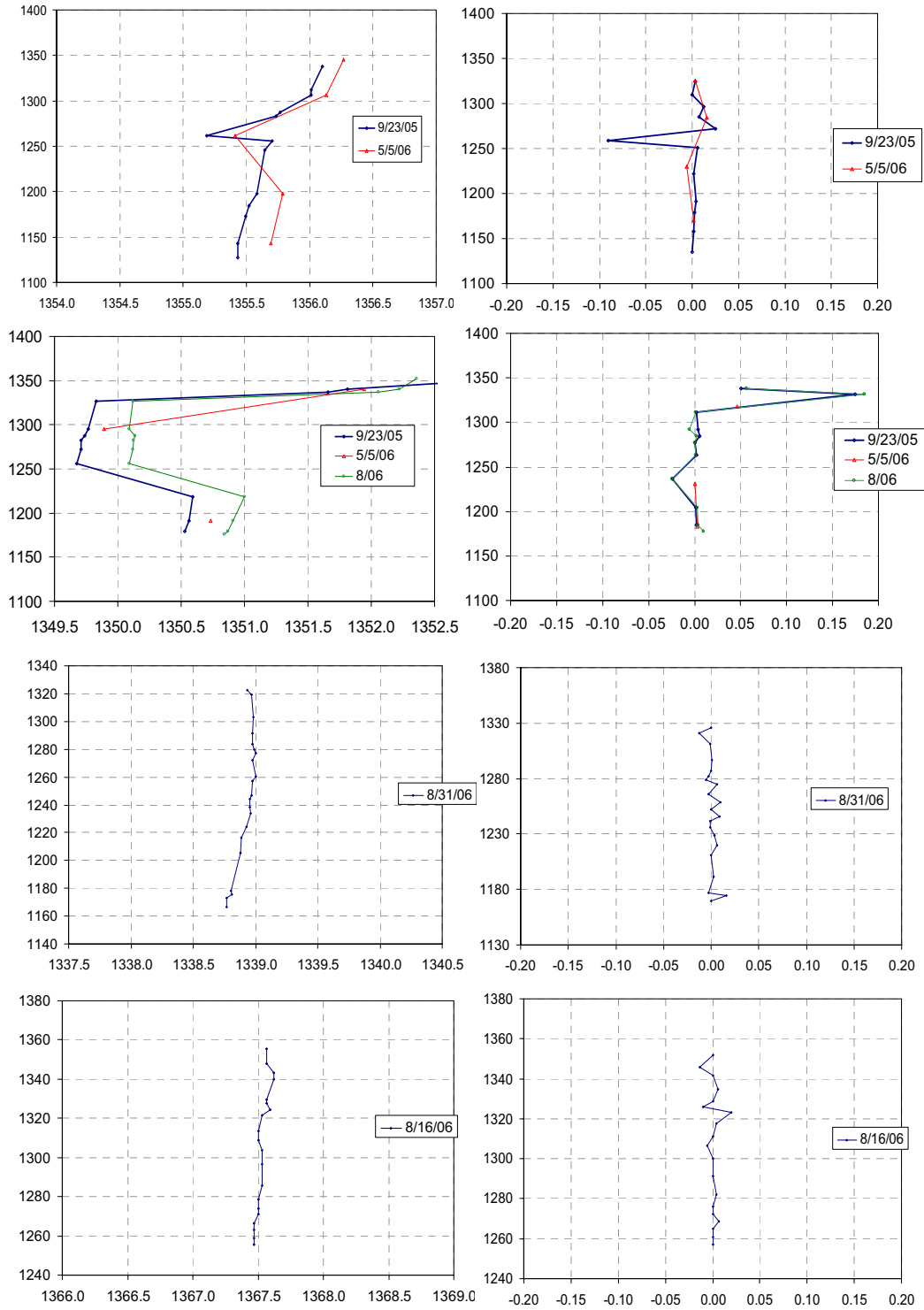


Figure 2-27. Total hydraulic head (left) and vertical gradients (right) as a function of depth in the aquifer for several sampling periods of Westbay systems in MIDDLE-2050A, -2051, USGS-132, -134 (top to bottom). Vertical scales are elevation in meters above mean sea level; heads are in meters above mean sea level, and gradients are dimensionless.

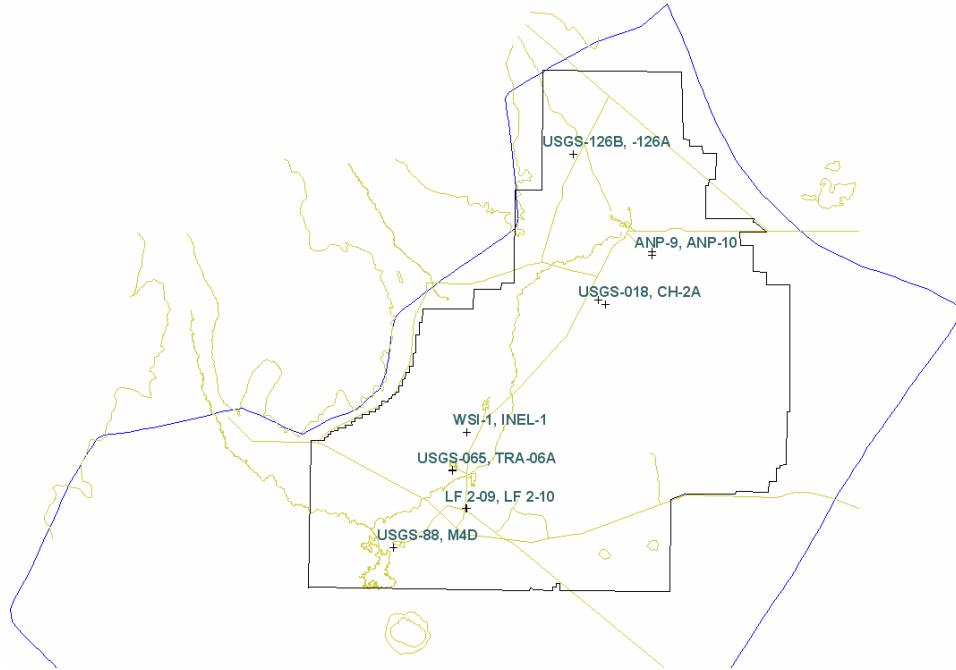


Figure 2-28. Seven well pairs used for additional vertical gradient analysis.

Figure 2-29 shows the results of all available vertical gradient from piezometers, Westbay systems, and well pairs. The three most southerly well pairs are relatively shallow and the direction of the gradient in those pairs is consistent with data from the upper ports in the Westbay wells (positive vertical gradients; downward flow). The two very deep well pairs, WSI-1: INEL-1 and USGS-018: Corehole-2A (CH-2A), indicate gradients in opposite directions, upward (negative gradient) for the former and downward (positive gradient) for the latter. Both of these pairs compare shallow aquifer heads to heads from depths far below the bottom of the aquifer.

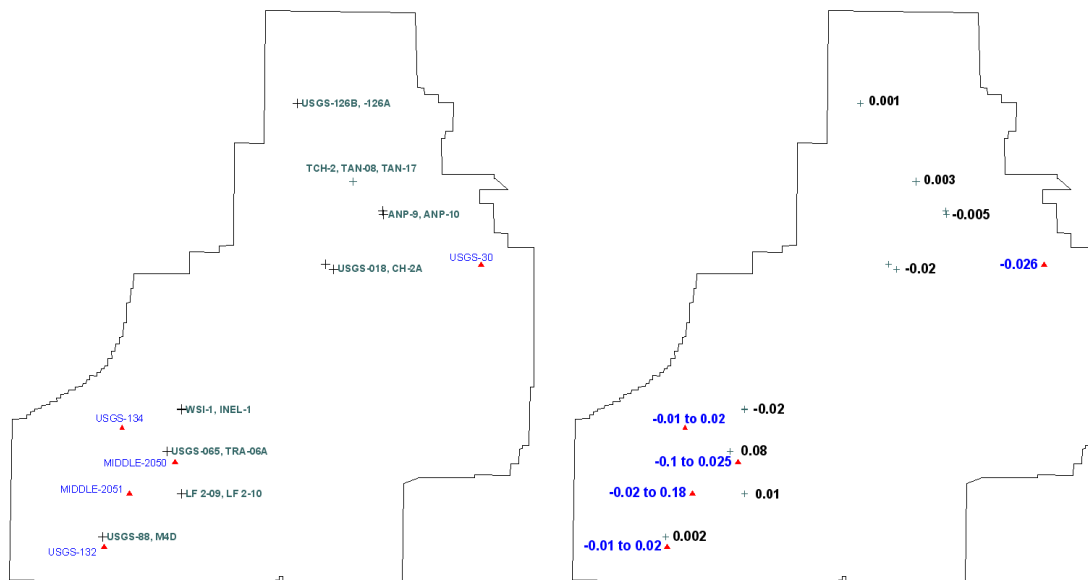


Figure 2-29. Locations and results of all available vertical gradient information. Red diamonds represent nested piezometers and blue plus signs represent closely located well pairs.

2.2.3.1.4 Summary of Water Level Data Evaluation—Data describing vertical gradients in the OU 10-08 modeling domain are sparse and generally insufficient to adequately describe the potential for vertical flow throughout the system. Nonetheless, two conclusions can be drawn from the available data.

First, data from locations in the southern part of the INL generally display downward (positive) gradients in the upper portion of the aquifer, which may reflect, at least in part, localized recharge from the Big Lost River. Otherwise, vertical gradients are generally inconsistent between locations, and even within a single borehole, with frequent changes in gradient direction appearing in both nested piezometers and multi-level Westbay sampling systems. This pattern of inconsistent vertical gradients (in some areas up, in other areas down) is consistent with a system of numerous discontinuous layers of alternating high and low hydraulic conductivity (K), as opposed to a system containing laterally extensive hydrogeologic units. Figure 2-30 illustrates the hypothetical effect of such a system on flow between two constant head boundaries in a 1-km long by 100-m deep aquifer with a 100:1 $K_h:K_v$ (horizontal to vertical hydraulic conductivity) ratio and background K 100 times that of the interspersed low-K units. Strong vertical gradients develop but direction is highly dependent on position. As the Snake River Plain is essentially a collection of overlapping lava flows with alluvium irregularly dispersed, that structure may explain the observed vertical gradients. As such a system would produce significant vertical mixing, this hypothesis is also consistent with the characteristic nearly isothermal temperature profiles of the aquifer, which appear to reflect strong vertical mixing.

Second, note that while the absolute value of the magnitude of some of the calculated vertical gradients is high compared to horizontal hydraulic gradients (which can be as much as 5 m/kilometer [0.005 m/m] along the margins of the eastern Snake River Plain), the magnitude of any resulting flow is equally dependent on vertical hydraulic conductivity. High vertical conductivity would produce relatively high vertical flow rates, but at the same time would greatly reduce the potential for strong vertical gradients to develop. Low vertical conductivity would produce stronger vertical gradients, but lower vertical flow rates.

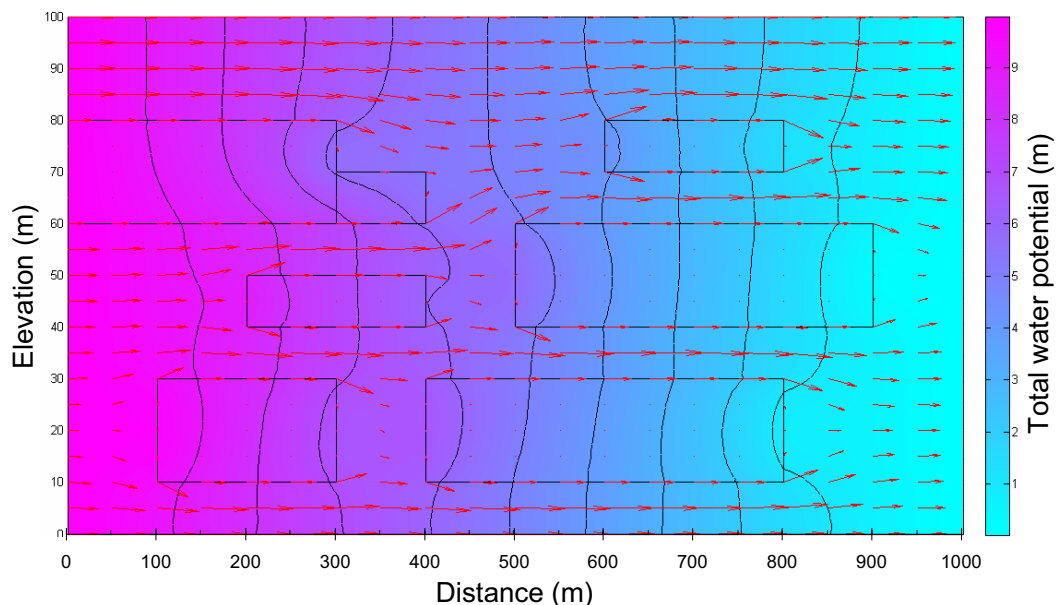


Figure 2-30. Schematic diagram illustrating the two-dimensional distribution of water potential (vertical contours, 1-m intervals) and specific discharge vectors (arrows) for flow through a hypothetical system of discontinuous blocks of contrasting hydraulic conductivity. The $K_h:K_v$ ratio of 100 is constant throughout system but blocks are 100-fold lower conductivity than background.

Given the sparsity of the vertical gradient information, the conclusions drawn from these analyses are not directly useable in calibrating the flow model. They are, however, useful in improving the general understanding of flow within the aquifer.

2.2.3.2 Temperature Data Evaluation. Water temperatures are helpful in understanding water movement in the eastern Snake River Plain because heat transport is analogous to solute transport and because temperature data are relatively abundant in the region. Temperature measurements are routinely collected at monitoring wells throughout the INL and at numerous public and private wells outside the INL. In addition, within the INL, temperature profiles have been collected in at least 12 very deep wells that in many cases penetrate into the lower conductivity basalt units that underlie the SRPA. Combined groundwater and heat flow studies are being conducted by the OU 10-08 project to use temperature data as a means of constraining groundwater flow directions and estimating hydraulic conductivity. These studies range in scale from single-well specific discharge estimates to a three-dimensional heat and groundwater flow model of the entire SRPA.

Studies relating temperature to groundwater movement require accurate and detailed two-dimensional and three-dimensional temperature maps. Smith (2002) used relatively evenly spaced temperature data from throughout the region to characterize vertical and horizontal groundwater flow in the SRPA. Subsequently, additional temperature maps have been developed for this OU 10-08 project using data from more wells in the Snake River Plain, to look for differences in temperatures over time and to examine temperature distribution in greater detail in certain areas.

2.2.3.2.1 Regional Groundwater Temperature Map—To provide detailed maps of the horizontal distribution of temperature across the SRPA, the USGS National Water Information System water quality database was sampled to collect temperature records from all wells and springs in the region. As part of the water quality program, these temperatures generally reflect water temperatures measured during periodic sampling events, and are thus assumed to represent an average temperature across the screened interval in the well. Although that information is not readily obtained from the database, most of the wells do not penetrate a great depth into the aquifer and the data can reasonably be assumed to represent approximately the temperature at the water table.

After eliminating surface water points from the records, mean and standard deviations of the temperature were calculated and wells with high standard deviations were eliminated to remove averages influenced by sampling errors. The remaining data set has relatively high density within the INL and along the Snake River along the southeastern edge model domain (Figure 2-31). Observation density is sparse, however, in the central portion of the SRPA, especially to the southwest of the INL.

Interpolation of the resulting data set provides a detailed plan-view temperature map for the region (Figure 2-32) that is generally consistent with that of Smith (2002). Primary differences between the maps are generally related to the contouring method used or data density. Several prominent temperature anomalies evident in the figure are clearly related to sources and sinks of groundwater in the region while other anomalies are more difficult to explain.

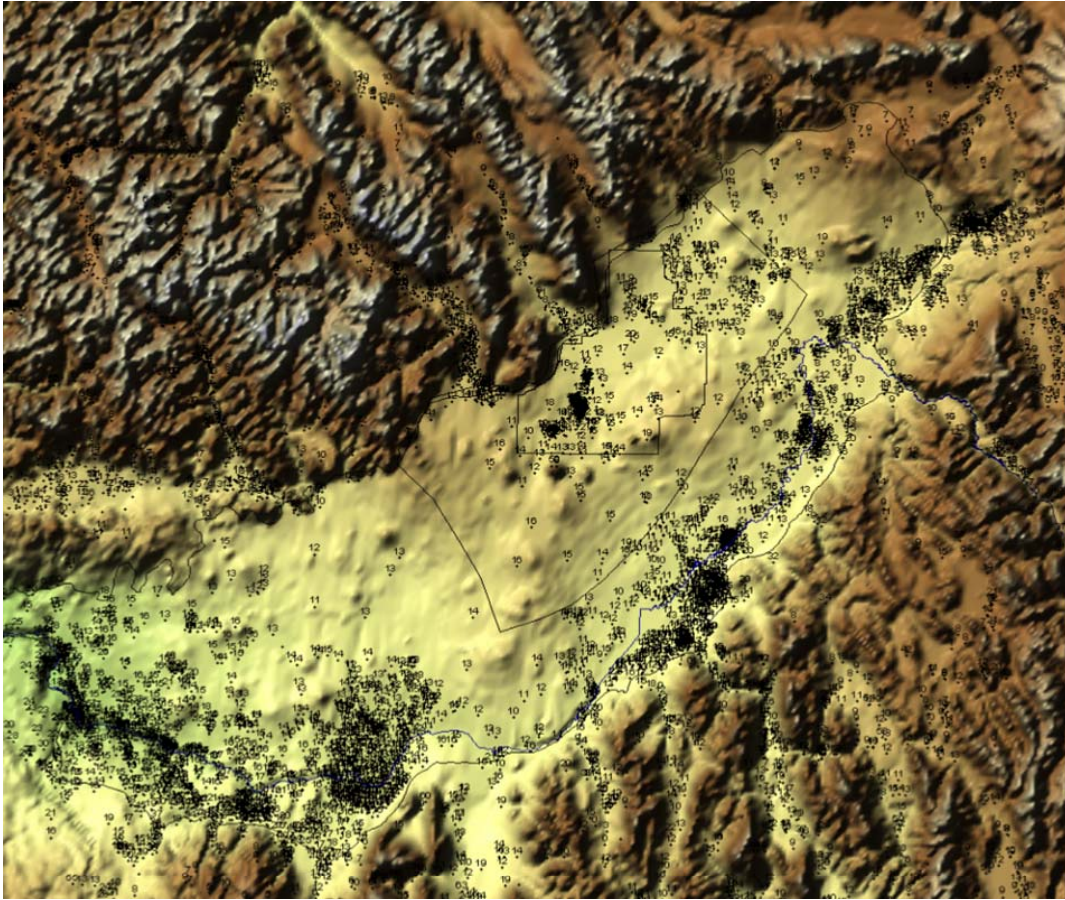


Figure 2-31. Locations of temperature measurements for the entire eastern Snake River Plain from National Water Information System.

High temperature groundwater is evident in several areas of the SRPA with highest temperatures restricted to the area surrounding Craters of the Moon, where temperatures locally exceed 30°C . Those temperatures may be associated with upward movement of deep groundwater at the boundary between the mountain front and the Snake River basalts or may be the result of much greater heating time where horizontal groundwater movement is very slow. At the regional geothermal gradient (approximately $60^{\circ}\text{C km}^{-1}$), groundwater temperatures of approximately 30°C occur at a depth of approximately 300 m below the water table, so sufficient upward flux of water from that, or greater, depth seems a plausible explanation at the edges of the aquifer where sharp changes in lithology may redirect groundwater flow. Conversely, the geologic contacts between the aquifer and the mountain fronts may also provide isolated zones of very slow groundwater flow that would lead to substantially increased temperatures. Because geothermal heating from below is balanced by a combination of horizontal heat transfer and vertical heat conduction to the surface, the latter explanation seems less plausible where the heat flux above the aquifer is greater than that below it. Less extreme temperatures evident at the toe of the Lost River Range, the Lemhi range, and at Lidy Hot Springs at the toe of the Medicine Lodge Range may thus be attributable to either of these mechanisms.

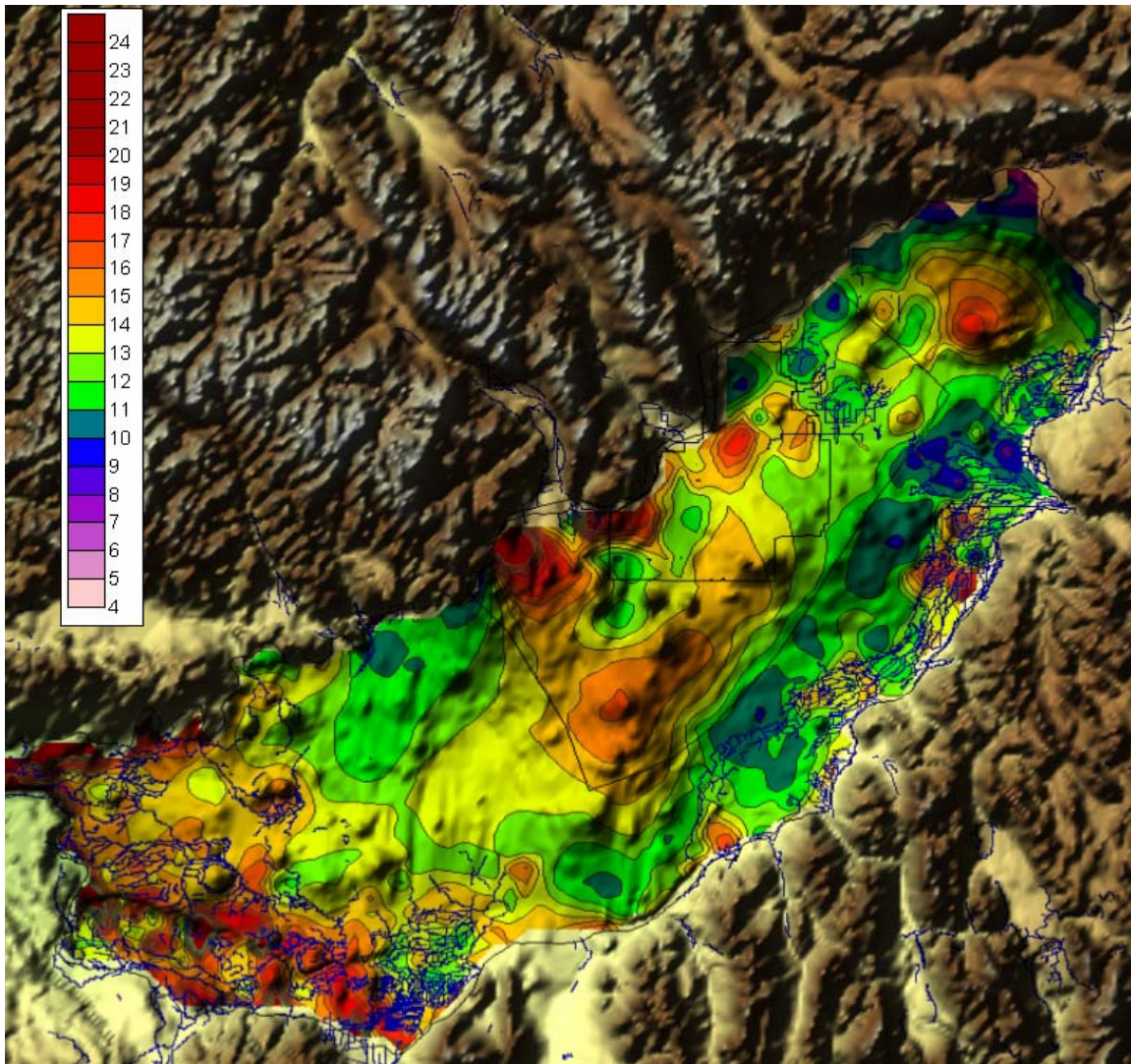


Figure 2-32. Mean groundwater temperature in the SRPA, based on interpolation of data from wells in southeastern Idaho. Blue lines represent major irrigation canals.

Significant warm water anomalies also result from recharge associated with irrigation. The most prominent of these is the wide band of warmer temperatures that follows the dense network of irrigation canals along the Snake River. Mean temperatures during the irrigation season in the Snake River Plain are approximately 17°C and surface water irrigation thus introduces warm water to the aquifer. Temperatures in surrounding areas suggest that background groundwater temperatures are approximately 9-12°C. While evident along the entire southern margin of the aquifer, the warming effect of irrigation is most prominent in the southwestern portion of the aquifer, where groundwater temperatures are commonly as high as 14-15°C. Higher temperatures in this area likely result, in part, from the higher air temperatures of the lower elevation area.

Significant warm water anomalies not obviously associated with irrigation or recharge also occur within the WAG 10 modeling domain. Most prominent of these is the warm water anomaly that extends southwesterly from the southeastern corner of the INL boundary, where the water table temperature in Corehole 1 is approximately 18.5°C. That high temperature anomaly extends approximately 65 km along the AVH of the Snake River Plain, and could result from upward convection of deep warm water or from

the increased heating time associated with reduced transmissivity in that area. A similar feature exists in the northeastern part of the Snake River Plain, centered on Big Grassy Ridge in the Juniper Buttes area.

Warm water zones along the northern margins of the aquifer are interrupted by plumes of cold water that extend from those areas where rivers recharge the aquifer (e.g., Little Wood River, Big Lost River, Little Lost River, and Birch Creek). Recharge temperatures in these areas have been estimated from noble gas studies of groundwater. Temperatures calculated from N₂ (nitrogen) Ar (argon) concentrations are approximately 9°C in the underflow from Birch Creek, Little Lost River, and Big Lost River (Busenberg et al. 1993). Cold groundwater temperatures are also evident all along the boundary between the aquifer and the Yellowstone plateau and at the confluence of the South Fork and Henry's Fork of the Snake River.

The temperature anomalies that are produced by localized sources of recharge, decreased transmissivity, or by localized introduction of water from below the aquifer appear to be diluted by mixing, either vertically or horizontally, as that water flows downgradient in the aquifer. Well-delineated plumes frequently form downstream of these areas and these plumes are excellent indicators of the direction of groundwater movement. In areas where significant horizontal anisotropy exists, temperature distributions can yield better flow direction information than water levels because flow directions may not be perpendicular to water potential gradients.

2.2.3.2.2 Vertical Profiles—Vertical profiles of groundwater temperature are available from approximately 12 wells that penetrate the entire aquifer thickness. Although this is a relatively small number of wells, they represent the most detailed three-dimensional data set at the INL, and have already been used to great advantage as a means of determining the thickness of the effective portion of the SRPA (Smith 2002) (Figure 2-33). Temperature profiles are affected by vertical and horizontal groundwater movement. Temperature profiles along a south-north transect through the INL Site (Smith 2002) indicate the presence of deep cold water in the south-central area of the Site, with very low vertical and horizontal thermal gradients. The essentially isothermal profiles observed at ANL-1 and other wells in that area have been interpreted to result from the high groundwater velocities. In contrast, strong horizontal gradients and greater vertical gradients in the northern and north-central part of the Site suggest low transmissivities in that part of the Site.

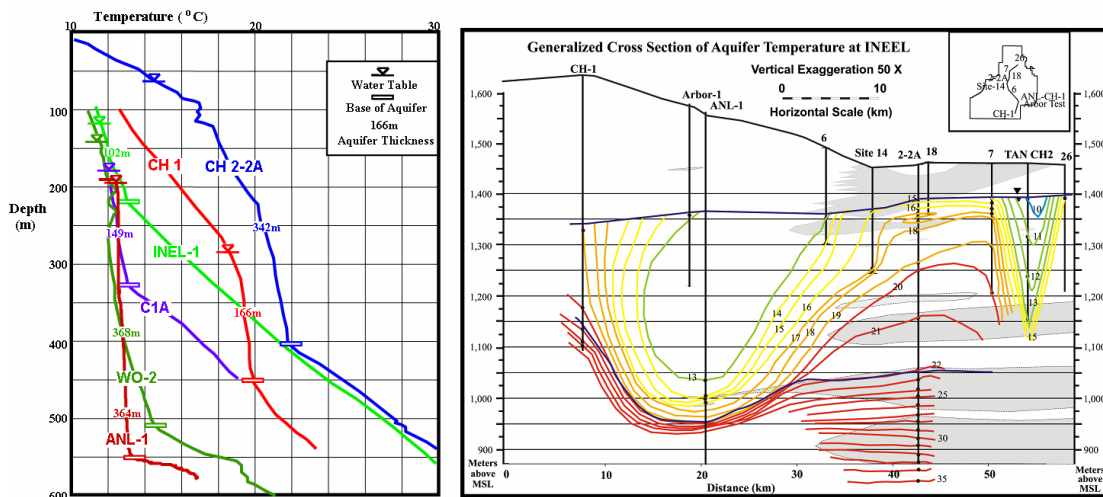


Figure 2-33. Temperature vertical profiles in deep aquifer wells and a cross section defining the base of the aquifer (Smith 2002).

2.2.3.2.3 Summary of Temperature Data Evaluation—As previous studies of groundwater temperatures in the aquifer demonstrate (Brott, Blackwell, and Ziagos 1981; Smith 2002), temperature data provide information about large-scale horizontal and vertical movement of groundwater not available from any other data set. The horizontal distribution of temperatures at the surface of the aquifer clearly delineate several temperature anomalies that are readily explained through recharge processes and/or processes likely to occur at the edges of the aquifer. The cold water plumes associated with stream discharges on the northwest boundary of the aquifer appear to be particularly useful as groundwater tracers because the background conditions and the source term (water flux and temperature) are readily estimated from available data. Examination of temperature profiles, combined with stratigraphic data have been used to delineate the bottom of the aquifer and to identify areas of high and low groundwater velocity. To date, however, the ability to test hypotheses about the effect of groundwater flow on groundwater temperature has been lacking, because a three-dimensional model of sufficient scale and resolution has been lacking. Because the three-dimensional OU 10-08 model focuses on both far-field and near-field transport processes at the INL, it provides an appropriate means of testing such hypotheses and thereby uses the temperature data to better define the relative rate of groundwater flow across the Site. In conclusion, the abundance of temperature data, and interpretation of its horizontal and vertical distribution indicates that heat transport modeling to match those data should significantly improve estimates of aquifer properties determined by inverse modeling of head alone.

2.2.4 Groundwater Flow Velocity Estimates

Over the last several decades, scientists have conducted a number of studies to address the nature and magnitude of groundwater flow across the INL. As a result of these studies, a substantial volume of geochemical data can be utilized to interrogate flow velocity at the INL. This section addresses the question of how fast groundwater flows beneath the INL, and utilizes the data collected from previous studies to extract this information. The velocities calculated from this exercise are at best an approximation, due to uncertainties in identifying exact flow paths between given well sets. The velocities are based on an assumption of one-dimensional flow paths between wells used in the analyses and as such represent minimum values. However, it is important to note that for each area of the aquifer for which data is available and calculations were made, the variation in velocity is small. Therefore, the results can be assumed to be internally consistent and can be utilized in model calibration activities.

Flow velocity estimations were made based on the aquifer domains defined by Roback et al. (2001) (Figure 2-34) as these domains were based on regions of the aquifer for which uniform flow characteristics exist. Additionally, the OU-10-08 modeling effort has established its flow domains based on this same set of geologic and geochemical information. In addition to the natural isotope and geochemistry data that are available to conduct this exercise, anthropogenic contaminant data also are available to support identification of groundwater flow paths/zones. The most compelling reason to utilize groundwater chemistry to define the velocity domains is that the data are consistent with the geologic conditions that prevail in the eastern Snake River Plain.

The following subsections are a compilation of many data sets that can be used to extract information regarding flow velocity for the areas of the aquifer defined by Roback et al. (2001). The primary source of chemistry data for these regions are reports published by Roback et al. (2001) and Lou et al. (2000). As a means of calibrating the velocity calculations obtained from these studies, data from reports by Robertson (1974) and Cecil et al. (2000) were used to make supporting calculations.

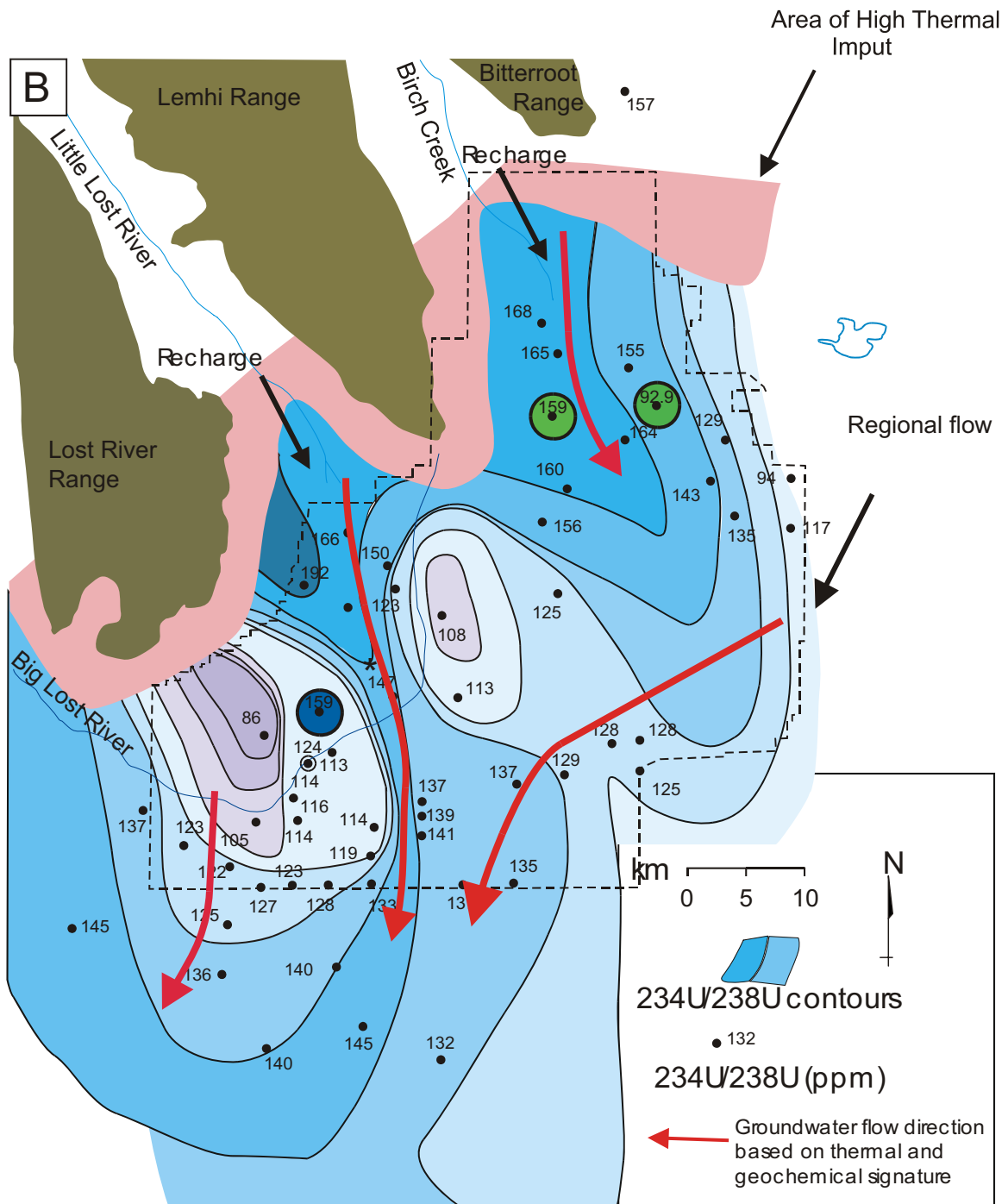


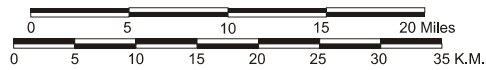
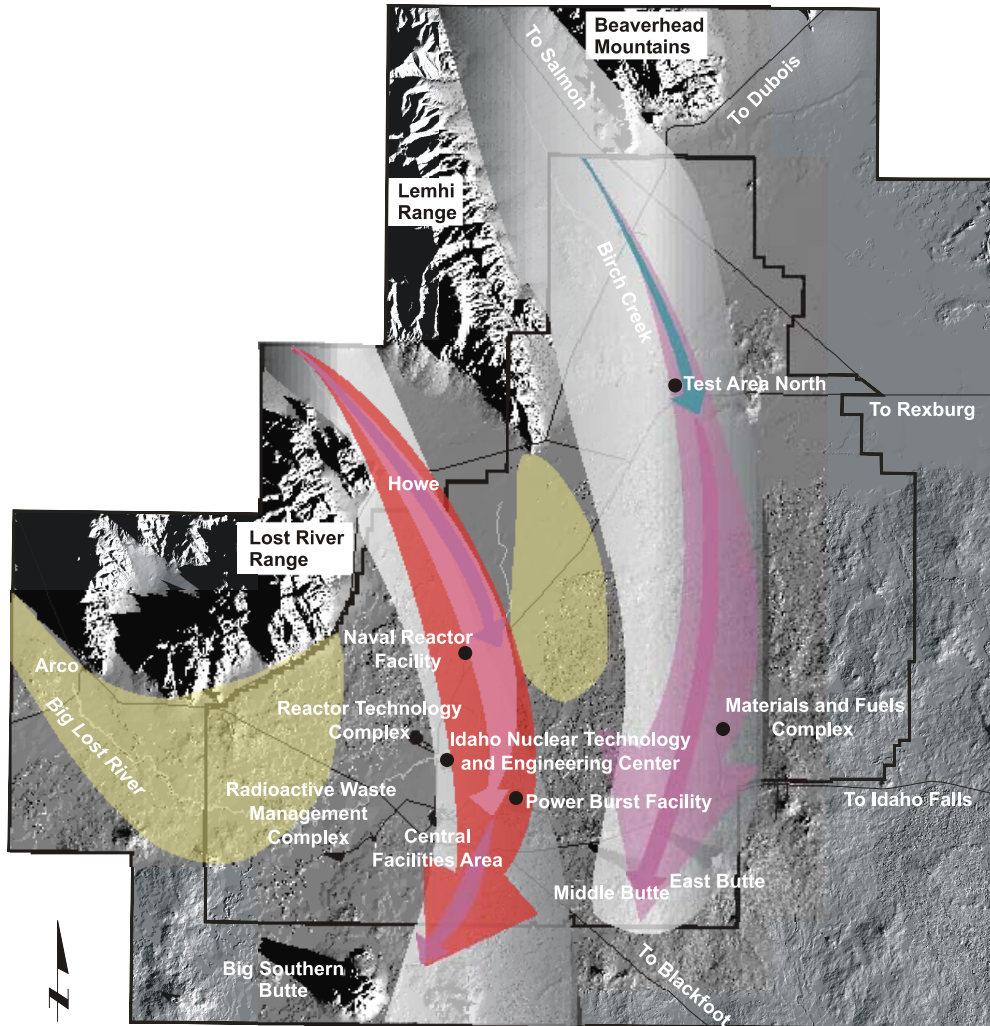
Figure 2-34. Interpreted preferential flow paths from stable isotope and thermal signatures (after Roback et al. [2001]).


2.2.4.1 Chlorine-36. Chlorine-36 released from INTEC provides valuable insight into groundwater velocity in the lower one-half of the Birch Creek flow path (Figure 2-35 shows both the Birch Creek and Little Lost River flow paths). Because chloride behaves conservatively in the aquifer and moves downgradient at near the same velocity as does the groundwater, first arrival of this constituent at a downgradient well provide an estimate of minimum velocity. Cecil et al. (2000) calculated the velocity of water traveling from INTEC to Wells USGS -011 and -014 located south of the INL boundary. By modeling the first arrival and concentration of Cl-36 arrivals at these two wells he calculated a travel time of approximately 28 years. Yielding a flow velocity of approximately 3 m/day, however, analysis of radioactivity in earlier water samples collected from these wells indicate that Cl-36-bearing water may have arrived at these wells much earlier. Cecil et al. (2000) determined that if peak Cl-36 production occurred in 1958, as well as first arrival of Cl-36 at USGS -011 and USGS -014, then the velocity in this region of the aquifer could be up to 2 times faster or 6 m/day and could indicate a maximum flow velocity of up to 6 m/day (Cecil et al. 2000).

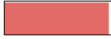
2.2.4.2 Natural and Anthropogenic Tracers. Robertson (1974) looked at natural and anthropogenic chemical data collected from 1959–1972 in an attempt to characterize the Snake River Plain Aquifer beneath the Idaho National Laboratory, then known as the National Reactor Testing Station. Although Robertson did extensive analysis of the natural chemical data available at that time, none of it yielded any insight into the aquifer flow velocity. They did however make some calculations of flow velocity based on contaminant transport. The velocity estimates from this work range between 1.5 and 6 m/day in the southern portion of the INL. Generally speaking, the 6 m/day estimate was for the southern portion of the Little Lost River flow path and the lower values were for the area located proximal or within the western slow flow region near the toe of the Lost River Range.

2.2.4.3 Isotope Velocity Estimates. The most comprehensive INL-wide geochemical data set available is from a series of reports conducted by Lou et al. (2000), Roback et al. (2001), and Johnson et al. (2001) as part of a DOE Environmental Management Science Program. Although these reports did not investigate flow velocity *per se*, they do contain data that can be used to calculate velocity. The chemistry-derived velocity estimates are based on a few simplifying assumptions. First, the chemistry data do not provide any information regarding the path that water takes between two wells; therefore it is assumed that the water flows in a direct path between the upgradient and downgradient wells. Second, because the data represent the amount of time that water has been in contact with the host rock, one can simply divide the time of reaction by the distance traveled to obtain the travel time. These assumptions are necessary due to the absence of a sufficient well spacing and should be considered a minimum velocity. Perhaps the most important assumption, however, is that the water along the flow path is chemically isolated from other water. That is, water traveling between two wells moves through a homogeneous media and does not contact water either from depth or from other flow paths. This assumption is problematic in that most of the sampling points are located in the uppermost part of the aquifer and do not have correlated open intervals. It is therefore appropriate to attribute these velocity estimates to the upper portion of the aquifer and any extrapolation to the vertical dimension remains problematic.

Flow velocity for the entire Little Lost River flow path (Figure 2-35) is 4.0 m/day. This means that over a length of 58 km originating at the mouth of the Little Lost River (transition to the eastern Snake River Plain) to Well USGS-124 south of the southern INL boundary, the water moves at a rate of 4.0 m/day. The upper one-third of the flow path starting from the transition to the eastern Snake River Plain down to Well USGS-17 is approximately 2.6 m/day. This assumes that water collected from Well USGS-17 is contained within the fast flow path originating at the mouth of the Little Lost River. Based on current understanding of the data, Well USGS-17 is on the edge of this flow path and may be affected by the slow flow area located to its east. This being the case and due to a lack of sampled wells between



Flow path 

Little Lost path average  4 m/day


Birch Creek path average  2.6 m/day



Figure 2-35. Interpreted groundwater velocities along preferential flow paths.

the mouth of the Little Lost River and the central INL, one must look to Wells USGS-83 and USGS-107 for the next velocity estimate along this flow path. Calculated ages of these waters are 33 and 21 years respectively. Water from Well USGS-83 has a calculated age of 33 years indicating that water originating at the mouth of the Little Lost River traveled an average of 3.1 m/day to arrive at the well. Well USGS-107 located more closely to the center of the fast path has an age of 21 years. If all of the water in this well has its origin in the Little Lost River Valley, then the water flow velocity between the mouth of the Little Lost River and USGS-107 is 4.8 m/day. The distal one-third of this flow path or the southern end from Well USGS-107 to Well USGS-124 is more constrained than the other sections of this zone due to the locations of many of the INL's contaminated facilities. An estimate of flow velocity along this section of the flow path can be made between Wells USGS-107 and USGS-124 located approximately 13 km south of the INL boundary. These two wells are located approximately 18 km from each other and are located within the recognized Little Lost River flow path. The travel time for water between USGS-107 and USGS-124 is 19 years and covers 18 km, yielding an average flow velocity of 2.6 m/day. This is approximately 3 m/day slower than the velocity estimates derived from Cecil et al. (2000) and Robertson (1974). The differences between these estimates could be due to (a) scale effects, (b) not considering dispersivity, or (c) the travel distance between the wells was simply assumed to be the linear distance between the two locations.

Slow flow zones located on the east and the west of the Little Lost River flow path have calculated water ages approximately 6–9 years older than the waters of similar latitude in the Little Lost River flow path. Because so few wells exist in these regions, it is necessary to extrapolate between available wells, which yields average flow velocities of 0.3 to 0.4 m/day. This estimate assumes that all of the equilibration of the water chemistry is a result of in situ diagenetic activities, and that no significant upwelling of deep equilibrated waters impacts water chemistry (a very questionable assumption according to McLing, Smith, and Johnson [2002]). Calculating flow velocities in these regions is severely hampered by a lack of well control and head data.

Calculations using the entire length of the Birch Creek flow path from the mouth of Birch Creek (transition to the eastern Snake River Plain) to the southern boundary of the INL yields an average flow velocity of 2.6 m/day. The upper one-third of this flow path passing through TAN yields a flow velocity of approximately 8.5 m/day. Velocity estimates based on chemistry for the area upgradient of TAN should be treated skeptically, as the location of the boundary between the Birch Creek Valley and the eastern Snake River Plain is not well understood. Additionally, there are numerous sources of young recharge water in this area, including the entire return flow from the Birch Creek which flows onto the Site just upgradient from TAN during the winter months. This is a problem in that the aquifer in this area is confined between the PQ and the QR interbeds into a 60-m thick aquifer, effectively increasing the impact of current year water. From TAN downgradient the velocity estimates for this flow path are better constrained due to the potential influence of the regional aquifer. However, the distal reaches of this region contains few control wells. Assuming that water flowing beneath TAN eventually contacts Well USGS-2, then it takes water approximately 42 years to travel within the flow path from TAN to Well USGS-2 a distance of 35 km. These data give an average flow velocity of 2.6 m/day, indicating that the velocity estimates from the upper section of the eastern flow path are affected by local conditions, including the arbitrary location of the Birch Creek Valley-eastern Snake River Plain contact.

Although this exercise yields some velocity estimates that are not internally consistent (such as the upper reaches of the eastern flow path), when all sources of data are placed into context, the variation in flow velocities between multiple data sets is generally very small. And in all cases, even the most extreme ranges are far less than an order of magnitude. In addition, the data collected from anthropogenic sources and the data collected from natural groundwater chemistry yield data that are remarkably similar. These velocity estimates provide valid field-based constraints on the simulated velocities that result from the flow model.

2.2.5 Estimates of Specific Discharge Based on Deep Well Temperature Profiles

Temperature profiles can be used to calculate specific discharges if aquifer conditions approximate those that allow simplification of the equations governing heat flow in groundwater systems. As first suggested by Stallman (1963), where heat flow has reached steady-state conditions and the vertical groundwater flux is negligible, the heat flux in the horizontal direction is generally much smaller than that in the vertical direction, because the primary source of heating is the geothermal heat flux. In that case, the governing equation for heat flow, assuming forced convection only, may be written as follows:

$$\frac{\partial^2 T}{\partial z^2} = \frac{\rho_w c_w}{\lambda_{bulk}} q_x \frac{\partial T}{\partial x} \quad (2-1)$$

where:

T is temperature

ρ_w is density of the water

c_w is the specific heat of water

λ_{bulk} is the thermal conductivity of the fluid-filled porous medium

q_x is the magnitude of the specific discharge in the x direction.

If the gradient of temperature in the direction of flow is constant, this equation implies that the velocity may be calculated from the shape of the temperature profile through the aquifer (e.g., Reiter 2001; McCord, Reiter, and Phillips 1992). This leads to the following equation for the magnitude of the specific discharge in the direction of flow, q_x :

$$q_x = \frac{\partial^2 T}{\partial z^2} \left(\frac{\rho_w c_w}{\lambda_{bulk}} \frac{\partial T}{\partial x} \right)^{-1} \quad (2-2)$$

Integrated, this yields a temperature – depth relation that is a second-order polynomial, $T(z) = a + bz + cz^2$, where the last coefficient defines the vertical gradient. The value of the coefficient c is thus related to the specific discharge in the direction of flow, q_x , by (Reiter 2001)

$$q_x = 2c \frac{\lambda_{bulk}}{\rho_w c_w} \left(\frac{\partial T}{\partial x} \right)^{-1} \quad (2-3)$$

Values of the coefficient c , for calculation of specific discharge were found by least-squares fit of a second-order polynomial to the vertical temperature profiles that penetrate deep into the aquifer. The assumed bulk thermal conductivity is $1.5 \text{ watts m}^{-1} \text{ }^\circ\text{C}^{-1}$ and the assumed heat capacity of water ($\rho_w \cdot c_w$) is $4.186\text{E}03 \text{ joules m}^{-3} \text{ }^\circ\text{C}^{-1}$. Results of calculations are provided in Table 2-5. The horizontal temperature gradient in the direction of flow, $\partial T/\partial x$, was calculated using interpolated temperature and head data for the upper portion of the aquifer, using the following vector expression:

$$\left\| \frac{\partial T}{\partial x} \right\| = \frac{\nabla T \bullet -\nabla h}{\|-\nabla h\|} \quad (2-4)$$

Results (Figure 2-36) indicate that the absolute value of $\partial T/\partial x$ typically ranges from $1E-03$ °C/m to $1E-05$ °C/m across most of the INL Site, but varies in sign as flow passes into or out of various temperature anomalies. These magnitudes (Figure 2-37) are consistent with a generally representative value (approximately 3.5×10^{-4} °C/m) calculated by Stallman (1963). The importance of the sign of that temperature gradient has however often been neglected in temperature profile based estimates of groundwater velocity. Reiter (2001), for example, calculated velocities for several wells in New Mexico using a single estimate of the horizontal temperature gradient calculated at one location. In this study, we consider the sign of the gradient as an indication of how well the assumptions of the method are satisfied.

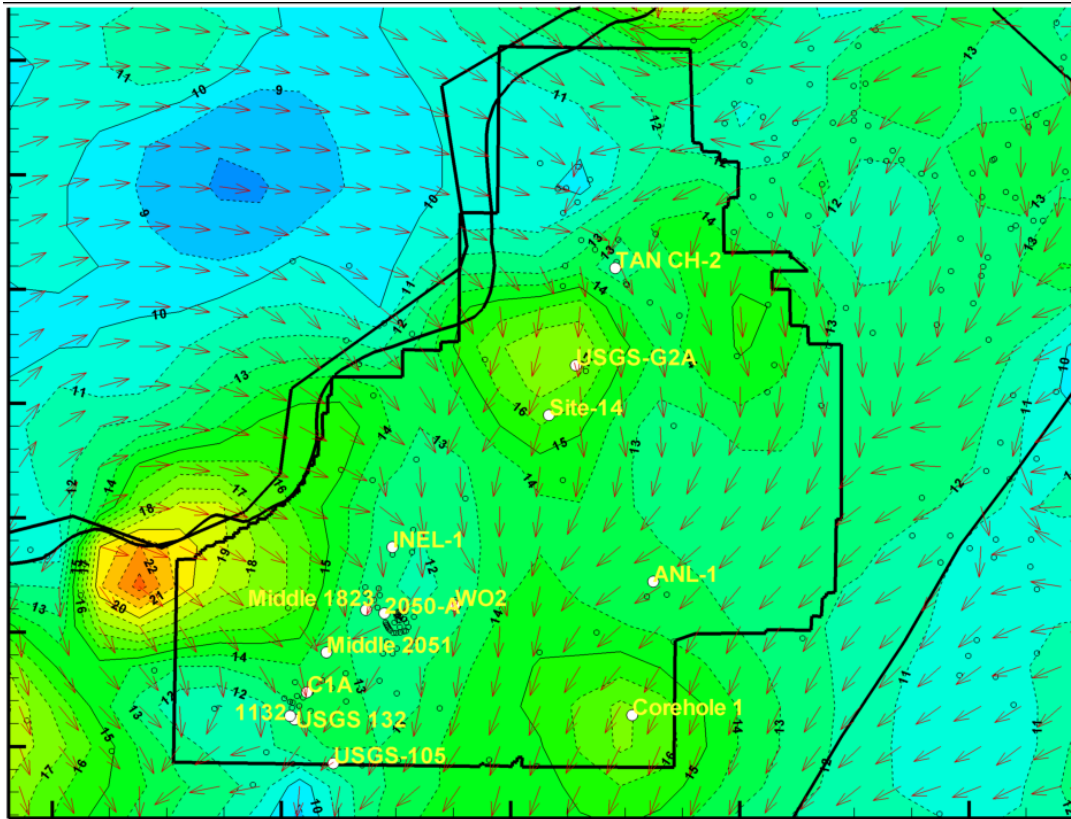


Figure 2-36. Temperature field (contours) and groundwater flow vectors used to calculate temperature gradients in the direction of flow.

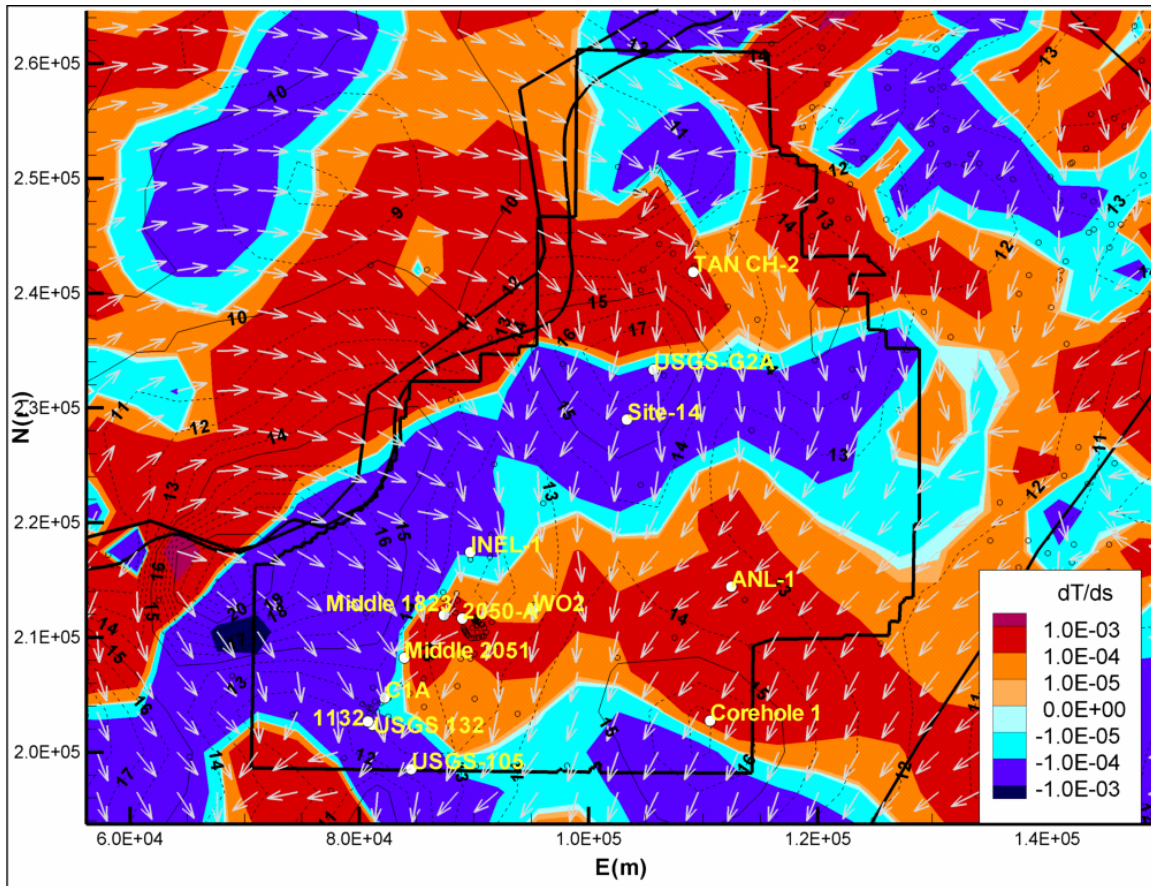


Figure 2-37. Magnitude of temperature gradient (contours) in the direction of groundwater flow (vector pointers).

2.2.5.1 Curve-fitting Method Results. Specific discharges have been calculated from application of Equation 2-4 for a limited number of wells at the Site (Figure 2-38, Table 2-5) where temperatures have been logged through sufficient aquifer thickness to determine the curvature of the profile. In each case, temperature profiles were compared with well construction details to eliminate wells in which intra-borehole flow might have influenced the temperature profile. If the assumptions of this method are valid, the signs of the values of d^2T/dz^2 and dT/dx for each well should be the same. That is, a concave upward temperature profile reflects groundwater temperatures lower than equilibrium condition and should be accompanied by a positive temperature gradient, whereas a concave downward temperature profile reflects temperatures warmer than the equilibrium condition, and should be accompanied by a negative horizontal temperature gradient. This is not the case at many of the deep wells, suggesting either an error in the estimate of one of those values, or indicating that the assumptions of the method do not hold at that location. Though specific discharge estimates from those locations are within the expected range for the aquifer, the estimates are considered invalid because of that discrepancy. Note that examination of the temperature distribution across the INL (Figure 2-36) indicates that many of these wells are located along the edges of temperature anomalies, where the calculations would be very sensitive to both temperature and water potential gradients. Further review of the temperature and head data at those locations may yield more robust estimates of groundwater discharge.

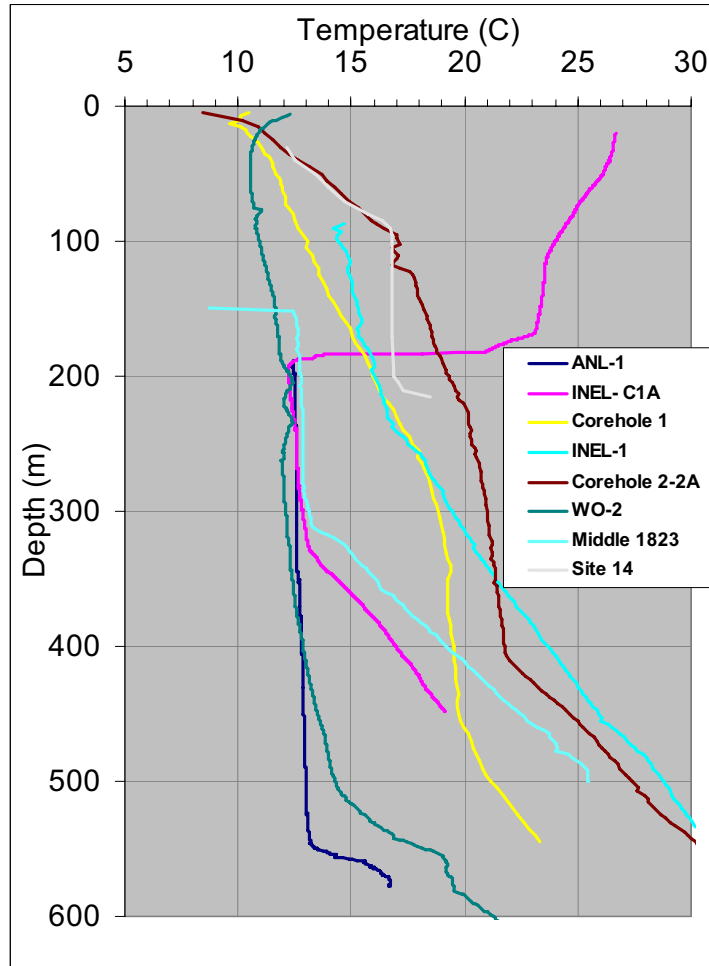


Figure 2-38. Temperature data at wells where profiles were used to calculate specific discharge.

Discrepancies in derivative signs for this curve-fit approach were not observed at wells Corehole 2-2A, WO-2, M-ETR-Disposal, 2050-A, Site-17, and TRA-04. At those locations, this approach yields specific discharges of 0.007 m day^{-1} to 0.3 m day^{-1} . Assuming a porosity of 0.05, this implies seepage velocities of $\sim 0.14 \text{ m day}^{-1}$ to 6 m day^{-1} , which is generally consistent with other estimates of seepage velocity from analysis of contaminant plumes at the Site (e.g., Pittman, Jensen, and Fischer 1989). The temperature data at Corehole 2A indicate an upstream warm water input along the flowline, while the opposite condition is indicated at WO-2. These inputs may be due to localized recharge from the surface, or due to upwelling warm water from localized high permeability zones below the aquifer.

2.2.5.2 Heat Flux Difference Method Results. Zschocke et al. (2005) describe an alternative method of using temperature profiles to infer groundwater velocities when temperature gradients above and below the aquifer are known. In the absence of convection, those gradients should be constant, and heat fluxes can be calculated from reasonable estimates of the thermal conductivity of the porous medium. The difference between those fluxes is thus the net divergence in heat flux across the aquifer, that is,

$$\frac{\partial}{\partial z} \left(\lambda_{bulk} \frac{\partial T}{\partial z} \right) = \frac{\partial Q_z}{\partial z} \approx \frac{\Delta Q_z}{b}, \quad (2-5)$$

where

Q_z is the heat flux in the vertical direction

b is the thickness of the aquifer.

The magnitude of the specific discharge can thus be determined from the relationship:

$$\frac{\Delta Q_z}{b} = \rho_w c_w q_x \frac{\partial T}{\partial x} \quad (2-6)$$

This approach was used to calculate horizontal-flow-specific discharge at eleven wells in the SRPA where possible, calculating the below-aquifer heat flux from temperature gradient but otherwise assuming a uniform geothermal heat flux of 110 mW/m². Likewise, vadose zone heat fluxes were calculated from vadose zone temperature data where that was possible. In some instances, however, temperatures above the aquifer suggested that they are strongly influenced by airflow. Where that appeared to be the case, the above-aquifer heat flux was estimated assuming a constant gradient between the temperature at the top of the water table and the estimated mean ground surface temperature. This approach assumes that air flow may affect borehole temperatures but does not have a significant affect on the geothermal gradient above the aquifer.

Well WO-2 (Figure 2-39) provides a good demonstration of how this approach is applied, as both the above- and below- aquifer temperature gradients at that location indicate conduction-dominated heat transport. Assuming a thermal conductivity of 1.5 w/m-C, the gradients above and below the aquifer imply heat fluxes of 110 mW/m² and 20 mW/m², respectively. Applying Equation 2-6, this gives a specific discharge of 0.13 m/day. Assuming an effective porosity of 5%, this implies a seepage velocity of approximately 3 m/day, which is consistent with the estimate based on Equation 2-3 and with other estimates of seepage velocities in the SRPA.

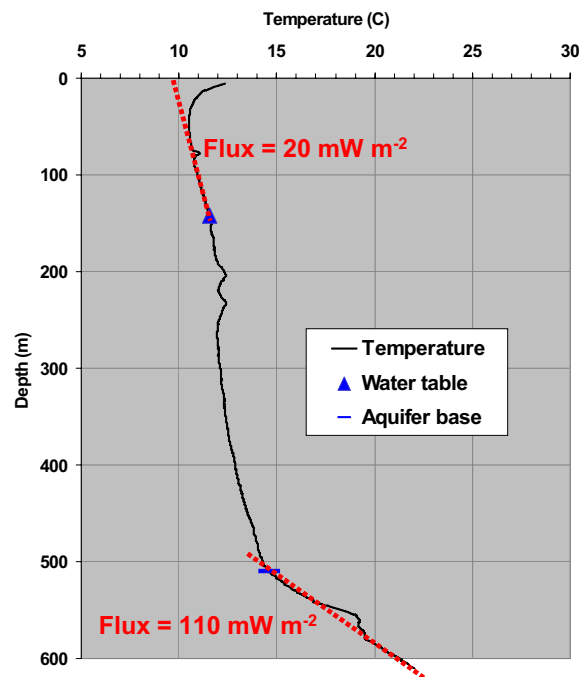


Figure 2-39. Temperature profile for Well WO-2, illustrating zones where temperature gradients were used to calculate heat fluxes above and below the aquifer.

Above- and below-aquifer gradients, estimated heat fluxes, calculated horizontal discharge rates and the basis for those calculations are summarized in Table 2-5. As with the curve-fit approach, temperature data at several wells provide an inconsistent indication of whether the aquifer water is warming or cooling, and specific discharge estimates from those locations are considered invalid. Specific discharge estimates at wells where this approach appears to yield valid results range from approximately 0.01 to 0.3 m/day. For those wells where sign discrepancies do not already suggest the need for reevaluation of the data, the discharge values obtained with this method are within an order-of-magnitude of those obtained with the curve fitting method, with the exception of Well 2050-A, where a high-resolution temperature profile has not yet been obtained.

2.2.5.3 Summary of Specific Discharge Based on Deep Well Temperature Profiles.

Because these analytical methods yield specific discharge measurements, rather than seepage velocities, an estimate of porosity is not needed to relate these values to hydraulic properties. Indeed, if the system is assumed to behave as a two-dimensional system, and reasonable estimates of the hydraulic gradient are available, these specific discharges can be directly related to hydraulic conductivity from Darcy's law:

$$q = -K\nabla h \quad (2-7)$$

Hydraulic gradients for each borehole were calculated from the interpolated head field. Hydraulic conductivities calculated from those gradients, combined with the temperature-based specific discharge estimates, range from approximately 20 m/day to 300 m/day.

Table 2-5. Summary of horizontal specific discharge magnitudes calculated from analysis of temperature profiles.

Well Name	Curve Fit Discharge (m/day)	Δ Heatflux Discharge (m/day)	Preferred Discharge Estimate (m/day)	Estimated Hydraulic Gradient (m/m)	Estimated Hydraulic Conductivity (m/day)
Corehole 2-2A	0.047	0.012	0.024	1.6E-03	15
WO-2	0.061	0.13	0.088	7.9E-04	110
M-ETR Disposal	0.30	0.22	0.25	1.1E-03	240
2050-A	0.007	0.17	0.035	8.1E-04	43
Site 17	0.041	0.062 ^a	0.041	1.4E-03	28
TRA-04	0.07	0.28	0.14	1.1E-03	130
Corehole 1	0.021 ^a	0.033	0.033	9.3E-04	35
Middle-1823	0.032 ^a	0.233	0.023	1.0E-03	220
ANL-1	0.006 ^a	0.17	0.17	5.7E-04	310
Site-14	0.003 ^a	0.22 ^a	0.026	1.5E-03	17
INEL-C1A	0.0170 ^a	0.11 ^a	0.043	4.1E-04	10
INEL-1	0.022 ^a	0.067 ^a	0.038	8.5E-04	45

a. Locations where a discrepancy exists between the sign of the horizontal temperature gradient and the change in vertical heat flux through the aquifer. Where multiple methods of analysis provided valid estimates, the preferred discharge estimates are obtained from means of their log values.

2.2.5.4 Conclusions. Analyses of temperature profiles based on an idealized two-dimensional system appear to provide reasonable estimates of groundwater discharge at the INL, thus providing an independent estimate of hydraulic conductivity at several locations. While conditions at each well (such as the potential for intra-borehole flow and below-aquifer and above-aquifer temperature gradients) add uncertainty to these specific discharge estimates, they are generally within the range of values expected for the aquifer and application of this approach appears to be valid at many locations. Nonetheless, for several reasons this approach is not considered to represent the best quantitative use of temperature data as a means of constraining aquifer properties. First, in several locations, horizontal temperature gradients indicate warming groundwater, while vertical temperature gradients indicate cooling temperatures. While this could reflect inaccuracies in the data used to calculate the gradients, it also is likely that the groundwater flow regime is not strictly two dimensional, as is assumed by the method. Substantial vertical movement of groundwater along a horizontal flow line would violate the assumptions of the method. In addition, these analytical approaches to inferring groundwater velocities from temperatures neglect differences in boundary conditions above the system, such as will exist as a result of varying vadose zone thickness, ground surface temperature and thermal conductivity. Use of the groundwater temperature data as a calibration target in three-dimensional flow and heat transport modeling (a) eliminates many of the assumptions that were made in the estimation of specific discharge from temperature gradients, and (b) appears to be a more robust application of the data.

2.3 Key Conceptual Model Issues

Several key issues exist regarding the steady-state three-dimensional numerical representation of the conceptual model of groundwater flow within the area of the OU 10-08 model domain. These issues generally are associated with limitations in the hydrogeologic database.

The delineation of hydrogeologic units provides an effective approach to identify discrete geologic volumes within the SRPA that could be represented by a layered model. Uncertainties exist in this delineation approach because of the extremely complex stratigraphic system within the SRPA and because of limited areal and vertical distribution of borehole data. Additionally, the thickness of the active flow system within the SRPA is not well known because only a few wells fully penetrate that system, particularly in areas near model domain margins.

It is generally agreed that the layered system of interflow zones and massive basalt-flow interiors results in a large ratio of horizontal to vertical hydraulic conductivity. The resulting anisotropy strongly affects three-dimensional flow and must be taken into account in a numerical representation.

The volume of regional groundwater underflow moving into the area of the OU 10-08 model domain is a secondary estimate derived from another numerical flow model (Spinazola 1994). This underflow estimate represents the integration of well-defined inflows and outflows within the area northeast of the OU 10-08 model domain. Although this total inflow estimate is a technically defensible value, uncertainty exists, particularly with depth and the vertical distribution within the layered system. Additional uncertainty exists regarding the lateral distribution of flows along that cross-sectional boundary.

Transient effects of most inflows (regional and tributary underflow, recharge from infiltration of precipitation) likely are minimal because of the attenuation that occurs because of a thick vadose zone and large permeability of the SRPA. However, transient effects of recharge from infiltration of stream flows along the channel of the Big Lost River locally may be large. These transient fluxes occur in proximity to known contaminant plumes and their effects must be evaluated.

Calibration of the three-dimensional model is dependent in part on use of a water-level data set. This data set is concentrated in areas of concern. In other areas, limited density of wells limits calibration. Additionally, these data sets are limited as to the definition of head with depth. Uncertainties require use of additional calibration targets, including chemical tracers and groundwater velocity estimates.

Groundwater flow velocities can be used to constrain the numerical model. These velocities are estimated based on water-chemistry data. Groundwater velocity data sets are limited by water chemistry data largely collected within the upper part of the flow system.

2.4 References

- Anderson, S. R., D. J. Ackerman, M. J. Liszewski, and R. M. Freiburger, 1996, *Stratigraphic Data for Wells at and near the Idaho National Engineering Laboratory, Idaho*, DOE/ID-22127, Open-File Report 96-248, U.S. Geological Survey.
- Anderson, S. R., M. A. Kuntz, and L. C. Davis, 1999, *Geologic Controls of Hydraulic Conductivity in the Snake River Plain Aquifer at and near the Idaho National Engineering and Environmental Laboratory, Idaho*, U.S. Geological Survey Water Resources Investigation Report 99-4033.
- Bestland, E. A., P. K. Link, D. Champion, and M. Lanphere, 2002, "Paleoenvironments of sedimentary interbeds in the Pliocene-Pleistocene Big Lost Trough (Eastern Snake River Plain, Idaho)," Link, P. K., and L. L. Mink, eds., *Geology, Hydrogeology, and Environmental Remediation, Idaho National Engineering and Environmental Laboratory, Eastern Snake River Plain*, Geological Society of America Special Paper 353.
- Blair, J. J., and P. K. Link, 2000, "Pliocene and Quaternary Sedimentation and Stratigraphy of the Big Lost Trough from Coreholes at the Idaho National Engineering and Environmental Laboratory, Idaho: Evidence for a Regional Pliocene Lake during the Olduvai Normal Polarity Subchron," Robinson, L., ed., *Proceedings of the 35th Symposium on Engineering Geology and Geotechnical Engineering, Pocatello, Idaho, Idaho State University*.
- Blair, J. J., 2002, *Sedimentology and Stratigraphy of Sediments of the Big Lost Trough Subsurface from Selected Coreholes at the Idaho National Engineering and Environmental Laboratory, Idaho*, M.S. Thesis: Idaho State University, Pocatello, Idaho.
- Brott, C. A., D. D. Blackwell, and J. P. Ziagos, 1981, "Thermal and Tectonic Implications of Heat Flow in the Eastern Snake River Plain, Idaho," *Journal of Geophysical Research*, Vol. 86, pp. 11,709-11,734.
- Busenberg, E., E. P. Weeks, L. N. Plummer, and R. C. Bartholemay, 1993, *Age dating ground water by use of chlorofluorocarbons (CCl₃F and CCl₂F₂), and distribution of chlorofluorocarbons in the unsaturated zone, Snake River Plain aquifer*, Idaho National Engineering Laboratory, Idaho, U.S. Geological Survey Water-Resources Investigations Report 93-4054, 47 p.
- Cande, S. C., and D. V. Kent, 1995, "Revised Calibration of the Geomagnetic Polarity Timescale for the Late Cretaceous and Cenozoic," *Journal of Geophysical Research*, Vol. 77, pp. 3057–3067.

- Cecil, L. D., J. R. Pittman, T. M. Beasley, R. L. Michel, R. L. Kubik, P. Sharma, U. Fehn, and H. E. Gove, 1992, "Water Infiltration Rates in the Unsaturated Zone at the Idaho National Engineering Laboratory Estimated from Chlorine-36 and Tritium Profiles, and Neutron Logging," Yousifk, Kharaka, and Ann S. Maestt, eds., *Proceedings of the 7th International Symposium on Water-Rock Interaction, July 13-18, 1992*, pp. 709-714.
- Cecil, L. D., J. A. Welhan, J. R. Green, S. K. Grape, and E. R. Sudicky, 2000, "Use of chlorine-36 to determine regional-scale aquifer dispersivity, eastern Snake River Plain aquifer, Idaho/USA." *Nuclear Instruments and Methods in Physics Research B 172*, pp. 679-687.
- Contor, B. A., 2004, *Recharge on Non-irrigated Lands*, Idaho Water Resources Research Institute Technical Report 04-006, Eastern Snake River Plain Aquifer Model Enhancement Project Scenario Document DDW-003, September 2004.
- Cosgrove, D. M., B. A. Contor, and G. S. Johnson, 2006, *Enhanced Snake River Plain Aquifer Model Final Report*, Idaho Water Resources Research Institute, University of Idaho, prepared for the Idaho Department of Water Resources, IWRI Technical Report 06-002, July 2006.
- Doherty, D. J., L. A. McBroome, and M. A. Kuntz, 1979, *Preliminary geological interpretation and lithologic log of the exploratory geothermal test well (INEL-1)*, Idaho National Engineering Laboratory, eastern Snake River Plain, Idaho: US Geological Survey Open File Report 79-1248, 9 p.
- Garabedian, S. P., 1992, "Hydrology and Digital Simulation of the Regional Aquifer System, Eastern Snake River Plain, Idaho," U.S. Geological Survey Professional Paper 1408-F.
- Goode, D. J., and L. F. Konikow, 1990, "Reevaluation of Large-Scale Dispersivities for a Waste Chloride Plume: Effects of Transient Flow," *International Conference on Calibration and Reliability in Groundwater Modeling, International Association of Hydrological Sciences, The Hague, The Netherlands*, September 1990.
- Greeley, R., 1982. "The Style of Basaltic Volcanism in the Eastern Snake River Plain, Idaho." Bonnichsen, B., and R. M. Breckenridge, eds., *Cenozoic Geology of Idaho. Idaho Bur. Mines Geol. Bull.*, Vol. 26, pp. 407-421.
- Helm-Clark, C. M., and D. W. Rodgers, 2004, "New 40AR/39AR data from Pleistocene basalts on the East Snake River Plain, Idaho, and their implications for the subsurface structure of the Big Lost Trough," *Abstracts with Programs – Geol. Soc. of America, Rocky Mountain/Cordillera Joint Section*, April 2004, Vol. 36, Issue 4, pp. 98.
- Helm-Clark, C. M., S. L. Ansley, T. McLing, and T. R. Wood, 2005, *Borehole and Well Middle-1823 and Its Relationship to the Stratigraphy of the South-Central Idaho National Laboratory*, ICP/EXT-05-00790, U.S. Department of Energy, Idaho Completion Project, March 2005.
- Houser, B. B., 1992, "Quaternary stratigraphy of an area northeast of American Falls Reservoir, eastern Snake River Plain, Idaho," in Link, P. K., M. A. Kuntz, and L. B. Pratt, eds., *Regional Geology of Eastern Idaho and Western Wyoming: Geological Society of America Memoir 179*.

- Hughes, S. S., M. McCurry, and D. J. Geist, 2002, "Geochemical correlations and implications for the magmatic evolution of basalt flow groups at the Idaho National Engineering and Environmental Laboratory," Link, P. K., and L. L. Mink, eds., *Geology, Hydrogeology, and Environmental Remediation, Idaho National Engineering and Environmental Laboratory, Eastern Snake River Plain*, Geological Society of America Special Paper 353, pp. 151–173.
- INL Environmental Data Warehouse (EDW) Higher spatial density water level data were obtained from the year 2004 and 2005 water level monitoring campaigns of the OU 10-08 project team, using conventional field equipment. The latter data are now available in the INL Environmental Data Warehouse (EDW).
- Jenks, M. D., 1984, *A morphometric analysis and classification of the Neogene basalt volcanoes in the south-central Snake River plain, Idaho*, M. S. Thesis: University of Idaho, Moscow, Idaho.
- Johnson, T. M., R. C. Roback, T. L. McLing, T. D. Bullen, D. J. DePaolo, C. Doughty, R. J. Hunt, M. T. Murrell, and R. W. Smith, 2001, "Groundwater Fast Paths in the Snake River Plain Aquifer: Radiogenic Isotope Ratios as Natural Groundwater Tracers," *Geology*, Vol. 28, pp. 871–874.
- Karlo, J. F., 1977, *The Geology and Bouguer Gravity of the Hell's Half Acre Area and Their Relation to Volcano-Tectonic Processes Within the Snake River Plain Rift Zone, Idaho*, Ph.D. Dissertation: State University of New York at Buffalo.
- Kjelstrom, L. C., 1986, "Flow Characteristics of the Snake River and Water Budget for the Snake River Plain, Idaho and Eastern Oregon," U.S. Geological Survey Hydrologic Investigations Atlas, HA-680, scale 1:1,000,000
- Knutson, C. F., K. A. McCormick, J. C. Crocker, M. A. Glenn, and M. L. Fischer, 1992, "3D RWMC Vadose Zone Modeling Report," EGG-ERD-10246, Idaho National Engineering Laboratory, Idaho Falls, Idaho.
- Kuntz, M. A., D. E. Champion, E. C. Spiker, and R. H. Lefebvre, 1986, "Contrasting magma types and steady-state, volume predictable, basaltic volcanism along the Great Rift, Idaho," *Geological Society of America Bulletin*, Vol. 97, pp. 579-594.
- Kuntz, M. A., D. E. Champion, R. H. Lefebvre, and H. R. Covington, 1988, "Geologic Map of the Craters of the Moon, Kings Bowl, and Wapi lava fields, and the Great Rift volcanic rift zone, south-central Idaho," United States Geological Survey Miscellaneous Investigations Series Map I-1632.
- Kuntz, M. A., H. R. Covington, and L. J. Schorr, 1992, "An overview of basaltic volcanism on the eastern Snake River Plain, Idaho," Link, P. K., M. A. Kuntz, and P. L. Platt, eds., *Regional Geology of Eastern Idaho and Western Wyoming*, Geological Society of America Memoir 179, pp. 227–267.
- Kuntz, M. A., B. Skipp, M. A. Lanphere, W. B. Scott, K. L. Pierce, G. B. Dalrymple, D. E. Champion, G. F. Embree, W. R. Page, L. A. Morgan, R. P. Smith, W. R. Hackett, and D. W. Rodgers, 1994, "Geological map of the Idaho National Engineering Laboratory and adjoining areas, eastern Idaho," United States Geological Survey Miscellaneous Investigations Series Map I-2330, scale 1:100,000.

- Kuntz, M. A., S. R. Anderson, D. E. Champion, M. A. Lanphere, and D. J. Grunwald, 2002, "Tension Cracks, Eruptive Fissures, Dikes, and Faults Related to Late Pleistocene-Holocene Basaltic Volcanism and Implications for the Distribution of Hydraulic Conductivity in the Eastern Snake River Plain, Idaho," Link, P. K., and L. L. Mink, eds., *Geology, Hydrogeology, and Environmental Remediation: Idaho National Engineering and Environmental Laboratory, Eastern Snake River Plain, Idaho*, Geological Society of America Special Paper 353, pp. 111–133.
- Kuntz, M. A., D. E. Owen, D. E. Champion, P. B. Gans, S. C. Smith, and C. Brossy, 2004, "Geology of the Craters of the Moon 30' × 60' map area and new perspectives on basaltic volcanism of the eastern Snake River plain, Idaho," in Haller, D. M., and S. H. Wood, eds., *Geological field trips in southern Idaho, eastern Oregon, and northern Nevada*, Geological Society of America Field Guide, pp. 136–155.
- Luo, S., T. L. Ku, R. Roback, M. Murrell, and T. L. McLing, 2000, "In Situ Radionuclide Transport and Preferential Groundwater Flows at INEEL (Idaho)," *Decay-Series Disequilibrium Studies, Geochemica et. Cosmochimica Acta*, Vol. 64, No. 5, pp. 867–881.
- Mankinen, E. A., T. G. Hildenbrand, M. L. Zientek, S. E. Box, A. B. Bookstrom, M. H. Carlson, and J. C. Larsen, 2004, "Guide to Geophysical Data for the Northern Rocky Mountains and Adjacent Areas, Idaho, Montana, Washington, Oregon, and Wyoming," U.S. Geological Survey Open-File Report 2004-1413.
- McCord, J., M. Reiter, and F. Phillips, 1992, "Heat-flow data suggest large groundwater fluxes through Fruitland coals of the northern San Juan Basin, Colorado-New Mexico," *Geology*, Vol. 20, pp. 419-422.
- McLing, T. L., R. W. Smith, and T. M. Johnson, 2002, "Chemical characteristics of thermal water beneath the eastern Snake River Plain," in Link, P. K., and L. L. Mink, eds., *Geology, Hydrogeology, and Environmental Remediation: Idaho National Engineering and Environmental Laboratory, Eastern Snake River Plain, Idaho*, Boulder, Colorado, Geological Society of America Special Paper 353, pp. 205–211.
- Olig, S. S., A. E. Gorton, R. P. Smith, and S. L. Forman, 1997, *Additional geologic investigations of the southern Lost River Fault and northern Arco Rift zone, Idaho*, Final Report submitted to Lockheed Martin Technologies, Idaho National Engineering and Environmental Laboratory.
- Pittman, J. R., R. G. Jensen, and P. R. Fischer, 1989, *Hydrologic Conditions at the Idaho National Engineering Laboratory, 1982 to 1985*, U.S. Geological Survey Water-Resources Investigations Report 89-4008, Idaho Falls, Idaho, December 1989.
- Reiter, M., 2001, "Using Precision Temperature Logs to Estimate Horizontal and Vertical Groundwater Flow Components," *Water Resources Research*, Vol. 37, pp. 663-674.
- Roback, R. C., T. M. Johnson, T. L. McLing, M. T. Murrell, S. Luo, and T. L. Ku, 2001, "Uranium isotopic evidence for groundwater chemical evolution and flow patterns in the eastern Snake River Plain aquifer," *Idaho, Geol. Soc. Amer. Bull.*, Vol. 113, pp. 1133–1141.
- Robertson, J. B., 1974, *Digital Modeling of Radioactive and Chemical Waste Transport in the Snake River Plain Aquifer at the National Reactor Testing Station, Idaho – 1952–1970*, U.S. Geological Survey Open-File Report IDO-22054.

- Smith, R. P., 2002, *Variability of the aquifer thickness beneath the Idaho National Engineering and Environmental Laboratory (INEEL)*, INEEL/EXT-02-01022, Idaho National Engineering and Environmental Laboratory, August 2002.
- Spinazola, J. M., 1994, *Geohydrology and Simulation of Flow and Water Levels in the Aquifer System in the Mud Lake Area of the Eastern Snake River Plain, Eastern Idaho*, U.S. Geological Survey Water-Resources Investigations Report 93-4227.
- Stearns, H. T., L. Crandall, and W. G. Stewart, 1938, "Geology and ground-water resources of the Snake River Plain in southeastern Idaho," U.S. Geological Survey Water-Supply Paper 774, 268 p.
- Stallman, R. W., "Computation of ground-water velocity from temperature data," U.S. Geological Survey Water-Supply Paper, 1544-H, 36-46, 1963.
- USGS, 2005, National Water Information System Database of the U.S. Geological Survey.
- Wood, T. R., C. M. Helm-Clark, H. Huang, S. O. Magnuson, T. McLing, B. Orr, M. Roddy, M. Rohe, M. Plummer, and R. Podgorney, 2005, *Operable Unit 10-08 Summary Report on the Subregional-Scale Two-Dimensional Aquifer Model*, ICP/EXT-05-00979, Rev. 1, Idaho National Laboratory, Idaho Cleanup Project, October 2005.
- Zschocke, A., R. Volker, C. Grisseemann, and C. Clauser, 2005, "Estimating Darcy flow velocities from correlated anomalies in temperature logs," *Journal of Geophysics and Engineering*, Vol. 2, pp. 332–342.

3. THREE-DIMENSIONAL FLOW MODEL IMPLEMENTATION

This section describes the development and implementation of the three-dimensional flow model. The three-dimensional flow model was developed using the two-dimensional flow model as a basis and by using lessons learned from the OU 10-08 Summary Report on the Two-Dimensional Model (Wood et al. 2005), which is referred to in the following text as the “two-dimensional flow model.” This three-dimensional flow model implementation section includes a description of the horizontal and vertical domains, domain discretization, methodology for hydrologic property assignment using hydrogeologic regions, and boundary conditions.

3.1 Horizontal Domain

The horizontal domain for the three-dimensional flow model is the same as the domain used for the two-dimensional flow model and is shown in Figure 3-1. In brief, this domain was selected to include a sub-regional area larger than the INL, based on: (1) an approximate flow line for the southeast boundary, (2) the approximate edge of the SRPA on the northwest boundary, (3) an extent to the northeast that captured the entire INL but excluded the complex hydrologic nature of the highly irrigated Mud Lake area, and (4) a margin reaching to an arbitrary distance to the southwest that was sufficient to capture any commingling contaminant plumes but still have some well control locations. Figure 3-1 demonstrates this domain and shows locations of facilities that were targeted for additional refinement for horizontal grid discretization.

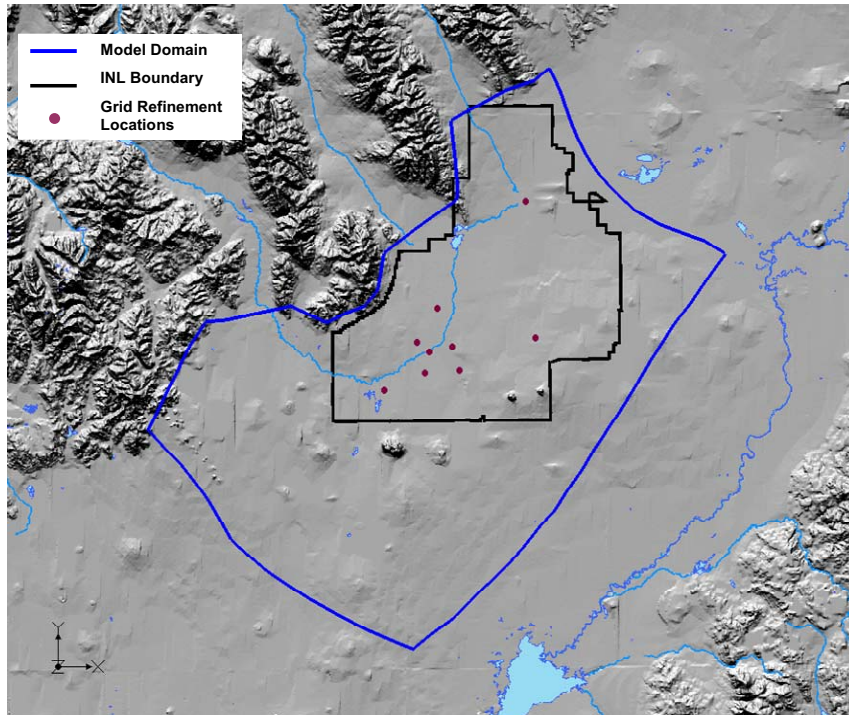


Figure 3-1. Operable Unit 10-08 model domain.

3.2 Vertical Domain

The vertical domain of the OU 10-08 three-dimensional flow model extends from the groundwater table to the effective aquifer base. Two interpretations from Smith (2002) are used in the OU 10-08 three-dimensional flow model to define the base of the aquifer. These two interpretations are termed the “thick” and “thin” scenarios. Figure 3-2 shows a perspective view of the bottom surface of the aquifer for the two aquifer thickness scenarios. These two interpretations were based on a limited number of temperature profiles and regional electrical resistivity data. Figure 3-3 shows the simulated aquifer thicknesses for both the thick and thin scenarios.

For the thick scenario, the bottom surface of the flow model has a slightly deeper channel near the center of the domain and gradually deepens toward the eastern boundary. In this interpretation, the aquifer is thickest along the longitudinal axis of the eastern Snake River Plain and tapers toward the plain margins. The aquifer also thickens considerably to the south. The thick scenario model aquifer thickness ranges from 30–500 m with an average thickness of 270 m. The aquifer bottom surface in the thick scenario ranges from 755–1,358 m above mean sea level.

The thin scenario is similar to the thick scenario in that there is a deep channel along the center of the model but without any gradual thickening toward the eastern boundary. There is also less thickening of the aquifer to the south. The thin scenario aquifer thickness ranges from 30–400 m with an average thickness of 212 m. The aquifer bottom surface in the thin scenario ranges from 955–1,360 m above mean sea level.

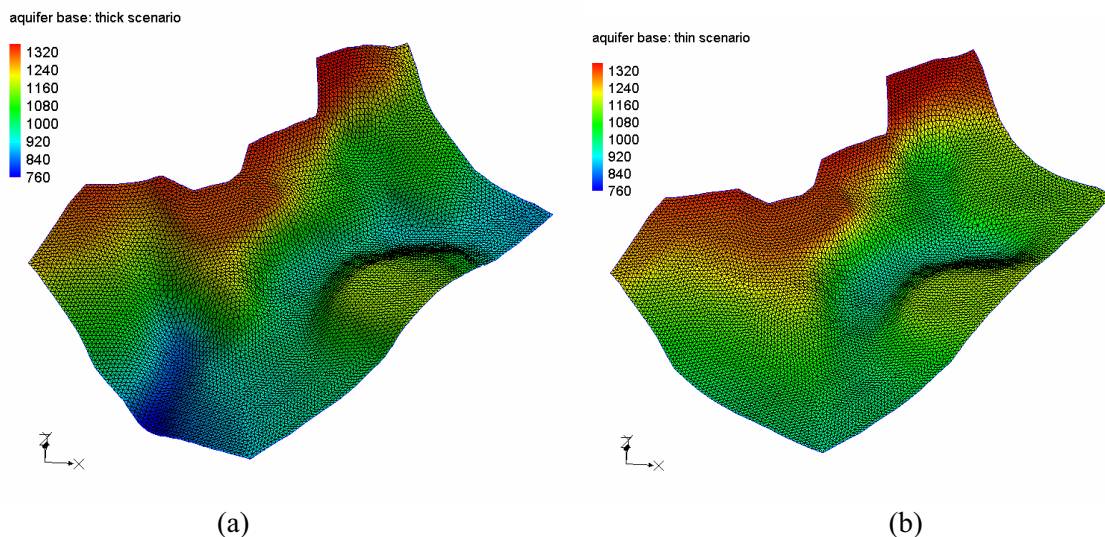
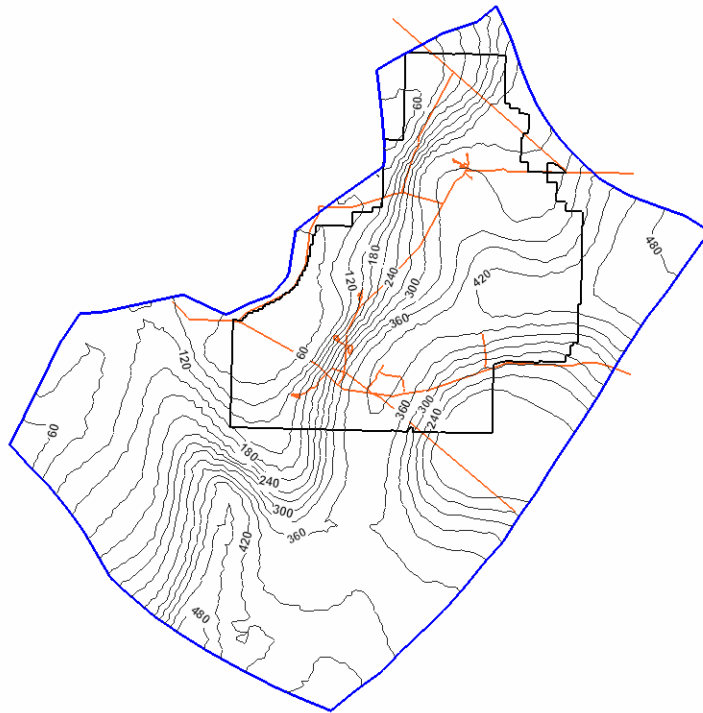


Figure 3-2. Model domain base of effective aquifer (meters above mean sea level) for the OU 10-08 three-dimensional flow model for (a) thick scenario and (b) thin scenario. View is from the south with a vertical exaggeration of 40X.

A



B

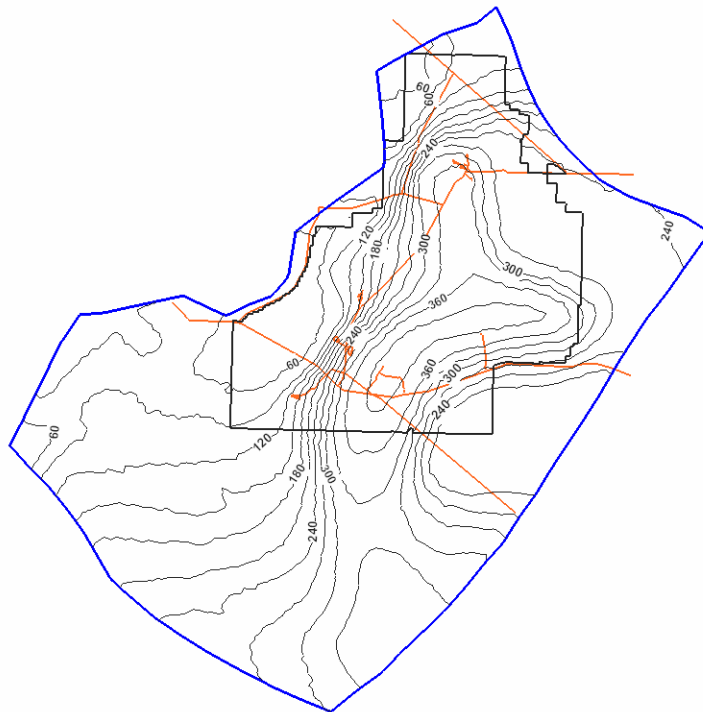


Figure 3-3. Simulated thickness (m) for the thick (A) and thin (B) aquifer scenarios.

3.3 Discretization of Three-Dimensional Model Domain

The horizontal domain for the three-dimensional flow model was discretized with a maximum grid size of 750 m on a side. The grid was oriented with the primary axis extending from the northeast to the southwest to match the general direction of flow in the SRPA (rotated 44.2 degrees east of true north). The horizontal grid was refined near major INL facilities to 150 m on a side to mimic the refinement used in the individual WAG models. Matching this refinement facilitates introducing contaminant sources from the vadose zone models for those respective facilities and incorporating important local scale heterogeneity features into the three-dimensional flow model. The maximum grid size allowed anywhere away from the facilities was 750 m.

The vertical discretization strategy was determined by balancing the objectives of the model. These competing objectives are to minimize computational time, yet maximally represent the complexity of the hydrogeologic conceptual model. In the initial three-dimensional hydrogeologic model developed by the conceptual model team, there were 12 horizons including multiple instances of highly dipping or pinching out embedded lenses of sedimentary material at different depths below the water table. In order to fully honor the initial three-dimensional conceptual model, a simulation grid with at least 12 layers with more than one million grid cells in total would have been required. This grid would have to be highly distorted vertically in order to capture the complex hydrogeologic model.

Such extensive vertical discretization would not only pose a significant computational burden, particularly for inverse simulations with hundreds of model parameters, but also would cause severe convergence difficulty of the numerical solution due to a highly distorted grid and highly heterogeneous model parameter fields. As discussed in greater detail later, most of the observation wells within the model domain only have open intervals within the top portion of the aquifer. Nearly two-thirds are completed in the top 50 m of the aquifer and over half are in the top 30 m. There are very few wells with open intervals into the lower portion of the aquifer. Therefore, from a calibration perspective, extensive vertical discretization is not justified.

In addition, it is widely accepted that the majority of the contaminants inside the INL Site resides within the upper portion of the aquifer. Thus, from a practical point of view, a model grid was selected that is more or less uniform and has a finer vertical resolution near the top of the aquifer. Given the size of the horizontal domain and resolution requirements near individual facilities, a grid with a total number of cells on the order of half million will be computationally practical for inverse simulations.

Based on these arguments, the vertical aquifer domain was discretized into six layers. The top four layers have a constant thickness of 35 m each, and the fifth layer has a thickness of 70 m. The sixth layer has variable thickness to match the undulating bottom of the aquifer. The thickest portion of this bottom layer is 190 m for the thick scenario and is 90 m for the thin scenario. All model layers were truncated where the interpreted aquifer base rose above the discretized model layers. Figure 3-4 shows the resulting discretized grid structures for each model layer for the thick aquifer scenario. Notice the truncation of model grid cells mostly occurs along the western edge of the model domain as the aquifer thins toward the Snake River Plain margin. The selected discretization results in a total number of grid cells of 320,322, which is a good balance between the computational burden of the numerical model and the modeling objectives. The comparable discretized grid structure for the thin scenario is shown in Figure 3-5.

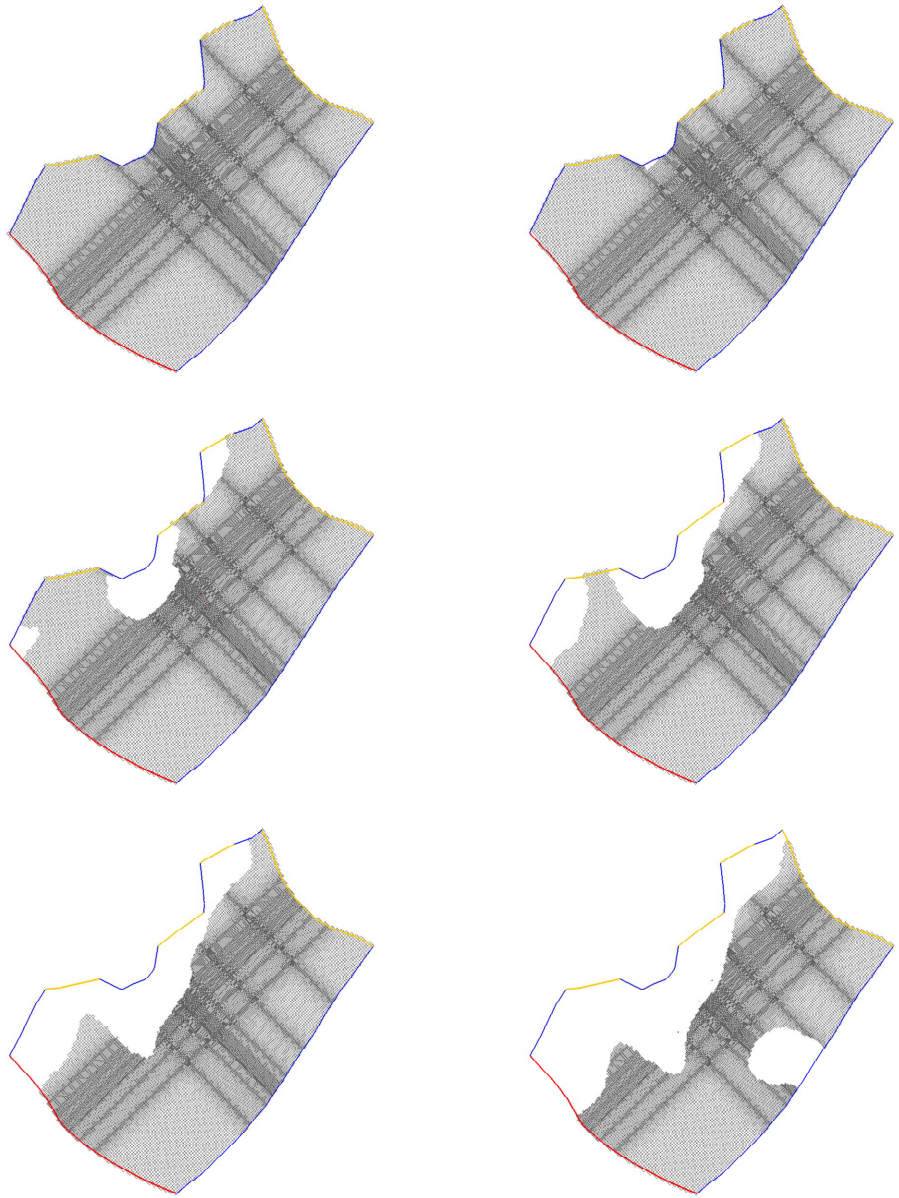


Figure 3-4. Grid structures of each model layer for the thick scenario (layer number increases from left to right and top to bottom).

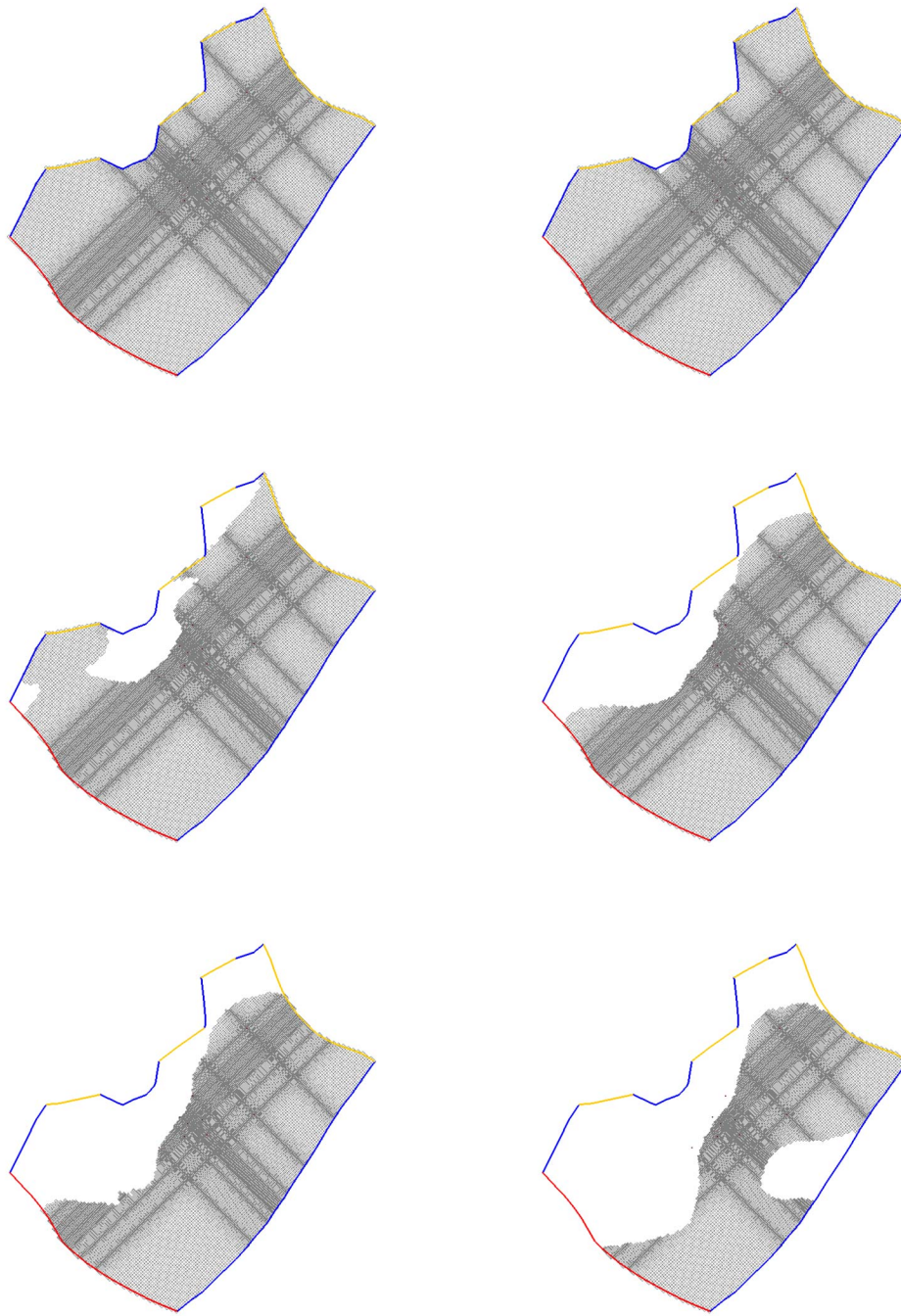


Figure 3-5. Grid structures of each model layer for the thin scenario (layer number increases from left to right and top to bottom).

3.4 Methodology for Assigning Model Parameter Zones

This section discusses how the model was parameterized based on the three-dimensional hydrogeologic conceptual model. The three-dimensional hydrogeologic conceptual model consists of a number of basalt hydrogeologic units and sedimentary hydrogeologic units. Although it was straightforward to assign different bounds to the hydraulic and transport properties for sedimentary hydrogeologic units, it was difficult to assign different bounds to different basalt hydrogeologic units because the estimated property ranges from the conceptual model largely overlapped. This overlap occurred because, within each basalt unit, the hydraulic conductivity can vary significantly by 5 to 8 orders of magnitude according to the pumping test data discussed in Section 2 of this report.

A lesson learned from calibrating the two-dimensional flow model was that a simple zonation approach with homogeneous hydraulic properties inside each zone was not able to satisfactorily fit the measured heads. As part of capturing the flow field near major facilities, the mismatch between observed and simulated heads near these facilities should be no more than 1 m and in most cases should be less than 1 m. Near some facilities, such as the Radioactive Waste Management Complex and Test Area North, mismatches should be even less than 1 m, due to the extremely flat water table in these areas. A pilot point inverse modeling approach was necessary to provide the flexibility in assigning hydraulic conductivity across the model domain to fit the measured water levels. Although the three-dimensional hydrogeologic conceptual model identifies lithology volumes that can be numerically mapped to contiguous grid cells in the model domain, inverse estimation of homogeneous properties inside each of these volumes was not attempted. This pilot point approach is discussed further in Section 4.

Because of the large overlap in hydraulic conductivity between the differing basalt hydrogeologic units identified in the three-dimensional numerical flow model implementation, the three-dimensional hydrogeologic conceptual model was further simplified into two hydrogeological units, basalt and sediment. For the basalt unit, a maximum horizontal hydraulic conductivity of 10,000 m/day was assigned with a horizontal to vertical anisotropy ratio of 100:1. The magnitude of the anisotropy is an estimate based on the hydrogeological conceptual model understanding of the layered structure of the basalts. The upper bound is the maximum permeability observed from pumping tests. For the sediment units, a maximum horizontal hydraulic conductivity of 2,000 m/day was assigned with a horizontal to vertical anisotropy ratio of 1 (isotropic). This maximum value for the sediment unit was set lower than the basalt but was still an arbitrary value that provided sufficient “room” for the inverse model to adjust permeabilities.

Figure 3-6 shows the parameter zones (location and shape of sedimentary units) for each model layer. These sedimentary zones were derived from the three-dimensional hydrogeologic conceptual model. In the constrained pilot point approach, different bounds were assigned to pilot points depending on whether the pilot points were located within the sedimentary zone or within the basalt unit. Furthermore, lower maximum conductivities were instituted for basalt in the lower layers; this resulted in decreasing fluxes with depth across the northeast boundary and is discussed in greater detail in Section 3.6.1.

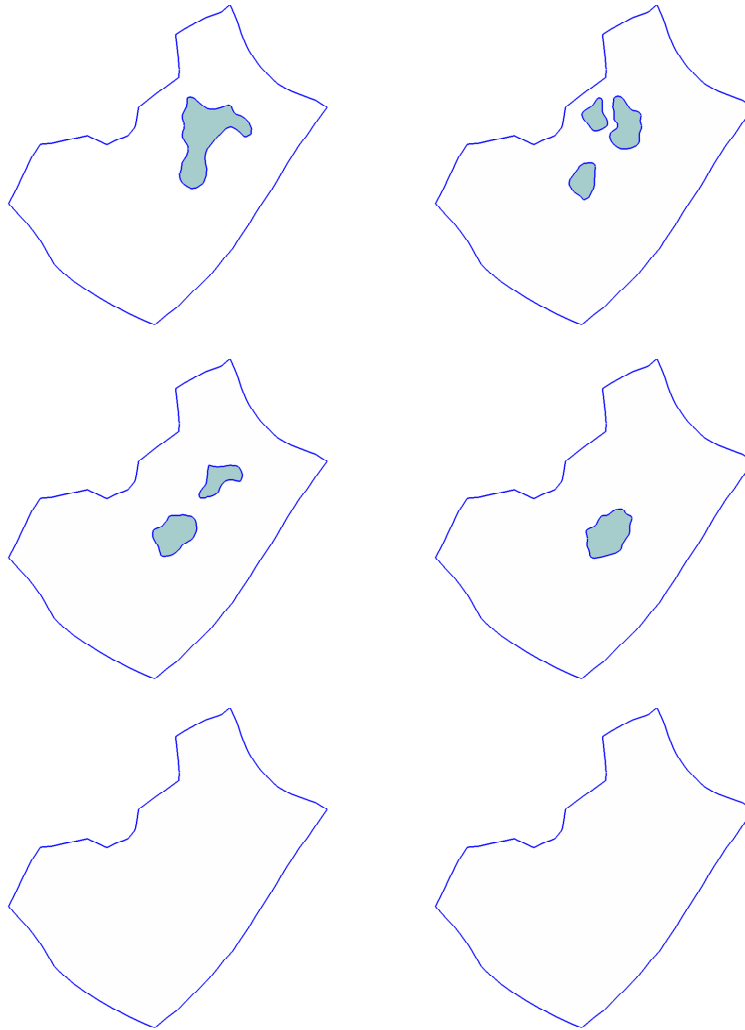


Figure 3-6. Parameter zones for each model layer (green-sediments, white-basalt).

3.5 Incorporation of WAG-Specific Permeabilities

The OU 10-08 Groundwater Model Work Plan (DOE-ID 2004) states that the assignment of hydraulic properties should be consistent with the individual WAG modeling efforts to ensure consistency in simulated water velocities. During development of the two-dimensional transport model (see Appendix C of DOE-ID [2007]), it was determined that water flux through the OU 10-08 model using prescribed head boundaries at both the northeast and southwest boundaries was underestimated when compared to the current best understanding of the flux through that portion of the eastern Snake River Plain (see Section 2.2.1). The WAG 7 model (Holdren et al. 2006) relied on prescribed head boundaries without necessarily calibrating to transport in the aquifer and could be similarly off in the flux of water moving through the aquifer. Because of this possibility, it is not sensible to constrain the calibration of the OU 10-08 flow model to strictly match the permeabilities used in the WAG 7 model. This is a direct result of a lesson learned during calibration of the two-dimensional flow model. The models for WAGs 1, 2, and 3 did include calibration to transport in the aquifer and are valid for comparison of simulated permeability. The WAG 7 model did include a low-permeability region that impacted transport and this region may have to be included when calibrating to transport.

In the joint water level and transport model calibration that will be conducted in the next phase of the INL Sitewide groundwater-flow and contaminant-transport numerical model development, comparisons will be made between (a) the permeability fields and simulated velocities used in the individual WAG models, and (b) the results of inverse modeling for the three-dimensional flow and transport model.

3.6 Three-Dimensional Boundary Conditions

Figure 3-7 shows the locations and types of boundary conditions implemented in the three-dimensional flow model. These are largely the same as were used in the two-dimensional flow model. Two primary differences are discussed in the following sections. The first difference was that the influx assigned to the northeast boundary in the two-dimensional flow model has been updated to explicitly distribute flux vertically across the three-dimensional model. The second difference is the method by which the tributary influxes are implemented into the three-dimensional model.

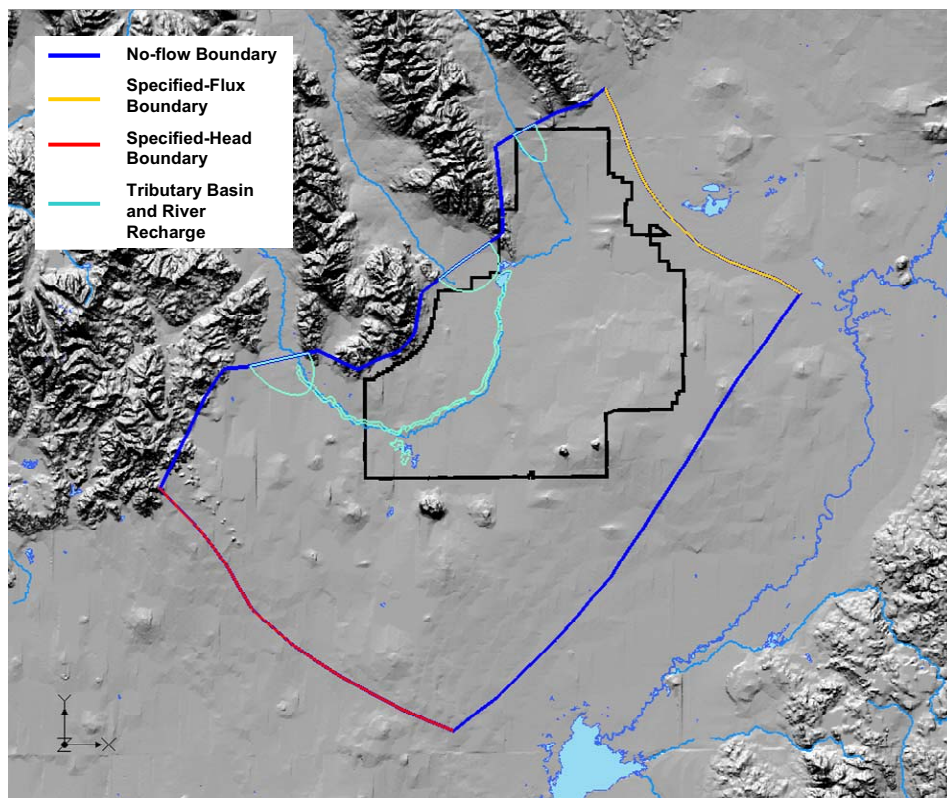


Figure 3-7. Location of boundary conditions for the OU 10-08 model.

3.6.1 Upgradient Boundary (NE) and Vertical Distribution of Inflow Fluxes

Regional underflow derived from the Yellowstone Plateau moves to the southwest across the northeastern boundary of the OU 10-08 model domain. Assigning the regional underflow across this northeastern boundary has been and continues to be a learning process in developing the three-dimensional flow model. A general description was provided in Section 2 for how this boundary flux was initially assigned and how the assignment was revised. The details of the final assignment are provided in this section.

The overall flux through the northeastern boundary of the OU 10-08 model domain was estimated to be approximately 833,000 acre-ft per year (2,820,000 m³/day) from the Spinazola (1994) model. Two primary assumptions were used in applying this flux. The first assumption was that the distribution of flux along this northeastern boundary is related to the thickness of the aquifer, which increases from the northwest to the southeast along the boundary. The second assumption was that decreasing permeability with depth resulted in more flux being applied in the upper model layers than in the lower layers.

To accomplish this increasing flux with increasing aquifer thickness, the northeastern boundary was subdivided into 18 segments and flow was apportioned to each segment based on a compilation of the Spinazola (1994) fluxes. This was also performed for the two-dimensional flow model. For the three-dimensional flow model these horizontal segment fluxes were subdivided into the six layers based on the percentages shown in Table 3-1, which also shows the percentages for the Spinazola (1994) model layers for comparison.

Table 3-1. Layer thicknesses and percentage of total flow by layer for the Spinazola five-layer model (1994) and for the OU 10-08 six-layer model.

Spinazola Model Layer	Thickness (m)	Percent of Total Flow by Layer	OU 10-08 Model Layer	Thickness (m)	Percent of Total Flow by Layer
1	31.5	16.3	1	35	23.3
2	31.5	15.3	2	35	21.9
3	92	38.1	3	35	18.2
4	Variable (<500)	24.0	4	35	18.2
5	Variable (<1,00)	6.3	5	70	12.4
			6	Variable	6.0

Figure 3-8 shows the assignment of fluxes by layers for the northeast boundary for both the thick and thin scenarios. Also shown in alternating colors are the eighteen horizontal divisions.

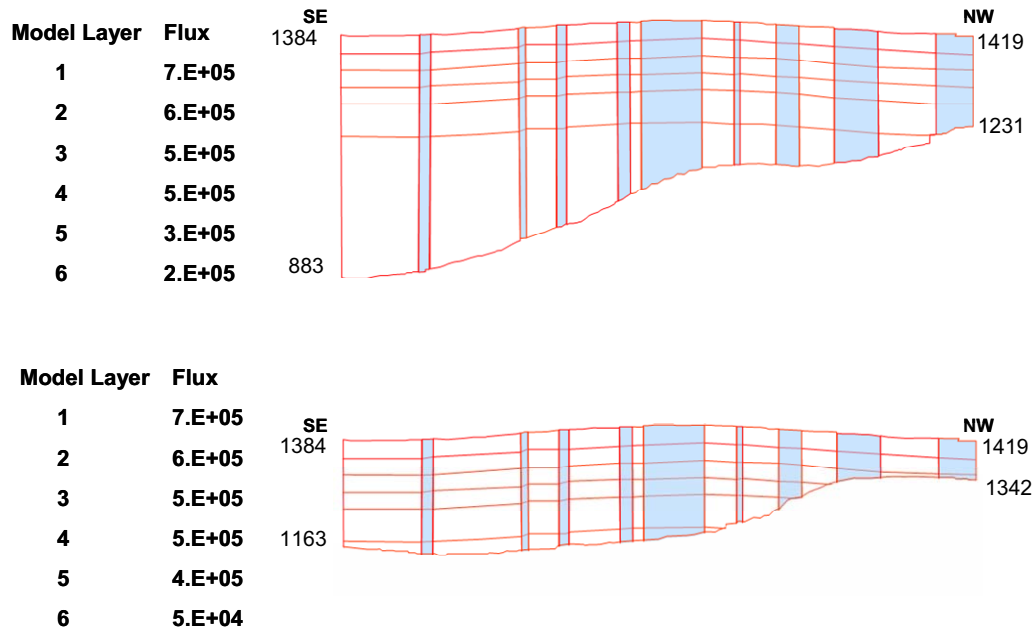


Figure 3-8. Underflow (water flux) across the northeastern boundary by model layer (m³/day) for the thick aquifer scenario (top) and the thin aquifer scenario (bottom). The elevation (m) is shown for each corner of the northeast boundary.

For completeness, the final assigned fluxes for each segment of each model layer on the northeastern boundary are provided in Table 3-2 for the thick aquifer scenario and Table 3-3 for the thin aquifer scenario. The zero-value entries are where the lower portions of the model grid have been truncated by the bottom of the aquifer.

Table 3-2. Water flux assigned to the northeastern boundary for the thick aquifer scenario, by horizontal boundary segment and model layer (m³/day).

Segment	Layer 1	Layer 2	Layer 3	Layer 4	Layer 5	Layer 6	Total
1	36249	34025	28243	28243	14093	0	1.4E+05
2	60415	56709	47072	47072	32596	3131	2.5E+05
3	48332	45367	37657	37657	26077	5056	2.0E+05
4	36249	34025	28243	28243	19558	4674	1.5E+05
5	24166	22683	18829	18829	13039	3471	1.0E+05
6	36249	34025	28243	28243	19558	5233	1.5E+05
7	6041	5671	4707	4707	3260	892	2.5E+04
8	30207	28354	23536	23536	16298	4790	1.3E+05
9	60415	56709	47072	47072	32596	11351	2.6E+05
10	12083	11342	9414	9414	6519	2858	5.2E+04
11	12083	11342	9414	9414	6519	3116	5.2E+04
12	48332	45367	37657	37657	26077	14433	2.1E+05
13	12083	11342	9414	9414	6519	4217	5.3E+04
14	30207	28354	23536	23536	16298	11314	1.3E+05
15	6041	5671	4707	4707	3260	2374	2.7E+04
16	96664	90734	75315	75315	52154	41489	4.3E+05
17	12083	11342	9414	9414	6519	5841	5.5E+04
18	89088	83622	69412	69412	48067	44681	4.0E+05
Total	6.6E+05	6.2E+05	5.1E+05	5.1E+05	3.5E+05	1.7E+05	2.8E+06

Table 3-3. Water flux assigned to the northeastern boundary for the thin aquifer scenario, by horizontal boundary segment and model layer (m³/day).

Segment	Layer 1	Layer 2	Layer 3	Layer 4	Layer 5	Layer 6	Total
1	37997	35666	6404	0	0	0	8.0E+04
2	63329	59444	7505	0	0	0	1.3E+05
3	50663	47555	23191	0	0	0	1.2E+05
4	37997	35666	32529	0	0	0	1.1E+05
5	25332	23777	23719	23128	0	0	9.6E+04
6	37997	35666	35579	41215	17401	0	1.7E+05
7	6333	5944	5930	6869	3906	0	2.9E+04
8	31664	29722	29649	34346	21484	0	1.5E+05
9	63329	59444	59298	68692	50164	5501	3.0E+05
10	12666	11889	11860	13738	10033	1456	6.0E+04
11	12666	11889	11860	13738	10033	1660	6.0E+04
12	50663	47555	47438	54954	40131	8079	2.4E+05
13	12666	11889	11860	13738	10033	1734	6.0E+04
14	31664	29722	29649	34346	25082	5286	1.5E+05
15	6333	5944	5930	6869	5016	1006	3.0E+04
16	101326	95110	94876	109908	80262	16020	4.8E+05
17	12666	11889	11860	13738	10033	1771	6.0E+04
18	93385	87656	87441	101294	73972	7038	4.4E+05
Total	6.9E+05	6.5E+05	5.4E+05	5.4E+05	3.6E+05	5.0E+04	2.8E+06

3.6.2 Influxes from Tributary Basins and Distribution onto Surface of Model

The implementation of inflow fluxes from tributary basins located along the western margin of the model domain was altered between the two-dimensional and three-dimensional flow models to more closely correspond with a revised interpretation in the hydrological conceptual model.

For the two-dimensional model, the tributary fluxes were simulated as entering via vertical cell faces along portions of the western boundary. These steady-state, specified-flux boundary conditions were simulated within GMS as arcs that provide the net flux per each basin. Along an arc representing an individual tributary basin/aquifer interface, a net flux crosses the vertical face of the grid cells. At each corresponding grid cell location, a portion of tributary underflow is injected into the model.

The three-dimensional model introduces the tributary fluxes across the top of a set of cells in the upper layer of the model, based on the revised interpretation from the conceptual model. These sets of cells comprise recharge polygons near the basin/aquifer interfaces. Instead of underflow entering the side of the model, as in the two-dimensional flow model, the underflow now enters through the top of the model and more closely resembles the conceptual model interpretation of how this tributary water enters the SRPA. This avoids excessive head build-up that results from forcing large underflows to enter through a small model thickness. An initial interpretation of these recharge polygons was subsequently

revised based on an attempt to improve comparisons between observed and simulated temperature patterns (discussed in Section 5). Figure 3-9 shows the original and revised recharge polygons that represent the location of recharge from the tributary drainage basins. Table 3-4 shows the revised polygon areas, recharge rates, and net applied water fluxes for the three tributary basins.

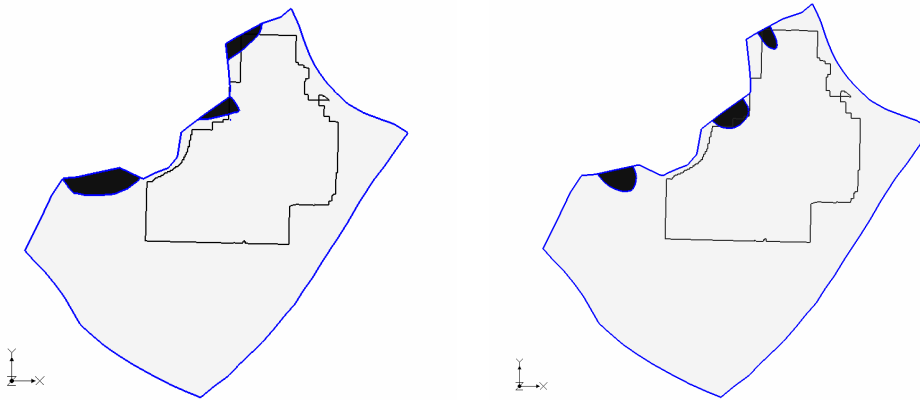


Figure 3-9. Recharge polygons to represent recharge from the tributary drainage basins. Image on left is original interpretation of recharge polygons; right-side image shows recharge polygons revised based on information from thermal modeling.

Table 3-4. Summary of areal recharge polygons representing tributary fluxes.

Tributary Basin	Big Lost River	Little Lost River	Birch Creek
Polygon area (m ²)	$5.50 \times 10^{+7}$	$5.38 \times 10^{+7}$	$2.27 \times 10^{+7}$
Infiltration rate (m/d)	2.01×10^{-2}	1.03×10^{-2}	1.10×10^{-2}
Tributary flux (m ³ /d)	$1.11 \times 10^{+6}$	$5.54 \times 10^{+5}$	$2.49 \times 10^{+5}$

3.6.3 No-Flux Boundaries along Mountain Ranges on Northwest

The entire northwest boundary of the three-dimensional model domain, formed by the western edge of the eastern Snake River Plain and the mountain ranges, is specified as no-flow (zero-flux) (see Figure 3-7). The boundary segments along the toes of the mountain ranges are assumed to have minimal recharge. Underflow from the tributary basins along this boundary has been changed from entering through the lateral boundary in the two-dimensional model, to entering through recharge polygons along the top surface in the three-dimensional model.

3.6.4 Lateral No-Flow Boundary on Southeast

The eastern boundary of the three-dimensional model domain extends in a northeast-to-southwest direction and corresponds to an estimated groundwater flow line across which there is no groundwater flow. Analysis of interpreted flow directions using a 25-year history of water levels in the SRPA (see Section 2) indicated that the flowpath along the southeastern boundary essentially varied minimally. Therefore, a no-flow condition is appropriate for the southeastern boundary.

3.6.5 Downgradient Boundary on Southwest

The southwestern boundary of the three-dimensional model domain is treated as a specified head boundary. For the three-dimensional model, head values need to be specified vertically along this boundary. However, there are no wells available in this area to indicate either the water level or head distribution with depth. Heads along this boundary were assigned using the interpolated June 2004 water table but with the slight revisions found necessary in the two-dimensional transport model (see Appendix C in DOE-ID [2007]) to ensure fluxes exit the domain along the entire boundary. For simplicity, these interpolated heads were applied vertically along this boundary to each model layer, assuming no vertical gradient.

3.6.6 Base of the Active Aquifer: Thick and Thin Scenario

There are currently two alternative versions of the OU 10-08 three-dimensional flow model. These two versions correspond to the thick and thin aquifer scenarios that evolved from different interpretations of the temperature and resistivity data used to define the effective base of the aquifer (Smith 2002). Unlike most previous models simulating groundwater flow beneath INL, the three-dimensional model does not have a flat lower surface. The bottom of the effective aquifer for each of the two thickness scenarios has an undulating surface. The base of the aquifer is treated as a no-flux boundary in the three-dimensional flow model.

3.6.7 Aquifer Top: Areal Infiltration and the Big Lost River

The top surface of the OU 10-08 three-dimensional flow model, for both aquifer thickness scenarios, follows the configuration of the water table, as defined by June 2004 water level measurements. The majority of the top model surface is simulated using specified flux boundary conditions to represent regional infiltration from direct precipitation. This was assigned as a uniform value of 2.33×10^{-5} m/day (from Section 2.2.1.3).

A previous sensitivity study of the effect of variable infiltration conducted using the two-dimensional flow model (Wood et al. 2005) showed little impact in the primary area of concern from INTEC to the southern INL boundary. This was potentially due to the use of vertically integrated heads in the two-dimensional model. When the three-dimensional model is used to simulate transport, the impact of spatially variable infiltration will be revisited. Until that time, the areally-constant infiltration approach will be used.

In addition to the areal recharge from precipitation, the other water source occurring vertically across this top surface of the model is percolation from the Big Lost River channel. The part of the Big Lost River that flows across the INL within the OU 10-08 model domain was subdivided into three reaches plus the spreading areas that are used to control flooding on the INL (see Figure 3-10). Since the upper reach overlapped onto the Big Lost River recharge polygon, the upper reach actually had to be further divided into two reaches. The GMS program does not allow overlapping recharge polygons. The infiltration rates assigned for the upper Big Lost River reach within the Big Lost River tributary basin recharge polygon was assigned an infiltration rate that combined the two sources. The areal extents and assigned flux rates for these recharge sources across the top model surface are summarized in Table 3-5.

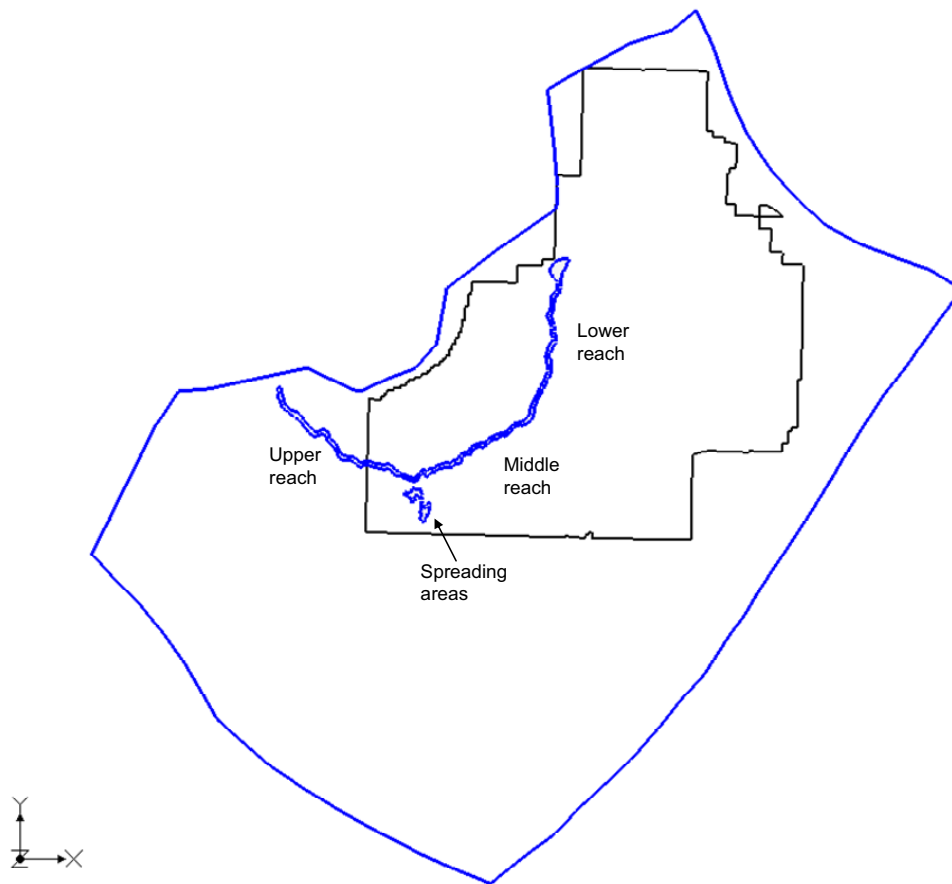


Figure 3-10. Recharge from percolation of Big Lost River channel streamflow divided into three reaches of river plus spreading areas.

Table 3-5. Other sources of recharge across the top boundary of the OU 10-08 flow model.

Source	Areal Precipitation	Spreading Areas	Big Lost River (upper reach within tributary recharge polygon)	Big Lost River (upper reach)	Big Lost River (middle reach)	Big Lost River (lower reach)
Polygon area (m ²)	$6.35 \times 10^{+9}$	$4.16 \times 10^{+6}$	$2.57 \times 10^{+6}$	$1.09 \times 10^{+7}$	$6.89 \times 10^{+6}$	$1.52 \times 10^{+7}$
Infiltration rate (m/d)	1.95×10^{-5}	1.51×10^{-2}	2.30×10^{-2}	2.88×10^{-3}	4.49×10^{-3}	7.30×10^{-3}
Total flux (m ³ /d)	$1.24 \times 10^{+5}$	$6.30 \times 10^{+4}$	$5.90 \times 10^{+4}$	$3.14 \times 10^{+4}$	$3.09 \times 10^{+4}$	$1.11 \times 10^{+5}$

The flux rates in Table 3-5 represent constant average infiltration over time. Another approach that will be used in the three-dimensional transport model will be assigning these Big Lost River infiltration fluxes as variable in time corresponding to periods where water was and was not present in the river.

3.7 References

- DOE-ID, 2004, *Idaho National Engineering and Environmental Laboratory Operable Unit 10-08 Site-wide Groundwater Model Work Plan*, DOE/NE-ID-11188, Rev. 0, U.S. Department of Energy Idaho Operations Office, December 2004.
- DOE-ID, 2007, *Waste Area Group 10, Operable Unit 10-08, Remedial Investigation/Feasibility Study Annual Status Report for Fiscal Year 2006*, Rev. 0, DOE/ID-11297, U.S. Department of Energy Idaho Operations Office, May 2007.
- Holdren, K. Jean, Danny L. Anderson, Bruce H. Becker, Nancy L. Hampton, L. Don Koeppen, Swen O. Magnuson, and A. Jeffrey Sondrup, 2006, *Remedial Investigation and Baseline Risk Assessment for Operable Unit 7-13/14*, DOE/ID-11241, Rev. 0, U.S. Department of Energy Idaho Operations Office, May 2006.
- Spinazola, J. M., 1994, "Geohydrology and Simulation of Flow and Water Levels in the Aquifer System in the Mud Lake Area of the Eastern Snake River Plain, Eastern Idaho," U.S. Geological Survey Water-Resources Investigations Report 93-4227.
- Smith, R. P., 2002, *Variability of the Aquifer Thickness Beneath the Idaho National Engineering and Environmental Laboratory (INEEL)*, INEEL/EXT-02-01022, Rev. 0, Idaho National Engineering and Environmental Laboratory, August 2002, 11 p.
- Wood, T. R., Helm-Clark, C. M., Huang, H., Magnuson, S. O., McLing, T., Orr, B., Roddy, M., Rohe, M., Plummer, M., Podgorney, R., 2005, *Operable Unit 10-08 Summary Report on the Subregional-scale Two-Dimensional Aquifer Model*, 2005, ICP/EXT-05-00979, Rev. 1, Idaho National Laboratory, Idaho Cleanup Project, October 2005.

4. FLOW MODEL CALIBRATION

4.1 Calibration Approach for the Three-Dimensional Flow Model

The flow model calibration is designed to provide the optimal set of hydraulic properties that provides satisfactory goodness of fit to the measured heads and other types of observations as available. The parameter values must also fit within a range of known property values from the literature, laboratory studies, or field investigations.

Groundwater flow models are often calibrated to water levels measured in aquifer wells that are within the modeling domain. Sometimes head gradient or flow velocity estimates are also used for calibration. The OU 10-08 Groundwater Model Work Plan (DOE-ID 2004) calls for a multi-objective, multi-calibration target approach to calibration. The work plan presents criteria for calibration target selection and lists some of the approaches. The approaches include the traditional zonation approach for parameterization and the pilot point approach, a novel technique embedded in the Parameter Estimation (PEST) calibration software (Dougherty 2004).

One of the lessons learned from the two-dimensional modeling activities is that the traditional zonation calibration approach proved difficult to achieve satisfactory matches between simulated and observed heads. A pilot-point approach was more successful at matching the measured heads. Therefore, the three-dimensional flow model calibration primarily follows the pilot point approach.

Within the framework of the pilot point approach, two different calibration methods were followed to inversely solve for the horizontal hydraulic conductivity distribution in the three-dimensional flow model. The first approach is based only on the pure pilot-point approach and uses no constraints except a maximum and minimum conductivity range assigned to every pilot point. The second approach attempts to honor the distribution of hydrogeologic materials in the aquifer that are summarized in the three-dimensional hydrogeologic conceptual model (Section 2). This latter approach also uses the pilot point approach, but with different bounds assigned to pilot points within the basalt-dominated and sediment-dominated hydrogeological units.

For the first approach, each of the six model layers is assigned a unique set of pilot points. Hydraulic conductivities of all pilot points are allowed to range within each layer between 1.0×10^{-10} and 10,000 m/day during the PEST inverse solution. The maximum of 10,000 m/day was derived from the upper end of the range of hydraulic conductivities determined from aquifer tests discussed in Section 2, with the lower range being prescribed such that the inverse solver can have adequate room to estimate the permeability field. For the second approach, zones representing sediment-dominated hydrogeologic units were delineated by polygons in each layer. These polygons represent known areas where sediments and sediment-dominated basalts are embedded within or cross among the various model layers.

The pilot points within these layer-specific sedimentary-defining polygons were assigned an upper bound of hydraulic conductivity of 2,000 m/day. This smaller range was based on the pumping test results available for wells within the model domain, and still allowed sufficient room for the solver to assign values to pilot points during the inverse simulations. Pilot points outside the polygons were allowed to range from 1.0×10^{-10} to 10,000 m/day. In this implementation, the different types of basalt flow groups, identified in the conceptual model, were not differentiated in the calibration process.

There is a significant difference between the two-dimensional and three-dimensional flow model coupled pilot point/zonation approaches. For the two-dimensional approach, pilot point interpolation was not permitted across zone boundaries. For the three-dimensional approach, greater continuity and

smoothing of the conductivity field is achieved by permitting interzone interpolation of adjacent pilot points between the basalt-controlled areas and the sedimentary units.

4.2 Calibration Data: Water Levels and Velocity Estimates

Initial calibration of the three-dimensional flow model was confined to measured heads as the sole calibration target. To a lesser extent, visual checks were made to ensure that the observed hydraulic head gradient, visualized by the water table contour line spacing, was matched with the model. An additional set of simulations were prepared, which included velocity estimates as additional calibration targets. The description of both of these calibration targets is provided here.

4.2.1 Three-Dimensional Water Level Data

All aquifer wells that exist within the area represented by the OU 10-08 model domain were considered for use as calibration targets for the three-dimensional flow model. Of these, over 200 wells were measured during a two-week period in June 2004. Additional aquifer wells, not specifically measured in June 2004 for the OU 10-08 groundwater modeling project, were used to supplement these June 2004 wells. In all, 224 wells comprised the calibration set for the previous (two-dimensional) flow model. Most of the same measurements were used for the three-dimensional flow model. Data from these wells were used to prepare contour maps of the water table, to investigate transient or vertical gradients, and to calibrate the three-dimensional flow model.

An important aspect of the three-dimensional flow model calibration is the use of aquifer well head data in a three-dimensional sense. In preparing contour maps of water table elevation, these data are typically regarded as two-dimensional. However, in the three-dimensional flow model, wells were assigned to different model layers based on where the well open screen interval is with respect to the top and bottom of these layers.

Some wells in the current observation data set have open intervals in the aquifer that cross several of the three-dimensional flow model layers. The Groundwater Modeling System and MODFLOW 2000 allow specification of the exact top and bottom of each well's open or screened interval with respect to the layering scheme. The model proportions the total measured head according to length of open interval spanning multiple layers. An example illustration of this calculation is provided in Figure 4-1.

MODFLOW calculates hydraulic head at centers of grid cells. The areal extent of even the smallest grid cell in the three-dimensional flow model is greater than 20,000 m² and most observation wells are not at the exact center of a model cell. For observation wells that are located within a grid cell away from the grid cell center, MODFLOW utilizes multi-cell bi-linear interpolation within the two-dimensional plane of a single layer to calculate the simulated head at the observation well location. Similarly, MODFLOW utilizes interpolation to calculate the simulated head of an observation well that is vertically away from a grid cell center. For wells that are open at intervals that represent more than one model layer, the simulated value is a weighted average of heads calculated for each of the layers involved. Simulated values are calculated by multiplying layer-specific interpolated heads by a user-specified proportion and then summing these. More detailed discussion of the horizontal and vertical spatial interpolation of simulated heads is presented in MODFLOW documentation (Hill et al. 2000). For the three-dimensional flow model, the proportions are based on the length of screened opening within each layer, as shown in Figure 4-1.

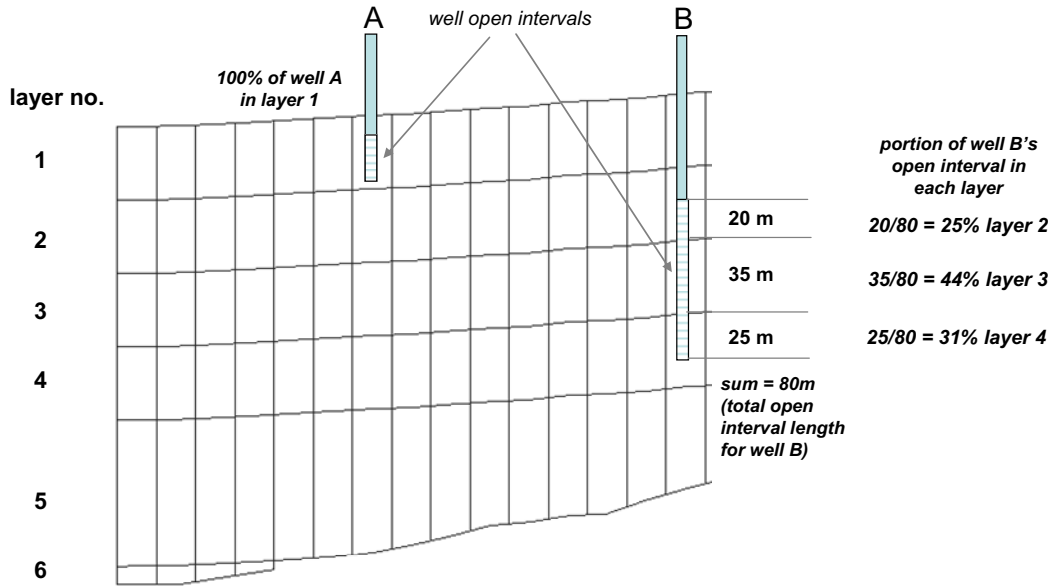


Figure 4-1. Generalized weighting scheme to vertically match observation wells that cross multiple layers of a three-dimensional flow model. The simulated head used to match the multilayer observation well B is composed of simulated heads from layers 2, 3, and 4, weighted according to the length of open interval in each layer.

The June 2004 water level data were incorporated into the previous two-dimensional flow model as 224 aquifer wells, all treated two-dimensionally. For the three-dimensional flow model, it was necessary to examine not only where in relation to model layers do the wells' open intervals align but also how to incorporate into the three-dimensional observation coverage wells that have multiple discrete open intervals in the aquifer. In several cases, wells with multiple open intervals below the water table were treated in the observation coverage as having a single open interval. This was done where these multi-open interval wells had very short separation distances between open intervals (2 m or less) or where all open intervals of a given well fell within a single model layer. At Test Area North (TAN) and Idaho Nuclear Technology and Engineering Center (INTEC), there is an over-abundance of closely-spaced wells in the two-dimensional set applicable to only the top layer of the three-dimensional model; some of these were removed from the three-dimensional set.

Also, there were several wells measured in June 2004 that were not included in the two-dimensional set because their completion intervals vastly differ from the majority of upper aquifer well completions; these were included in the three-dimensional calibration set. Two piezometers (TCH-2 and USGS-30) were divided into separate wells representing each piezometer tube. Two wells (USGS-6 and USGS-17) with multiple open intervals with sufficient vertical separation were also divided into individual wells representing each open interval.

Finally, representative heads for new Westbay wells, which each have five distinct vertical ports but were not measured in June 2004, were also included in the three-dimensional calibration set. The two newly completed Westbay installations, Wells MIDDLE-2050A and MIDDLE-2051, were undergoing construction during the June 2004 water level measurement campaign. The first fully-ported hydraulic pressure measurements were available in September 2005. These data were converted to head measurements and then, using the average water table rate of change for wells in the vicinity of these two Westbay wells, they were back-casted to June 2004. It was necessary to include these two wells in the

model observation coverage due to the paucity of real nested piezometer clusters capable of measuring head in different model layers. However, the bottom two ports in Well MIDDLE-2051 are below the base of the modeled aquifer domain in both aquifer thickness scenarios for the flow model developed in this report.

In summary, data from a total of 214 unique wells were gathered either from the two-dimensional calibration set or were supplemental wells from USGS data or the new Westbay systems. Of these, 181 wells are constructed with only a single open interval. Thirty-four of the 214 have multiple open intervals. Table 4-1 is a summary of the treatment of these particular multiple open interval observation wells. The distribution of well open intervals over the OU 10-08 three-dimensional flow model layers is displayed in Figure 4-2. Layer-specific distributions of head calibration targets are shown in Figure 4-3.

Table 4-1. Treatment of single and multiple open-interval wells in three-dimensional calibration.

Well or Well Type	Number of Wells	Number of Open Intervals	Resulting Number of Calibration Targets	Notes
Single interval wells	181	181	181	
Multi-open interval wells reduced to single	27	58	27	All treated as single intervals
TCH-2	1	2	2	Piezometers
USGS-6	1	2	2	Multi-open interval well
USGS-17	1	2	2	Multi-open interval well
USGS-30	1	3	3	Piezometers
MIDDLE-2050A	1	5	5	Piezometers
MIDDLE-2051	1	5	3	Piezometer; two ports are below modeled domain
Totals	214	258	225	

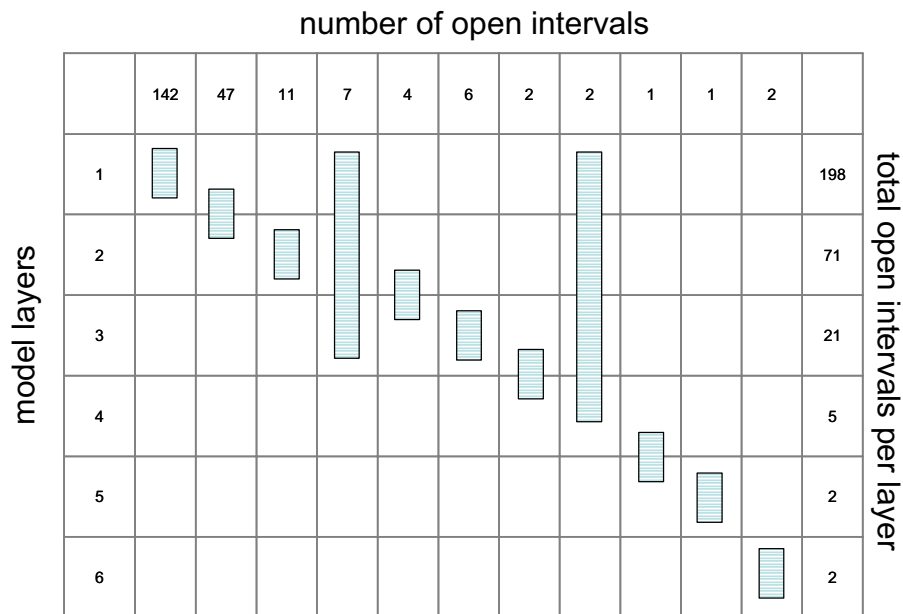


Figure 4-2. Numbers of wells, open-screen intervals, and alignment with three-dimensional model layers.

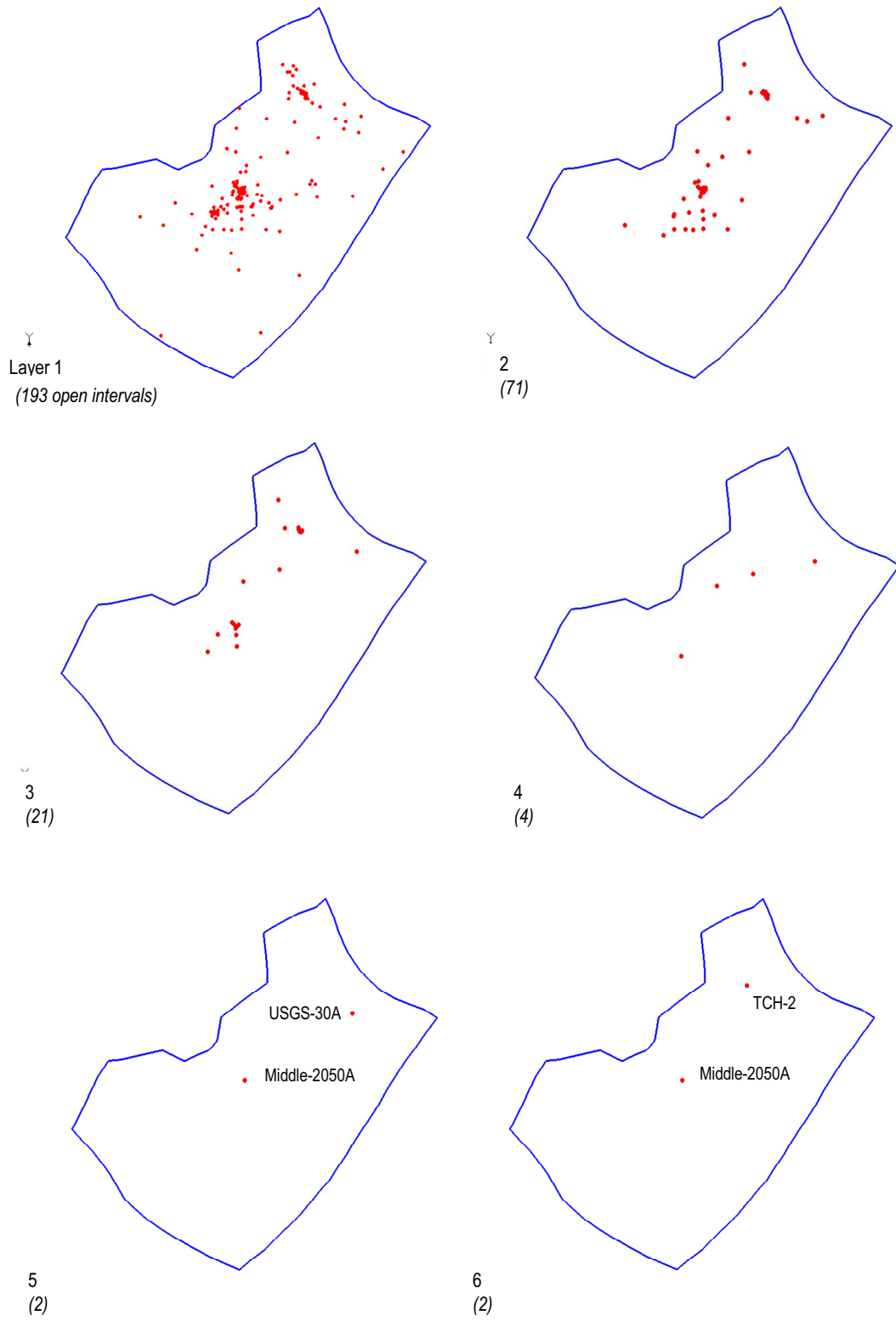


Figure 4-3. Layer-specific spatial distribution of hydraulic head calibration targets.

4.2.2 Velocity Estimates

Geochemical studies indicate a range of localized and long-range velocities occurring in the OU 10-08 modeling domain. A compilation of these studies presented in Section 2 indicates that velocities range from 0.3 to 8.5 m/day within the modeling domain, with an estimate of 2.6 m/day considered appropriate for the eastern portion of the model domain from TAN to Well USGS-2 while 4.8 m/day is appropriate for areas covered by a central fast path. Flow velocities of 8.5 m/day are estimated for fast paths near TAN, while 1.5 to 6 m/day is estimated for fast portions of the aquifer near the southern INL boundary, and 0.3 or 0.4 m/day is estimated for slower portions between these fast paths. Figure 4-4 summarizes the flow velocity estimates and shows the locations of 28 discrete points where estimated velocities (direction and magnitude) were extrapolated for use with the numerical modeling efforts. All of the velocity estimates available from field measurements coincide with layer 1 in the numerical model and only provide estimates of horizontal velocity. As discussed in Section 4.5, these data were used for a joint water-level-velocity inverse simulation. In all cases, horizontal conductivity is assumed to be isotropic due to a lack of information that would suggest otherwise.

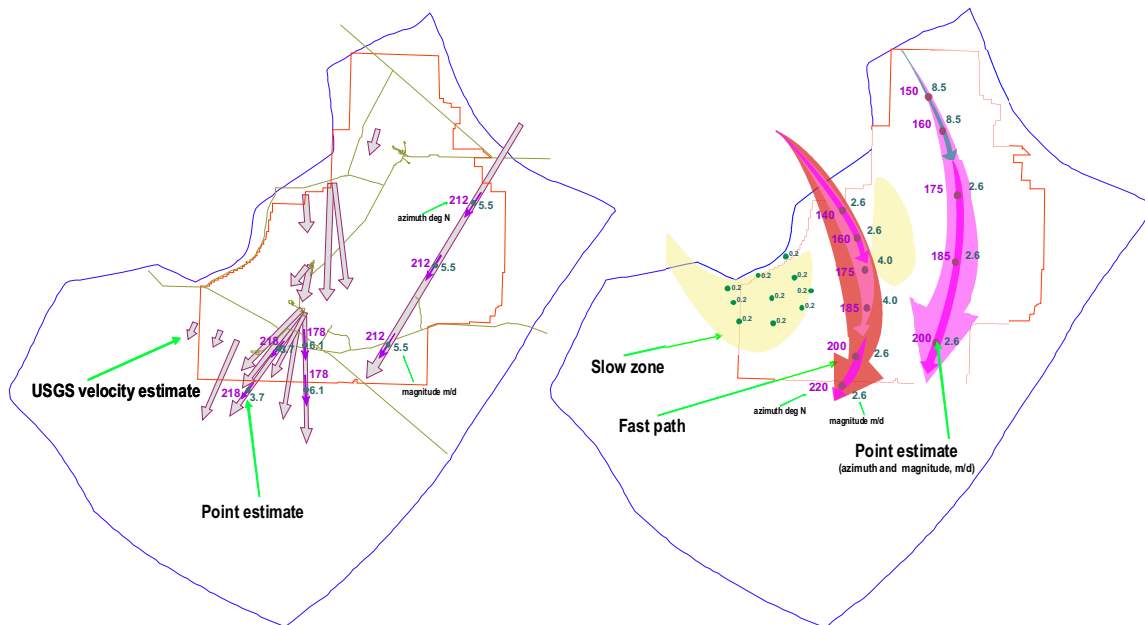


Figure 4-4. Point estimates of groundwater velocity obtained from recent geochemical studies.

4.3 Multi-Objective Calibration Approach and Weighting of Calibration Targets

If velocities and data types other than heads were used to calibrate the three-dimensional flow model, then a weighting scheme would be required to balance the priorities of data matching. Typically, weights (that sum to unity) are assigned as coefficients to each head measurement based on confidence in that data. Confidence, expressed as the measurement standard deviation, is a specified input parameter for each head measurement. Weights are calculated in the Groundwater Modeling System as the inverse of the measurement standard deviation. If, however, more importance was placed on a measured head from the center of the modeling domain, particularly near contaminated portions of the aquifer, this measurement could be assigned a lower measurement standard deviation and therefore a higher weight than that assigned to a head measurement in a well located on the periphery of the model domain.

Similarly, weighting could be assigned to other types of calibration data such as velocity estimates, based on the confidence or importance of the individual estimate. For a multi-objective calibration approach, these weighting schemes could be structured such that velocity estimates as a whole are given a larger priority in the calibration process than measured heads.

At the current stage of model development, the three-dimensional flow model is still calibrated primarily to the measured heads. There are 225 hydraulic head calibration targets within the three-dimensional flow model domain. In the previous two-dimensional flow model, each head measurement was assigned a measurement standard deviation of 1 m, which resulted in a uniform weight of 1, and the inverse solution was able to provide a satisfactory match to all measurements. Although each well has the same weight, a large number of wells were clustered inside the INL Site and near major facilities. Since there is over-representation of head near the major facilities, effectively larger weights are assigned to these wells. The three-dimensional flow model follows the same strategy and assigned a consistent measurement standard deviation of 1 m or the same uniform weight of 1 to every head measurement. For clarity, there is not an explicit convergence criterion specified within which each simulated head must match the observed head. Rather, PEST uses the calculated weights for each measurement and minimizes the objective function which is the sum of the weighted squared differences between the observed and simulated heads. It is the responsibility of the PEST user through analysis of the final optimized results to determine whether the solution at each location is adequate. Graphical post-processing facilitates this analysis. The objective in this model application was to have the simulated head be within 1 m of the observed head. As can be seen in the simulated results below, this objective was easily met for the most part and in many cases was exceeded.

As discussed in following sections of this report, calibration to the head data alone is not sufficient to constrain the parameter field obtained from inverse simulation. Through joint velocity-head inversion simulation, it is demonstrated that additional types of measurements, such as groundwater velocity estimates, provide valuable constraints to the estimated parameter field. In the joint velocity-head inverse simulation, each velocity estimate is assigned a constant weight of 1, for simplicity. As discussed later in Section 4.5, such assignment is reasonable.

4.3.1 Overview of Simulations

In order to test multiple conceptual models of the OU 10-08 model domain, a number of simulations were performed. These simulations are summarized in Table 4-2. As stated in the conceptual model section, two thickness scenarios are available for the model domain. In addition, incorporating the basalt-dominated and sediment-dominated hydrogeologic units determined by the conceptual modeling team within the modeling domain required testing of multiple modeling scenarios.

Two methods of applying pilot point methods were used in the calibration. The first method, referred to as the *pure pilot point approach*, used a set of pilot points where all pilot points were generally constrained with the same range of hydraulic conductivity values, with the same maximum value for hydraulic conductivity varying between the model layers. The second method, referred to as the *sediment-constrained pilot point* approach, incorporated information from the hydrogeologic units developed by the conceptual modeling team. In this scenario, the values of maximum hydraulic conductivity for pilot points within a model layer was variable, with pilot points falling within areas defined as *sediment controlled* having a lower maximum allowable hydraulic conductivity. In this way, the simulations honored the conceptual model hydrogeologic units while still allowing for an optimized hydraulic conductivity field using inverse modeling methods.

Table 4-2. Summary and numbering of the modeling scenarios carried out to test the various conceptual models on the flow domain.

	Pure Pilot Points	Sediment-Constrained Pilot Points
Thick Scenario	Model 1	Model 2
Thin Scenario	Model 3	Model 4

4.3.2 Pilot Point Methodology

As mentioned previously, calibration of the OU 10-08 groundwater model uses a pilot point inverse modeling approach implemented within the PEST inverse modeling framework. In general, inverse modeling is a systematic method of estimating a parameter field (in this case hydraulic conductivity) by adjusting a set of input parameters (initial estimates of hydraulic conductivity) until the difference between simulated and observed values is minimized. Compared to the conventional zonation approach, the pilot point method is a relatively new method for applying inverse methods to numerical models, where a fixed set of points (the pilot points) are defined within the numerical modeling domain and initial estimates for hydraulic conductivities at those points are assigned. The hydraulic conductivity value for each model grid cell is interpolated from the values at the pilot points. The number of pilot points is generally small when compared to the number of total grid nodes of the numerical model. During each iteration of an inverse simulation, the values of hydraulic conductivities at pilot points are adjusted and then interpolated onto the model grid cells in order to minimize the objective function. The final optimal hydraulic conductivity (K) field is then obtained by interpolating the final optimal K values at pilot points. In general, pilot point inverse simulation often leads to much better match to measured data, especially for highly heterogeneous flow systems, such as the OU 10-08 model domain.

In order to apply the pilot point method to the OU 10-08 flow model, the following items were required to be specified:

- Initial estimates of hydraulic conductivity
- Range of allowable hydraulic conductivity
- Interpolation methods for the hydraulic conductivity field.

These three items represent the minimum set of specifications required. Additional control on the pilot point procedure can be obtained by forcing regularization, a method by which a spatial dependence is constrained on the pilot points, i.e., the value of hydraulic conductivity at each point not only varies according to its sensitivity to measured heads, but also is related to the nearest pilot points. A full discussion of all the controls on the pilot point method is beyond the scope of this document and can be found in the PEST user manual (Dougherty 2004).

4.3.2.1 Pilot Point Spatial Distribution. Pilot point distribution in the modeling domain was determined by considering a number of factors, such as variations in the hydraulic head field, inferred changes in hydraulic conductivity, and spatial density of observation data. Initially, pilot points were uniformly distributed within each layer. The variable elevation of the bottom surface causes some grid truncation with depth in the domain, causing the number of pilot points to decrease with layer depth. At the beginning of the initial inverse simulation, the pilot point distribution near major facilities including Radioactive Waste Management Complex (RWMC), INTEC, and TAN was refined in order to capture local-scale heterogeneities, given the fact that most observation wells are clustered in those areas. After several initial trial inverse simulations were completed, additional pilot points were added to areas with large head gradients and the vicinities of wells with large mismatches. This iterative process was repeated

until a reasonable match to the observed heads was achieved. Once a final distribution of pilot points was determined, the pilot point locations and numbers remained fixed for all subsequent simulations. The final distribution of pilot points in each layer for the thick aquifer scenario is shown in Figure 4-5. The thin scenario models used largely the same pilot point distribution, with the exception that the truncation with depth is somewhat different due to differences in the aquifer bottom topography. Table 4-3 summarizes the number of pilot points for each modeling scenario.

Table 4-3. Summary of the number of pilot points used in the simulations.

Layer	Number of Pilot Points	
	Thick Scenario	Thin Scenario
1	94	94
2	94	94
3	86	86
4	80	73
5	70	65
6	62	56

4.3.2.2 Constraints on Pilot Points. As discussed above, the range of allowable hydraulic conductivity estimates must be specified for all pilot points. Implementation of the allowable ranges allowed for constraining inverse simulations and also allowed for capturing the basic features of the conceptual model in the numerical formulation. Initial guesses of estimates of hydraulic conductivity were based upon examination of aquifer test data, with an initial estimate of 100 m/day for the pilot points in the upper 4 model layers. Pilot points in the lowermost two layers were assigned an initial estimate of 10 m/day based on observed decrease in the average hydraulic conductivity with depth in the aquifer.

Simulations were performed to test the sensitivity of the model solution to these initial pilot point values. For a well-posed problem, the final solution is not sensitive to initial conditions. From these simulations, it was found that the availability of a large number of head observations in the upper four model layers adequately constrains these layers and the distribution of hydraulic conductivity in these layers is fairly insensitive to initial pilot point values. However, the small number of head observations in the lowest two layers makes them sensitive to initial parameter values.

The specified lower bound of hydraulic conductivity for all pilot points was 1.0×10^{-10} m/day. While this value is significantly lower than any measured value from aquifer tests, it provides the inverse procedure room to vary the hydraulic conductivity, and allows for faster convergence toward an optimized hydraulic conductivity field. The final hydraulic conductivity fields never contained values anywhere near this lower bound.

The upper bound placed on the pilot point hydraulic conductivity allowed for incorporation of the conceptual model into the numerical model. The two modeling scenarios were implemented by changing the specifications on the maximum hydraulic conductivity at the pilot points. The *pure pilot point* approach was implemented by setting the upper bound to a uniform 10,000 m/day for the top four model layers. This value is in qualitative agreement with aquifer test observations, where a maximum of approximately 8,000 m/day was estimated. The lower two layers were specified a maximum of 200 m/day, which is consistent with the observations of lower hydraulic conductivity with depth in the aquifer due to reductions in porosity and permeability caused by alteration of the basalts and secondary mineralization within the pore spaces and fractures.

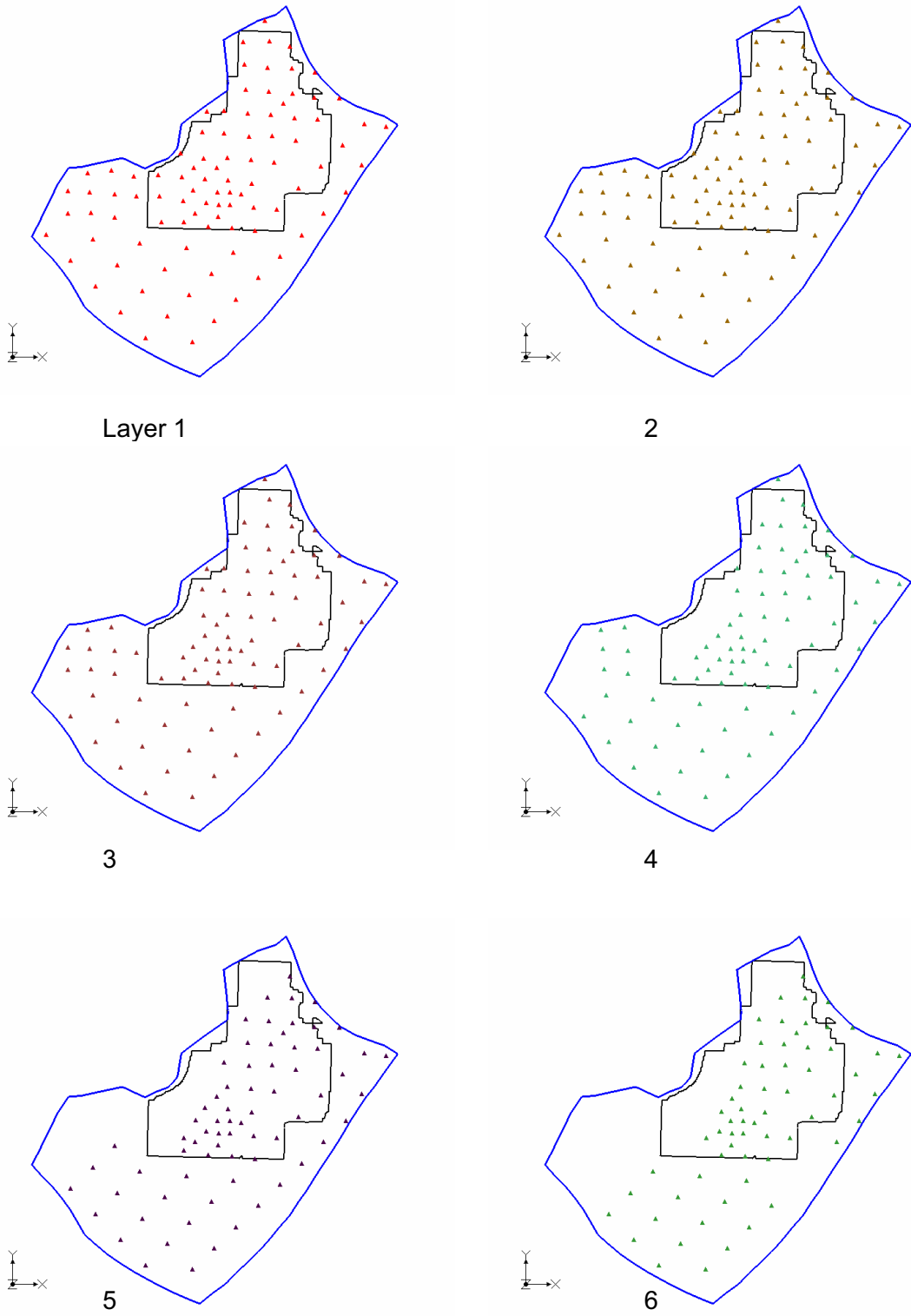


Figure 4-5. Pilot point distribution in each layer for inverse solution with pure pilot point calibration approach, three-dimensional flow model, thick aquifer scenario (layer number increases from the upper-left to lower-right).

To implement the *sediment-constrained pilot point* approach, polygons were constructed within each model layer that encompassed the extents of the sediment-controlled hydrogeologic units. Any pilot point that fell within the polygon was assigned a lower maximum allowable hydraulic conductivity. In this way, the lower hydraulic conductivity sediments were incorporated into the primarily basalt-dominated aquifer. Figure 4-6 shows the outlines of the sediment-dominated polygons for each model layer. For the upper 4 model layers, pilot points within the sediment-dominated units were prescribed a maximum hydraulic conductivity of 2,000 m/day. In the lowermost two model layers, the upper bound prescribed for the basalts (200 m/day) adequately constrained the model and therefore no further bounding of the layers were required. A summary of initial estimates and maximum permitted conductivities allowed during the inverse calibration process is given in Table 4-4.

Table 4-4. Initial guesses and maximum values of hydraulic conductivity for the pilot points by model layer.

Model Layer	Initial Guess Hydraulic Conductivity (m/day)	Max Allowed Hydraulic Conductivity (m/day)
1	100	10,000
2	100	10,000
3	100	10,000
4	100	10,000
5	10	200
6	10	200
Sediment Dominated	10–100	200–2,000

4.3.2.3 Hydraulic Conductivity Field Interpolation Based on Estimates at Pilot Points.

During each iteration of a particular PEST inverse run, the hydraulic conductivity values at all pilot points are adjusted first, according to the current mismatches and parameter sensitivity matrix. Then the hydraulic conductivity values for all model grid cells are obtained by interpolating the adjusted hydraulic conductivity values at pilot points before another forward model run is performed. Ideally, a geostatistically based Kriging interpolation scheme would be best for such interpolation. However, Kriging requires a variogram fitted to the log-transformed hydraulic conductivity field.

Despite the large number of aquifer tests performed within the INL, however, a variogram of the $\ln K$ field still cannot be inferred with reasonable confidence from these data in order to use Kriging methods to interpolate $\ln K$ values from pilot points to individual grid cells. This is largely due to the scale discrepancies among those tests and scale difference between our model grid cells and aquifer tests. Therefore, in the pilot point inverse simulations, a simpler inverse distance interpolation approach using the nearest five pilot points to interpolate parameter values from pilot points to model grid cells was implemented. The more of these nearest neighbor points used for interpolation, the smoother the resulting estimated K field; however, an over-smoothed K field will not accurately reproduce local variations of observed heads. Tests were conducted to arrive at the final choice of five nearest neighbor points for interpolation that produce a good compromise between local variation of heads and spatial correlation of parameter values.

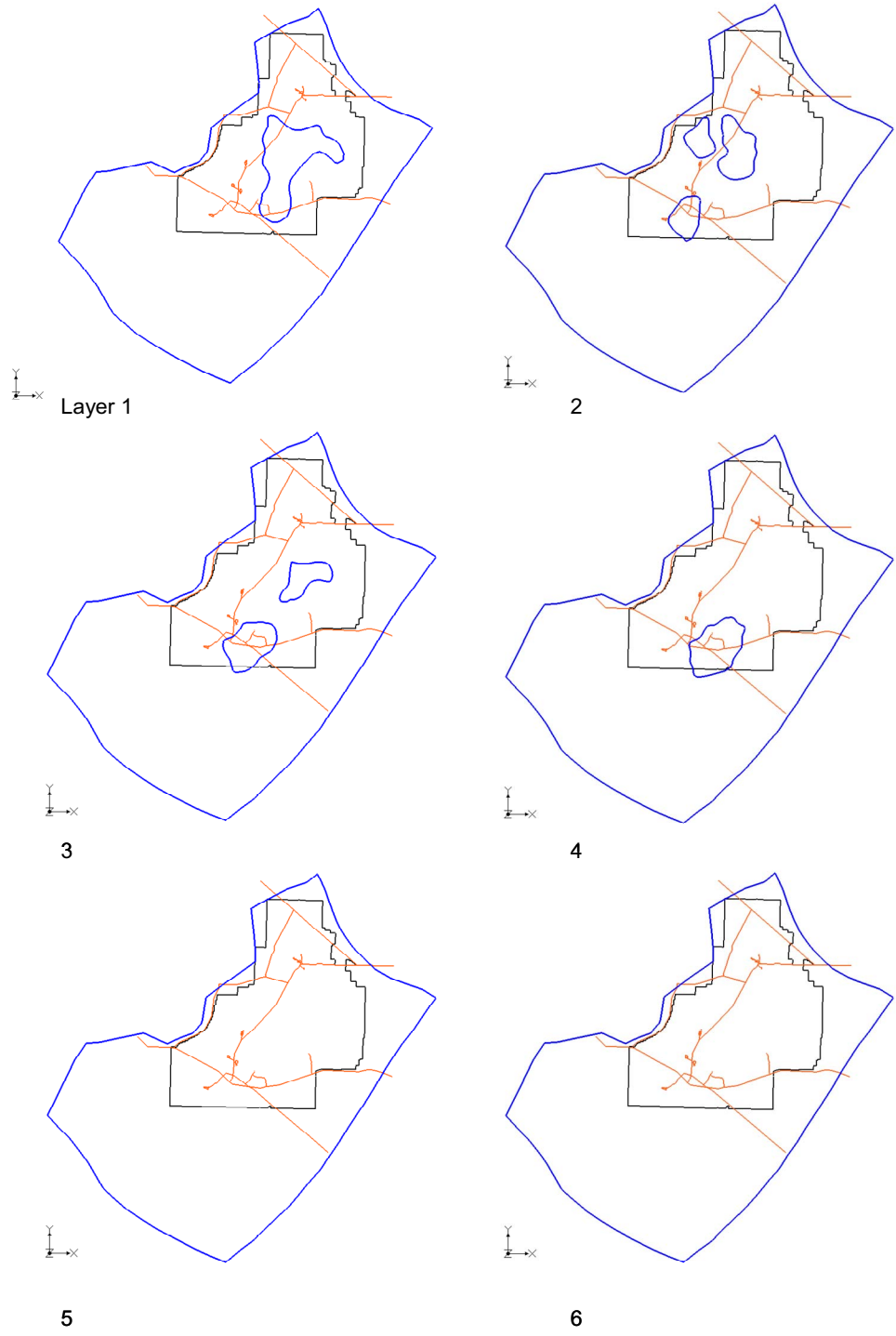


Figure 4-6. Spatial distribution of the sediment-controlled polygons. Layer 1 is at the top left corner, and layer 6 at the bottom right. The INL boundary and roads are shown for each layer.

4.3.2.4 Regularization of Hydraulic Conductivities at Pilot Points. For most subsurface hydrogeological inverse simulation problems there is always a lack of measurements compared with the number of parameters to be estimated, which is often referred to as non-uniqueness or ill-posed problem. Regularization refers to a common practice of adding additional constraints to the parameter field to reduce the degree of nonuniqueness associated with the inverse simulation. One typical regularization procedure is to minimize the differences between parameters. With regularization, the total objective function includes two groups, (1) measurements: the sum of weighted squared mismatches between the measured and simulated heads, and (2) regularization observations: the sum of weighted squared differences between hydraulic conductivities at pilot points. In the Groundwater Modeling System, the difference of $\ln K$ valued for each pair of pilot points within the same model layer is automatically considered as one ‘regularization observation.’ The corresponding weight is simply taken as the inversed distance between two pilot points. In this application, a constant group weight of 1 was assigned to the first group (actual head measurements). However, the group weight for the second group, often referred to as the *regularization weight factor*, is determined automatically during each optimization iteration and can be different for different iterations. For details on the algorithm of parameter regularization, refer to the PEST user manual (Dougherty 2004). Regularization often leads to larger mismatches to measured data, but usually a more reliable parameter field. Various regularization weighting schemes were tested with the optimal regularization weights selected that give both satisfactory match to measured heads and a reasonably reliable parameter field, as measured by the confidence intervals for estimated parameters.

4.4 Inverse Simulation Results

The inverse simulation results from all modeling approaches showed a large number of similarities in the simulated head contour maps, goodness of fit to the observed head data, and hydraulic conductivity distribution. In addition, the confidence intervals for the hydraulic conductivity estimates at each pilot point generally fall within reasonable bounds. In the following sections, each modeling scenario shown in Table 4-2 will be discussed separately, with a summary discussion of results in Section 4.4.3. Simulated heads, error plots (difference of observed and simulated heads as a function of observed head), residual distribution and statistics, and final estimated hydraulic conductivity distributions are presented for all cases: (1) thick aquifer scenario inversely calibrated with the pure pilot point approach; (2) thick aquifer scenario calibrated using the pilot point approach with sedimentary bounds; (3) thin aquifer scenario calibrated using the pure pilot point approach, and (4) thin aquifer scenario calibrated using the pilot point approach with sedimentary bounds. For all four base model cases, a constant horizontal to vertical anisotropy ratio of 100 was used. Tables in Appendix E list all measured and simulated heads, residual errors, and well screen elevations for all calibration wells used in these four base cases. The table also provides summaries for wells near major facilities.

4.4.1 Thick Aquifer Scenario

4.4.1.1 Model 1: Pure Pilot Point Approach. Figure 4-7 shows the simulated head contours (top layer only). The simulated head contours in general agree with the field measurements. For example, the simulated head contours exhibit a very flat water table north of TAN and a large decline of heads immediately south of TAN that is believed to be a consequence of more sedimentary deposits within that area, reducing the horizontal hydraulic conductivity. Additionally, it is worthy to mention that the simulated head distribution inside the INL, particular in the southern portion of the INL Site, exhibits a generally flat water table, but with some significant local variations. For example, the head contours within the area south of INTEC and northwest of RWMC show a relatively large gradient. However, it is hard to see the differences on the simulated head contours among the model layers simply from these head contours. Figure 4-7 also shows simulation residuals on whisker plots for all observation wells. The whisker plots show the residual against a constant plus or minus 2-m whisker bar for each measurement location. The simulation residual is plotted against the whisker bar relative to the center zero line with the

size and color of the error bar indicating magnitude. A green bar represents a residual error within plus or minus 2 m, a yellow bar for errors between 2 and 3 m, and a red bar for errors greater than 3 m. For the majority of the observation wells, the mismatch is less than 1–2 m. There are a few wells (represented by yellow) with mismatches around 3 m. The bottom plot in Figure 4-7 also shows the simulation residuals of head observations in a more quantitative way with the residual plotted against the observed value. In this Groundwater Modeling System-generated plot, the different symbols for the data points have no meaning. Most importantly, there is no systematic bias on residuals observed in this figure, as manifested by the mean error of 0.07 m, close to zero. This residual distribution map shows more quantitatively that the majority of observation wells has mismatch less than 1 m, indicating a satisfactory fit to the measured heads, given the large number of head measurements and the complexities of the hydrogeologic conditions within the model domain. The simulation residuals are presented alternatively as contours in Figure 4-8 using inverse distance weighting to interpolate between the measurement locations, which are indicated by symbols. Figure 4-8 shows the residuals for all model layers combined into one contour plot. There were 225 observation locations in total, with 213 observations occurring within the top two model layers. Figure 4-9 shows a close-up of the residuals for the southern half of the INL with wells identified that have the larger mismatches. In the region from RTC and INTEC down to RWMC, the residuals are mostly less than 0.5 m.

Figure 4-10 shows the horizontal hydraulic conductivity map for each model layer. In general, the conductivity distributions are consistent with the conceptual model; for example, the top four layers all show a relatively more conductive zone in the southwest corner of the INL Site, which coincides with the location the Arco rift zone. It is also noteworthy that inside this relatively high K zone there are still significant local variations. Further southward (downgradient from the Arco rift) is the area called Quaking Aspen Butte rift, which consists of a number of inactive volcanic vents. This is also the area where large head drops are observed, an indicator of low hydraulic conductivity. The simulated hydraulic conductivity in this area also agrees with this assumption. These maps are all plotted with the same range for comparison purpose. The blank or white areas in those maps are truncated portions by the aquifer base. All layers exhibit significant variations of the hydraulic conductivity as can be seen in the figure.

Figure 4-11 shows the 95% confidence bounds of the model-estimated hydraulic conductivity values at each individual pilot point. These confidence bounds are calculated from the diagonal elements of the covariance matrix for the optimal solutions. These model parameter confidence bounds are useful for the information they provide on the relative sensitivities of the estimated parameters to the overall optimization objective function. The narrower the confidence bound, the more impact that parameter has on the objective function. Conversely, an extremely wide bound means the model result could be anywhere within those bounds and not substantially reduce the objective function. It is ideal during PEST inverse runs for all parameters to be equally sensitive to the objective function, avoiding dominance by only a few parameters. This would imply the correct number of parameters or pilot points were being used in the optimization. From Figure 4-11, it can be seen that the confidence bounds of most model parameters, in this case the K values of the pilot points, vary over a range of magnitudes. Some pilot points have wider bounds and some have narrower bounds, indicating there are both sensitive and nonsensitive parameters. Figure 4-11 implies that the current approach of how we parameterized the three-dimensional flow is not optimal. There are probably too many pilot points being used and some pilot points are likely dominating the optimization. The number and locations of pilot points will be revisited in the transport modeling phase of the model development.

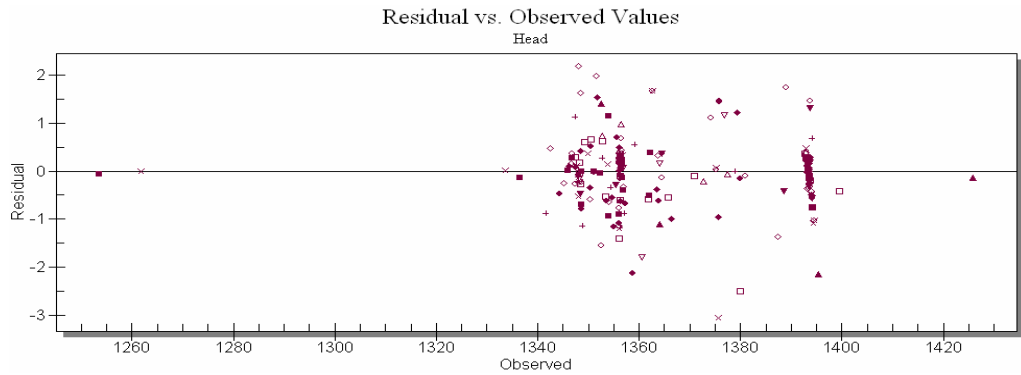
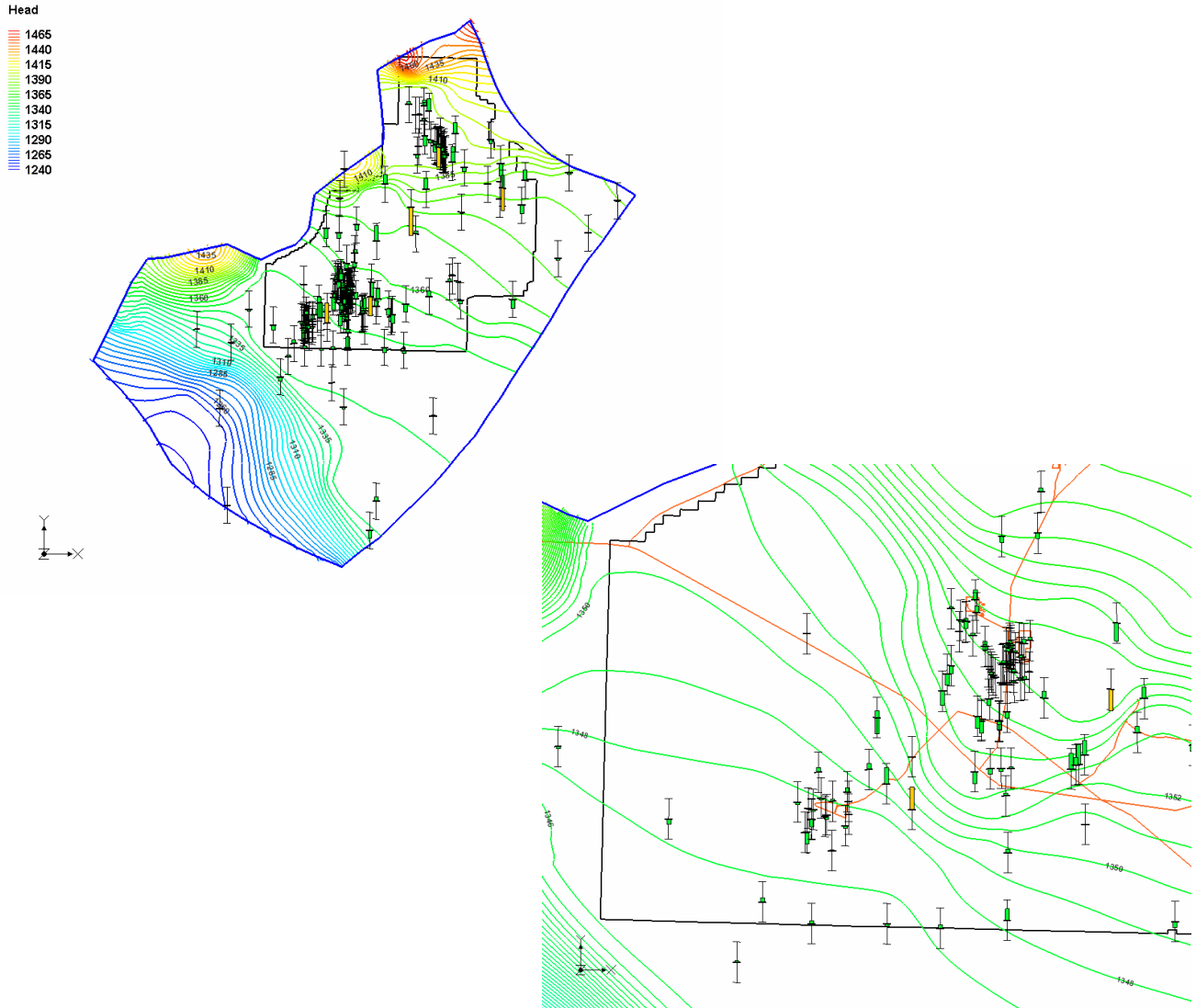


Figure 4-7. Simulated heads (m) in the top layer of the three-dimensional flow model, thick scenario, pure pilot point calibration (base case model 1). Simulation residuals shown with green bars are less than 2 m and those with yellow bars are from 2 to 3 m.



Figure 4-8. Head residuals (simulated minus observed) for all model layers, thick scenario, pure pilot point calibration (base case model 1).

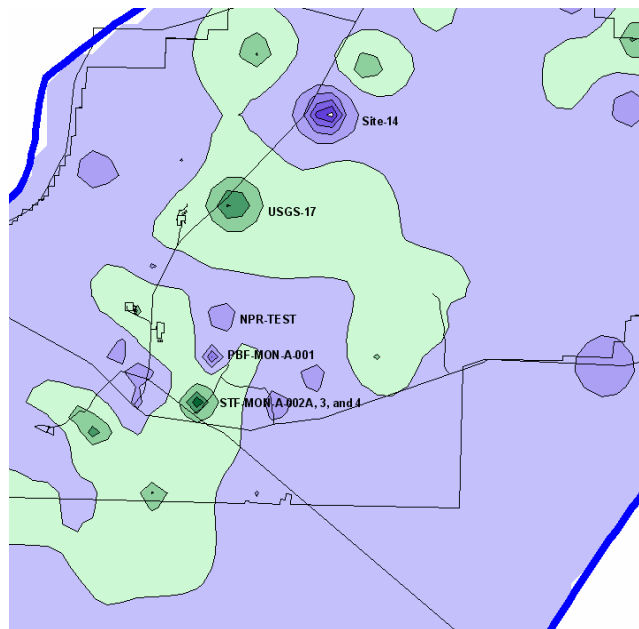


Figure 4-9. Head residuals (simulated minus observed) for all model layers, thick scenario, pure pilot point calibration (base case model 1) for the southern half of the INL. The contour color ranges are the same as that shown in Figure 4-8.

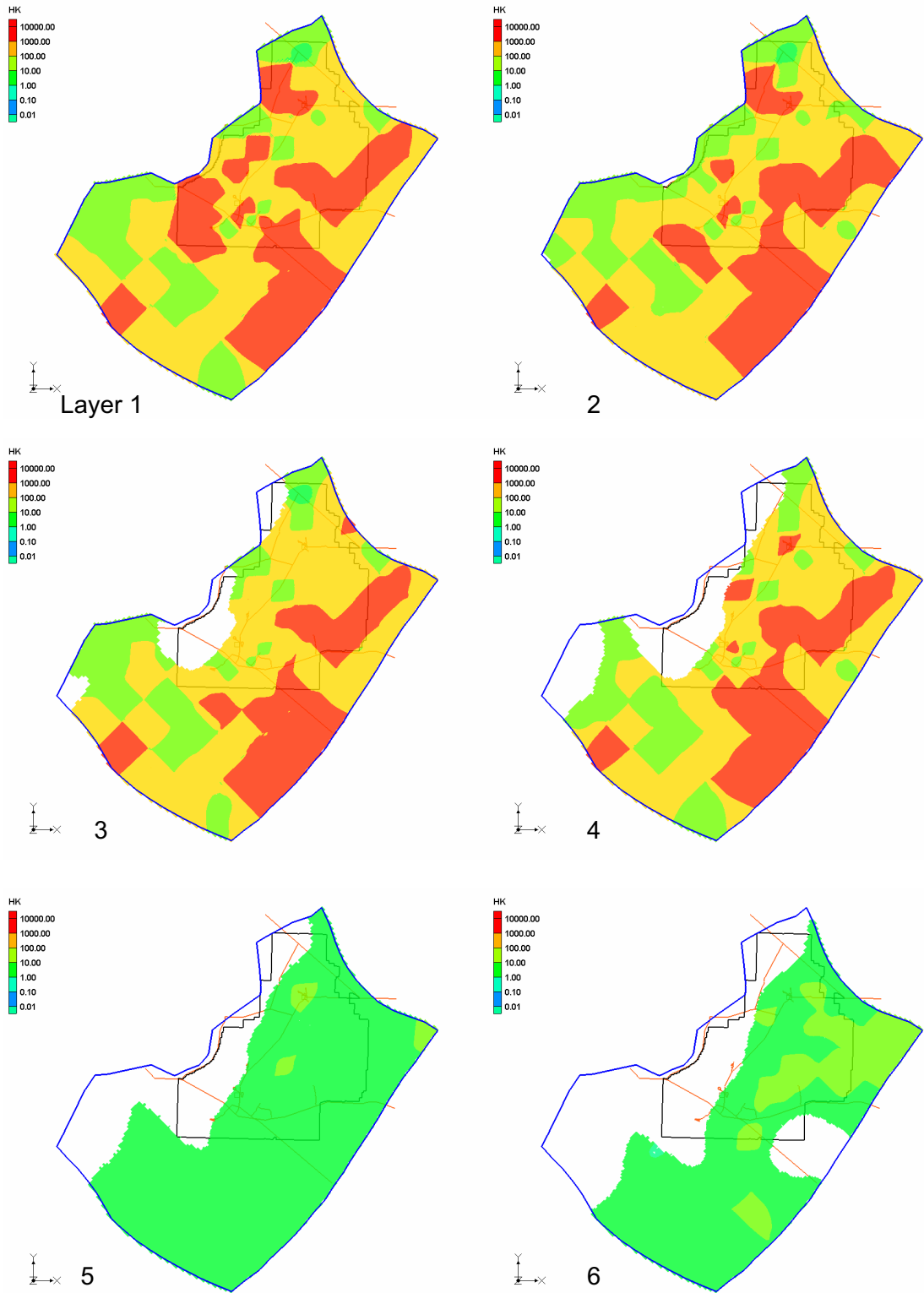


Figure 4-10. Horizontal hydraulic conductivity distribution for OU 10-08 three-dimensional flow model estimated from inverse solution using pure pilot point approach, thick scenario (base case model 1).

Model 1

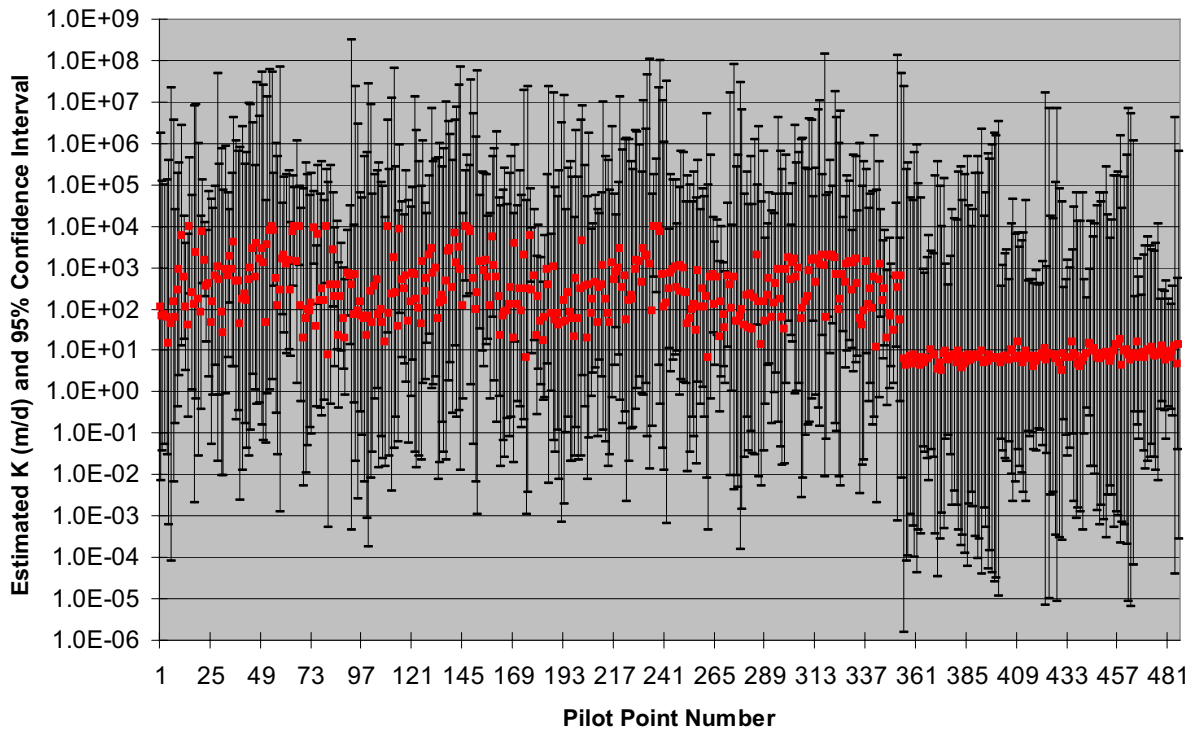


Figure 4-11. Confidence bounds of model parameters estimated by PEST for base case model 1.

4.4.1.2 Model 2: Sediment-Constrained Pilot Point Approach. The pure pilot approach described above resulted in the satisfactory matches between observed and simulated heads in the thick aquifer scenario, as expressed in the error summary terms. This is expected since in the pure pilot point approach there are no constraints on the values of the pilot points, except for the upper bound of 10,000 m/day assigned to every pilot point and a constant horizontal to vertical anisotropy ratio of 100 assigned to each layer during the PEST inverse solution process.

However, this pure pilot approach does not consider the three-dimensional hydrostratigraphic conceptual model as described in Section 2. To honor the information describing the interpreted sediment-impacted hydrogeologic units in the OU 10-08 modeling domain, the pure pilot point inverse solution approach was modified to assign a much smaller upper bound to hydraulic conductivities, 200 m/day, for pilot points located within those volumes. There are two reasons behind this simplification of the three-dimensional hydrostratigraphic model: one is that although the conceptual model describes a complex three-dimensional hydrostratigraphic system consisting of a number of basalt units, it is difficult to distinguish these different basalt units in terms of assigning different hydraulic property ranges. The hydraulic conductivity inside the basalt-dominated units varies significantly, and ranges of hydraulic conductivities for different basalt units overlap significantly. The second reason is that the sedimentary units inside the model domain are assigned hydraulic property ranges that are significantly different from the basalt units. In addition, the sedimentary units are assumed to be isotropic both horizontally and vertically, compared to the highly anisotropic nature of the basalt units.

Figure 4-12 depicts the simulated head contours, residual error bars of all observation wells, and residual statistics for the thick scenario with this bounded pilot point approach. The simulated head contours are very similar to those shown in Figure 4-7. The goodness of fit is also satisfactory since the majority of the observation wells has mismatch less than 1 m. The bounded pilot point approach resulted in slightly higher mismatches, as manifested by the slightly higher root mean square error, 0.722, compared to that of pure pilot point approach, 0.713. This slight increase of residuals is expected since the approach places constraints on the model parameters, which in turn results in less searchable parameter spaces for the inverse solution. The simulation residuals for all the layers are shown in Figure 4-13.

Figure 4-14 shows the horizontal hydraulic conductivity maps of model layers obtained from the inverse model simulation. When comparing this figure with Figure 4-10, the K field obtained with pure pilot point approach, one can immediately draw a conclusion that the large-scale spatial features of the hydraulic conductivity field obtained by two approaches are essentially unchanged. However, a closer comparison of these two figures reveals that there are considerable local variations on the magnitudes of the hydraulic conductivity field. Since the bounded pilot point approach explicitly honors the distribution of sediment-impacted units in the model domain, the conductivity fields shown in Figure 4-14 might have higher technical credibility and less uncertainty (more geological information honored) than that obtained from pure pilot point approach. Another point worth noting is that as shown in Figure 4-14, the hydraulic conductivity inside sedimentary units varies considerably in the inverse results, indicating the inadequacy of the conventional zonation approach in terms of capturing the local scale heterogeneity features. In addition, all hydraulic conductivity values inside the sedimentary units range from a few meters per day to a value close to 2,000 m/day, implying that it is appropriate to assign a 2,000 m/day upper bound for pilot points located inside the sedimentary units.

Figure 4-15 shows the 95% confidence bounds of estimated K values at all pilot points for base case model 2. Similar to the plot for model 1 (see Figure 4-11), this graph shows some parameters with smaller ranges than others indicating larger sensitivity of the objective function to those parameters.

4.4.2 Thin Aquifer Scenario

4.4.2.1 Model 3: Pure Pilot Point Approach. For the thin aquifer scenario, the three-dimensional flow model was treated in a similar manner to the thick scenario. Pilot points were distributed within the six layers, hydraulic conductivity fields for individual layers were inversely solved using PEST, and the goodness of fit was checked against the June 2004 head observations. The final near optimal pilot point distributions within individual model layers for the thick scenario were also used for the thin scenario, except for additional truncations of pilot points by the aquifer base of the thin scenario. In general, for this scenario the same pilot point distribution was used as in the final thick aquifer scenario.

Figure 4-16 depicts the head distribution, residual error bars for all observation wells, and error statistics for the thin aquifer scenario as found from inverse solution with pure pilot point approach. In general, the thin scenario provides the same level of match between simulated and observed heads as does the thick scenario. The majority of the observation wells have mismatches less than 1 m. There is also no systematic bias on the residual distribution. The simulated head contours for the thin scenario are very similar to the thick scenario, as expected since both thin and thick models are calibrated with the same set of head measurements. Figure 4-17 shows the simulated residuals for all model layers.

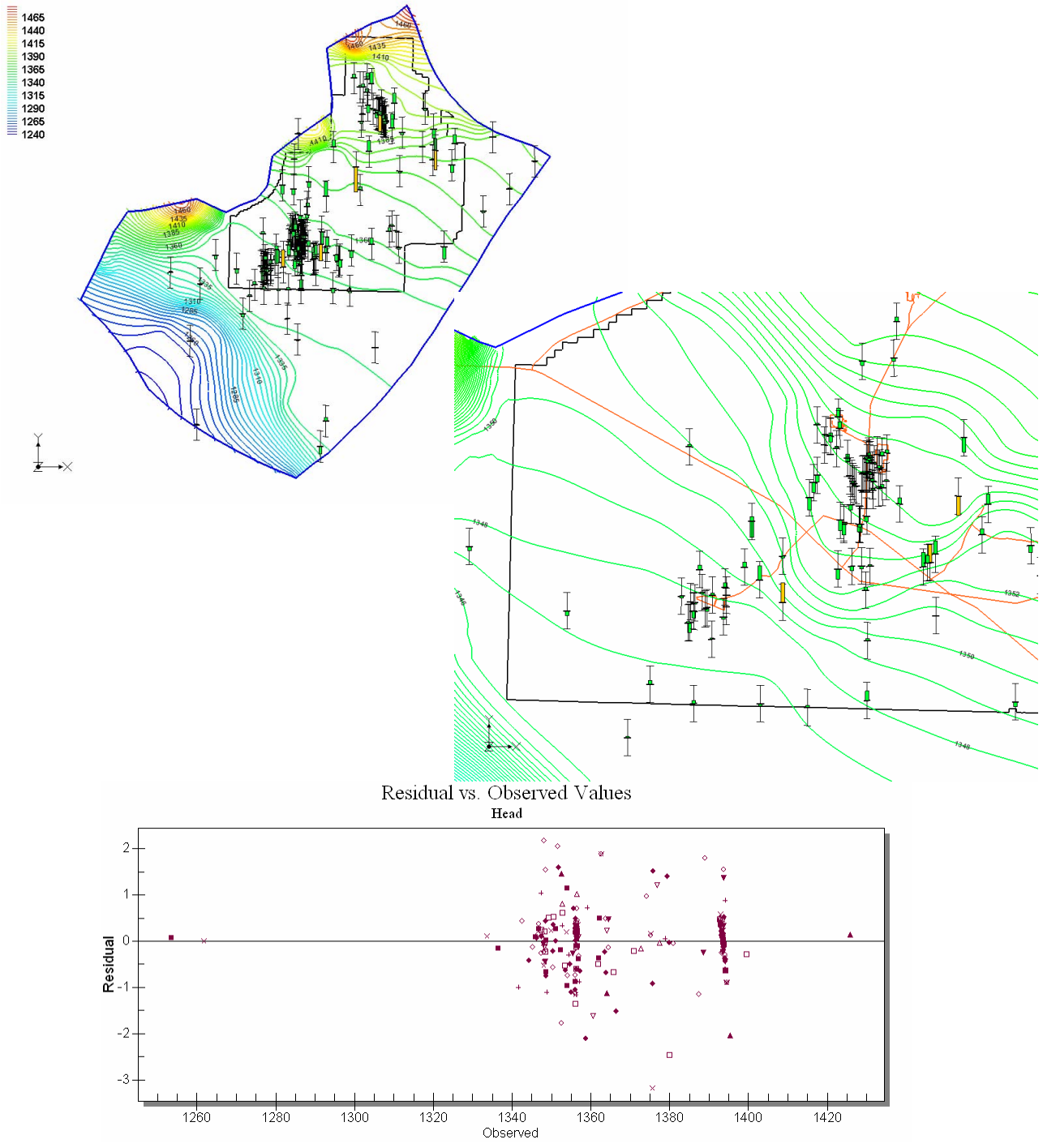


Figure 4-12. Simulated heads (m) in the top layer of the three-dimensional flow model, thick scenario, calibrated with pilot point approach using sedimentary layer bounds (base case model 2). Simulation residuals shown with green bars are less than 2 m and those with yellow bars are from 2 to 3 m.



Figure 4-13. Head residuals (simulated minus observed) for all model layers, thick scenario, calibrated with pilot point approach using sedimentary layer bounds (base case model 2).

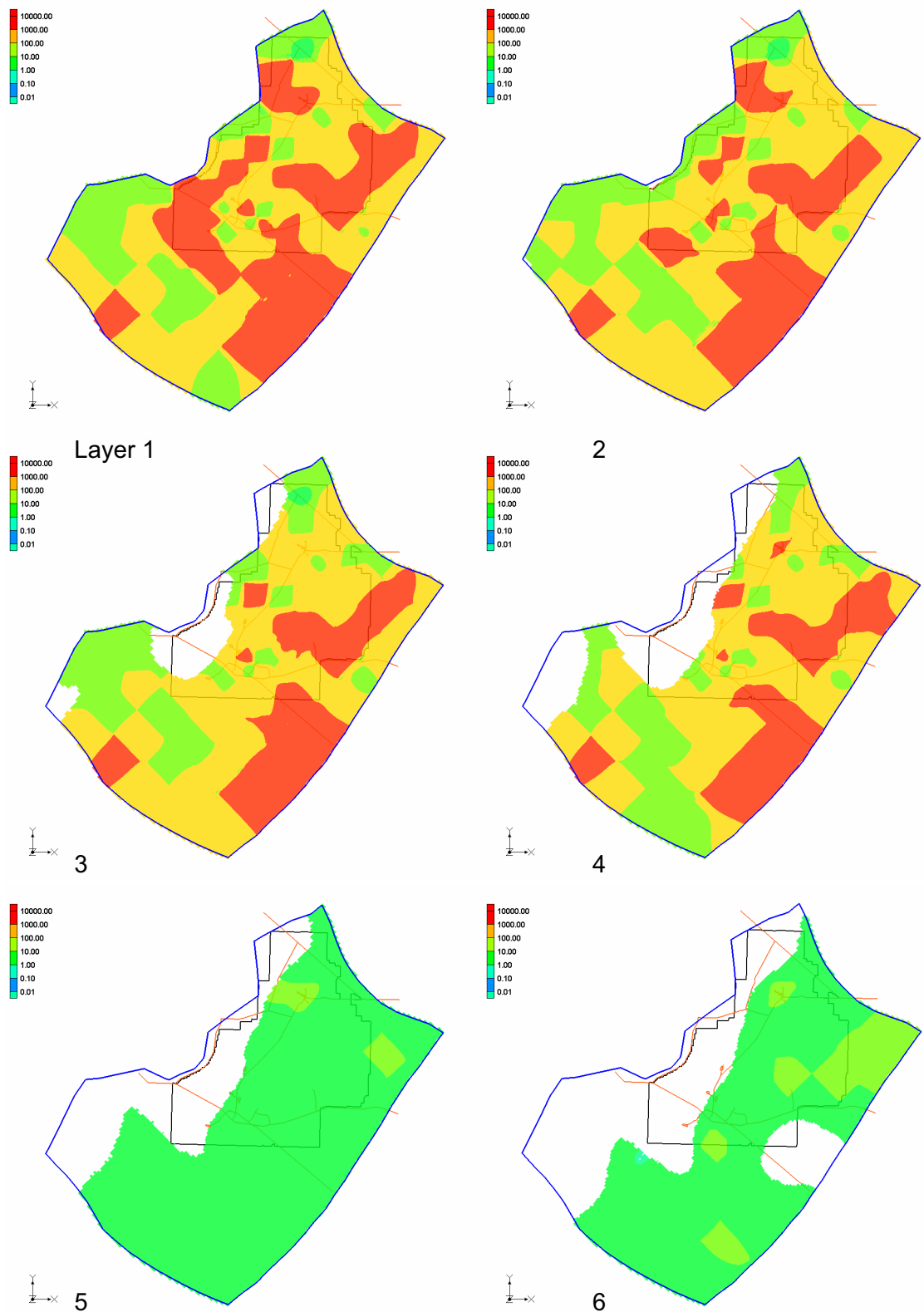


Figure 4-14. Conductivity distribution (m/day) within six model layers for thick aquifer scenario estimated using the pilot point approach with sedimentary layer bounds (base case model 2).

Model 2

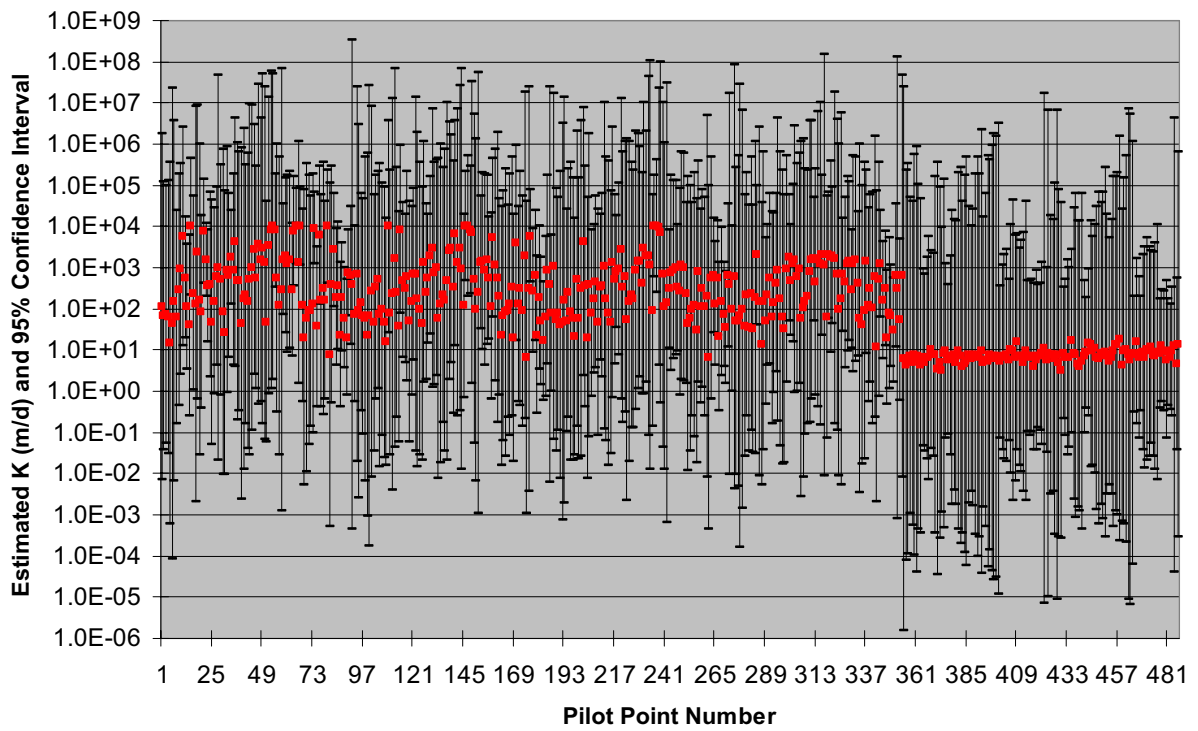
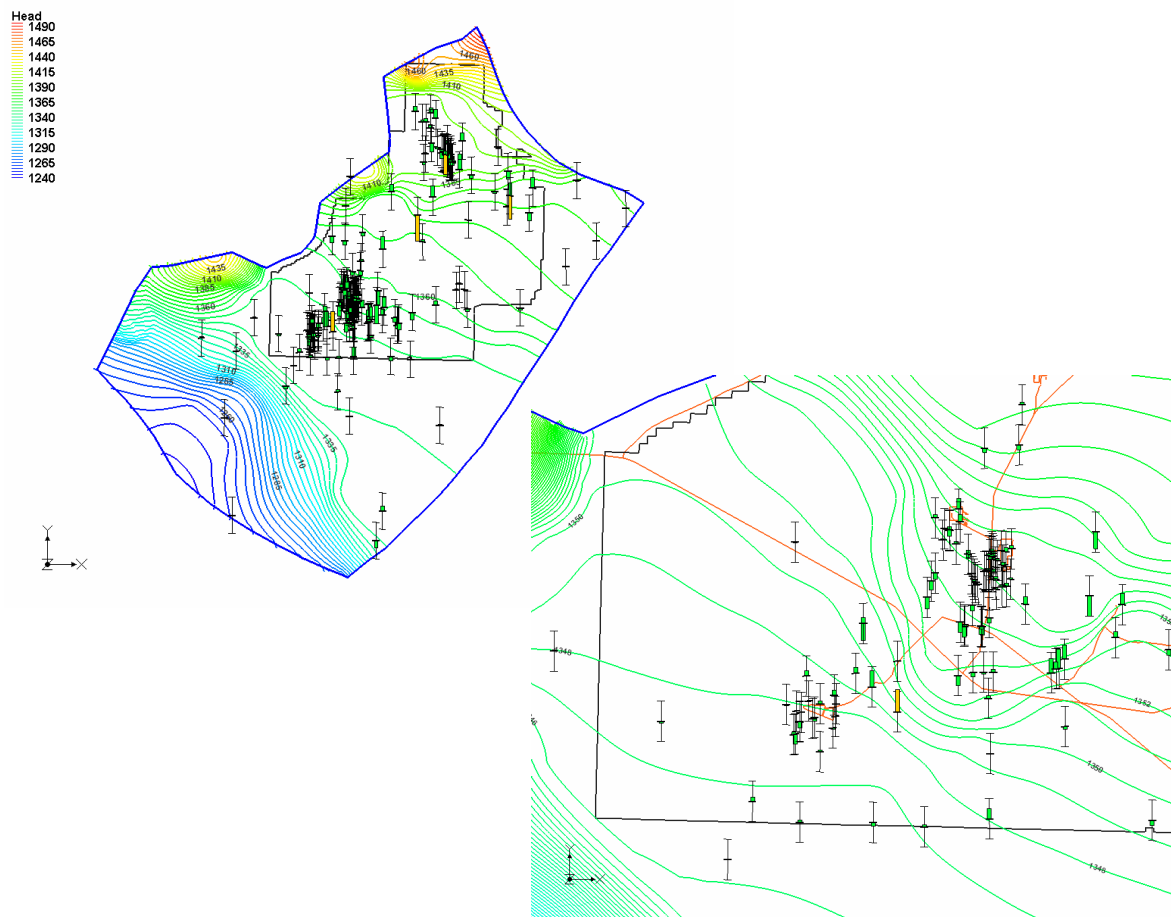


Figure 4-15. Confidence bounds of model parameters estimated by PEST for base case model 2.



Residual vs. Observed Values

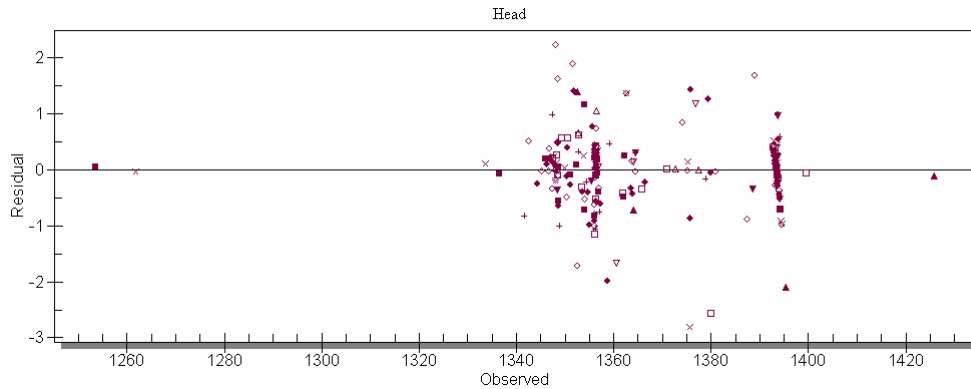


Figure 4-16. Simulated heads (m) in the top layer of the three-dimensional flow model, thin scenario, calibrated with the pure pilot point approach (base case model 3). Simulation residuals shown with green bars are less than 2 m and those with yellow bars are from 2 to 3 m.

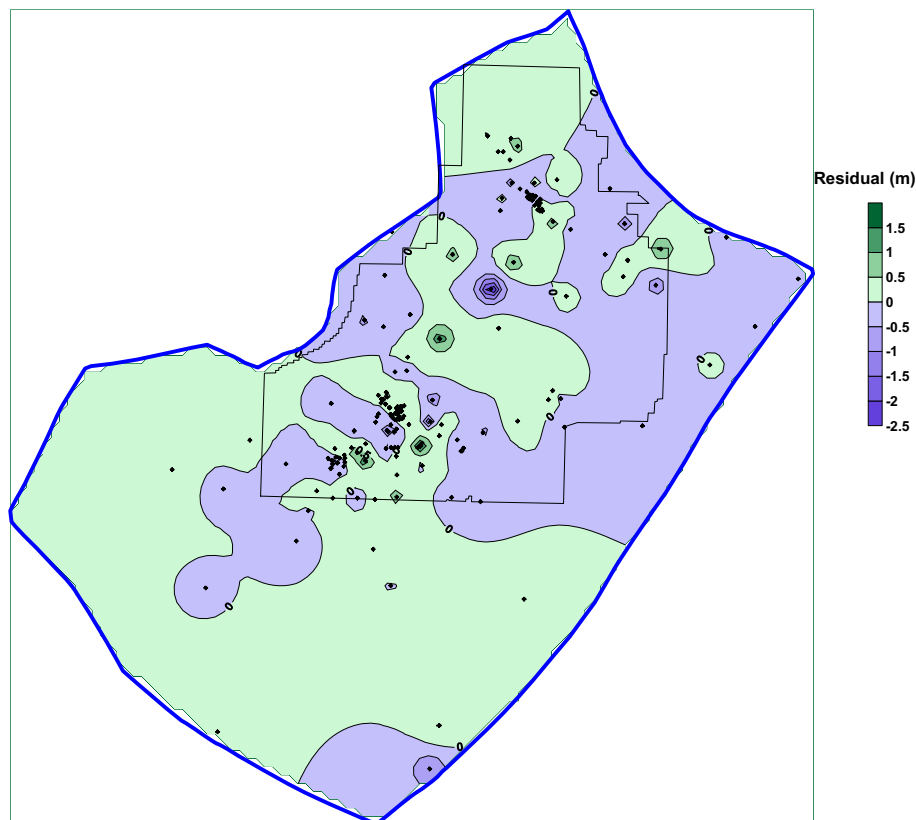


Figure 4-17. Head residuals (simulated minus observed) for all model layers, thin scenario, calibrated with the pure pilot point approach (base case model 3).

Figure 4-18 shows the resulting hydraulic conductivity fields of individual model layers for the thin aquifer scenario for the pure pilot point approach. As shown in Figure 4-18, the thin aquifer model also shows similar spatial features of the hydraulic conductivity field, particularly in the upper layers, for example, a relatively more conductive zone in the area of Arco rift and a low conductivity in Quaking Aspen Butte rift area. The bottom two layers of the thin scenario show the overall lower hydraulic conductivity values imposed from the conceptual model. However, there are some important differences on the final hydraulic conductivity distributions between the thick and thin scenarios, particularly for the top model layers of the two scenarios. Within the Arco rift area, the top layer of the thin scenario appears to be more conductive than that of the thick scenario. This is important since this area is downgradient from INTEC and adjacent to RWMC; therefore its hydraulic conductivity will have significant impact on transport predictions, which is particularly germane since most contaminants reside in the upper portion of the aquifer.

For both scenarios, the top layer is always 35 m thick everywhere in the model domain. Thus, the differences of the K field for this layer are not caused by the variation of the grid layer thickness. It is necessary to investigate which case is more reasonable. Although the spatial patterns of the hydraulic conductivity field of the lower model layers, for both thick and thin scenarios, are similar, the two scenarios do have variations in magnitude, mainly due to the changes of the model layer thickness between two scenarios. The bottom layer of the thin scenario also shows larger hydraulic conductivity values, similar to the thick scenario, due to the high inflow flux from the northeastern boundary assigned to this layer. This is a natural result of using the similar boundary conditions and observation heads with a thinner aquifer.

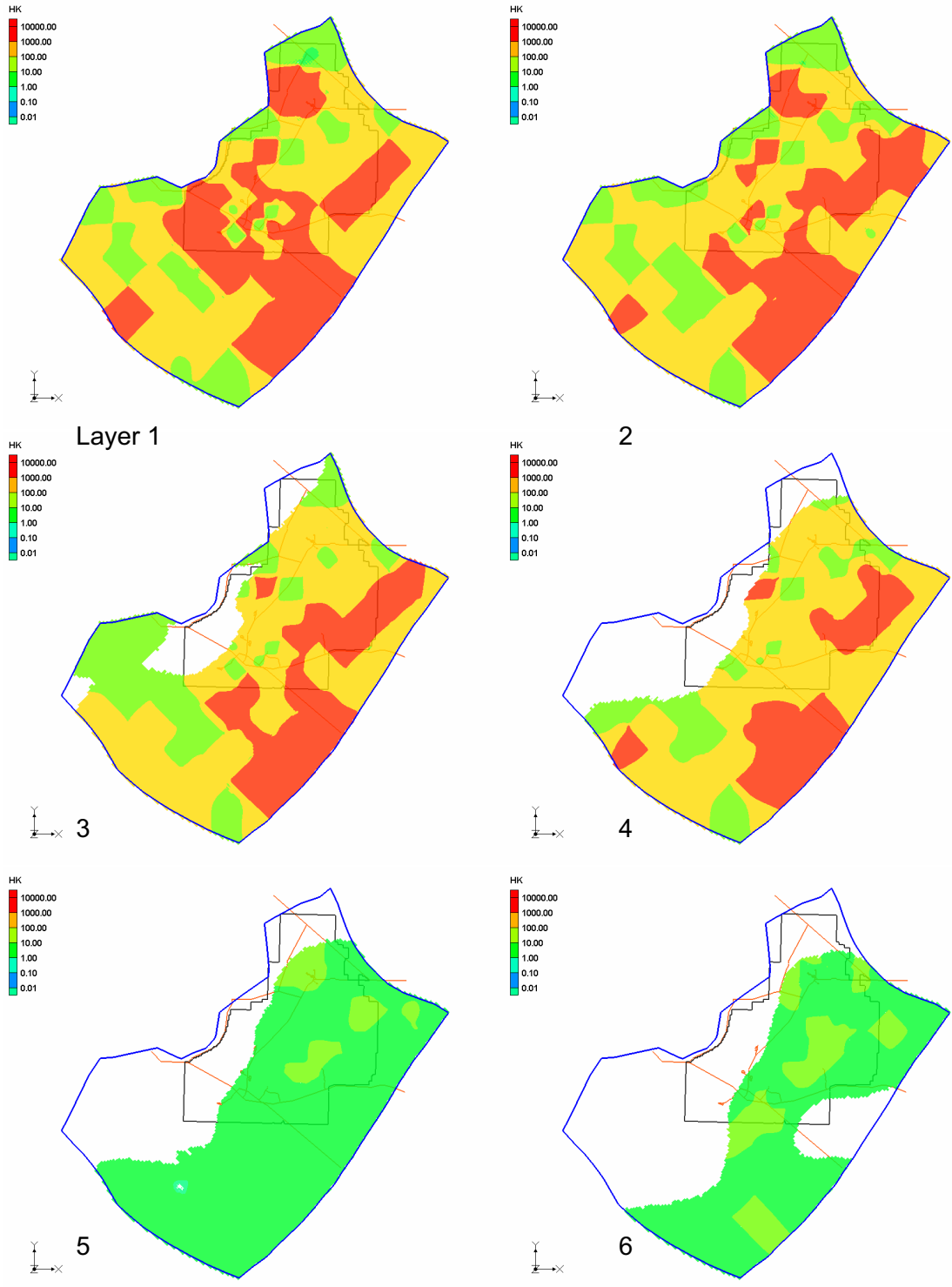


Figure 4-18. Conductivity distribution (m/day) within six model layers for thin aquifer scenario estimated using the pure pilot point inverse solution approach (base case model 3).

Figure 4-19 shows the 95% confidence bounds of estimated K values at all pilot points for base case model 3. As before, the graph shows increased sensitivity of the objective function to some model parameters.

Model 3

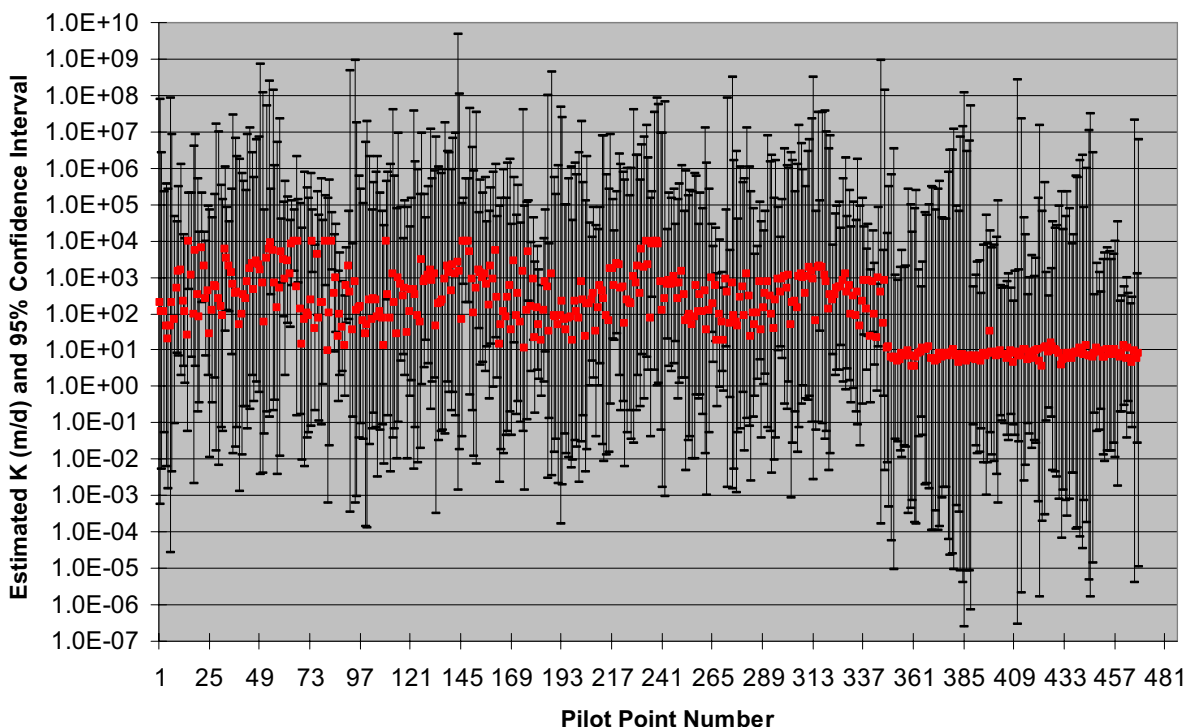
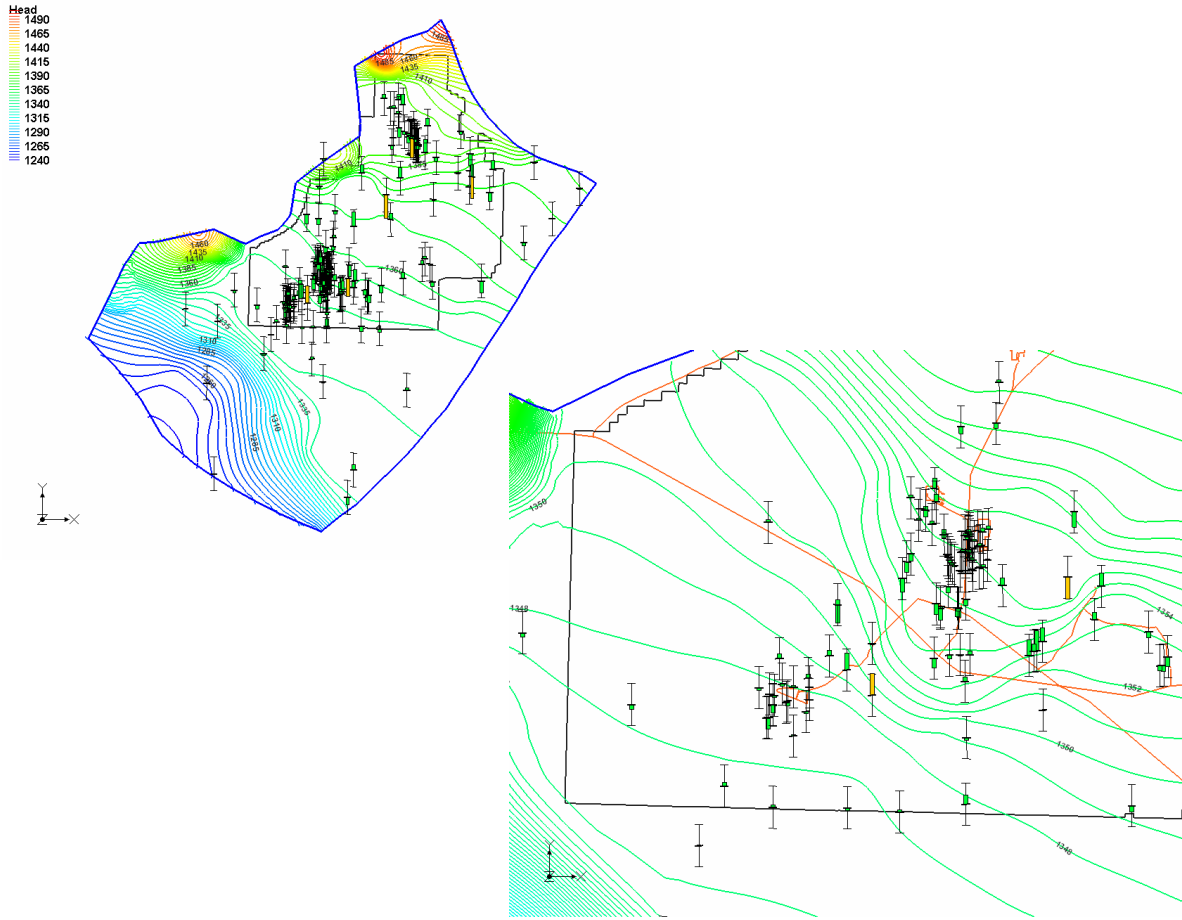


Figure 4-19. Confidence bounds of model parameters estimated by PEST for base case model 3.

4.4.2.2 Model 4: Sediment-Constrained Pilot Point Approach. Similar to the pure point approach, which was applied to both thick and thin aquifer scenarios, the same sediment-bounded pilot point approach was applied to the thin aquifer scenario. Figures 4-20, 4-21, and 4-22 depict the simulation results of the sediment-constrained pilot point approach for the thin scenario. In general, the bounded pilot point approach also provides satisfactory fit to the measured heads, with slightly higher residuals due to the additional constraints to the model parameters. Table 4-5 summarizes the root mean square errors for the two aquifer thickness scenarios and two inverse simulation approaches.

Similar to the thick scenario, the estimated hydraulic conductivity maps for the thin scenario (Figure 4-22) with the bounded pilot point approach also show essentially the same large-scale spatial patterns as shown in Figure 4-18 (which is obtained from the pure pilot point approach); however, there are significant local variations in magnitude of the estimated hydraulic conductivity values obtained by two inverse simulation approaches.

Figure 4-23 shows the 95% confidence bounds of estimated K values at all pilot points for base case model 4. Like the other three base cases, this graph shows some sensitivity to model parameters as indicated by the variable bound width.



Residual vs. Observed Values
Head

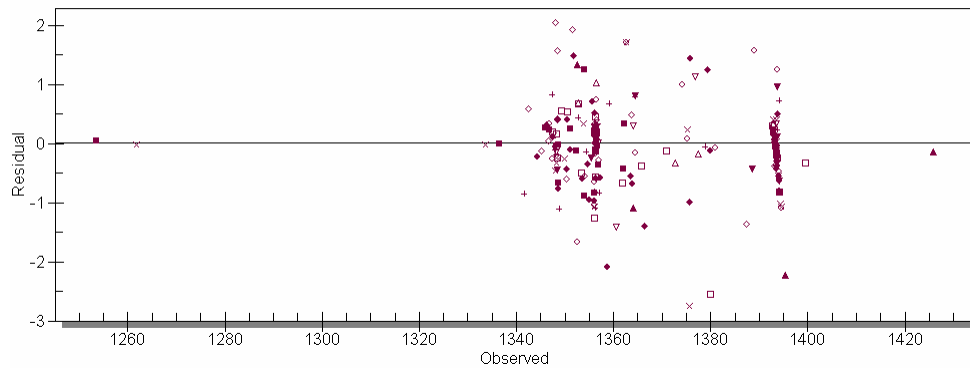


Figure 4-20. Simulated heads (m) in the top layer of the three-dimensional flow model, thin scenario, calibrated with pilot point approach using sedimentary layer bounds (base case model 4). Simulation residuals shown with green bars are less than 2 m and those with yellow bars are from 2 to 3 m.

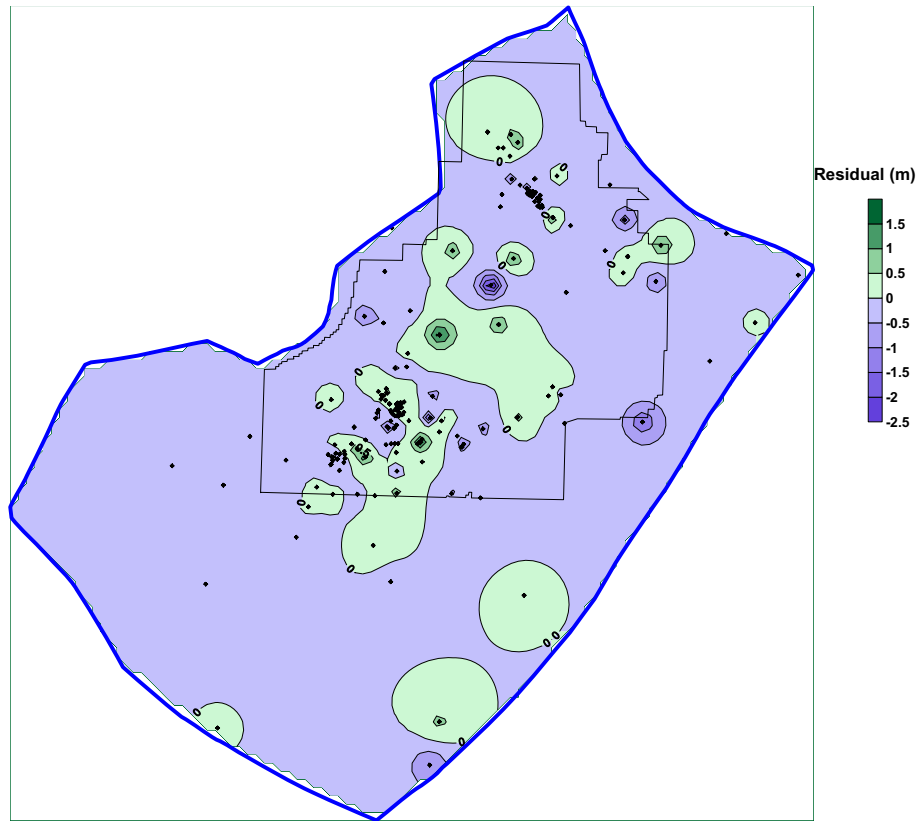


Figure 4-21. Head residuals (simulated minus observed) for all model layers, thin scenario, calibrated with pilot point approach using sedimentary layer bounds (base case model 4).

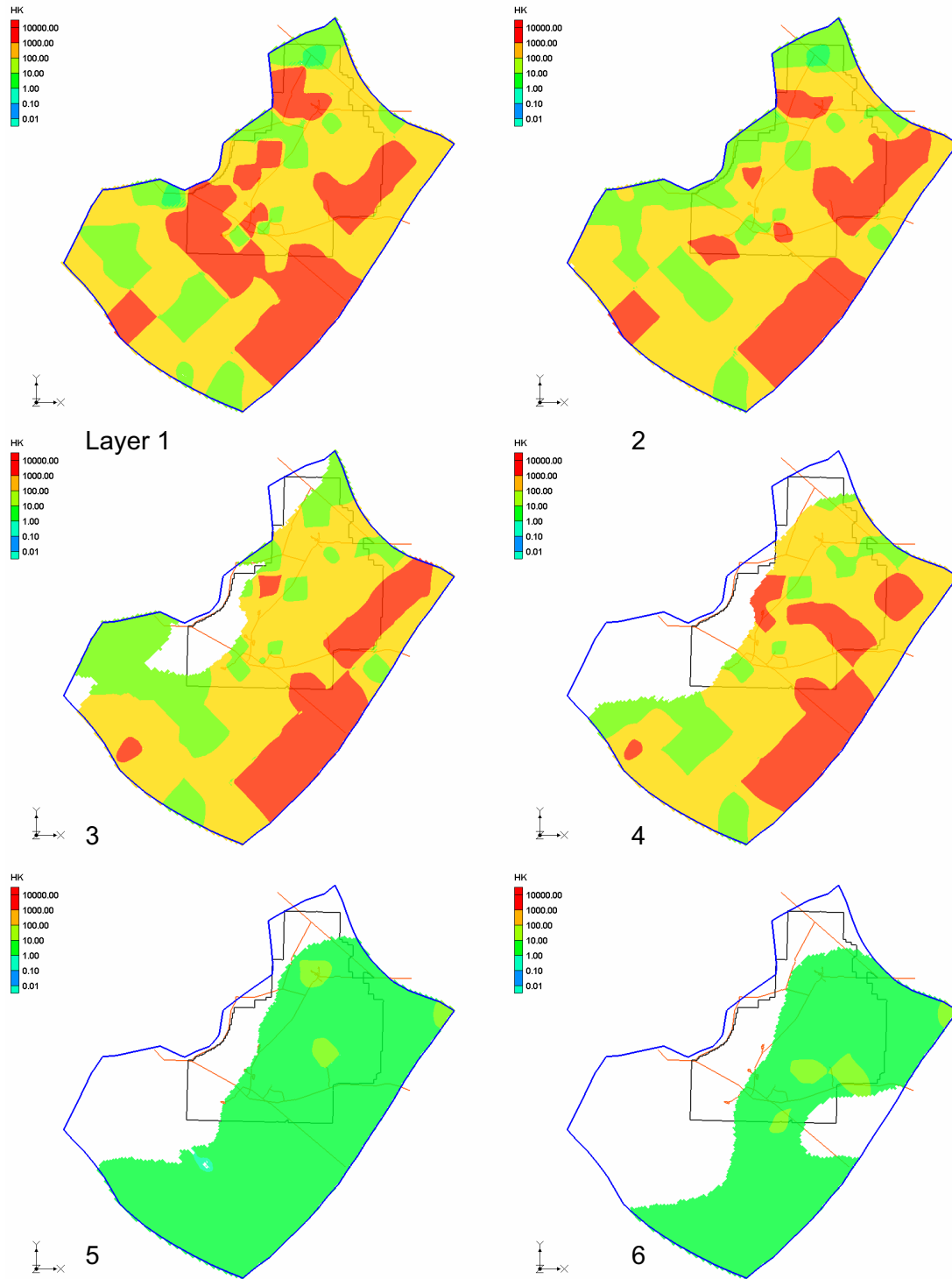


Figure 4-22. Conductivity distribution (m/day) within six model layers for thin aquifer scenario estimated using the pilot point inverse solution approach with sedimentary bounds (base case model 4).

Model 4

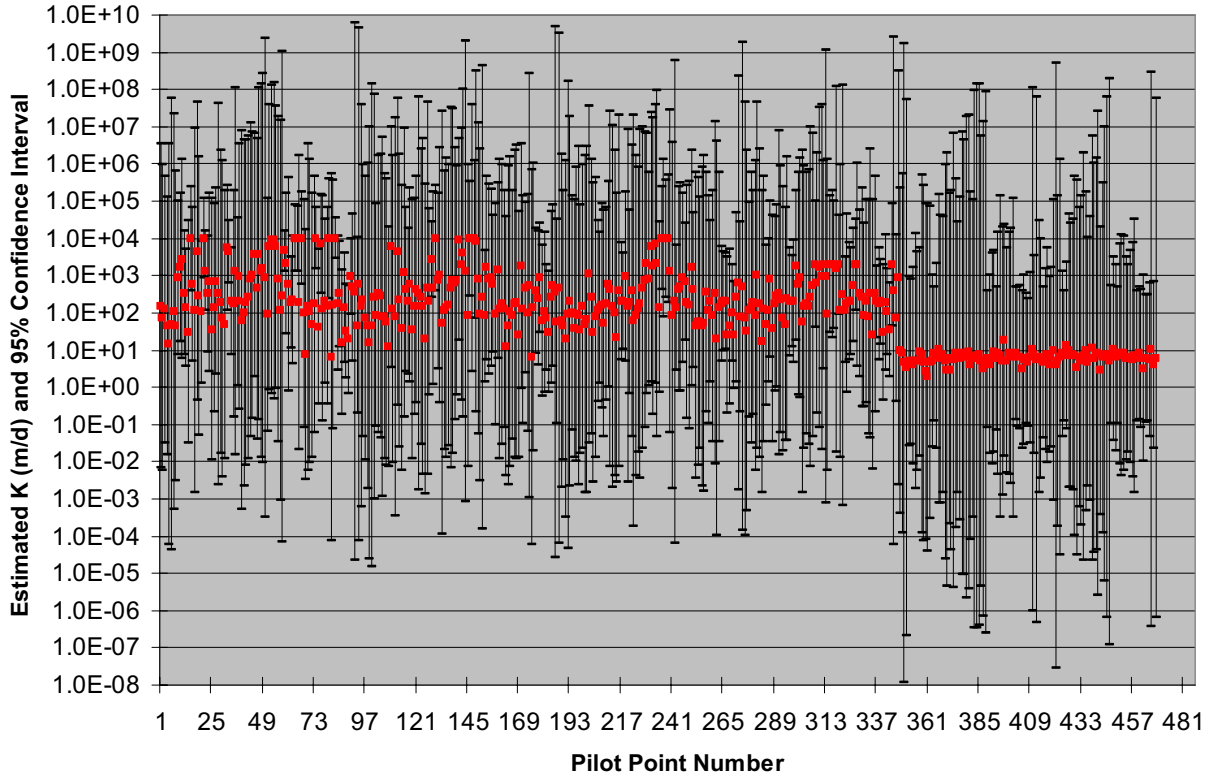


Figure 4-23. Confidence bounds of model parameters estimated by PEST for base case model 4.

4.4.3 Discussion of Inverse Simulation Results

The results of the inverse solution using pure pilot point and bounded pilot point approaches for the thin and thick scenarios results all show satisfactory fits to the measured heads. Table 4-5 summarizes root mean absolute errors between observed and simulated heads for the four base modeling cases of the three-dimensional flow model. All four base modeling cases have rather similar mean absolute errors.

Table 4-5. Summary of root mean square error (meters) for four base model cases.

	Pure Pilot Points	Sediment-Constrained Pilot Points
Thick Scenario	0.713	0.722
Thin Scenario	0.656	0.697

All four scenarios have similar confidence intervals and estimated hydraulic conductivity fields that are generally consistent with known large-scale geological features presented inside the model domain. This is due in part to using the same set of head measurements to calibrate these models. In particular, most of the head measurements are found in the top two layers; thus, the estimated K fields for the top two layers of all four base case models are very similar.

However, there are still local variations of those estimated hydraulic conductivity fields between the thick and thin aquifer scenarios and between the pure pilot point and sediment-constrained pilot point simulations. The sediment-constrained pilot point approach appears to honor some aspects of the geologic conceptual model information. However, from these simulation results alone it cannot be determined which aquifer thickness scenario more realistically represents the actual aquifer based on the inverse simulation results for the four base cases. Therefore, it is necessary to look closely at the simulated groundwater velocities for all four base model cases (see Figure 4-24). For these velocity comparisons, a constant effective porosity of 0.1 was assumed to calculate groundwater velocity for each model grid cell.

Figure 4-24 shows the velocity vector plots within the top model layer for four base cases (red color represents high velocity and blue color represents low velocity). All four cases show significant local variations on the simulated groundwater velocities within the top model layer. All four cases also show similar large-scale velocity distribution pattern, which is quite different from the pattern inferred from geochemical and isotope studies shown previously in Figure 4-4. The two most significant features shown in simulation results of all four base cases include: (1) a long, fast flow channel between the mountain foot and INTEC-RWMC; and (2) an S-shaped, fast flow path immediately east of INTEC. While the S-shaped fast flow path is partially consistent with the Little Lost River fast flow path (see Section 2.2.4), the fast flow channel between the mountain foot and INTEC-RWMC is not. The latter is absolutely contradictory to the conceptual understanding of the hydrogeologic conditions in that area, where it is believed that the groundwater flows extremely slowly as evidenced by isotopic velocity studies. Furthermore, this unrealistic fast flow channel appears on all four base case models, which indicates none of these inverse simulation results would be acceptable for contaminant transport predictions.

As Figure 4-24 shows, the simulated velocities in the upper aquifer for all scenarios do not match the velocity field suggested by geochemical data (see Figure 4-4). The problem with all the scenarios using head-data-only is mainly from this mismatch. The inverse-modeling velocity fields all place a fast flow path through the probable slow zone that is west of the modern Big Lost River floodplain, between USGS-19 and USGS-22. This fast path under the tableland west of the floodplain is not physically defensible: there is one known fossil rift zone, the AEC Butte rift feature, with a documented high-cinder content (Helm-Clark and Link 2006) plus several seemingly-isolated volcanic vents north of NRF, also with high cinder contents. The evidence of USGS-118 and USGS-119 at RWMC as well as the Lava Ridge Rift Zone immediately adjacent to TAN all argue that the presence of copious cinder in the aquifer can impede groundwater flow—so it is a logical inference that the near-vent facies in the NRF tableland will impede groundwater flow. An additional impediment to flow in this area is the south-dipping dammed-river and lacustrine deposits discussed in Appendix B, which will act to refract any groundwater flowing south from Howe and its environs. The velocity results shown in Figure 4-24 also imply that this fast flow path originates slightly to the east of the line defined by USGS-19, USGS-15 and USGS-12, but this is still not probable since the wells in this area show the same or similar south-dipping clayey beds, which again will act to refract and thereby impede groundwater flow.

The tails of the geochemical fast flow paths exiting the Little Lost River and Birch Creek are not obviously present in any of the inverse-model velocity fields and the deep, cold, fast velocity channel as mapped out by Smith (2002) to the east of the New Production Reactor site is conspicuous by its absence, with the exception of a fast spot in the sediment-bounded thin scenario to the east and south of INTEC.

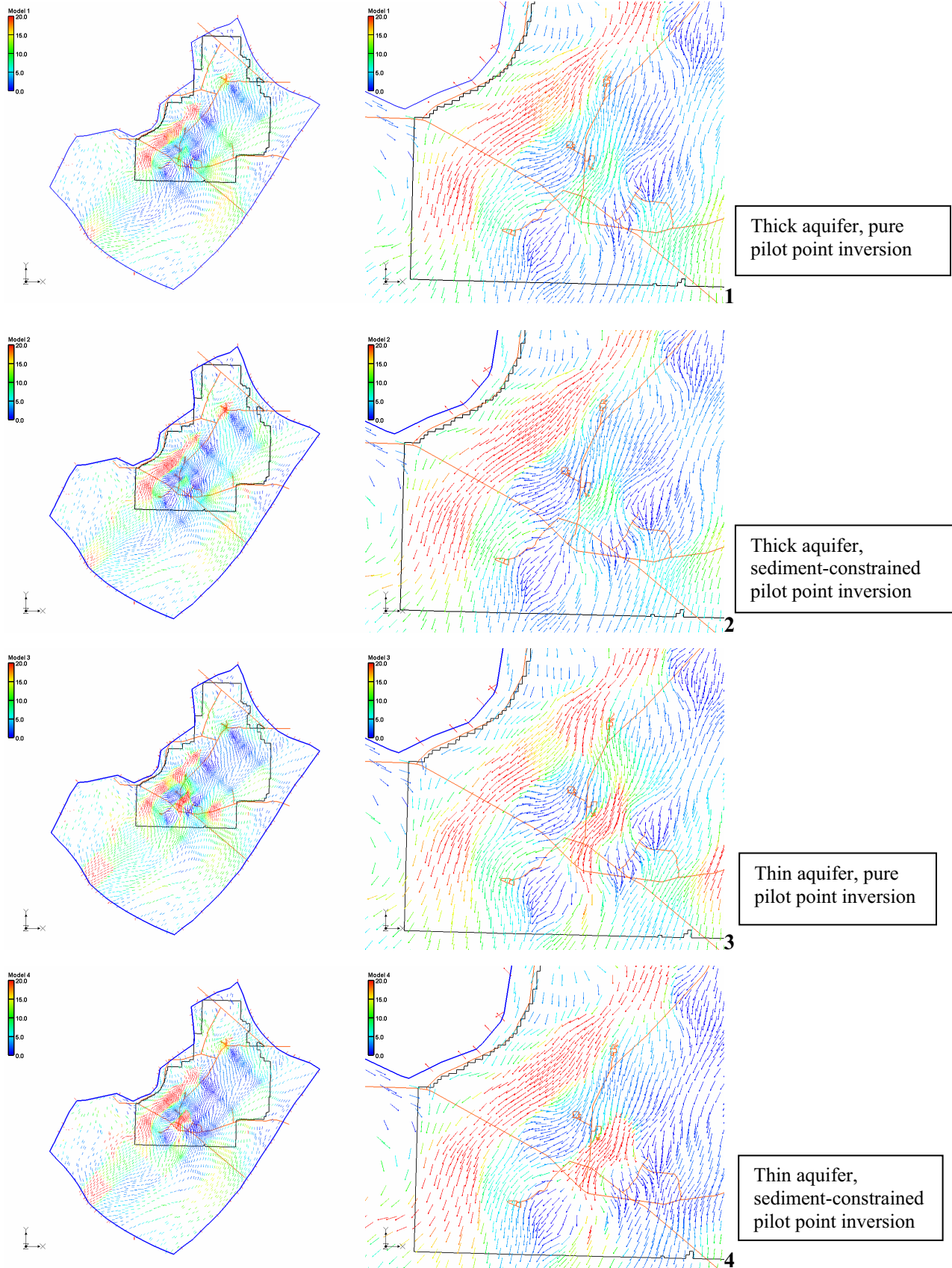


Figure 4-24. Simulated groundwater velocity (m/day) in model layer 1 within the top model layer for models 1 to 4 in order. The outward velocities along some boundaries are an artifact of the Groundwater Modeling System.

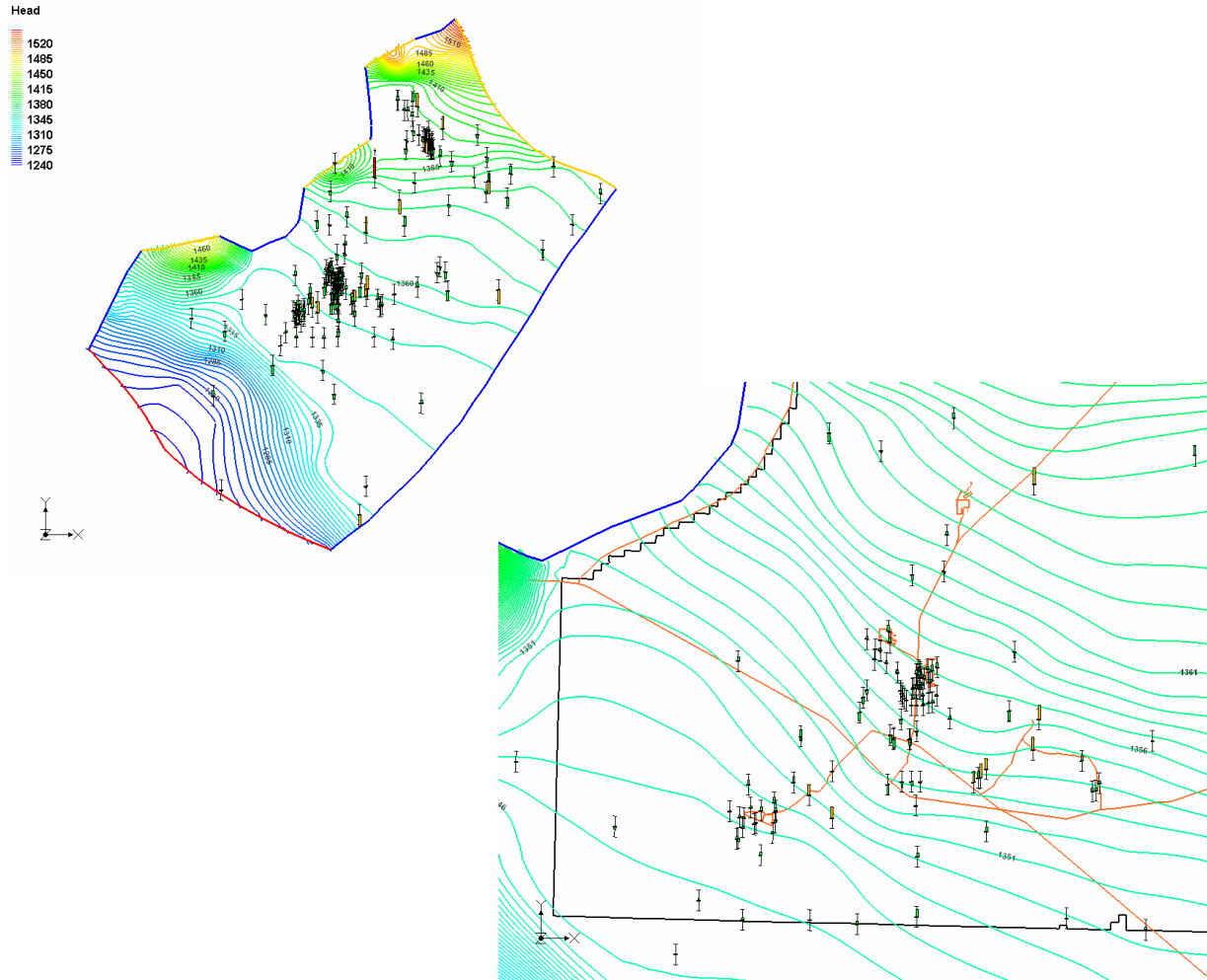
In Figures 4-14 and 4-22, which show the hydraulic conductivity inverse model results for the thick and thin scenarios with sedimentary bounds, it is interesting to note that both of these place a lowered conductivity spot in the upper model layers coinciding with the fissures of the Holocene Hells Half Acre lava field, which may be the effect of copious cinders in this short fissure system. Alternatively, given the uncertainties of the head-only inversion results, this could also be an artifact with no meaning. Given that in all the velocity models, there is increased flow down the Axial Volcanic High and the upper layers of the Arco Rift, the head-only inversions on all the scenarios appear to be reflecting the influence of these important large-scale features. The lack of corresponding increased flow at the Great Rift may be due to the very large amount of ash and cinder in this unusual mafic-to-intermediate volcanic fissure system.

One conclusion that can be drawn is that calibrating the OU 10-08 flow model to just the measured heads is not sufficient to provide a reliable velocity field for contaminant transport modeling, despite all four base cases achieving satisfactory fits to the measured heads. Selecting between the thick and thin aquifer scenarios will be deferred to the three-dimensional transport model and will likely require using additional aquifer thickness data available since that used by Smith (2002). The next section includes a discussion of a joint inverse simulation and results obtained by calibrating the three-dimensional flow model to both measured head and groundwater velocity estimates inferred from geochemical/isotope studies.

4.5 Sensitivity Simulations

4.5.1 Model 2 with Reduced Anisotropy

In the previous four base model cases, a constant vertical to horizontal anisotropy ratio of 100 for hydraulic conductivity was utilized. This large anisotropy value was mainly chosen from the understanding of lava flow structures inside the model domain. To investigate the impact of anisotropy on the inverse simulation results, an inverse simulation was performed with a reduced horizontal to vertical anisotropy ratio of 10 to 1. The base case model 2 (thick aquifer scenario with sediment constraints) was chosen for this sensitivity study. Figures 4-25, 4-26, and 4-27 show the simulated head contour map, residual distribution, hydraulic conductivity maps for each layer and groundwater velocity vector map for the top model layer, respectively. In general, these new inverse simulation results are very similar to their corresponding base case simulation results. However, the reduced anisotropy model has slightly larger mismatches to measured heads. More importantly, the simulated high-velocity channel to the west of NRF, RTC, INTEC, and RWMC now appears lower in magnitude but also spread across a wider portion of the top layer. This portion now joins the S-shaped high-velocity channel east of INTEC, which also shows a lower magnitude. It appears that, due to reduced anisotropy between horizontal and vertical conductivity, more water is able to move across lower layers of this model, thereby accommodating more horizontal spreading of the large flux that previously created the high-velocity channel west of these facilities. The three-dimensional flow model, therefore, shows some sensitivity to the vertical to horizontal anisotropy ratio, which can be further evaluated in the three-dimensional transport modeling.



Residual vs. Observed Values
Head

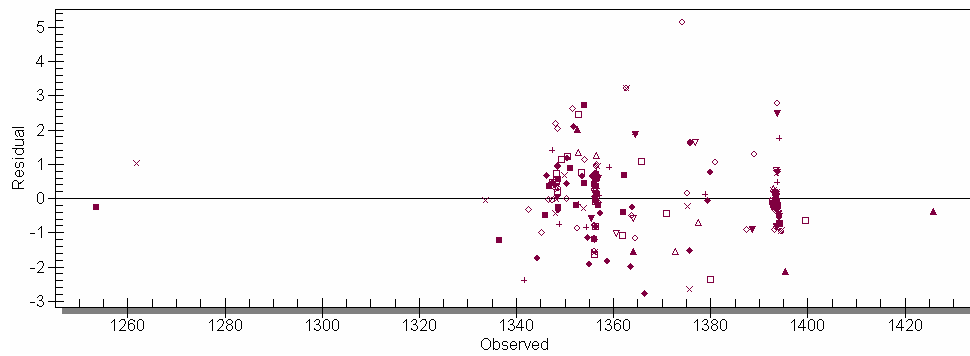


Figure 4-25. Simulated heads (m) in the top layer of the three-dimensional flow model, thick scenario, with reduced anisotropy, calibrated with pilot point approach using sedimentary layer bounds (model 2, reduced anisotropy). Simulation residuals shown with green bars are less than 2 m and those with yellow bars are from 2 to 3 m.

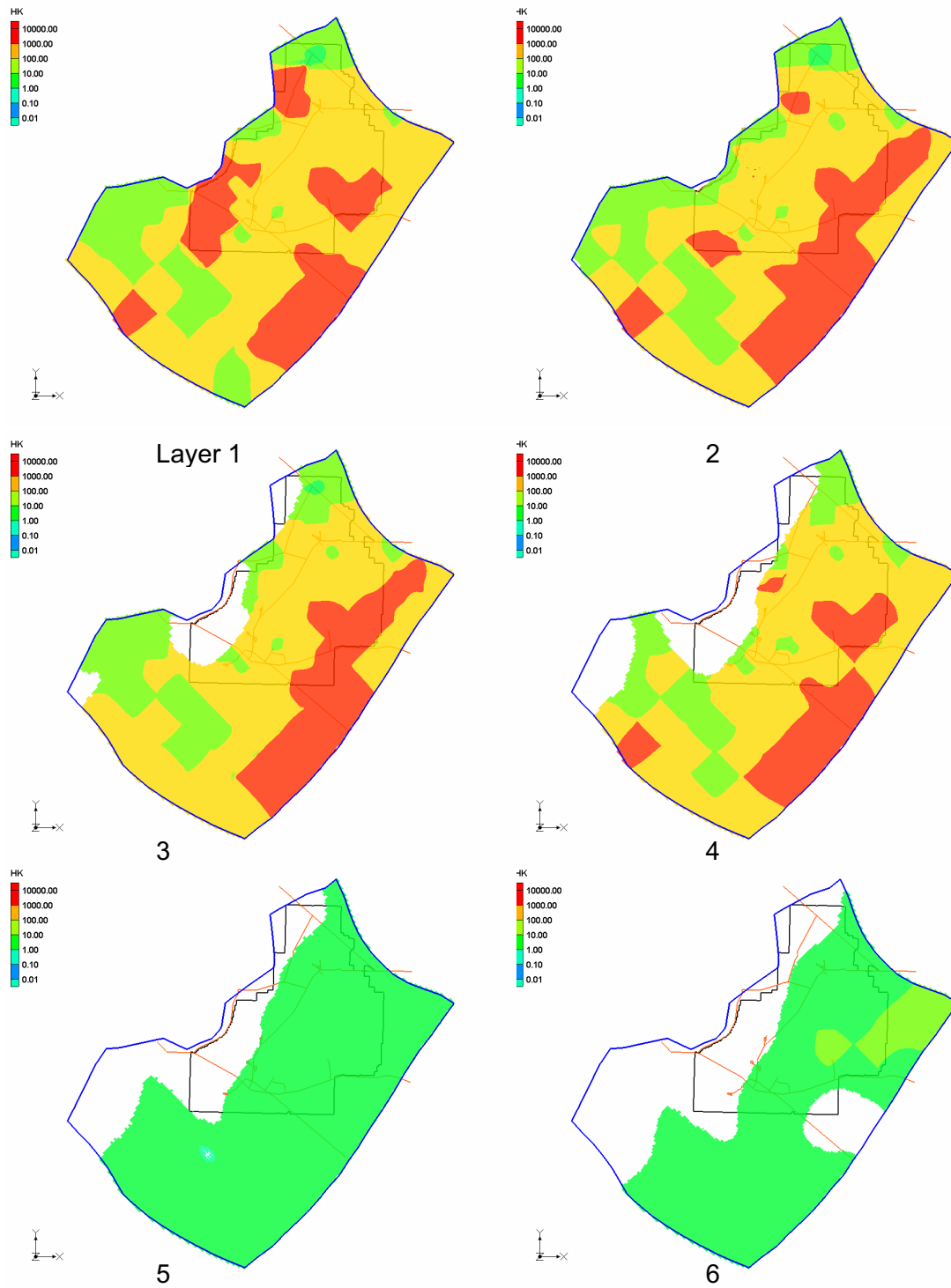


Figure 4-26. Conductivity distribution (m/day) within six model layers for the thick aquifer scenario, with reduced anisotropy, estimated using the pilot point inverse solution approach with sedimentary bounds (model 2, reduced anisotropy).

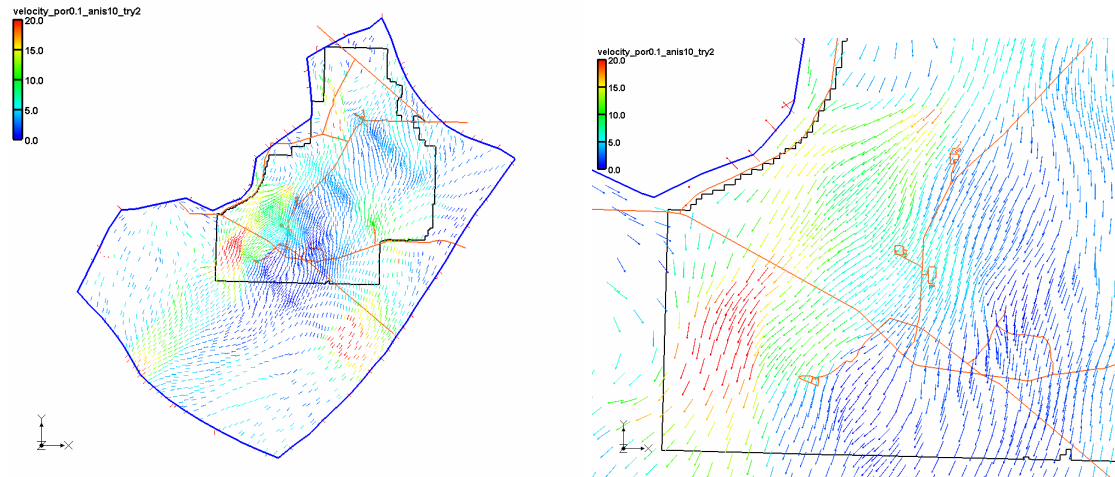


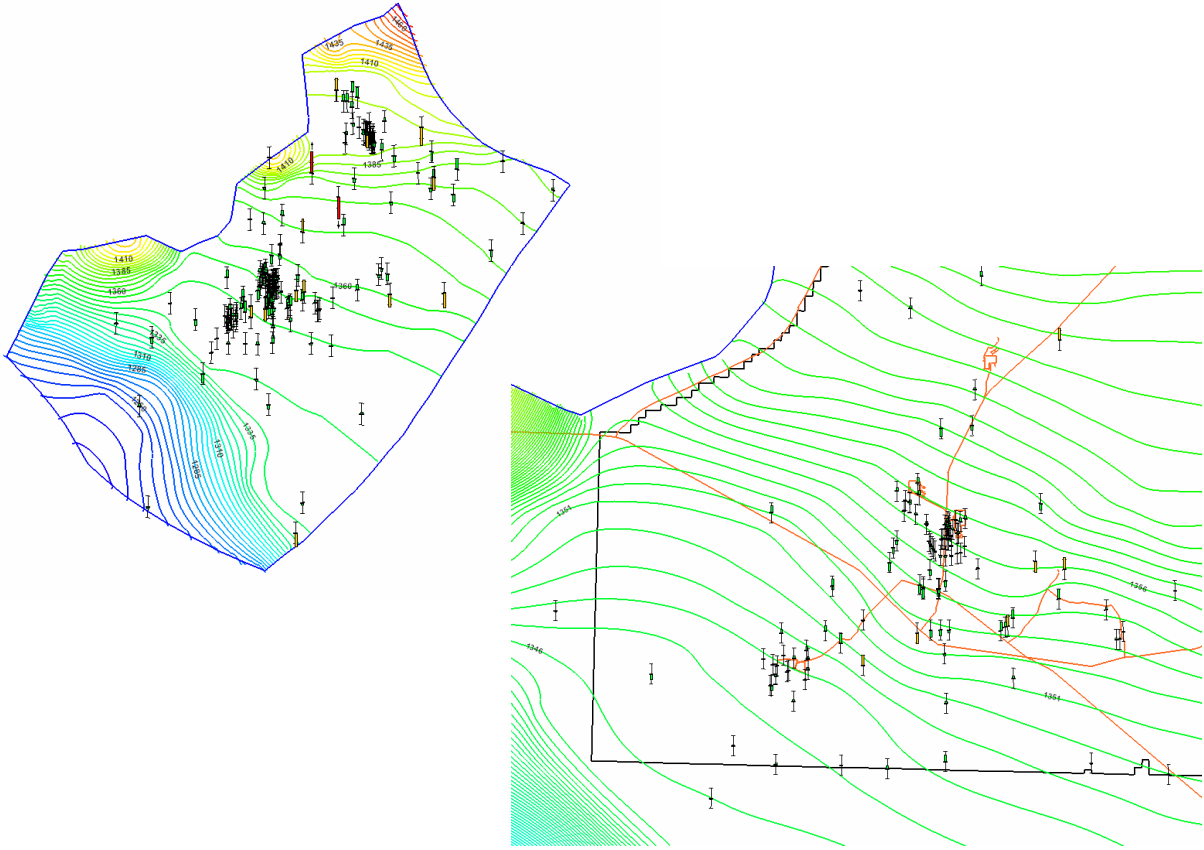
Figure 4-27. Simulated groundwater velocity (m/day) in model layer 1 with reduced vertical to horizontal anisotropy. The outward velocities along some boundaries are an artifact of the Groundwater Modeling System.

4.5.2 Joint Inversion with Measured Heads and Velocity Estimates

As discussed in Section 4.4.3, calibrating the three-dimensional flow model to measured head alone can lead to unrealistic features in the simulated groundwater velocity field, even though the fit to measured heads is satisfactory. A joint inverse simulation was performed using both measured heads and velocity estimates inferred from geochemical/isotope studies as calibration targets (shown in Figure 4-4). This joint inverse run utilizes the base case model 2 (thick aquifer scenario with sediment constraints). In total, there are 28 discrete points obtained from Figure 4-4 assigned as velocity calibration targets. It is assumed that all of these velocity estimates are within the top model layer. This assumption is consistent with the fact that most data for geochemical/isotope studies were sampled from the upper portion of the aquifer. It is further assumed that those velocity estimates are only for horizontal components, since there currently are no vertical velocity estimates.

The objective function is different with velocities added to the calibration. As before, each measured head was assigned a constant calibration weight of 1; each velocity estimate was also assigned a constant weight of 1. These weight assignments resulted in a final contribution to the optimization objective function of 922 from head mismatches and 193 from velocity mismatches. The heads had an approximate order of magnitude larger contribution, but the velocity contribution was still large enough to impact results. Ideally, the two different measurement groups should contribute equally to the objective function; otherwise, the contribution to the objective function is biased more toward the measurement group that is most reliable. Given that the total number of head observations is much larger than that of velocity estimates, which are very uncertain estimates, the ratio of initial contributions to the objective function of these two groups in this joint inversion is not a bad choice. Regularization of the inverted permeabilities was also included in this simulation, as it was in all others.

A constant horizontal to vertical hydraulic conductivity anisotropy ratio of 100 to 1 was used. In addition to hydraulic conductivity values at pilot points, two additional parameters, (1) effective porosity of sediments and (2) effective porosity of fractured basalt, are also estimated during the inverse simulation. Figures 4-28, 4-29, and 4-30 show the simulated head contour map, head residual distribution, and hydraulic conductivity distribution. The joint head-velocity inverse simulation had produced larger head mismatches, but was still within the assigned range of plus or minus 1 m.



Residual vs. Observed Values
Head

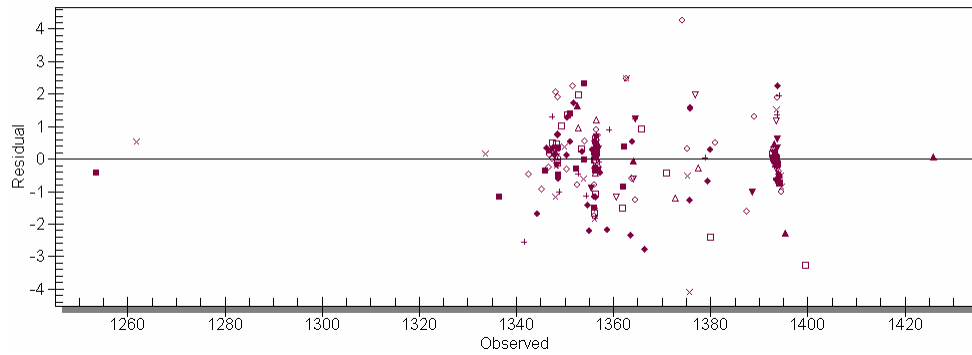


Figure 4-28. Simulated heads (m) in the top layer of the three-dimensional flow model, thick scenario, calibrated jointly with pilot point approach using sedimentary layer bounds and velocity estimates. Simulation residuals are shown with yellow for 2 to 3 m and green for less than 1 m.

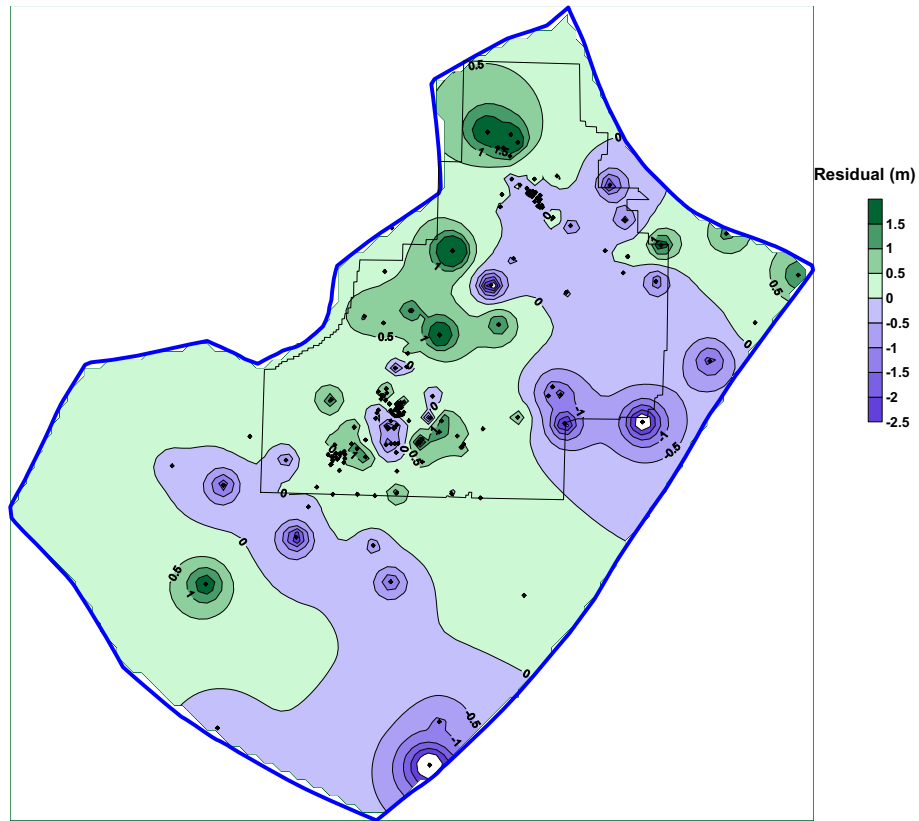


Figure 4-29. Head residuals (simulated minus observed) for all model layers, thick scenario, calibrated jointly with pilot point approach using sedimentary layer bounds and velocity estimates.

The simulated conductivity maps for all model layers in general have similar large-scale spatial features compared to those obtained by calibrating to head measurements alone. However, there is a change on K distribution next to the area west of the INTEC-RWMC area. In the joint head-velocity inverse simulation, the unrealistic high K area next to the west of INTEC and RWMC appearing in all four base cases now disappears due to the addition of velocity calibration targets in this area. The joint head-velocity inverse simulation demonstrates the necessity to incorporate different types of data, such as head and velocity estimate, into the model calibration processes.

Figure 4-31 shows the simulated groundwater velocity vector obtained from the joint head-velocity inverse simulation. Compared with the velocity vectors for all four base case models, the most significant change is that the fast flow channel west of NRF-RTC-INTEC-RWMC facilities disappears in the joint head-velocity simulation, which is more consistent with the conceptual understanding of hydrogeology in that area. However, the fast flow channel seems to be shifted eastward, underneath the Big Lost River and passing through RWMC. Such features might not be physical, and more velocity estimates in this area from the individual WAG facility models will help further constrain the joint inverse simulation. Figure 4-32 shows the point locations where velocities were used for calibration. Table 4-6 compares the model-simulated velocities and velocity estimates for these locations.

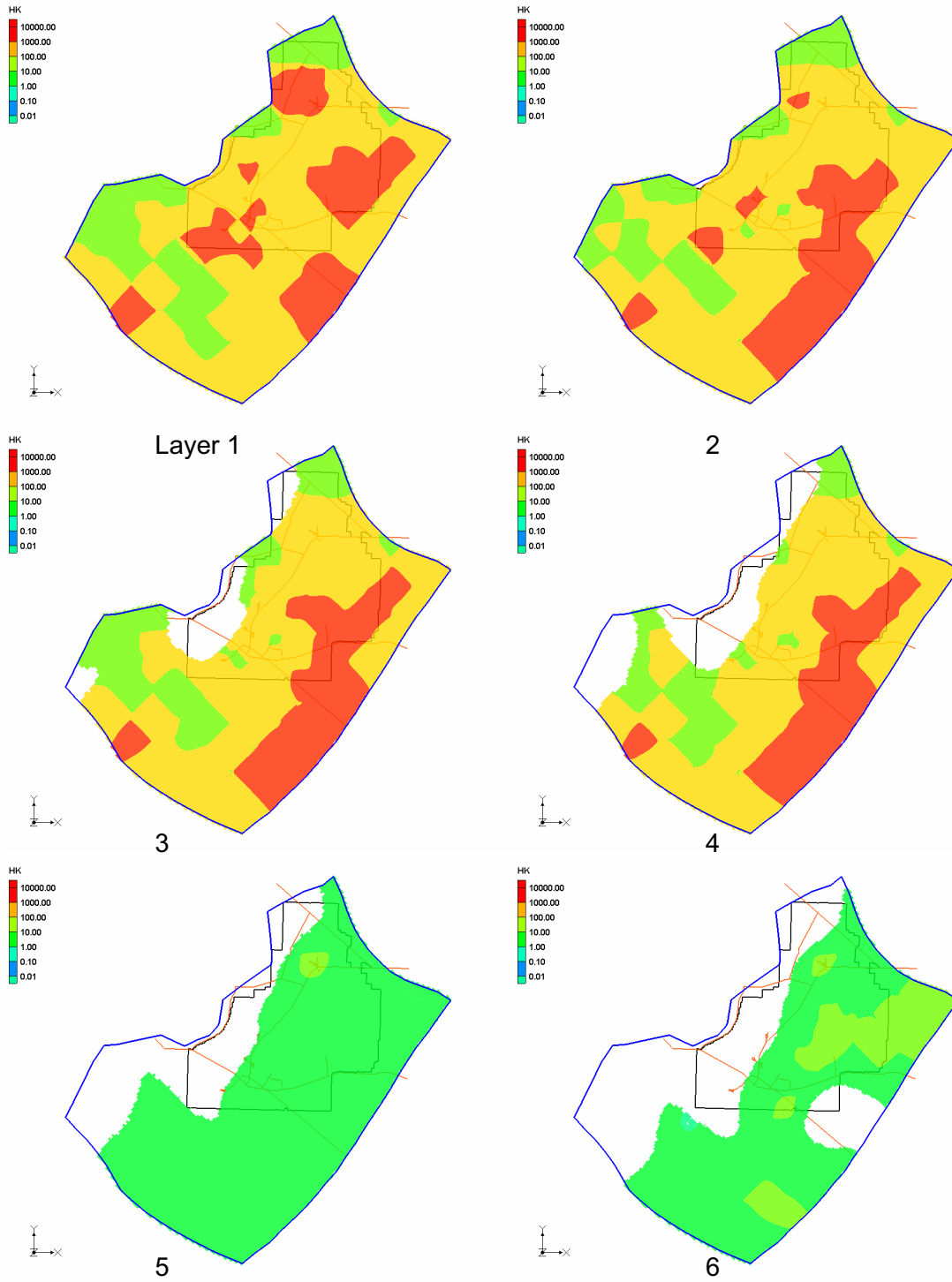


Figure 4-30. Conductivity distribution (m/day) within six model layers for thick aquifer scenario estimated using the joint pilot point inverse solution approach with sedimentary bounds and velocity estimates.

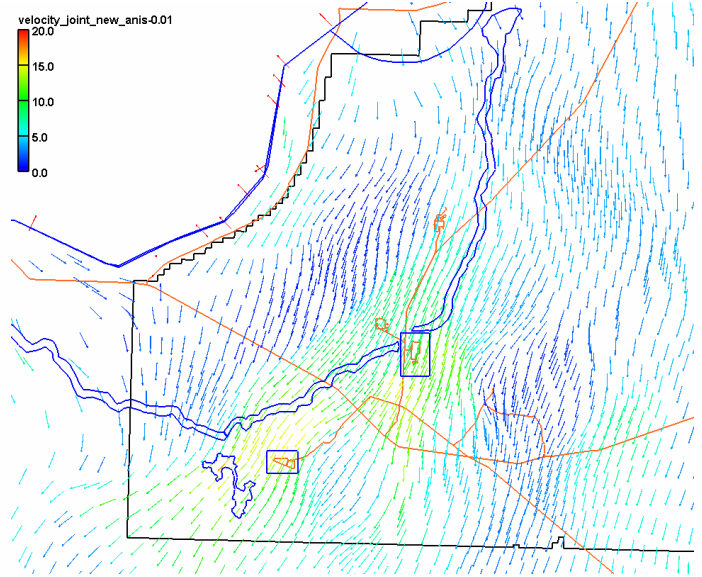
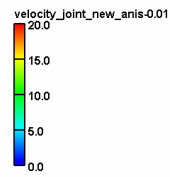
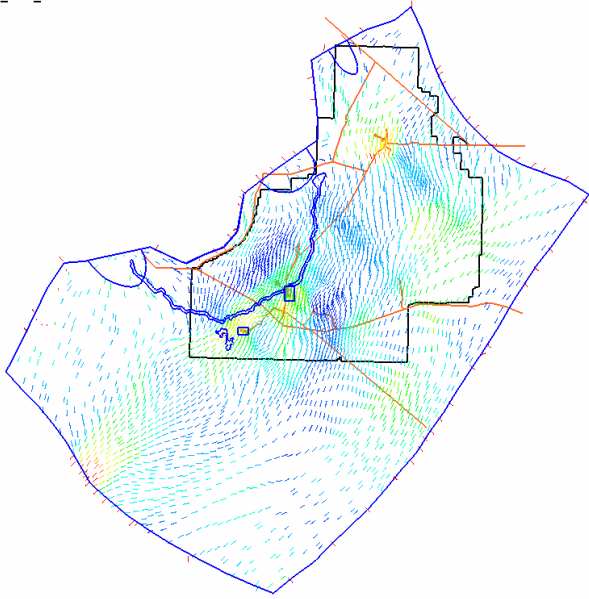
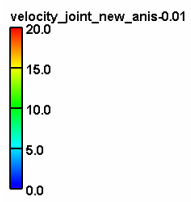


Figure 4-31. Simulated groundwater velocity (m/day) in model layer 1 for joint water level-velocity inverse simulation sensitivity simulation. The outward velocities along some boundaries are an artifact of the Groundwater Modeling System. Compare to interpreted velocities in Figure 4-4.

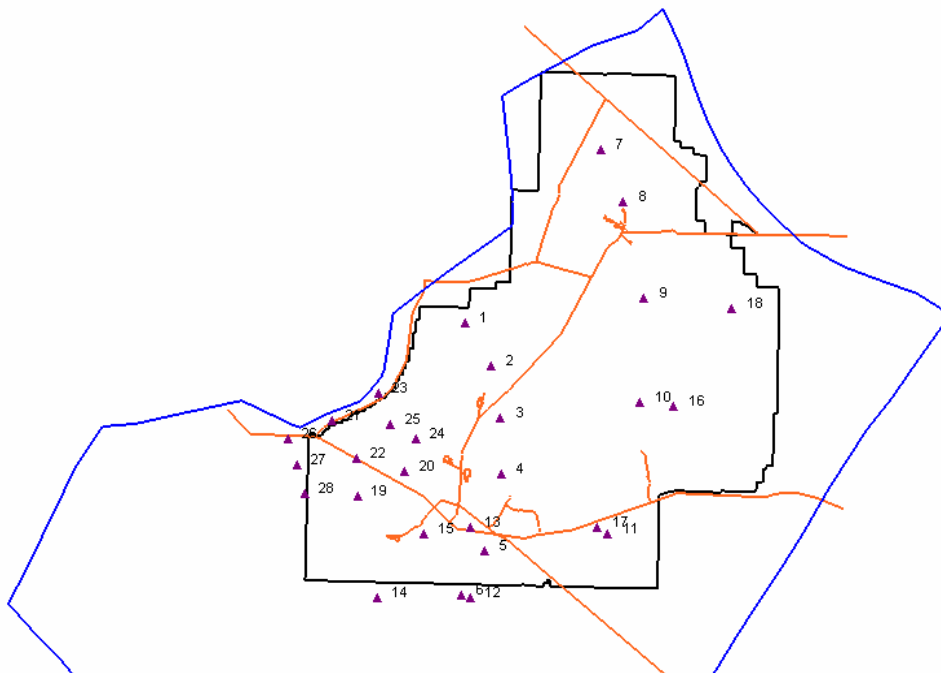


Figure 4-32. Combined points from Figure 4-4 used to compare simulated and estimated velocities.

Table 4-6. Comparison of components of estimated point velocities with results of joint inversion model (values are magnitude in meters per day).

Point	Vx (X component)				Vy (Y component)		
	Measured	Modeled	Residual		Measured	Modeled	Residual
1	0.263	0.835	-0.572		2.587	2.546	0.041
2	1.132	2.023	-0.891		2.341	1.521	0.820
3	2.614	3.303	-0.689		3.028	1.650	1.378
4	3.100	3.221	-0.121		2.528	0.615	1.913
5	2.372	2.342	0.030		1.066	1.304	-0.238
6	2.593	3.771	-1.178		0.190	1.557	-1.367
7	2.314	4.477	-2.163		8.179	1.797	6.382
8	3.700	6.954	-3.254		7.653	4.426	3.227
9	1.699	1.668	0.031		1.968	2.060	-0.092
10	2.015	2.390	-0.375		1.643	1.895	-0.252
11	2.372	2.983	-0.611		1.066	1.387	-0.321
12	4.219	3.569	0.650		4.400	1.710	2.690
13	4.219	3.478	0.741		4.400	2.814	1.586
14	3.636	3.898	-0.262		0.395	1.162	-0.767
15	3.636	2.381	1.255		0.395	0.381	0.014
16	5.363	4.383	0.980		1.159	1.913	-0.754
17	5.363	4.379	0.984		1.159	2.097	-0.938
18	5.363	3.605	1.758		1.159	3.318	-2.159
19	0.200	1.398	-1.198		0.000	0.594	-0.594
20	0.200	1.435	-1.235		0.000	0.145	-0.145
21	0.200	0.753	-0.553		0.000	0.073	-0.073
22	0.200	1.345	-1.145		0.000	0.844	-0.844
23	0.200	2.325	-2.125		0.000	0.577	-0.577
24	0.200	1.532	-1.332		0.000	0.794	-0.794
25	0.200	1.394	-1.194		0.000	0.567	-0.567
26	0.100	-0.366	0.466		0.000	0.847	-0.847
27	0.100	0.040	0.060		0.000	0.436	-0.436
28	0.100	0.482	-0.382		0.000	0.913	-0.913

Given the pattern of impeded flow where there are large amounts of cinder and related near-vent facies, any fast paths through RWMC are not realistic if we assume that the lowered transmissivity zone immediately south of RWMC actually exists as some pump test and head data suggest. The lack of the fast flow path tails originating from the Little Lost River and Birch Creek is still problematic as is the lack of Smith's (2002) deep channel through the New Production Reactor site and its environs immediately to the west. The high-permeability nature of the Axial Volcanic High is still present as is the lowered transmissivity feature roughly corresponding to the postulated Quaking Aspen Butte Rift feature. Given future refinements in model scenarios, the model may actually shed some light on the mostly-unexplored subsurface of features like the Quaking Aspen Butte and Great Rifts, where the modeled lower transmissivity of these features in the south of the model domain may indicate a predominance of fine-grained, near-vent facies at aquifer depths; and such a result would fulfill one of the ultimate goals originally stated in the initial work plan (DOE-ID 2004) for this project (i.e., to provide insight into the geology of areas where data are sparse).

4.6 References

- DOE-ID, 2004, *Idaho National Engineering and Environmental Laboratory Operable Unit 10-08 Sitewide Groundwater Model Work Plan*, DOE/NE-ID-11188, Rev. 0, U.S. Department of Energy Idaho Operations Office, December 2004.
- Dougherty, J., 2004, "PEST Model-Independent Parameter Estimation Users Manual: 5th Edition," Watermark Numerical Computing, July 2004.
- Helm-Clark, C. M., and P. K. Link, 2006, "Sediment-Basalt Architecture, Pliocene and Pleistocene Eastern and Central Snake River Plain," *Eos Transactions, American Geophysical Union*, 87(52), Fall Meeting Suppl., Abs. V51D-1709.
- Hill, M. C., E. R. Banta, A. W. Harbaugh, and E. R. Anderman, 2000, *MODFLOW-2000, The U.S. Geological Survey Modular Ground-Water Model – User Guide to the Observation, Sensitivity, and Parameter-Estimation Processes and Three Post-Processing Programs*, USGS Open-File Report 00-184, Denver, Colorado.
- Smith, R. P., 2002, *Variability of the Aquifer Thickness Beneath the Idaho National Engineering and Environmental Laboratory (INEEL)*, INEEL/EXT-02-01022, Rev. 0, Idaho National Engineering and Environmental Laboratory, August 2002.

5. THERMAL MODELING

5.1 Introduction

Studies of heat flow in the eastern Snake River Plain Aquifer are being conducted to help constrain hydraulic conductivities in the system, particularly in those areas where temperature data are available but solute transport data are not. In those areas, the primary calibration target has traditionally been head data, which are generally confined to the uppermost portion of the aquifer. As Mary Anderson (2005) pointed out in a recent review of groundwater heat flow studies, “it is generally recognized that head data alone are not sufficient to calibrate a groundwater flow model, and information on the movement of solutes and/or heat can help constrain that calibration.”

Information on the movement of heat in groundwater can help constrain aquifer properties because the equations describing heat transport in groundwater are nearly identical to those describing solute transport. Thus, given adequate temperature data and sufficient knowledge of the sources and sinks of heat in the aquifer, temperature distributions can be used to supplant or complement solute distribution data as a means of determining groundwater flow rates and directions. At and beyond the boundaries of the INL, there is considerable data to describe both the horizontal and vertical distribution of groundwater temperature. This stands in marked contrast to solute concentration data, which is essentially available only for the uppermost portion of the aquifer, and only in areas already affected by Site facilities.

Temperature data can be used in a number of different ways to make inferences about groundwater movement. Where sufficient two-dimensional temperature data are available, for example, the shapes of temperature anomalies can be used as indicators of flow direction and discharge rate. Smith (2002) used that approach in the first detailed study of temperatures in the SRPA, successfully identifying broad patterns of groundwater flow in both vertical and horizontal directions and providing the first temperature-based estimates of aquifer thickness based on changes in temperature gradients in deep wells. At another level, analytical methods can be applied to make quantitative inferences about groundwater discharge rates and direction (e.g., Reiter 2001; McCord, Reiter, and Phillips 1992) if vertical temperature profiles are available. Finally, using modern numerical methods, recent studies (Bravo, Feng, and Hunt 2002) have accomplished what Stallman (1965, 1967) suggested: “that head and temperature measurements could be used jointly in numerical models to solve the inverse problem for groundwater flow and hydraulic conductivity.” While that approach is the primary goal of heat flow studies of the OU 10-08 project, a number of preliminary studies have been conducted as the necessary precursors to a full three-dimensional joint-inversion modeling effort. These include the aforementioned analytical methods of inferring groundwater discharge from temperature profiles, several two-dimensional modeling studies that examine controls on the evolution of temperature along a flow line in a high-velocity system, and a three-dimensional study aimed at identifying the major heat sources and sinks in the region.

This section presents results of several groundwater flow and heat transport modeling applications. Section 5.2 contains results from a preliminary two-dimensional vertical model. Section 5.3 presents groundwater flow and heat transport results for a three-dimensional regional model of the entire SRPA, and for a subregional model using a flow model developed in Section 4.

5.2 Two-Dimensional Heat Flow Modeling Studies

Several two-dimensional heat transport simulations were conducted in 2006 to examine how certain parts of the aquifer system could be expected to behave in a high-conductivity aquifer like the SRPA. This section describes results from a two-dimensional cross-sectional model that was used to

illustrate the evolution of the vertical distribution of temperature along a flow line under idealized conditions.

5.2.1 Two-Dimensional Modeling and Evolution of Temperature Profiles along a Flow Line

Temperature profiles in the eastern Snake River Plain commonly display nearly isothermal conditions through what is interpreted as the aquifer. To illustrate how temperatures evolve in the hypothetical two-dimensional cross-sectional model of groundwater and heat flow and, therefore, how the nearly isothermal conditions observed in the eastern Snake River Plain might develop, the two-dimensional (cross-sectional view) steady-state heat flow equations (Equation 5-5) were solved for an idealized groundwater flow system. The system considered includes a vadose zone, aquifer, and subaquifer. The hydraulic conductivity of the saturated subaquifer unit is assumed to be insufficient to allow significant convection. Heat transfer in the subaquifer is therefore by conduction only. The subaquifer is included primarily to illustrate the background geothermal gradient. Heatflow in the overlying aquifer, in contrast, occurs both by conduction and advection, with the latter specified by the specific discharge in the x-direction. There is no water flow in the y-direction. A vadose zone overlies the aquifer. To maintain a 1-D flow system in the aquifer, heat conduction in the vadose zone is also simulated as conduction without convection. Numerical solution to the problem is found using the PDE Toolbox in MATLAB.

The bottom boundary condition is most easily specified as the geothermal heat flux. While the average crustal heat flux is about 60 mW m^{-2} , a value of 100 mW m^{-2} is specified, which is closer to that observed in the eastern Snake River plain. The upper boundary is the ground temperature at the top of the vadose zone, which, in arid regions, is typically several degrees higher than mean annual air temperature. In these simulations, in which the primary interest is the change in the temperature field along a flow line, a temperature of zero is specified along the entire upper boundary. At the downstream boundary, a zero-gradient condition is specified, so that the only heat flux is the convective heat flux. The remaining upstream boundary condition is a primary influence on the overall temperature distribution of the system. The temperature at this upstream boundary was specified the same as that of the upper boundary, which simulates a system where cold recharge occurs. Thermal properties used in the simulation are the bulk thermal conductivity and the heat capacity of water, which were assigned values of $2 \text{ watt m}^{-1} \text{ K}^{-1}$ and $4.186\text{E}06 \text{ joules m}^{-3} \text{ K}^{-1}$, respectively.

Given sufficient distance along a flowline, when the heat flux is along the bottom of the system, the temperature gradient will evolve so that heat flux from the top of the aquifer balances that into the aquifer from below. The final temperature field within each unit will thus be such that the product of the vertical thermal conductivity and the vertical temperature gradient will equal the heat flux supplied to the bottom of the aquifer. The distance required to produce that condition is thus proportional to the temperature difference between the initial condition and the final temperature and inversely proportional to the groundwater velocity (Figure 5-1).

If the groundwater temperature at the inflow boundary is less than the mean temperature when the heat flux is entirely upward, the horizontal temperature gradient and the second derivative in the vertical direction will both be positive. Both of these gradients will decrease with distance, until the horizontal temperature gradient is virtually zero and the vertical temperature gradient is uniform. As the accuracy of the specific discharge calculated from application of Equation 5-5 depends on how accurately those values can be determined, the distance along a flowline beyond the point where the temperature profile is externally influenced clearly affects the accuracy of that approach.

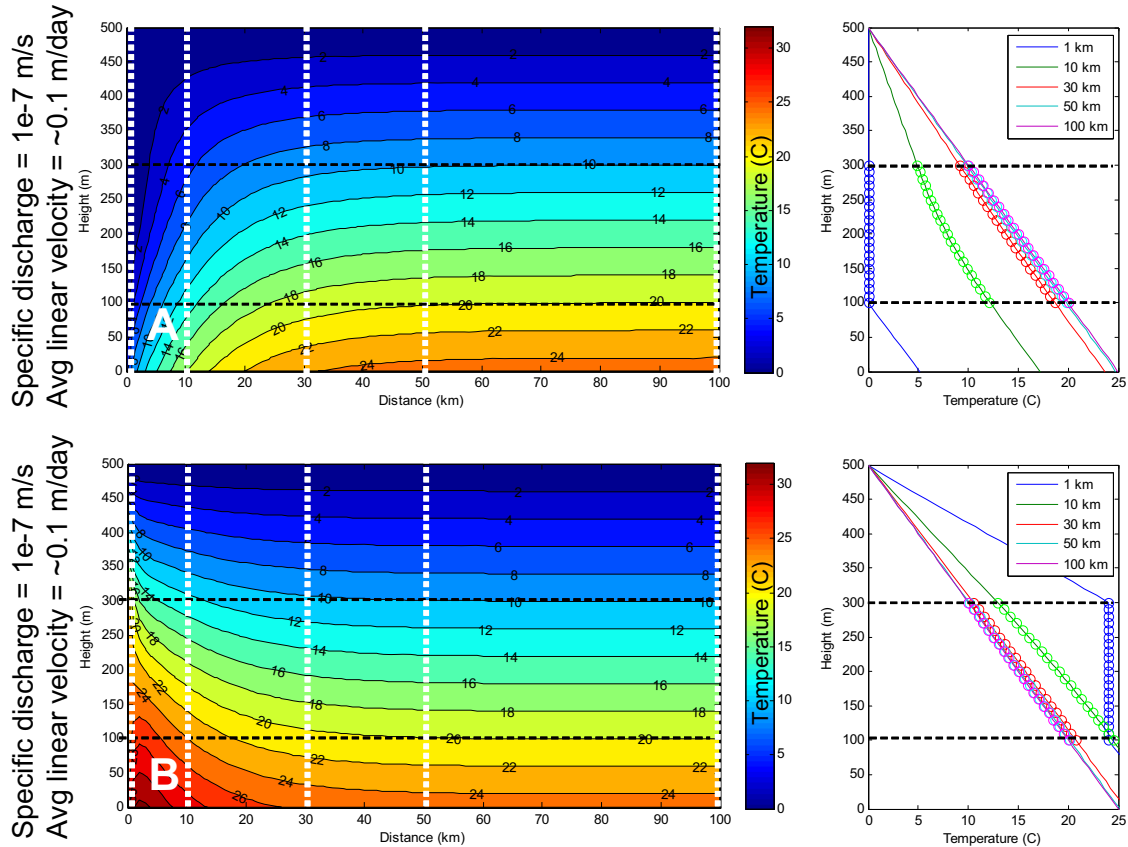


Figure 5-1. Evolution of temperature distribution (contour plots) along a flow line in an idealized two-dimensional system, with (A) inflow temperatures colder than the steady-state profile for conduction-dominated flow and (B) inflow temperatures warmer than the steady-state profile for conduction-dominated flow. Line plots show temperature profiles at the specified distances along the flow line (indicated by vertical dashed white lines in the contour plots). Dashed horizontal lines show top and bottom of aquifer domain.

If the inflow temperature is greater than the average groundwater temperature under conduction-dominated conditions, then the increased heat flux through the vadose zone will cool the system until the temperature distribution again approaches that necessary to conduct all the heat flux upward. The distance needed to reach the zero-horizontal gradient condition is the same as for the previous case.

Whether water temperatures are increasing or decreasing, the temperature profiles are isothermal only very close to the upstream boundary, where the heating from below has not been sufficient to significantly change the uniform temperature of the inflow. Approximately isothermal profiles in the SRPA appear to occur, however, throughout the aquifer, and are difficult to explain as a simple result of high discharge rates (Figure 5-2A), as is commonly stated (Brott, Blackwell, and Ziagos 1981). One adjustment to the flow regime that may resolve this discrepancy is substantial transverse dispersivity. The simulation depicted in Figure 5-2 reflects a horizontal seepage velocity of approximately 1 m/day-1. Assuming a transverse dispersivity of 10 m effectively triples the thermal conductivity within the aquifer and yields temperature profiles (Figure 5-2) much more similar to those of deep wells through the aquifer. As several studies indicated that the longitudinal dispersivity in the aquifer is on the order of 100 m (Robertson 1974; Goode and Konikow 1990), this may not be an unreasonable estimate of the vertical mixing that occurs across large distances.

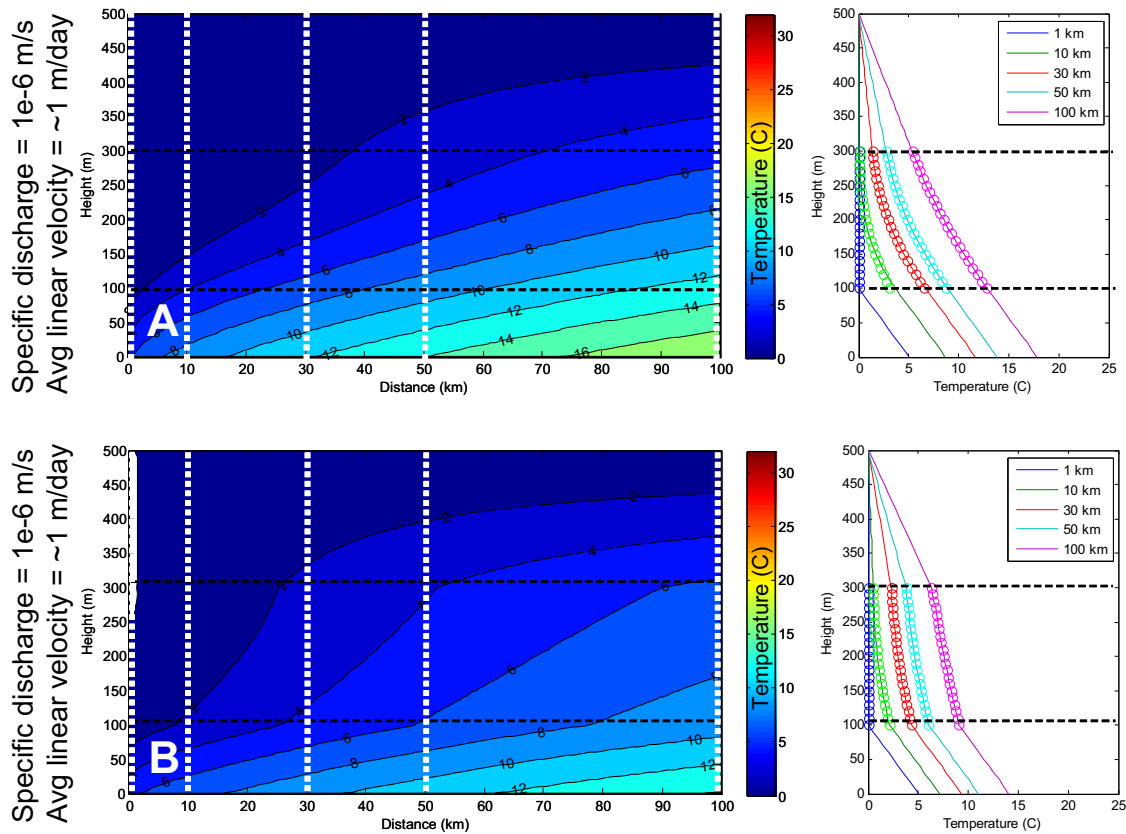


Figure 5.2. Effect of a 10-fold increase in velocity (A) and an increase in vertical thermal conductivity (B) on the evolution of temperature profiles in the two-dimensional system described in the text. The increase in thermal conductivity (B) is approximately what would occur with a transverse dispersivity of 10 m. Line plots show temperature profiles at the specified distances along the flow line (indicated by vertical dashed white lines in the contour plots). Dashed horizontal lines show top and bottom of aquifer domain.

5.3 Three-Dimensional Heat Flow Modeling

5.3.1 Phase 1 - Heat Flow Modeling of the Regional Aquifer

The primary goal of heat flow modeling is to use joint inversion modeling methods to estimate hydraulic conductivity from known heads and known temperatures. To that end, the primary heat flow modeling task is to develop a subregional three-dimensional groundwater flow and heat flow model for the INL Site that can be repeatedly run to fit simulated heads and temperatures to observed heads and temperatures by adjustment of the three-dimensional hydraulic conductivity field. Prior to development of a three-dimensional heat and groundwater flow model for the INL study area, however, groundwater flow and heat transport modeling was conducted on a larger scale to attempt to identify the primary controls on groundwater temperature distribution in the region, which is a necessary precursor to identifying boundary conditions for the subregional scale model. The entire SRPA was selected as the domain for this large-scale study, which is advantageous for several reasons:

- The natural boundary conditions for the larger aquifer are easier to define than for a subsection of the system, because recharge rates and recharge temperatures are generally better known

- It allows comparison with simple two-dimensional models cross-sectional models of large-scale aquifer behavior developed by previous authors (Brott, Blackwell, and Ziagos 1981)
- It tests our ability to model the temperature field of a large system with a wide variety of boundary conditions for both heat and groundwater flow
- It allows use of the detailed groundwater modeling data set developed for the Idaho Water Resources Research Institute (IWRI) groundwater model.

The SRPA heatflow study was conducted concurrently with the two-dimensional (in-the-horizontal-plane) groundwater modeling study but was independent of that work because heat flow modeling in groundwater requires consideration of the vertical movement of heat. To simulate heat and groundwater flow in the SRPA, the USGS simulation package HST3D (Kipp 1997) was utilized, using the Argus Open Numerical Environment, and Richard Winson's HST3D extension to Open Numerical Environment, as a preprocessing environment.

5.3.1.1 Model Description

5.3.1.1.1 Confined Flow—While the SRPA is an unconfined aquifer, the system can be approximated as a confined system when transient storage effects of a changing water table can be neglected and when the slope of the water table is nearly constant over large distances. Also, as this investigation of heat flow in the system focuses on understanding the primary controls on temperature distribution rather than on analyzing temperature distribution as a means of constraining aquifer properties, the accuracy of the flow calculations is a secondary consideration.

5.3.1.1.2 Horizontal Boundary Conditions and Domain—The horizontal dimensions of the system (Figure 5-3) were chosen to match the natural boundaries of the aquifer. That is the Snake River along the southwestern and southern margins, and the mountain front along the northern and northeastern margins. The rectangle enclosing the domain is divided into 65 columns by 27 rows, yielding approximately 5 km × 5 km grid cells. The domain is divided into 26 layers.

5.3.1.1.3 Vertical Boundary Conditions and Domain—The available boundary conditions for the model largely define the required vertical domain for the system. In this case, the best available information to define heat-flow boundary conditions are (a) the heat flux below the bottom of the aquifer, and (b) the temperatures at the land surface. Heat flux at the bottom is readily specified as a Neumann condition at the bottom of the system. Consistent with previous heat flow studies of the aquifer, an upward geothermal heat flux of 110 mW m⁻² was defined, which is expected to be relatively uniform within the SRPA.^e Ground temperature was chosen as the land surface boundary condition because it can be reasonably accurately estimated from a combination of abundant air temperature data and limited ground temperature measurements. Specification of temperature at the land surface forces temperatures at the surface of the aquifer to evolve so that the upward heat flux through the aquifer matches the upward heat flux defined by the temperature gradient between the aquifer and the land surface and the thermal conductivity of the vadose zone.

e. Communication with D. Blackwell, Southern Methodist University, February 2006.

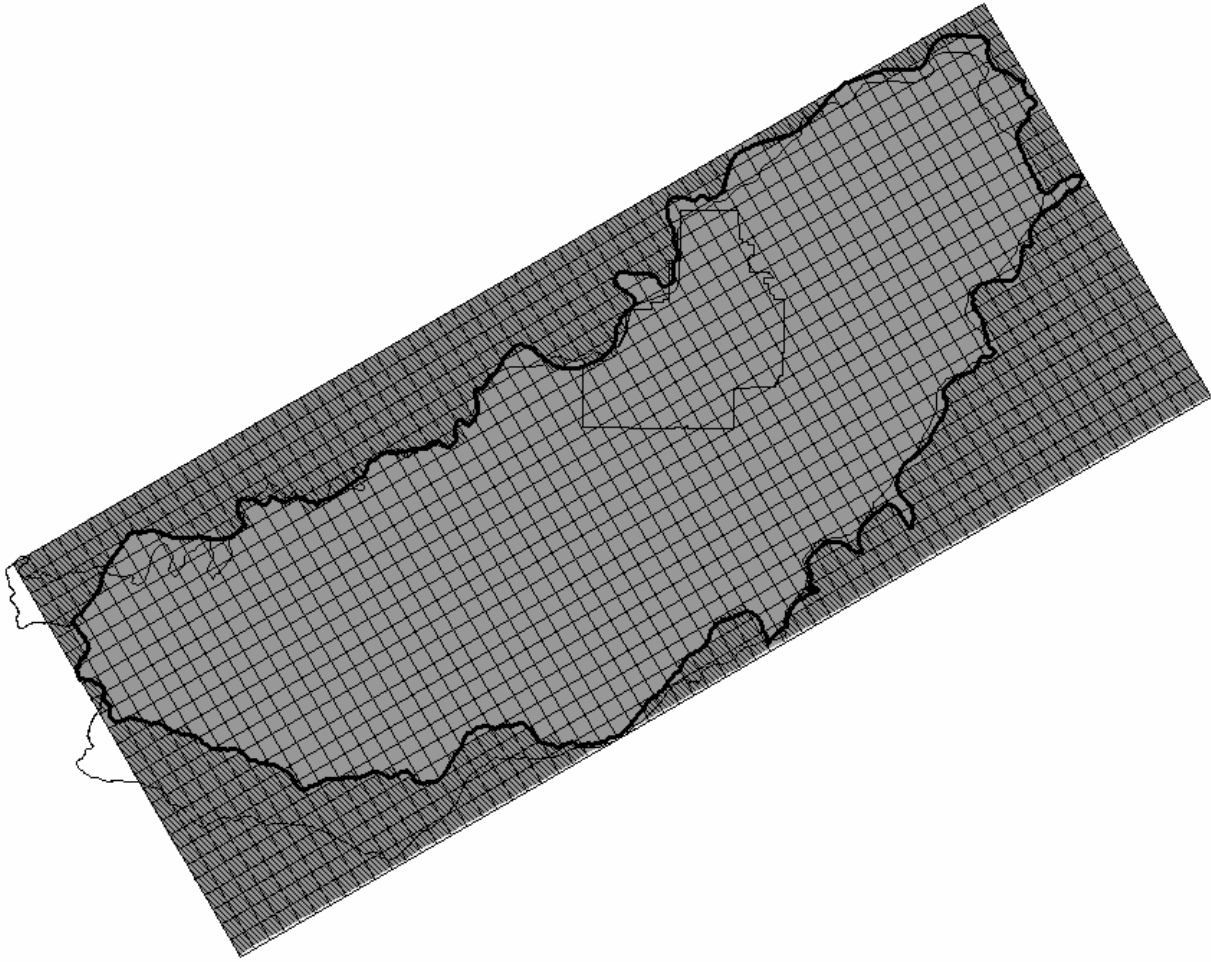


Figure 5-3. Horizontal extent (heavy black line) and grid dimensions of the SRPA heat flow model. Thin black lines show the boundaries of the full aquifer and the INL.

5.3.1.1.4 Subaquifer—The bottom of the system was chosen as the elevation of the deepest point in the aquifer, because it allows assignment of the geothermal heat flux to a single model layer. This requires that cells below the aquifer, but above the elevation of the bottom layer, assigned subaquifer properties that allow transfer heat by conduction but not by advection. That condition is imposed by assigning very low horizontal and vertical conductivities of (1E-15 and 1E-16 m/day, respectively) to the subaquifer.

5.3.1.1.5 Unsaturated Zone—The top of the system was chosen as land surface. Using a land surface boundary condition requires including the vadose zone overlying the aquifer in the simulation domain. This had to be performed in a manner that allowed heat transfer both by conduction and, where downward vertical water fluxes are significant, by advection. Because simulation of unsaturated flow is not an option in HST3D, the vadose zone was simulated as a saturated unit, with low hydraulic conductivities in horizontal directions to preclude horizontal advection of energy. Specified heads were increased proportionally across the system to maintain saturation in the vadose zone. This increases the absolute pressure across the aquifer by that constant value, but does not otherwise affect the head distribution or velocities within the simulation domain.

Because the potential advective transfer of heat exists only along the vertical axis, horizontal advective heat transfer was limited by imposing very low hydraulic conductivities in the horizontal plane. In the vertical direction, the advective term was assigned by defining the vertical flux and the associated water temperature. In order that these fluxes do not alter the pressure distribution in the aquifer, vertical conductivities were specified that are high enough that the pressure gradient is negligible within the saturated-unsaturated zone.

Inclusion of vadose zone heat transport is only necessary where there is significant downward recharge. At recharge locations, the desired boundary condition is the heat flux prescribed by the recharge rate and the mean annual temperature at the land surface. In some areas, groundwater pumping and surface irrigation occur simultaneously, and where the pumping rate from a given cell is larger than the recharge due to irrigation, the net groundwater flux, and therefore heat flux, is assumed to be upward and dependent primarily on the net upward water flux. In these areas, the upward heat flux is essentially the product of the water temperature, water flux, and the heat capacity of the water, and the flux boundary condition is imposed at the upper surface of the aquifer. Thus, except over areas where the IWRRI model specified a net upward flux, the model domain extends vertically from an elevation of 700 m to the land surface. A three-dimensional representation of the model domain is provided as Figure 5-4.

5.3.1.1.6 Thermal and Hydraulic Properties Summary—Horizontal hydraulic conductivities for the regional heat flow model were taken directly from the IWRRI model (Cosgrove, Contor, and Johnson 2006). Vertical hydraulic conductivities within the aquifer were calculated from the horizontal conductivities, assuming a vertical anisotropy (K_h/K_v) of 10. Hydraulic conductivities in the remainder of the model were assigned, and these values are summarized in Table 5-1. For heat transport, a porosity of 0.1 was assumed for the entire model domain. The applied thermal conductivity and specific heat values for water were $0.461 \text{ watts m}^{-1} \text{ }^\circ\text{C}^{-1}$ and $4.186\text{E}06 \text{ joule m}^{-3} \text{ }^\circ\text{C}^{-1}$. For the solid media, representative values for basalt were applied ($2 \text{ watts m}^{-1} \text{ }^\circ\text{C}^{-1}$ and $2.3\text{E}06 \text{ joule m}^{-3} \text{ }^\circ\text{C}^{-1}$). Similar properties were chosen for each medium to emphasize, in the results, the effects of convection, rather than differences in conduction.

Table 5-1. Hydraulic conductivities in the remainder of the model.

Stratum	K_h , or Source	K_v	α_L	α_T
Vadose zone	1e-18	high	0	0
Aquifer	K_h from IWRRI model	$K_h/10$	100 m	10 m
Subaquifer	1E-18	$K_h/10$	0	0

IWRRI = Idaho Water Resources Research Institute

5.3.1.1.7 Recharge—Recharge to the aquifer, whether from precipitation, river leakage or irrigation is a primary source of heatflow to the system. The IWRRI modeling study (Cosgrove, Contor, and Johnson 2006) of the aquifer included a detailed analysis of the recharge to the aquifer and data from that study was used as the recharge input to the groundwater and heat flow model. The recharge map (Figure 5-5) includes natural infiltration from the balance of precipitation and evapotranspiration, recharge from tributary flows on to the Snake River Plain, recharge due to irrigation, and negative recharge due to groundwater pumping.

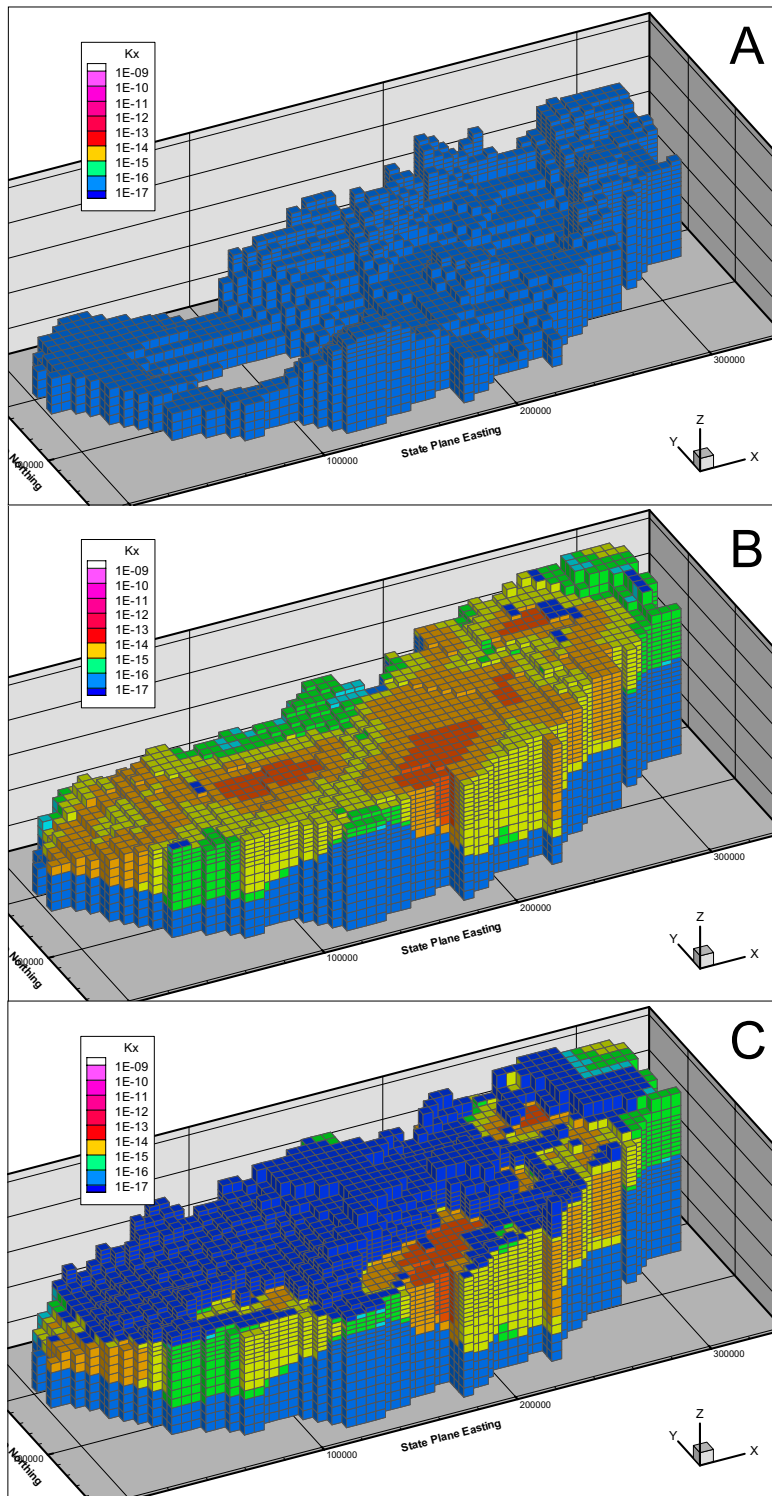


Figure 5-4. Perspective views of the three-dimensional heat and groundwater flow model grid illustrating (A) shape of the subaquifer, (B) combined shape and hydraulic conductivity distribution of the aquifer, and (C) vadose zone cells overlying the aquifer - subaquifer.

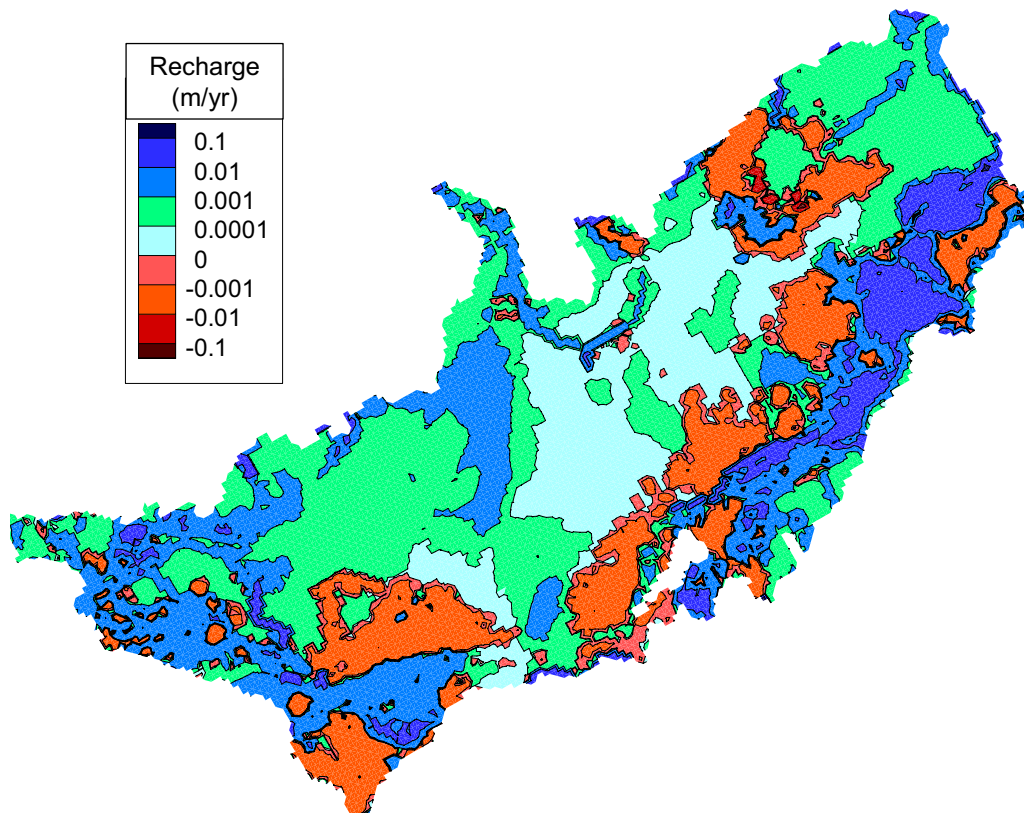


Figure 5-5. Recharge distribution, from the IWRII model.

5.3.1.1.7.1 Recharge Temperatures—A heat flow boundary condition for the top of the model requires a known heat flux or temperature at the top of the domain. In this study, it was assumed that the most accurate estimate of the upper condition derives from specifying the recharge and recharge temperature at the surface. In some areas of the SRPA, recharge temperatures can be estimated from noble gas studies of groundwater. Recharge temperatures calculated from N₂ (nitrogen) and Ar (argon) concentrations are about 6°C in the underflow from Birch Creek, Little Lost River, and Big Lost River and between 9 and 13°C for the Snake River Plain Aquifer at INL (USGS 2007) (<http://water.usgs.gov/lab/chlorofluorocarbons/research/inl/>). Temperature data from shallow monitoring locations at the RWMC (i.e., USGS Test Trench study [Davis and Pittman 1990]). For constant natural recharge sources, the recharge temperature was estimated at the surface from the mean annual air temperature, assuming an offset of + 4.7°C.

5.3.1.1.8 River Fluxes—Inflows to the model, which result primarily from tributary inflow, natural and anthropogenic recharge, are simulated as vertical fluxes to the top of the domain, which is the land surface for cells with net downward flux and the top of the aquifer where the net vertical flux is upward. The Snake River is both a large source and sink of water, and flows into and out of it have been estimated by the IWRII modeling team by inverse modeling to fit observations of head throughout the aquifer. In this effort, the IWRII-calculated river heads were used to calculate gaining and losing fluxes along the Snake River (Figure 5-6).

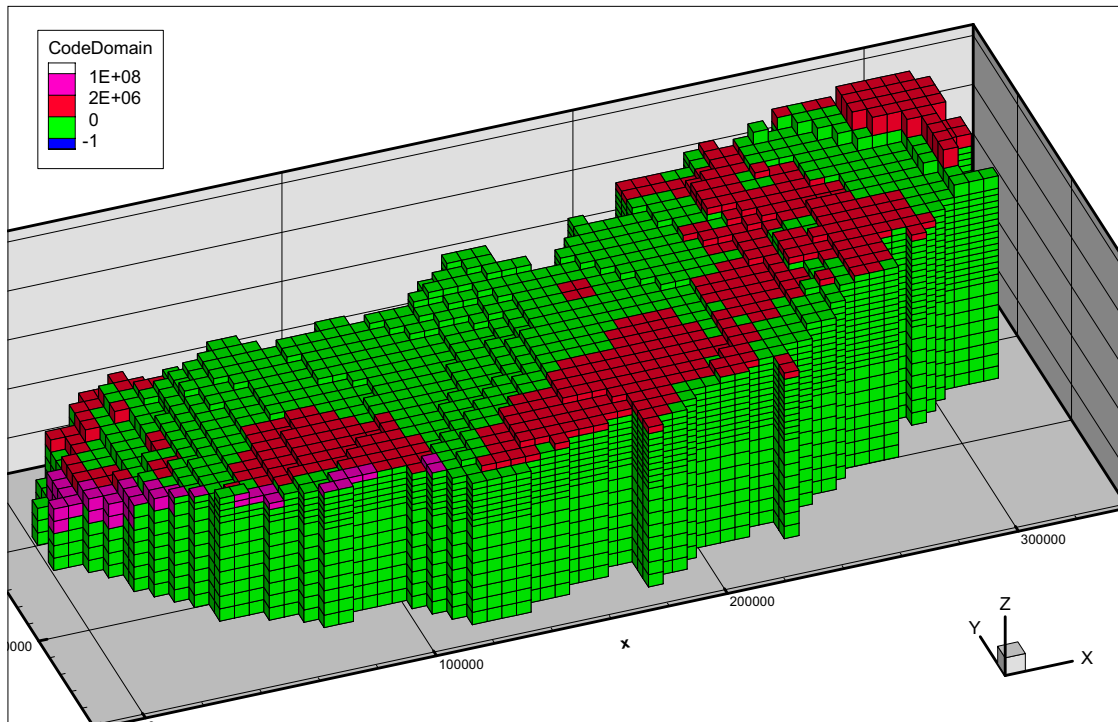


Figure 5-6. Three-dimensional model grid showing discharge cells (red) and specified head cells (purple) of preliminary simulation discussed in the text.

5.3.1.2 Results. To test the three-dimensional model prior to incorporation of specified river fluxes along the Snake River, a preliminary simulation was conducted using very simplified treatment of the river that specifies river heads only along the gaining reach along the southwest border of the aquifer. Results indicate that the gradient of the potentiometric surface is reasonably close to the observed gradient (Figure 5-7), with head contours generally mirroring the shape of the aquifer surface. Although gradients appear overly steep, simulated temperatures (Figure 5-8) across most of the aquifer are similar to measured temperatures and generally demonstrate that the model can reproduce the large-scale changes observed in temperature maps of the aquifer. Temperatures along the edges of the model domain in some places exceed those that should occur under conduction-only equilibrium with the ground surface temperature, which are believed to be due to errors in property assignments along the boundary. In summary, several preliminary treatments to the input data limit the value of the results, and further use of the model would require appropriate modifications. As this model is not being continued, the following changes are offered only to document what would be necessary. The necessary changes would include

- Correction of background ground surface temperatures to values based on ground surface temperature data recently made available from studies at INTEC.
- Adjustment of stream inflow recharge temperatures to match USGS reported estimates of recharge temperatures at tributary.
- Adjustment of recharge fluxes from the IWRI data so that differences in grid dimensions are appropriately reflected in the distribution.
- Modification, as follows: Specification of fluxes along the Snake River; these fluxes can be obtained from results of forward simulations with the IWRI model.
- Aquifer bottom is currently derived from a combination of OU 10-08 and IWRI thickness data. Full-aquifer domain should match IWRI model for better comparison application to that study.

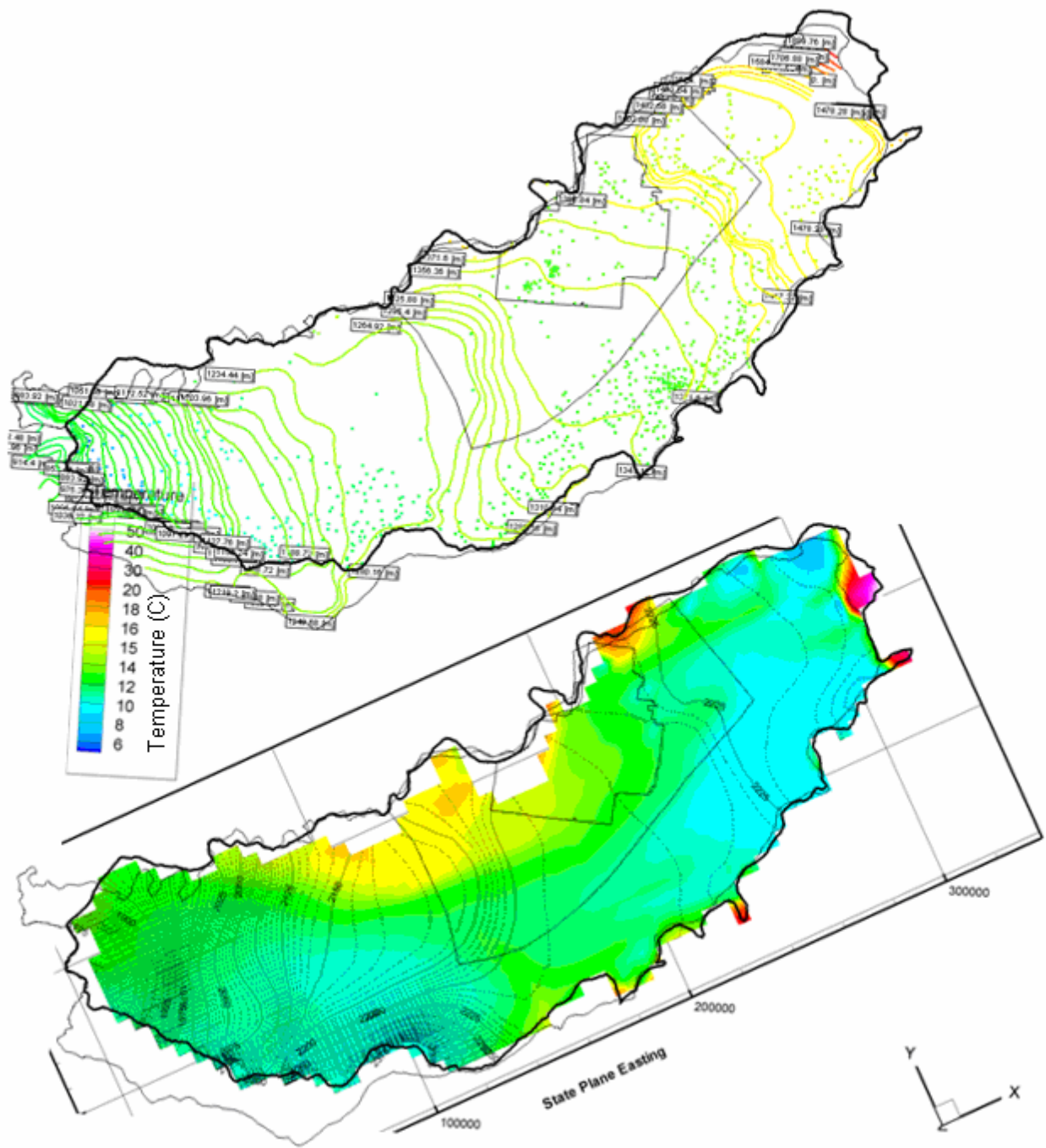


Figure 5-7. Comparison of the potentiometric surface calculated from a preliminary groundwater and heat flow simulation and the water potential map interpolated from aquifer well data. Boundary layer overlay in bottom figure is approximate. Contour interval of upper figure is approximately 30.5 m. Contour interval of lower figure is 5 m, with labels at 25-m intervals.

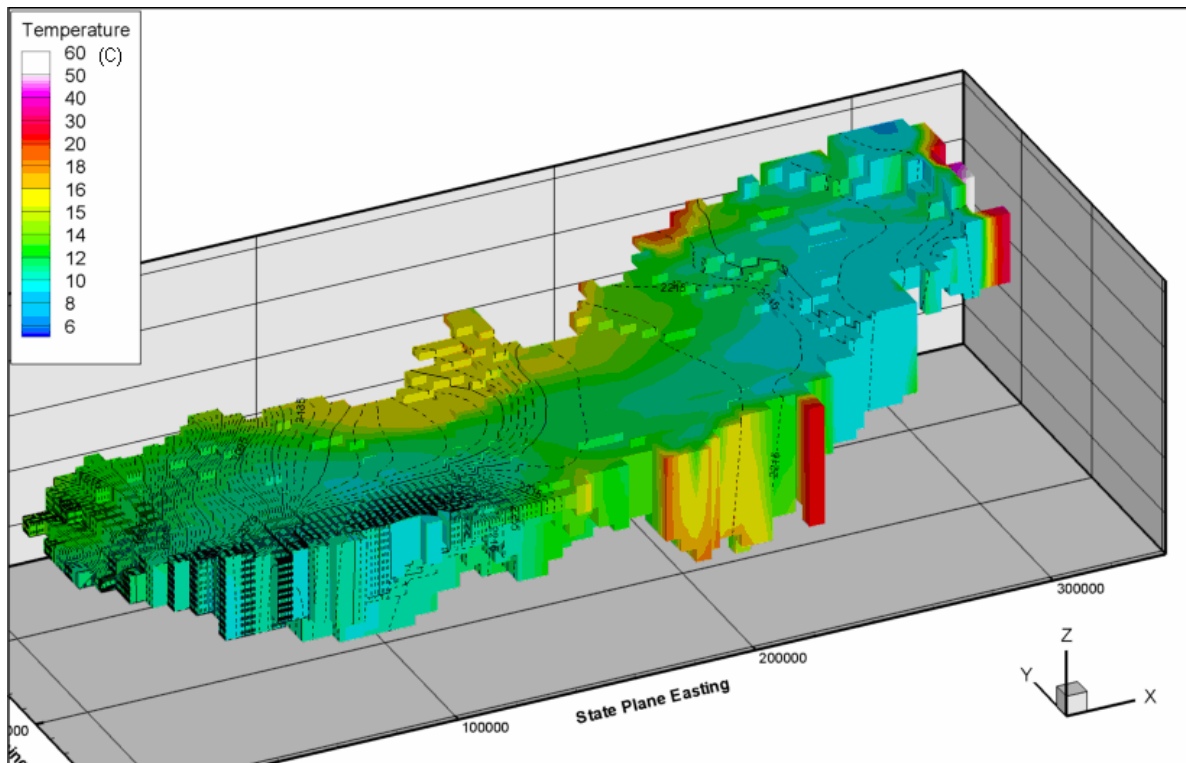


Figure 5-8. Calculated temperature field (color contouring) and contours of total water potential, from preliminary simulation of heat flow in the SRPA. Subaquifer and vadose zone grid cells not shown.

Densities output from the three-dimensional model indicate very little potential for buoyancy-driven flow in this system, which confirms results of preliminary two-dimensional flow line studies. These results demonstrate that free convection terms in the groundwater flow equations can be neglected in future flow and transport modeling.

5.3.1.3 Conclusion. Results of the three-dimensional heat flow study of the SRPA demonstrate that adequate information is available to constrain a heat flow model, even for an area much larger than is the focus of the OU 10-08 study. The model application presented in the following section is focused on using temperature data as a secondary constraint for inverse modeling-based estimation of hydraulic conductivity for the WAG 10 subregional flow and transport model. Heat flow calculations for the following model application were performed using the solute transport package MT3DMS, which is valid as long as density and viscosity dependences on temperature do not significantly affect groundwater flow. The three-dimensional groundwater and heat flow studies just presented using HST3D demonstrate that these assumptions are justified.

5.3.2 Phase 2 - INL Subregional Groundwater Flow and Heat Transport Model

To provide a means of performing joint inversion on both head and temperature for the OU 10-08 groundwater flow model, a heat transport model was developed using the three-dimensional flow model from Section 4.

5.3.2.1 Description of the Flow Model. The flow model is described in Sections 3 and 4 of this report and is a deterministic, six-layer, groundwater flow model.

5.3.2.2 Description of the Heat Transport Model. To simplify the joint inversion process, one of the goals for the heat flow model was that it be integrated with the existing flow model and, if possible, run within the MT3DMS Version 4.0 package incorporated in the GMS 6.0 package. Among the forms of the advection-dispersion equation that MT3DMS (Zheng and Wang 1999) solves is

$$\left(1 + \frac{\rho_{bulk} K_d}{\theta}\right) \frac{\partial(\theta C)}{\partial t} = \frac{\partial}{\partial x_i} \left(\theta (D^* + D_{ij}) \frac{\partial C}{\partial x_j} \right) - \frac{\partial}{\partial x_i} (\theta v_i C) + q_s C_s + \sum R_n, \quad (5-1)$$

where

- ρ_{bulk} = porous medium bulk density
- K_d = linear isotherm sorption coefficient
- θ = volumetric water content
- C = dissolved phase concentration of species of interest
- D^* = molecular diffusion coefficient
- D_{ij} = dispersion tensor
- v = average linear seepage velocity vector
- q_s = source/sink volumetric flow rate per unit volume
- C_s = source/sink concentration
- R_n = gain or loss of solute by reaction.

The reaction terms are first-order rate expressions for dissolved and sorbed phases:

$$\sum R_n = -\lambda_1 \theta C - \lambda_2 \rho_{bulk} K_d C, \quad (5-2)$$

where λ_1 and λ_2 are the first order rate constants.

Heat transport in groundwater occurs via conduction in the rock and via conduction and convection in the fluid. If variations in fluid density, thermal conductivity and thermal capacity are neglected, an equation that incorporates the primary heat transport processes is (Thorne, Langevin, and Sukop 2006)

$$\frac{\partial}{\partial t} \left[\left(1 + \frac{(1-\theta) \rho_s c_{p-s}}{\theta \rho_f c_{p-f}} \right) (\theta T) \right] = \frac{\partial}{\partial x_i} \left([D^* + D_{ij}] \frac{\partial(\theta T)}{\partial x_j} \right) - \frac{\partial}{\partial x_i} (v_i \theta T) + q_s T_s + \frac{\theta \gamma_f}{c_{p-f}} + \frac{(1-\theta) \gamma_s \rho_s}{c_{p-f} \rho_f} \quad (5-3)$$

where the subscripts f and s denote fluid and solid, respectively

- ρ is density
- c_p is specific heat
- D^* is now the bulk thermal diffusivity

$$k_{T\text{ bulk}}/(\rho_f c_{p_f})$$

with the bulk thermal conductivity approximated as the volume-weighted average of the thermal conductivities of the fluid and solid phases.

This is essentially Equation 5-1 with substitution of T for C. The retardation coefficient, R, for heat transport, for example, is given by the multiplicand of θT in the first term, i.e.,

$$R = 1 + \frac{(1-\theta) \rho_s c_{p_s}}{\theta \rho_f c_{p_f}}. \quad (5-4)$$

By equivalence with the retardation term in the solute transport equation, the linear sorption term, or K_d , needed for implementation of Equation 5-3 via the equation implemented in MT3DMS (Equation 5-1) is

$$K_d = \frac{(1-\theta) \rho_s c_{p_s}}{\rho_{\text{bulk}} \rho_f c_{p_f}}. \quad (5-5)$$

Although the first-order decay processes described in Equation 5-2 have no direct corollary in heat flow transport, they can be used to simulate a radiation-like boundary condition, where heat flow depends on concentration. For that reason, the equivalence between decay rate terms in the solute transport equation and the heat transport equation are also provided. The equivalent temperature-dependent heat loss terms are

$$\sum R_{\text{heat}_n} = -\lambda_{\text{heat}_1} \theta T - \lambda_{\text{heat}_2} \rho_{\text{bulk}} \frac{c_s}{\rho_w c_w} T. \quad (5-6)$$

Temperature-dependent heat loss from the fluid phase is essentially the same as in Equation 5-2, while the solute transport decay term used to simulate heat transport incorporates factors that account for the difference between the solute transport K_d and the actual ratio of the energy contained in the fluid to the energy contained in the solid:

$$\lambda_2 = \lambda_{\text{heat}_2} \frac{c_s}{K_d \rho_w c_w} \quad (5-7)$$

The values of the thermal energy transport that were implemented in the model are given in Appendix D. In general, thermal conductivities and specific heats implemented were those considered representative of basalt. However, thermal properties of the subsurface vary over a relatively small range, at least compared to the range of hydraulic conductivity that can exist for the same materials. Thus, while uncertainty in thermal properties contributes to the uncertainty of heat flow simulation results, the results should still be useful in estimating the otherwise very poorly constrained hydraulic properties.

5.3.2.2.1 Boundary Conditions—Boundary condition options available in MT3DMS include 1st type and 2nd type conditions, which are suitable for simulation of some, but not all, of the boundary conditions desired for heat transport in the system. Implementation of the desired boundary conditions for heat transport thus requires some non-standard techniques, which are described below. Additional details of the implementation of these conditions in MT3DMS are provided in Appendix D.

Where recharge enters the model the temperature of that water must be specified. In the OU 10-08 model, recharge is applied to simulate both underflow and surface recharge from the Big Lost River, Little Lost River and Birch Creek. Data for estimation of these recharge temperatures comes from several sources. Noble gas studies of aquifer water samples indicate that recharge temperatures at the primary tributaries are approximately 6°C (Busenberg, Plummer, and Bartholomay 2001). Temperature data close to the tributary mouths is, however, rarely lower than 9°C. Preliminary tests with the heat flow model indicated that a tributary inflow temperature of 6°C was inconsistent with the water fluxes specified, in that large plumes of cold water developed that are not observed in the available temperature data. For that reason, recharge temperature at the tributaries was specified as 9°C in subsequent simulations.

Natural infiltration across the model domain, outside the areas mentioned above, is assumed to recharge at a temperature of 12°C, which is consistent with the temperature of water in perched layers above the aquifer and with noble gas studies (Busenberg, Plummer, and Bartholomay 2001) indicating recharge temperatures of 9 to 13°C for the Snake River Plain at INL. The recharge rate applied in the model is 7 mm yr⁻¹, so that the applied heat flux is approximately 1 mW m⁻² for every degree difference between the temperature of the recharge and the groundwater. At 1/1000th of the geothermal heat flux, this term is thus virtually negligible.

The other major source of recharge in the OU 10-08 model is the specified flux across the northeastern boundary, which varies with depth and horizontal position. Temperatures along that flux boundary were specified to match observed temperatures along that line, and those temperatures were assumed to extend to the bottom of the aquifer. While temperatures likely vary somewhat with depth there, the available temperature–depth data are insufficient to prescribe meaningful values for each layer.

Heat flow to the bottom of the model domain is assumed to be a constant heat flux of 110 mW m⁻², as determined by several previous studies of heat flow in the Snake River Plain (Smith 2004; Brott, Blackwell, and Ziagos 1981). As this is a conductive heat flux, not associated with a water flux through the bottom of the system, it is implemented as a mass loading rate in MT3DMS, using a special case designed for sources independent of water flow.

The preferred boundary condition for the top of the domain is that the heat flux depends on the difference between groundwater temperature and temperature at the land surface. If it is assumed that heat flow through the vadose zone is effectively vertical only, then the appropriate equation for the heat flux, J , is

$$J = k_T \frac{\partial T}{\partial x_3}. \quad (5-8)$$

For a steady-state flow model, the distance between the ground surface and the water table is constant. Written in terms of a known vadose zone thickness, the heat removed from the aquifer by conduction to the ground surface is

$$J = k_T \frac{T - T_{ground}}{b_{vz}}. \quad (5-9)$$

While Equation (5-9) cannot be directly implemented as a boundary condition, it can be split into two terms that are readily incorporated as a combination of source/sink terms in MT3DMS:

$$J = \frac{k_T}{b_{vz}} T - \frac{k_T}{b_{vz}} T_{ground} \quad (5-10)$$

The first term on the right hand side is equivalent to a first-order reaction rate, where the rate of loss is dependent on the temperature of the groundwater and is proportional to a constant related to the rate of heat conduction through the vadose zone. This is implemented in MT3DMS by specifying a specific reaction term for each cell. The second term on the right hand side is effectively a constant source term, representing the heat flux to the groundwater that would occur if the groundwater temperature were at 0°C. Because this conductive heat flux is considered to be independent of any vertical water flux to the system, it is specified using a mass loading rate for each cell of the top layer of the aquifer. Again, this mass loading rate is not associated with a water flux, and is implemented with the corresponding mass loading type in MT3DMS.

5.3.2.2.2 Conversion of Water Flux—Independent boundary fluxes to mass loading rates in MT3DMS requires that the known flux per unit area be multiplied by the area of each cell, as the units of the mass loading term are mass per unit time per cell volume. GMS does not provide a simple means of accessing cell area or volume within the interface, so cell areas were calculated using map objects and exported for use outside of GMS. A temporary water flux of 1 m³ per day was applied to a polygon of the entire domain. GMS then apportions that volumetric flux according to the area of each cell. The resultant value for each cell multiplied by the area of the entire polygon provides the cell surface area. The GMS spreadsheet view of those data was then copied to Excel to check that the data were correctly calculated. The indices and area values were then read into MATLAB for final processing. The MT3DMS file for the desired heat flow simulations consists of three primary sections: (1) a recharge temperature section, in array format, with one value for each cell in the grid and (2) a mass loading vector section, with a mass loading rate and set of grid indices for each cell where a mass loading rate is specified. The first section is readily implemented with GMS, as the specified concentration associated with each recharge polygon. The second section includes (a) mass loading rates associated with specified concentrations at cells of specified water flux and (b) mass loading rates not associated with any water flux. Calculation of the latter terms, particularly those related to boundary conditions for the upper and lower surface of the domain often required access to information not readily accessible in GMS. The mass loading rate section of the *.ssm file was thus calculated and written via a MATLAB script, and then appended to the file written by GMS, with appropriate modifications to other descriptors. The MATLAB script used to perform those calculations is included in Appendix D.

5.3.2.2.3 Initial Conditions and Response Time—A uniform temperature of 12°C was specified as the initial condition for heat transport, as groundwater temperatures over much of the domain are close to that value. Because the flow paths are relatively long through the system (on the order of 100 km or more along the longest axis), velocities are in some places slow and retardation significant (on the order of 5), and temperatures require considerable time to reach steady state. The simulation described here, for example, effectively reached steady state only after 4,000 years of a 6,000-year stress period. Execution speed for steady-state simulations could thus be increased dramatically by specifying a retardation of zero. Note that time to reach steady state would be significantly longer if heat transport above and below the aquifer were simulated more realistically, i.e., if heat transport through adjoining systems were included in the solution, as would be desirable for transient simulations. In these simulations, the upper and lower boundary conditions assume instantaneous equilibrium outside the aquifer, consistent with our focus on the steady-state temperature distribution within the aquifer.

5.3.2.3 Results. The MT3DMS heat flow simulator setup is designed to provide a test of the flow model, in the sense of whether it can produce not only a reasonable match to the observed head field, but also a reasonable match to the observed temperature distribution in the model domain (Figure 5-9). Developed so as to run on the existing flow arrangement, without modification for simulating heat flow through the vadose zone or within the subaquifer, it is also well-suited to joint inversion approaches to estimation of the hydraulic conductivity field, via optimization on a combination of head data and temperature data.

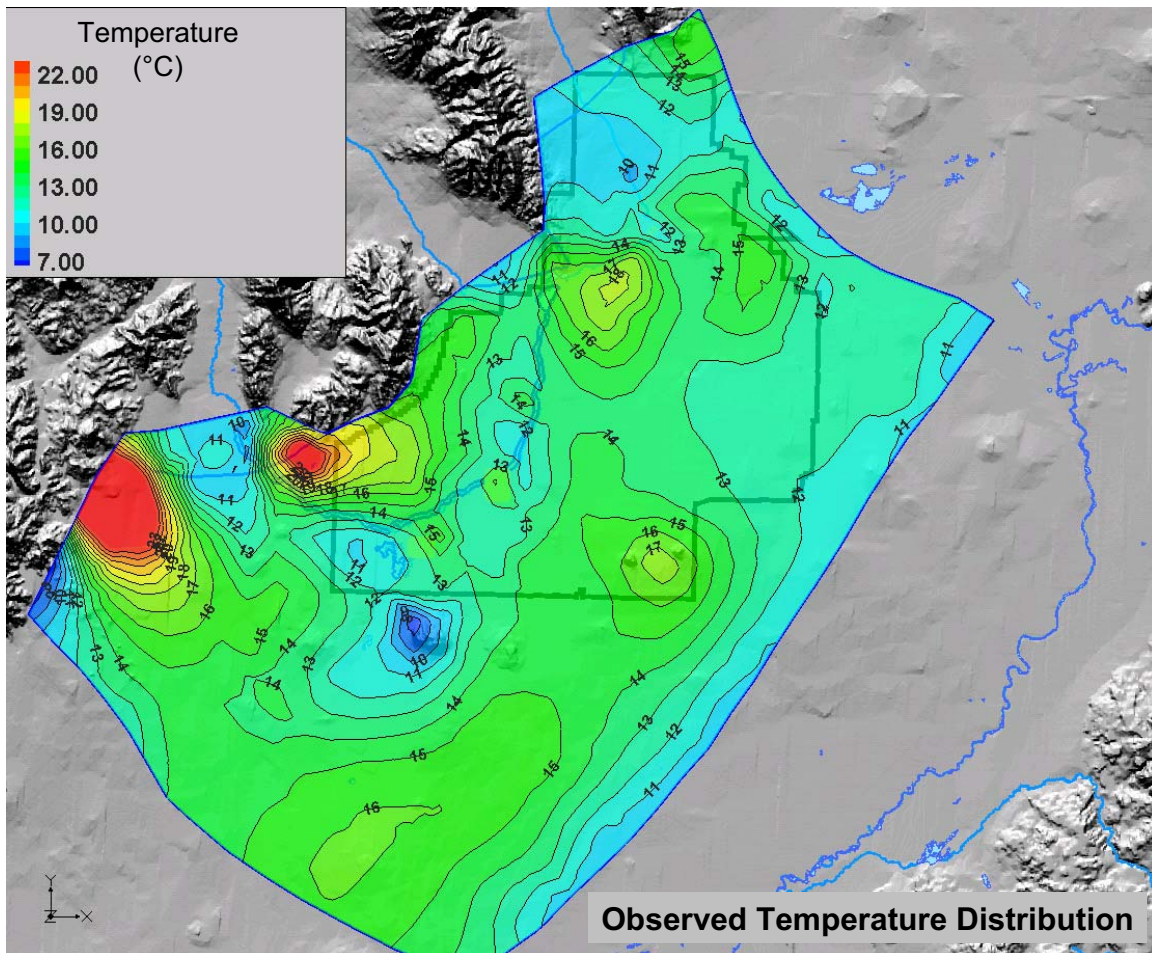


Figure 5-9. Observed temperature distribution across the OU 10-08 model domain.

Modeling efforts for this report have focused on separate development and improvement of the three-dimensional flow model and the three-dimensional heat flow model, and the joint inversion process has not been implemented. Heat transport simulations have been run for several of the models developed in Section 4 and these results demonstrate the value of the approach for corroborating the flow simulations.

Results for heat flow simulations for three different flow models are presented in Figure 5-10, with the observed temperature distribution (Figure 5-9, Figure 5-10A) for comparison. In each case presented, no attempt has been made to calibrate the heat flow model to observations and although the general range and behavior of the temperature field is comparable at large scale, many of the dominant near-field features are poorly matched in the simulations.

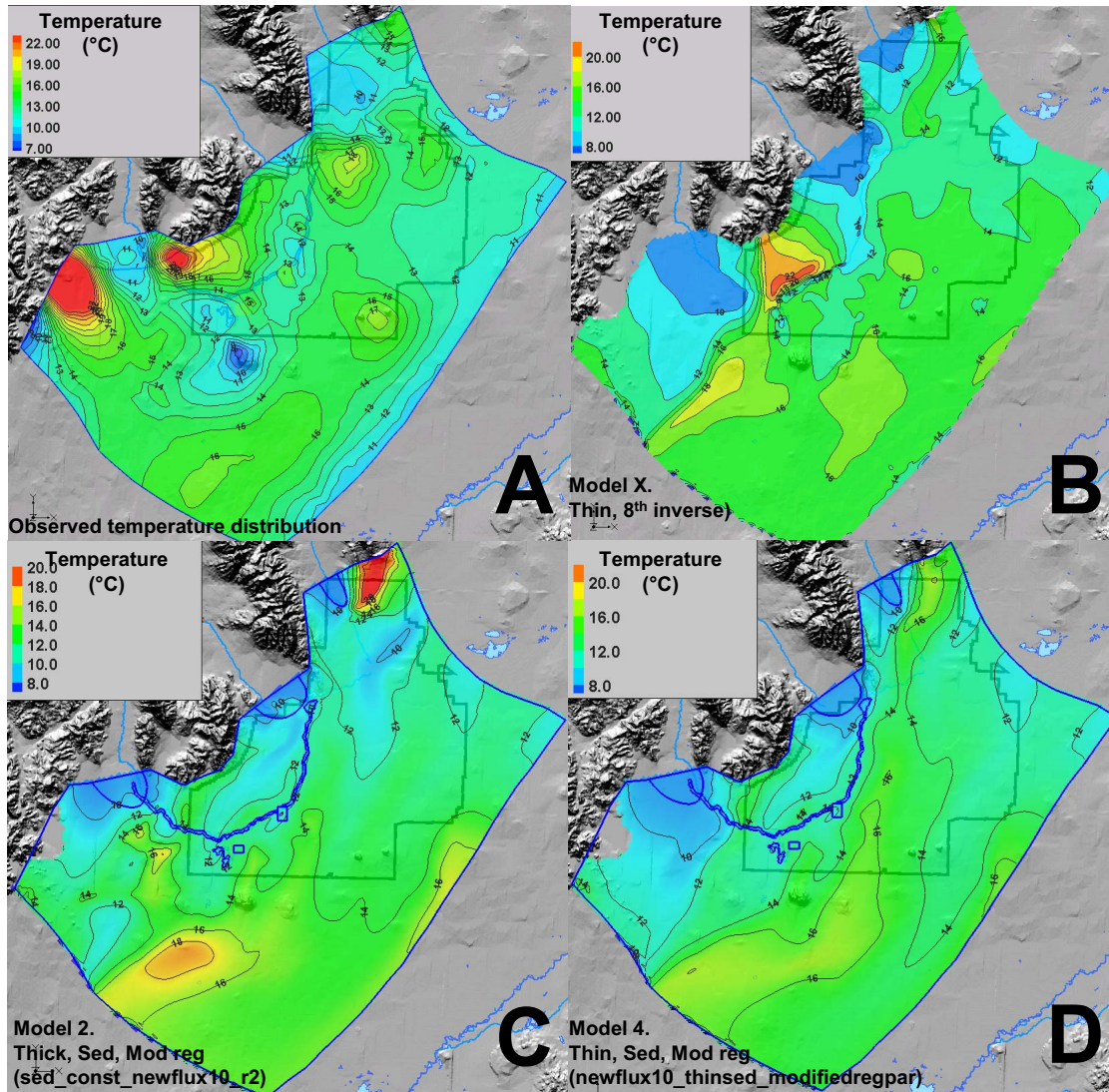


Figure 5-10. Observed temperature distribution in the uppermost portion of the aquifer (A) and simulated temperatures in the uppermost layer of the OU 10-08 flow model for (B) the preliminary 8th inverse thin-aquifer model, (C) final sediment-constrained thick aquifer model, and (D) final sediment-constrained thin aquifer model. Blue lines show boundaries and recharge areas representing tributary underflow and recharge from the Big Lost River.

Before discussing specific details of the simulated temperature fields, it is important to point out that the simulated temperature fields demonstrate three features critical for successful application of this approach as an aid to defining aquifer properties. First, the heatflow inputs are essentially uniform across the top and bottom of the domain, yet simulated temperatures are highly variable, with temperature plumes emanating from flux boundaries propagating great distances downgradient. This demonstrates that the temperature field, as modeled, is sensitive to the relatively simple boundary conditions and that the model does require complicated boundary conditions or a variable geothermal heat flux in order to produce significant temperature variations within the system. Second, the range of temperatures in the simulations is consistent with the observed range, suggesting that the heat fluxes to the top and bottom of the aquifer are reasonable approximations of the actual values. Finally, all three simulations provide a good match to the observed head field, but with different hydraulic conductivity distributions and/or

boundary conditions. This demonstrates that the simulated temperature distribution is sensitive to the flow field, i.e., changes in the hydraulic conductivity distribution within the range of uncertainty create easily discernible differences in the temperature field. Thus, the model demonstrates the behavior and sensitivity necessary to use temperature as a means of constraining hydraulic properties.

Detailed examination of simulated temperature distributions (Figure 5-10) suggest that the heat flow simulations could reproduce the observed temperature distribution more faithfully with some calibration by adjustment of hydraulic conductivity. Three simulation results are presented in this section. The first is an interim result from the three-dimensional flow model termed the 8th inverse thin-aquifer scenario. The second and third correspond to the final thick- and thin-aquifer models (Model 2 and Model 4) described in Section 4. The 8th inverse thin-aquifer scenario (Figure 5-10B) displays several features similar to those in the observed temperature map. The most prominent of these is a zone of very warm water along the toe of the Lost River Range. The high temperatures there reflect a combination of low groundwater velocities that allows the temperature profile to approach a steady-state conduction-only profile, and a relatively thick vadose zone, which increases the temperatures necessary for conduction-only equilibrium with the ground surface temperature. The corresponding feature in the observed data extends further to the west and reaches higher maximum temperatures, but the similarity between the two suggests that the low simulation velocities in that area accurately reflect conditions in the aquifer. Although warm-water anomalies along the margins of the aquifer could also reflect upwelling of warm water from below the aquifer, expression of that effect would still require relatively low horizontal discharge of groundwater in that area. Given that the maximum temperatures in that warm-water anomaly are consistent with those that might develop at that depth under conduction dominated conditions, explanations incorporating other mechanisms seem unwarranted.

A second prominent feature of the 8th inverse thin-aquifer simulation is the tongue of cold water that extends from the mouth of the Little Lost River. This cold water zone extends the entire distance to Cedar Butte, just east of Big Southern Butte and is similar to a less intense zone of cold water seen in the observed data (Figure 5-10A), extending from the Little Lost River to beyond Big Southern Butte. In both cases the cold-water zone, as seen at the top of the aquifer, is in places interrupted by zones of slightly warmer water. While this likely results from substantial vertical water movement in the simulation, causes for similar variations in the observed data are unknown.

Those features of the 8th inverse model that best match the data are very different in the final thin and thick models (Figures 5-10C and D), which are generally quite similar to one another. In both of these simulations, the cold water discharge from the Little Lost River is contained within the arc formed by the Big Lost River on the plain, and does not mimic the southerly flow apparent in the temperature map. Because of the much greater flow along the mountain front, these simulations also do not display the zone of warm water that exists between the toe of the Big Lost River range and the arc of the Big Lost River.

Many features of the observed temperature distribution are only poorly matched or not matched at all in the simulations presented here. These include (1) the warm water zone centered just south of TAN, (2) the warm water anomaly that underlies the axial volcanic high, and (3) the cooler temperatures that extend along the southeastern boundary of the domain. The first and second of these items may reflect overestimated hydraulic conductivities, which do not provide sufficient heating time during transport through those areas. The last item, conversely, likely represents the opposite problem, as cold water introduced at the upgradient boundary appears to move too slowly to maintain the observed cooler temperatures of the flux boundary section nearest the northeastern corner of the domain.

Examination of velocity vector maps for the simulations (Figure 5-11) demonstrates (a) the inverse relationship between groundwater velocity and temperature, and (b) that very different flow fields can result from different inversed hydraulic conductivity fields that each provide a good match to observed

heads. Vector maps for the uppermost layer of the aquifer for the 8th inverse thin-aquifer model and for the final aquifer model are very different in both general magnitude and in variance. Velocities in the 8th inverse simulation are generally a few meters per day or less, whereas extensive linear zones of velocities on the order of 20 m per day occur in the final thin aquifer model and thick aquifer (not shown) model. These velocity differences result from a simple redistribution of flux along the northeastern boundary, which, forced, in models subsequent to the 8th inverse simulations, higher water flux along the northwestern portion of the Site.

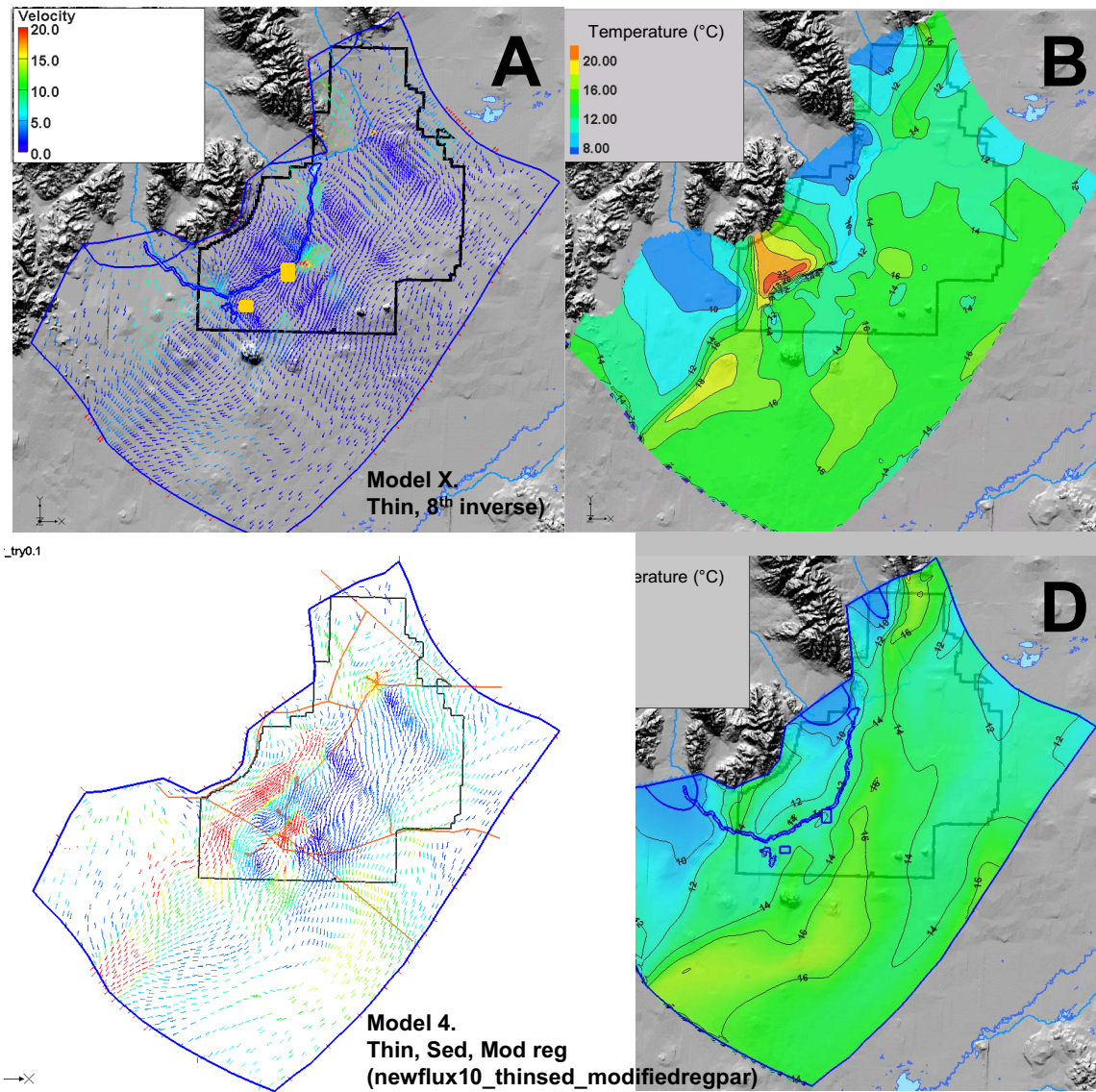


Figure 5-11. Simulated groundwater seepage velocity vectors (colored by magnitude) and temperatures for the 8th inverse thin-aquifer model (A, B) and for the final sediment-constrained thin aquifer model (C, D).

Because tributary recharge is substantially colder than groundwater temperatures in most of the aquifer, large differences in velocities in tributary vicinities produce very different temperature distributions. In this case, the slower velocities along the toe of the Big Lost River range produce a much better match to observations. While it can be argued that the slower velocities along the toe of the

mountains seems intuitively more correct or is more readily reconciled with isotope data, the temperature data in this case provide a direct and quantitative means of making that determination.

The vertical distribution of temperature also varies significantly with the hydraulic conductivity field, as lower velocities generally allow greater vertical gradients to develop. Strong vertical gradients develop in several places in the final thin aquifer model, for example, where velocities in the lowermost layers are lowest. In contrast, vertical temperature gradients were negligible throughout most of the 8th inverse model, likely because of the greater flux through the thickest portion of the aquifer.

Vertical temperature profiles also can be compared to observed profiles in places where deep wells penetrate the aquifer. Figure 5-12 displays simulated temperatures in the final thick aquifer model that developed at the locations of Corehole 1, Corehole 2A, and INEL-1. In each case, the temperature profile is essentially isothermal throughout most of the aquifer, either as a result of high velocities or vertical movement of water. The simulation profiles (Figure 5-12A) are, in fact, more uniform than is actually observed (Figure 5-12B) at these example locations, but similar to the essentially isothermal profiles that are observed at many locations. Because no attempt has been made to calibrate the flow field to the temperature data, the relatively poor match between simulated and observed temperatures at these locations cannot be considered representative of the potential match that could be obtained.

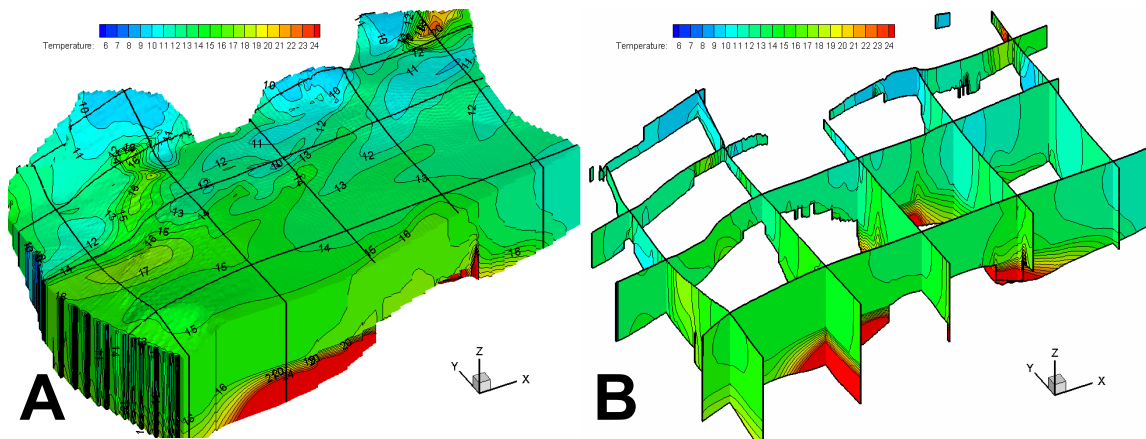


Figure 5-12. Perspective view of the heat flow simulation results for model 2 from Section 4 (A) and cross-section temperature plots from that simulation (B). Black lines in A show locations of cross sections.

At Corehole 2A, a strong temperature gradient develops at the bottom of the borehole, suggesting that the inversed hydraulic conductivity at that location may have effectively truncated the active aquifer at an elevation above the imposed aquifer bottom for the thick aquifer scenario. The heat-flow simulations (Figure 5-13) thus appear to provide a means of evaluating how well the effective aquifer bottom in each simulation matches the target surface.

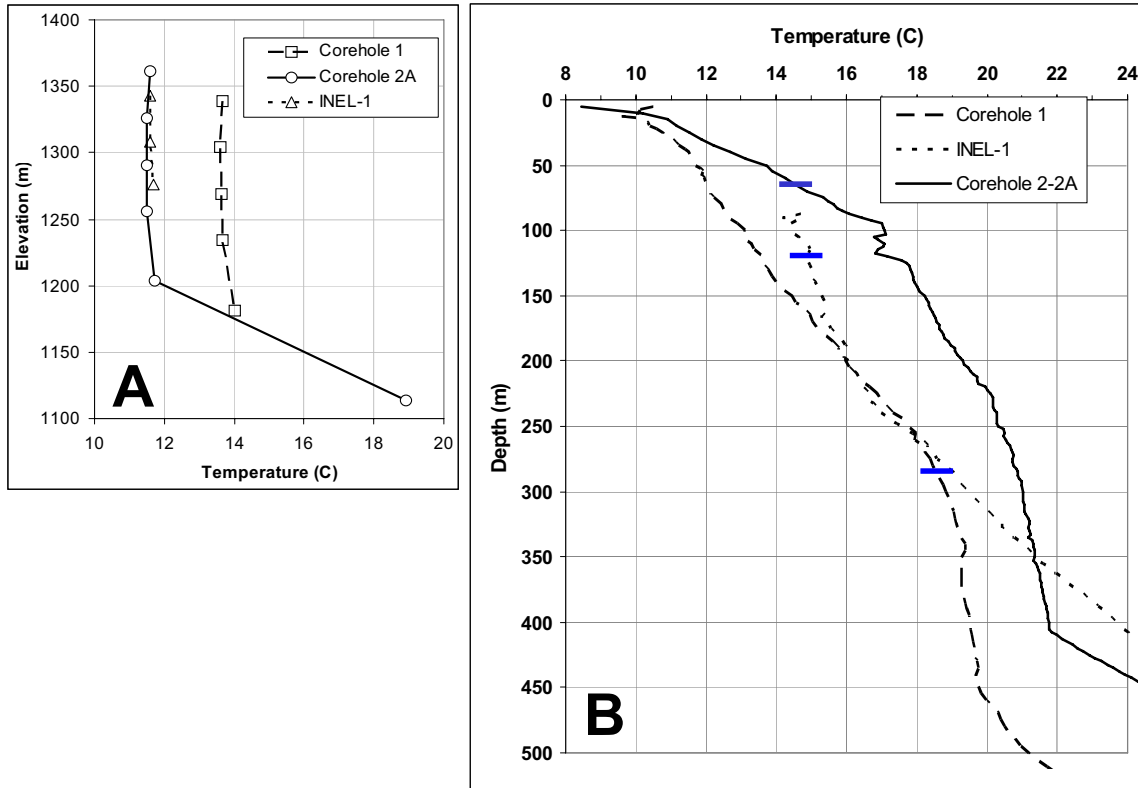


Figure 5-13. Simulated temperatures (A) and observed temperatures (B) at locations of several deep boreholes. Symbols in A indicate center of the finite difference block at each layer. Depth of the water table is noted with horizontal lines in B, and tops of simulated profiles begin approximately 15 m below that depth.

In the joint inversion approach, the hydraulic conductivity field may be the only variable adjusted in the optimization process, but early simulations with the heat flow model also demonstrated that the temperature data and heat flow simulations are useful in helping to define or refine boundary conditions for the model. Preliminary simulations with the thin aquifer model, for example, strongly suggested that initially estimated recharge polygons were too wide, as cold water introduced across the mouths of the tributaries produced much more laterally extensive cold-water plumes than is actually observed (Figure 5-14A). Reducing the area of the zones representing tributary underflow provided better separation of the cold water plumes emanating from the mountain front and allowed a better match to the observed temperature distribution. The northeastern flux boundary is another area where the heat flow simulations can aid in determining water fluxes because temperatures at a boundary are relatively easy to constrain, while specified fluxes are not. Where temperature plumes emanating from recharge boundaries (Figure 5-14B) differ dramatically from observed temperature behavior, it may reflect inaccurate flux distribution, and iterative modification of the boundary fluxes may, in some cases, yield a more accurate flow model.

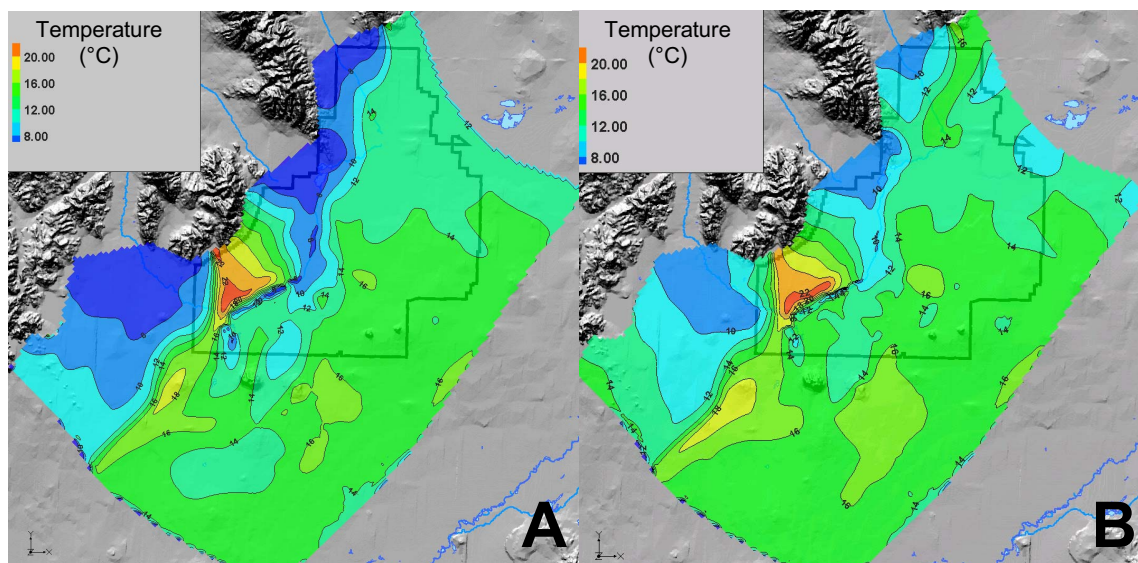


Figure 5-14. Illustration of the effect of different boundary conditions on simulated temperature distribution. Two simulations utilizing the thin aquifer model with different tributary basin recharge areas, illustrating how heat flow simulations can help define flow boundary conditions. Recharge areas in (left) simulation A extend across mouths of tributaries, but are approximately half-valley width in simulation B. Tributary recharge temperature is 6°C in A and 9°C in B. Note that inflow along the northeastern boundary in simulation A is uniform at 12°C, but matches observation data in simulation B.

5.3.2.4 Conclusions. The primary objectives of the heat flow modeling efforts of Fiscal Year 2006 were to develop and calibrate a heat flow model for the OU 10-08 model domain. These objectives were based on work plan recognition (DOE-ID 2004) that “development and calibration of an integrated model of saturated groundwater flow and thermal energy transport would provide a valuable means of better constraining hydrogeologic conditions in the SRPA” and thereby “improve the reliability of contaminant transport predictions based on numerical modeling of the aquifer.” Although calibration was not attempted, the forward simulations with the groundwater flow and heat transport model still serve to corroborate the flow models developed in this report. The simulations also serve to corroborate the potential value of the joint inversion approach.

The primary accomplishments related to heat flow modeling include:

- Development and successful testing of a three-dimensional, rigorous model of heat flow in the entire SRPA that could be adapted to any subset of that system
- Development and testing of a heat flow transport simulator for the OU 10-08 flow model domain.

There will not be further development of the heat flow transport modeling for the OU 10-08 model. The following observations are made to document the favorable aspects of the joint-inversion approach.

- The signal-to-noise ratio in the temperature data is excellent, as indicated by
 - Observed temperatures in the aquifer that vary widely above the noise component of the measurements, indicating thermal features that can, in many cases, be directly related to known sources
 - Adequate information describing the vertical temperature distribution at many locations and describing the temperature at the top of the aquifer throughout most of the model domain

- Previous studies demonstrating that groundwater velocities are sufficiently high and variable, creating strong horizontal temperature gradients as a result of transport of cold water, in some cases, or heating of slow-moving water, in others.
- Simulated temperatures behave as expected, with cold-water discharge inputs extending significant distances into the aquifer and with the degree of heating along flowlines generally consistent with that observed in the aquifer.
- Simulated temperatures are sensitive to hydraulic conductivity variations, as evidenced by the generally inverse relationship between simulated temperature and velocity.
- Simulated temperatures are sensitive to changes in boundary conditions for the flow model, as evidenced by
 - The dramatic differences that arise from differences in the distribution of flux along the NE boundary
 - The differences in temperature distribution that arise from changes in the shape and prescribed temperature at areas of tributary recharge.
- Simulated temperature profiles display, in some cases, the generally isothermal behavior widely considered characteristic of the Snake River Plain Aquifer and, in other places, the strong temperature gradients that should develop in areas of conduction-dominated heat flow.
- Despite the fact that the groundwater flow models have not been calibrated to match temperature data, some simulations demonstrate a good match to conspicuous thermal features in the observed temperature distribution.
- The heat transport model is well-suited for estimation of hydraulic conductivity by inversion on temperature and head since
 - The heat transport model accounts for steady-state heat losses through the vadose zone in an innovative way that precludes running a separate vadose zone heat transport model
 - The heat transport model was constructed using the standard MT3DMS, Version 4.0 package provided with the Groundwater Modeling System, the tool used to construct the OU 10-08 three-dimensional groundwater model
 - The interface needed to let PEST control an inverse process operating both MODFLOW and MT3DMS, Version 4.0 has already been developed.

5.4 References

- Anderson, M., 2005, "Heat as a groundwater tracer," *Groundwater*, Vol. 43, pp. 951–968.
- Bravo, H. R., J. Feng, and R. J. Hunt, 2002, "Using groundwater temperature data to constrain parameter estimation in a groundwater flow model of a wetland system," *Water Resources Research* 38, No. 8: 10.1029/2000WR000172.
- Brott, C. A., D. D. Blackwell, and J. P. Ziagos, 1981, "Thermal and Tectonic Implications of Heat Flow in the Eastern Snake River Plain, Idaho," *Journal of Geophysical Research*, Vol. 86, pp. 11, 709-11, 734.

- Busenberg, Eurybiades, L. N. Plummer, and R. C. Bartholomay, 2001, *Estimated age and source of the young fraction of ground water at the Idaho National Engineering and Environmental Laboratory*, U.S. Geological Survey Water-Resources Investigations Report 01-4265 (DOE/ID-22177), 144 p.
- Cosgrove, D. M., B. A. Contor, and G. S. Johnson, 2006, *Enhanced Snake River Plain Aquifer Model Final Report*, Idaho Water Resources Research Institute, University of Idaho, prepared for the Idaho Department of Water Resources, IWRRI Technical Report 06-002, July 2006.
- Davis, L., and J. R. Pittman, *Hydrological, Meteorological, and Geohydrological Data for an Unsaturated Zone Study near the Radioactive Waste Management Complex, Idaho National Engineering Laboratory, Idaho—1987*, DOE/ID-22086, U.S. Geological Survey Open-File Report 90-114, Idaho Falls, Idaho, January, 1990.
- DOE-ID, 2004, *Idaho National Engineering and Environmental Laboratory Operable Unit 10-08 Sitewide Groundwater Model Work Plan*, DOE/NE-ID-11188, Rev. 0, U.S. Department of Energy Idaho Operations Office, December 2004.
- Goode, D. J., and L. F. Konikow, 1990, "Reevaluation of Large-Scale Dispersivities for a Waste Chloride Plume: Effects of Transient Flow," International Conference on Calibration and Reliability in Groundwater Modeling, International Association of Hydrological Sciences, The Hague, The Netherlands, September 1990.
- Kipp, K. L. Jr., 1997, *Guide to the Revised Heat and Solute Transport Simulator: HST3D -- Version 2*, U.S. Geological Survey Water Resources Investigations Report 97-4157, Denver, Colorado, 149 p.
- McCord, J., M. Reiter, and F. Phillips, 1992, "Heat-flow data suggest large ground-water fluxes through Fruitland coals of the northern San Juan basin, Colorado – New Mexico," *Geology*, Vol. 20, p. 419–422.
- Reiter, M., 2001, "Using Precision Temperature Logs to Estimate Horizontal and Vertical Groundwater Flow Components," *Water Resources Research*, Vol. 37, pp. 663–674.
- Robertson, J. B., 1974, *Digital Modeling of Radioactive and Chemical Waste Transport in the Snake River Plain Aquifer at the National Reactor Testing Station, Idaho*, Open-File Report IDO-22054, U.S. Geological Survey.
- Smith, R. P., 2002, *Variability of the Aquifer Thickness Beneath the Idaho National Engineering and Environmental Laboratory (INEEL)*, INEEL/EXT-02-01022, Rev. 0, Idaho National Engineering and Environmental Laboratory, August 2002.
- Smith, R. P., 2004, "Geologic setting of the Snake River Plain Aquifer and vadose zone (*in* Understanding subsurface flow and transport processes at the Idaho National Engineering and Environmental Laboratory (INEEL) site, *Vadose Zone Journal*, Vol. 3(1), pp. 47–58.
- Stallman, R. W., 1965, "Steady one-dimensional fluid flow in a semi-infinite porous medium with sinusoidal surface temperature," *J. Geophysical Research*, Vol. 70, pp. 2821–2885.
- Stallman, R. W., 1967, "Flow in the zone of aeration," *Advances in Hydrosience*, Vol. 4, pp. 151–195.

- Thorne, D. T., C. D. Langevin, and M. C. Sukop, 2006, "MODFLOW/MT3DMS-Based Simulation of Variable-Density Groundwater Flow with Simultaneous Heat and Solute Transport," in *Proceedings of the XVI International Conference on Computational Methods in Water Resources*, Binning, Philip J., Peter K. Engesgaard, Helge K. Dahle, George F. Pinder and William G. Gray, eds., Copenhagen, Denmark, June 2006.
- USGS, 2007, "Idaho National Laboratory," Reston Chlorofluorocarbon Laboratory, U.S. Department of Interior, U.S. Geological Survey, <http://water.usgs.gov/lab/chlorofluorocarbons/research/inl/>, Web page modified March 13, 2007, Web page visited August 10, 2007.
- Zheng, Chunmiao, and P. Patrick Wang, 1999, *MT3DMS, A modular three-dimensional multi-species transport model for simulation of advection, dispersion and chemical reactions of contaminants in groundwater systems; documentation and user's guide*, U.S. Army Engineer Research and Development Center Contract Report SERDP-99-1, Vicksburg, Mississippi, 202 p.

6. SUMMARY

A subregional scale, three-dimensional flow model of the SRPA has been developed to support Comprehensive Environmental Response, Compensation and Liability Act (CERCLA) (42 USC § 9601 et seq.) decisions for OU 10-08 at the INL. This model has been calibrated primarily to water levels and secondarily to velocities interpreted from stable isotope disequilibrium studies and the movement of anthropogenic contaminants in the aquifer from facilities at the INL. The three-dimensional flow model described in this report is another step in the process of constructing a fully three-dimensional groundwater fate and transport flow model as prescribed in the OU 10-08 Groundwater Model Work Plan (DOE-ID 2004).

Earlier steps in the tiered process of model development have supported and been used in the work presented in this report. The two-dimensional flow model (Wood et al. 2005) was the initial model developed under the work plan and was used as the basis for extending the two-dimensional model to three dimensions. A two-dimensional transport model (Appendix C of the OU 10-08 Fiscal Year 2006 Annual Monitoring Report [DOE-ID 2007]) was developed to test implementation of individual facility sources. The regional water influx across the northeastern boundary was revised from a prescribed-head to a prescribed-flux boundary to ensure the amount of water going through the model was consistent with the conceptual model.

In the development of the three-dimensional flow model, sediment-dominated three-dimensional volumes were used to represent the geology and constrain groundwater flow appropriately. Hydrological, geochemical, and geological data were summarized and evaluated to infer aquifer behavior. A primary observation from development and evaluation of the conceptual model was that relative to flow on a regional scale, the aquifer can be treated with steady-state conditions. Although there are changes in the water table with time, these changes generally occur across the aquifer uniformly so that the hydraulic gradients do not change appreciably. Water levels were evaluated to determine vertical velocities at those locations where three-dimensional data existed. The results of this analysis indicated a complex mixture of upwards and downwards velocities without any regional consistency. Horizontal velocities were estimated from the advance of anthropogenic contaminant plumes, geochemical disequilibrium studies, and from vertical profiles of temperature in the aquifer. These three methods resulted in relatively consistent velocity estimates.

The three-dimensional model did a reasonable job of matching water levels (see Section 4). The water levels were almost all matched within 1 m. However, as can be seen in the water flux/average linear velocity figures, this good match to water levels alone did not guarantee that the model sufficiently represented groundwater velocities for simulation of contaminant transport. For example, there was a persistent high flux/velocity zone present in model results in both the thick and thin scenarios in an area of interpreted slower velocity around Well USGS-22 (at the western margin of the model domain). The area of lower velocity was interpreted on the basis of stable isotope disequilibrium data and temperature data. Currently, the best explanation for this discrepancy between the numerical model and the conceptual model is a high sensitivity of simulated velocities to the assignment of regional flux across the northeast boundary. Continued development during the next step in the tiered approach to model development (i.e., three-dimensional transport modeling) will address this discrepancy.

Thermal modeling accomplishments included (1) development and successful testing of a three-dimensional model of heat flow in the regional Snake River Plain Aquifer that could be adapted to any subset of that system, and (2) development and testing of heat flow transport for the subregional OU 10-08 model. The latter was used to corroborate the results of the OU 10-08 model by comparing simulated temperature to observed temperature patterns.

An explanation of the model sensitivity to northeast boundary flux is offered below along with an outline of work to further revise that boundary.

6.1 Northeastern Boundary Flux Assignment Impacts

The assignment of flux across this northeastern boundary has evolved during the development of the three-dimensional flow model. This evolution started with efforts to revise the assignment of flux across this northeastern boundary based upon the two-dimensional transport model (DOE-ID 2007). In an effort conducted after finalization of the two-dimensional transport model but before starting on the three-dimensional flow model, the northeastern boundary condition in the two-dimensional model was switched back to a prescribed head, and the total flux emanating from the southwestern prescribed head boundary was added as a calibration target within the PEST inverse simulation. This additional calibration target ensured that the total water flux through the model matched the interpreted water flux through the domain from the conceptual model. With this approach, permeabilities in the model domain were allowed to adjust within the inverse solution so that water flux across the northeastern boundary combined with the other water sources from the tributary basins, seepage from the Big Lost River, and so that areal infiltration of precipitation matched the assigned southwestern boundary flux calibration target. This approach worked very well in maintaining an excellent head match and had the correct amount of water going through the model.

As development of the three-dimensional flow model progressed, this same approach was attempted. Prescribed head boundary conditions were assigned at both the northeastern and southwestern model boundaries and the flux out the southwestern boundary was used as a calibration objective in an inverse simulation. The approach was not successful because the inverse process would not converge to a solution. The cause for non-convergence was interpreted to be that, even with regularization, the problem was ill-posed and was not sufficiently constrained. Essentially, this means that with the additional degrees of freedom available from having hydraulic conductivity vary vertically, there was not sufficient three-dimensional data for the inverse process to distinguish an optimal direction to proceed. The only choice was to use prescribed fluxes across the northeastern boundary. As discussed in Section 2, the initial attempt with prescribed fluxes across the northeast boundary resulted in too much water being assigned at depth and high conductivity regions at depth were necessary in the inverse process to accommodate this assigned water. These high-conductivity regions at depth conflicted with the conceptual model, so the prescribed water flux was shifted to the upper layers to more accurately represent the conceptual model (e.g., decreasing flow with depth in the aquifer). This upward shift of the boundary flux combined with an assumed high horizontal to vertical anisotropy ratio (100:1) appeared to keep water in the upper layers to the extent that the assigned tributary influx from the Little Lost River was forced westward through the interpreted low-flow zone at the toe of the Arco Hills. Unfortunately, this was not discovered in time to correct for this modeling report, but it will be addressed in the next step of model development. In the next phase of the modeling development this interpreted low-flow area will be preserved through reducing the upper permeability limit that the inverse model can assign in this region.

6.2 Approach to Assigning Northeastern Boundary Fluxes

A large sensitivity to the assignment of boundary fluxes along the northeastern face of the three-dimensional model domain has been demonstrated in this report. To avoid this problem, the next phase of model development will return to the approach of using prescribed head boundary conditions at both the northeastern and southwestern model boundaries with the flux out the southwestern boundary used as a calibration objective for the inverse simulation. To overcome the non-convergence problems discussed in the previous section, the permeability will be kept the same vertically at each horizontal

location for the upper three or four model layers. This does not achieve one of the original objectives in the OU 10-08 Groundwater Modeling Work Plan (DOE-ID 2004) but reflects a necessity, given that the limited three-dimensional data are not sufficient to constrain a fully three-dimensional flow model. Transport, however, will continue to be three-dimensional— a fact that precludes the problems pointed out earlier of using two-dimensional models that result in extensive vertical averaging.

6.3 Approach to Selecting Between Thick and Thin Aquifer Interpretations

The results presented in this report do not allow distinguishing one or the other (thick or thin) scenarios as better for flow and transport. Even with the graphical-user interface available for running GMS, evaluating both scenarios for each iteration during the inverse process has been cumbersome. To reduce this burden in the next phase of model development, the additional data on aquifer thickness that has become available since the Smith (2002) interpretation will be used in an attempt to discern which interpretation is most likely. Thicknesses can be interpreted from approximately six additional wells, which almost doubles the seven wells used by Smith (2002).

6.4 Conclusion

Model development for the OU 10-08 Sitewide groundwater model was planned and has been implemented as a phased process. Various benefits to this approach exist; the foremost of these is that lessons learned are applied in subsequent stages of model development. This benefit has been realized with the application of two-dimensional understandings to solve the three-dimensional boundary condition problem.

Some authors have suggested that calibration to water levels alone is insufficient to develop a credible model of aquifer flow and transport (Anderson 2005). Indeed, the work presented herein tends to support this point of view. Any number of simulations produced reasonable matches to the observed heads without matching velocity patterns inferred from other information. In the next step of model development, contaminant data from anthropogenic plumes will be included as a third calibration target. The combined and integrated use of water levels, velocity data, and concentration data will provide additional constraints to the model. The next and last phase of the model, the three-dimensional transport model, will include additional data and thereby result in a model with increased credibility.

6.5 References

- 42 USC § 9601 et seq., 1980, “Comprehensive Environmental Response, Compensation and Liability Act of 1980 (CERCLA/Superfund),” *United States Code*, December 11, 1980.
- Anderson, M., 2005, “Heat as a groundwater tracer,” *Groundwater*, Vol. 43, pp. 951–968.
- DOE-ID, 2004, *Idaho National Engineering and Environmental Laboratory Operable Unit 10-08 Sitewide Groundwater Model Work Plan*, DOE/NE-ID-11188, Rev. 0, U.S. Department of Energy Idaho Operations Office, December 2004.
- DOE-ID, 2007, *Waste Area Group 10, Operable Unit 10-08, Remedial Investigation/Feasibility Study Annual Status Report for Fiscal Year 2006*, DOE/ID-11297, Rev. 0, U.S. Department of Energy Idaho Operations Office, May 2007.

Smith, R. P., 2002, *Variability of the Aquifer Thickness Beneath the Idaho National Engineering and Environmental Laboratory (INEEL)*, INEEL/EXT-02-01022, Rev. 0, Idaho National Engineering and Environmental Laboratory, August 2002.

Wood, T. R., C. M. Helm-Clark, H. Huang, S. Magnuson, T. McLing, B. Orr, M. Roddy, M. J. Rohe, M. A. Plummer, and R. Podgorney, 2005, *Operable Unit 10-08 Summary Report on the Subregional-scale Two-dimensional Aquifer Model*, ICP/EXT-05-00979, Rev. 1, Idaho National Laboratory, Idaho Cleanup Project, October 2005.

Appendix A
Software Management Agreement

Software Management Agreement Between ICP WAG 10 and BEA Modeling and Measurement

October 24, 2006

Definitions

Customer: Idaho Cleanup Project (ICP) OU 10-08 RI/FS project
Performer: Battelle Energy Associates Modeling and Measurement Department

Customer Requirements:

The codes and analyses used to generate results used to make decisions for the OU 10-08 RI/FS will conform to quality and documentation consistent with the level of effort performed for the OU 7-13/14 RI/FS. The codes and analyses for the OU 10-08 RI/FS include the Groundwater Modeling System application suite for development of the calibrated 3D flow and transport model and the Response Surface Modeling code which will mimic the results of the 3D model.

The work is being performed according to the requirements of the INL Research and Development General Software Management Plan (PLN-1726, 2004), which was also used for guidance for software quality and assurance for OU 7-13/14. End User Category 9 from PLN-1726 specifies “codes and results generated to support decisions at the INEEL” and demonstrates applicability of PLN-1726 to control software quality and assurance for the OU 10-08 RI/FS project.

There are three key requirements of the PLN-1726 to ensure quality of results. These are:

1. Reproducibility of the final results. Results presented as the final product to ICP, for acceptance by the regulatory agencies must be reproducible.
2. Verifiability of the final results. This will require that simulation results can be qualitatively verified by an expert in the field using a similar simulation approach. To accomplish this sufficient detail will be provided on the results generation processes such that they could be independently verified. Sufficient detail includes an explanation of the pre-data analysis phase, the simulation phase, the post-processing phase, and an explanation of the results.
3. Review and approval of the results. This requirement compliments the second requirement in that the accuracy will be verified through a peer and customer review process.

These three requirements meet the intent of End User Category 9 under the Research and Development General Software Management Plan (PLN-1726).

Implementation of the Requirements:

Modeling and Measurement will ensure that the following is documented and placed in the project file at the time the final results are released.

The first and second additional requirements will be addressed through:

- Reference list of commercial software and version used in simulations.
- Frozen version of non-commercial software and other routines used to generate results (i.e., electronic backup of excel spreadsheets, PVWAVE routines, etc.).
- Frozen version of the input and output results and files throughout the data analysis, pre- and post-processing stages.

- Reference to the operating system and hardware specifications for reproducibility
- Documentation of the simulation and analysis process.. This will include a flow-chart or sequencing of the data analysis steps involving use of the pre-processing steps, the simulation phase, and the post-processing phase.. This will not include documentation of commercial software, but will include a description of internally written routines in the form of readme files or internal code comments.

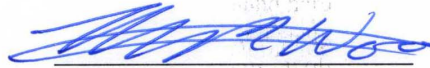
The third requirement will be met through the

- Internal (performing organization) peer review of results
- Any customer-required external reviews,
- Performing organization management approval, and
- Customer approval.

Action to be taken by Performer:

A checklist will be created by the performer and placed in the project file, where code/documentation quality and quantity will be tracked. The checklist will contain the bullets above.

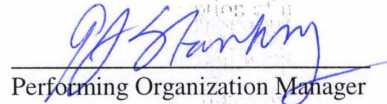
Concurrence:



Performer

10/31/06

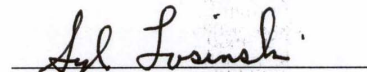
Date



Performing Organization Manager

10/31/06

Date



Requesting Organization

11/2/06

Date:

Appendix B

Fiscal Year 2006 Volcanic Stratigraphy Supporting Revision of the Geologic Conceptual Model

Appendix B

Fiscal Year 2006 Volcanic Stratigraphy Supporting Revision of the Geologic Conceptual Model

At the beginning of the Operable Unit (OU) 10-08 groundwater and contaminant transport modeling project, critical data needs for a robust conceptual model were recognized and a work plan was created and implemented to address those needs (DOE-ID 2004). The specific conceptual model needs included lithologic and basalt geochemical data to address (a) the nature of the stratigraphic mismatch between the Idaho Nuclear Technology and Engineering Center (INTEC) and Reactor Technology Complex (RTC), (b) more complete geochemical profiling of deep coreholes within the conceptual model study area, and (c) supplementary radiometric age dating of deep basalts in the southern half of the study area to resolve the subsurface structure of the Big Lost Trough. In addition, all available known geological mapping, borehole data, and geophysical data were reviewed and analyzed to expand our knowledge of the subsurface, especially in areas outside the Idaho National Laboratory (INL) boundaries. This analysis was both crucial and timely because of substantial new surface and subsurface data that has become available since 2002 (e.g., Mankinen et al. 2004; Kuntz et al. 2004).

During the 2004, 2005, and 2006 fiscal years, two deep coreholes were drilled through the base of the aquifer and their core sampled for geochemical profiling and age dating. Previously unsampled cores from several existing coreholes were also sampled for geochemical profiling. These data were analyzed along with previous deep refraction seismic and resistivity data (Smith et al. 1982; Zohdy and Stanley 1973), new borehole geophysical surveys collected by the USGS, new gravity data collected by S. Payne (2006),^a new interpretations of seismic data in the tributary basins (Payne and Oldow 2005), and the new gravity and aeromagnetic data set for the Northern Rocky Mountains compiled by the USGS (Mankinen et al. 2004). New geological mapping (Kuntz et al. 2003) and radiometric age dates (Champion et al. 2002; Hughes, McCurry, and Geist 2002; Helm-Clark and Rodgers 2004; Kuntz et al. 2004; Tauxe et al. 2004) also were included in the conceptual model synthesis. All of these data plus the many other studies from before 2002 were reviewed, analyzed, and incorporated into the geologic conceptual model, excluding two deep radiometric age date samples collected in Fiscal Year (FY) 2006 from INL deep coreholes MIDDLE-2050A and MIDDLE-2051.

The synthesis of data collected for the OU 10-08 conceptual model with both new and previously available data sets resulted in a defensible working hypothesis to explain the INTEC-RTC data gap and resulted in revisions to the conceptual model presented in Wood et al. (2005). Both of these subjects are discussed in subsequent sections.

B-1. GEOCHEMICAL PROFILING AND STATISTICAL SIGNIFICANCE

As of the date of this report, major and trace element analyses have been completed on the 121 samples collected from coreholes MIDDLE-2050, MIDDLE-2050A and MIDDLE-2051. Deep coreholes MIDDLE-2050A and MIDDLE-2051 were drilled, cored, and completed with Westbay casings in support of the OU 10-08 groundwater and contaminant modeling effort. MIDDLE-2050 was drilled and cored to ~385 ft below land surface (bls) and was abandoned when the hole collapsed, trapping the drill steel. MIDDLE-2050A was subsequently drilled ~30 ft west of MIDDLE-2050. It was cored from 418 to 1,427 ft bls and completed as an observation well with a Westbay casing. For convenience, since these two holes are adjacent to one another and their stratigraphic differences are minimal, their geochemical

a. Payne, S., INL, unpublished dissertation.

results have been combined and are treated as if they originated from just one corehole, referred to here as MIDDLE-2050A.

In addition to the geochemical profiling of MIDDLE-2050A and MIDDLE-2051, additional geochemical sampling was performed during 2004–2005 on core from USGS-118, C1A, TRA-5A, TRA-8, and USGS-80: for the former two coreholes, to provide geochemical data in support of laboratory-directed research and development related to geochemical logging; and for the latter three coreholes, to improve data density and provide data in critical unsampled intervals for geochemical profiling. Further geochemical data have become available through the research efforts of Idaho State University (ISU) graduate students Mazurec (2004), Scarberry (2003) and Chadwick (2004), in support of their master's theses. Mazurec analyzed core from Middle-1823 to study basalt alteration; Scarberry sampled the F-flow in several coreholes in the south central portion of the INL Site, and Chadwick sampled coreholes USGS-127 through USGS-129 to study petrological relationships and geochemical stratigraphy between Radioactive Waste Management Complex (RWMC), Central Facilities Area (CFA) and INTEC. In addition, almost all known previous geochemical studies of basalts at the INL and its environs have been tabulated in the ISU geochemical database maintained by Profs. Hughes and McCurry (Hughes, McCurry, and Geist 2002) and ongoing stratigraphic studies at the INL have used this database extensively.

Geochemical profiling techniques constitute a very powerful tool for stratigraphic correlation. An early recognition that elemental trends could be used for stratigraphic correlation was made by Anderson and Bartholomay (1995), who used natural gamma log wireline data to correlate potassium content in individual flows. Reed, Bartholomay, and Hughes (1997) used a variety of elemental data to correlate flows at INTEC. Helm-Clark et al. (2005) noted that a geochemical signature based on a combination of K, Na, Ca, Fe, Ti, Mg, Mn, and Al worked well to identify differences between flows. Data developed by Helm-Clark and Hertzog during the 2003 laboratory-directed research and development project on geochemical logging showed that geochemical signatures can be used to correlate flows in boreholes separated by several miles.^b Scarberry (2003) demonstrated the utility of using geochemical signatures in correlating an important basalt marker bed, the F-flow of Kuntz et al. (1980) through the south-central portion of the INL Site. The results from Scarberry (2003) and Chadwick (2004) show that geochemical profiling can resolve flow units at a finer scale than paleomagnetic inclination data.

Some variation occurs in elemental results for any basalt flow (Bates 1999). It is therefore necessary to know if two different measurements are part of the same Gaussian distribution about a mean or if they are truly statistically distinct. Reed, Bartholomay, and Hughes (1997) approached this problem by using hierarchical K-cluster analyses on a combination of Fe, Ca, K, Na, Sc, Co, La, Ce, Sm, Eu, Yb, Hf, Ta, and Th data. Their results identified several INTEC flows with large discrimination confidence levels, including the E, G, and I flows (using the nomenclature of Anderson et al. [1996]), which suggest that these flows are the most suitable to use as marker beds.

Using the ISU geochemical database for basalts on the eastern Snake River Plain compiled by Profs. Hughes and McCurry, Miller calculated 2σ values for individual flows at INTEC and RTC and then compared results for flows of similar age under the two facilities.^c He found that at the 2σ significance level, there were significant differences for Si, Mn, Ca, K, and Sr when comparing RTC and INTEC flows. He also determined that RTC flows with approximate ages of ~460 ka were statistically distinct from those of similar age at INTEC; but RTC flows with ages of ~640 ka were not distinguishable from equivalently aged flows at INTEC.

b. Helm-Clark, C. M., and R. Hertzog, unpublished data, 2003.

c. Miller, M., C. M. Helm-Clark, and T. McLing, unpublished data, 2005.

K-cluster analysis or some other multi-variable method is likely the best way to analyze the large geochemical data sets now available for places like Test Area North (TAN), RWMC, RTC, and INTEC. Trace element results for MIDDLE-2050A and MIDDLE-2051 were delivered in December 2006 and a rigorous statistical treatment of these data is now possible and constitutes the next logical step to refine the stratigraphy of the aquifer in the south central INL where the majority of facilities are located. A preliminary review of the trace element data, however, indicates that trace element behavior and variation between flows is similar to the major element trends discussed immediately above.

Because a multi-variable analysis of both major and trace elements is not yet available for RTC and INTEC, 2σ values and other statistics were calculated for this report using existing major element geochemical data. These statistical measures were derived for the TRA-B3 flow at RTC as defined by Helm-Clark et al. (2005), the upper and lower members of the F-flow as defined by Scarberry (2003), and the upper and lower members of the I flow at INTEC as defined by Anderson et al. (1996). Though not rigorous, an average 2σ value was calculated for each element as a semi-quantitative guide to evaluate statistical significance.

B-1.1 Stratigraphy of Big Southern Butte Basalts and RWMC

The new geochemical data for deep corehole C1A have permitted the testing of a long-standing hypothesis (Spear 1979; Fishel 1993), namely that the two uplifted and exposed basalt sequences on the north flanks of Big Southern Butte should correlate with the stratigraphy below neighboring 400 ka Cedar Butte (Kuntz et al. 1994), which should also correlate with units older than 400 ka under the southern portions of the INL. The basic argument of this hypothesis is that the trachydacite unit at the stratigraphic top of the Big Southern Butte basalt sequence corresponds to the intermediate-composition lavas of 400 ka Cedar Butte. The basalts under Cedar Butte should correlate at least partially with basalts under the neighboring southern portions of the INL Site.

If the hypothesis is true, geochemical profiles should match between the Big Southern Butte data and the newly augmented C1A data. Data for the Big Southern Butte basalts were taken from the ISU geochemical database for the section exposed on the northeast flank of the butte and from Fishel (1993) for the section exposed on the northwest flank of the butte. These were compared with the newly augmented data for deep corehole C1A and are shown in Figure B-1. Though a more rigorous analysis using multi-variant methods would be an appropriate next step, it does appear from simple inspection of the data that, indeed, intervals of basalt match between the C1A and Big Southern Butte basalt sequences.

B-1.2 Stratigraphy of Corehole MIDDLE-2051 and RWMC

Deep corehole MIDDLE-2051 was drilled to 1,179 ft and completed with a Westbay casing. It also was logged with borehole geophysical tools for natural gamma, neutron, gamma-gamma density, and 16-in. and 64-in. normal resistivity. The upper 300 ft of this corehole do not share many features with coreholes in the nearby RWMC area, but starting with a geochemical match for the RWMC D flow, the stratigraphy seen in MIDDLE-2051 matches with most of the deeper units of the RWMC subsurface for the rest of its length, including a thinner but still recognizable F flow (see Figure B-2). The bottom of the aquifer at ~1,125 ft bls was identified based on the onset of authigenic mineral growth and also on the neutron-log baseline shift which is often observed at the top of the sub-aquifer zone.

This corehole was notable for two reasons. First, despite a location next to the Big Lost River, very few sediments were penetrated in this hole. Second, the upper 300 ft were very different from the upper strata of the nearby RWMC, especially the reworked hydroclastic ash unit from 92 to 127 ft bls, an unusual lithology for the INL.

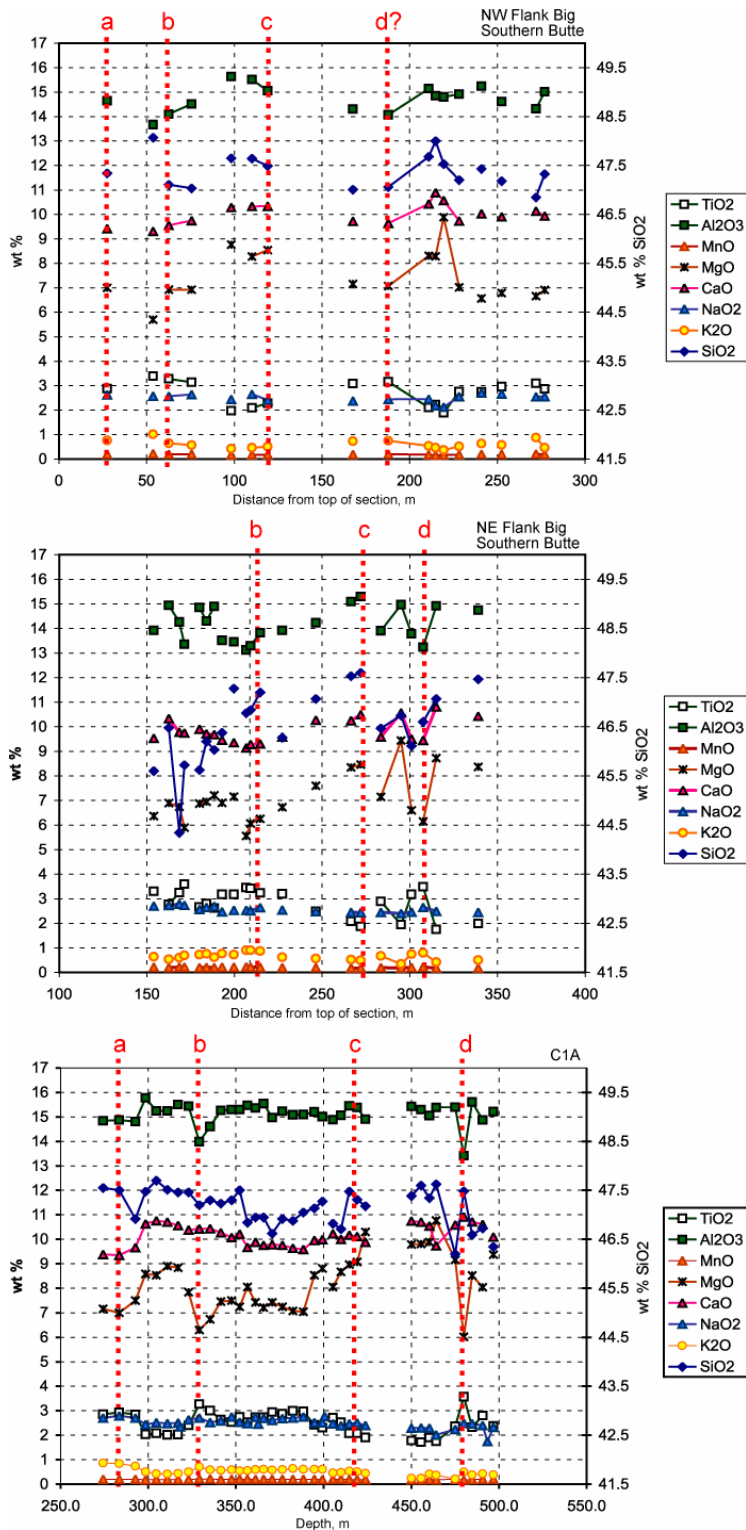
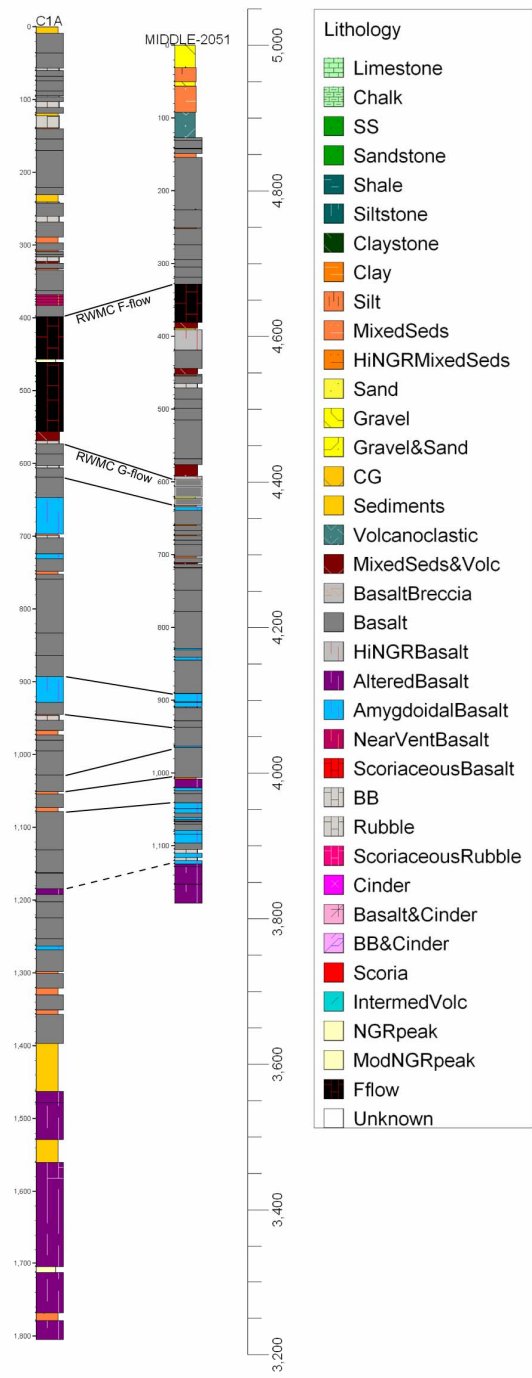


Figure B-1. Geochemical profiles for Corehole C1A, the northeast flank of Big Southern Butte, and the northwest flank of Big Southern Butte. Lettered tielines mark the depths/locations along the respective basalt sequences which are probably correlated based on this preliminary analysis and the preliminary evaluation of statistical significance. Finalization of correlated sections is contingent on recalculating the Big Southern Butte data to the anhydrous and iron basis used in the ISU Geochemical Database.

Figure B-2. Fence diagram of Coreholes C1A and MIDDLE-2051. Correlations are based on lithology, borehole geophysical logs and geochemical profiles.



In retrospect, the lack of fluvium in this corehole is not too unusual in light of the subsurface evidence between Arco and the INL of repeated damming, ponding, and relocation of the Big Lost River. The widespread spatial occurrence of fluvial units in the local stratigraphy shows that the Big Lost River had much greater travel during the Pleistocene than its modern channel and floodplain indicate (Helm-Clark and Link 2006).

B-1.3 Revised Stratigraphy of the RTC and Environs

Newly available geochemical data for the RTC area require only minor changes to the OU 10-08 geological conceptual model. Helm-Clark et al. (2005) proposed a stratigraphic sequence with seven named flows in the subsurface south of RTC. These initial results, originally shown in Figure 4-2 from their report, are reproduced below in Figures B-3 and B-4. The plots on the left in Figures B-3 and B-4 show the geochemical profiles for Wells USGS-80 and TRA-5A based on the data available when that report was written. Flow TRA-B1 was the uppermost basalt in Well USGS-80 but was absent from Well TRA-5A. Flow TRA-B2 was the uppermost flow in Well TRA-5A and hypothesized as present in Well USGS-80 based on lithology, geophysical logs and one anomalous paleomagnetic inclination. In addition, the geochemical profile for the upper half of flow TRA-B6 in Well TRA-5A did not match its lower half nor did it match the profile of this flow in USGS-80. Thus, Helm-Clark et al. (2005) speculated that the upper half of TRA-B6 in Well TRA-5A might be an unidentified flow unit distinct from TRA-B6 as represented by the lower portion of the original unit.

To resolve questions raised in the Helm-Clark et al. (2005) study, additional samples were gathered for further geochemical analyses: five from TRA-5A and six from USGS-80 including the interval proposed for TRA-B2. At the time of the Middle-1823 study (Helm-Clark et al. 2005), other than USGS-80 and TRA-5A, no wells near RTC had been profiled geochemically due to a lack of available core. Most of the aquifer wells at RTC were drilling in the 50s and early 60s when cores were not collected on the cable-tool rigs in use at the time. In addition, no core was collected from the upper 500 ft of Well Middle-1823, one of the few deep boreholes near RTC drilled with modern rotary equipment. Subsequently, TRA-8, the closest corehole to Middle-1823, was targeted for geochemical analyses to help fill the gap in data for the upper 500 ft of the RTC subsurface. Unfortunately, there was less TRA-8 core than the core library records indicated so only five geochemical samples were collected. Even with the additional geochemical data for the newly collected samples from USGS-80, TRA-5A, and TRA-8, the interval from 300 to 500 ft bls remains unsampled in the RTC subsurface.

The revised stratigraphy and geochemical profiles for USGS-80 and TRA-5A are shown on the right side in Figures B-3 and B-4. The updated geochemical profiling suggests that the interval proposed by Helm-Clark et al. (2005) as flow TRA-B2 in USGS-80 cannot be statistically distinguished from flow TRA-B3 immediately below it; also, this interval is clearly distinct from the type location for flow TRA-B2 in Well TRA-5A. In addition, the updated geochemical profile for USGS-80 suggests that flow TRA-B1 in this well may be two distinct flow units.

Flows TRA-B3, TRA-B4 and TRA-B5 in Wells USGS-80 and TRA-5A remain unchanged from Helm-Clark et al. (2005). The new data from TRA-8 indicates that the intervals sampled in this well are the same as TRA-B3 and TRA-B5 in Well TRA-5A.

In Well TRA-5A, the additional geochemical results make it clear that there is an additional unnamed flow unit distinct from TRA-B6 immediately underneath it. The additional data point also improves the available geochemical fingerprint for flow TRA-B7.

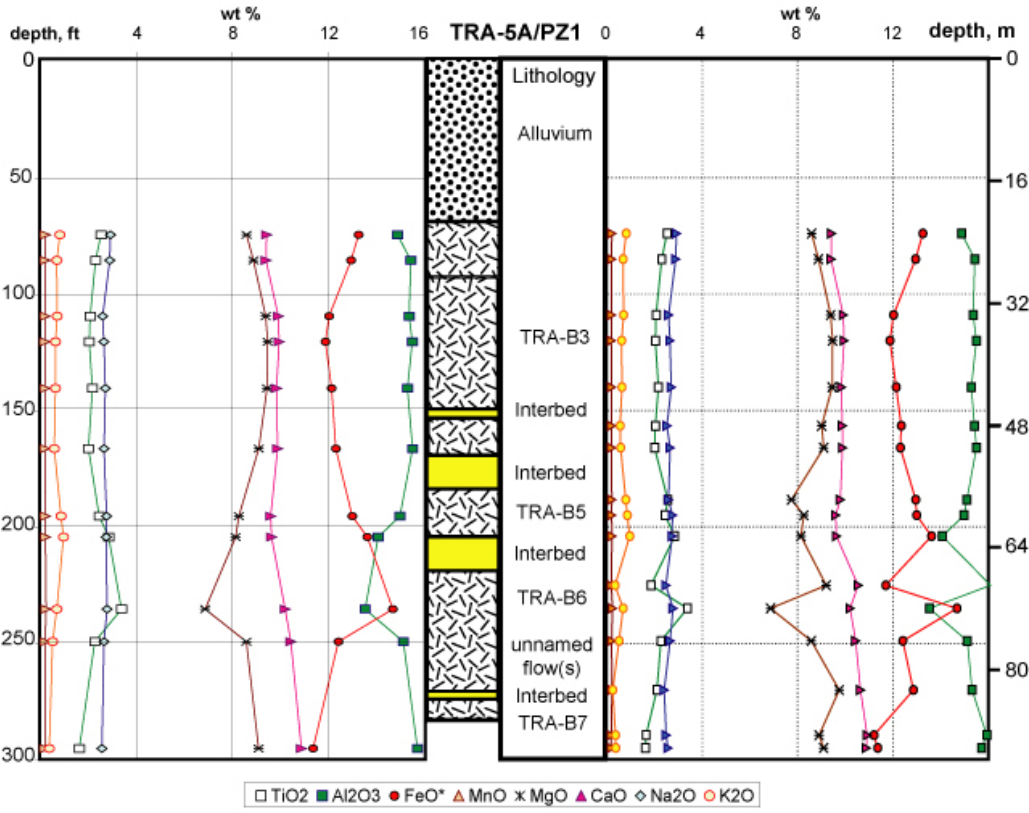


Figure B-3. Stratigraphic columns and geochemical profiles for Well TRA-5A (sometimes referred to as PZ1). The left-side plot shows the data available to Helm-Clark et al. (2005). The right-side plot shows the combined data from Helm-Clark et al. (2005) and this study.

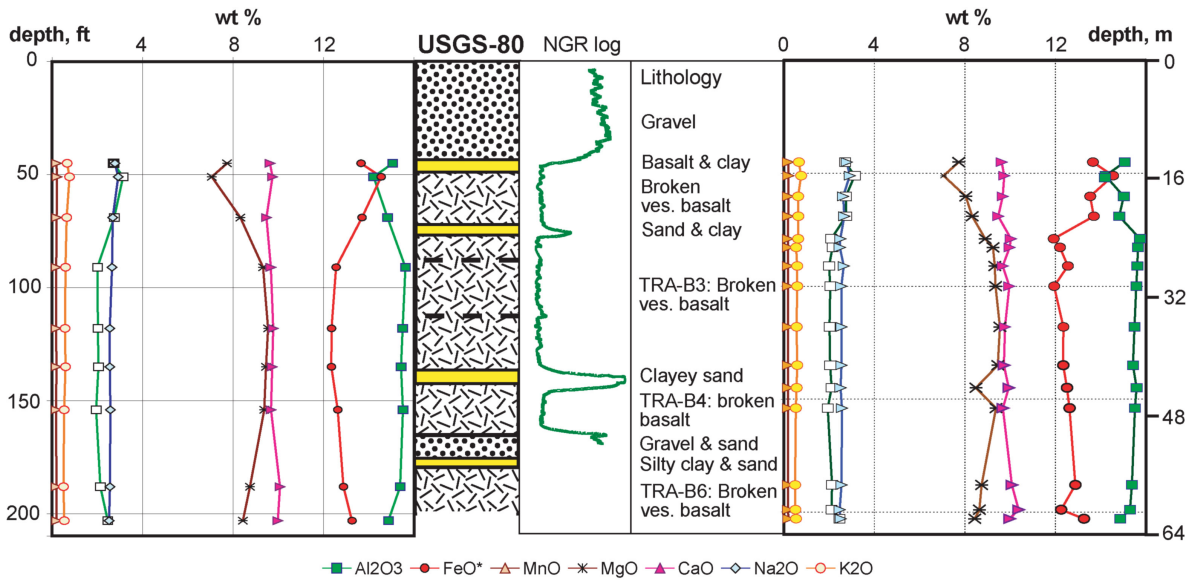


Figure B-4. Stratigraphic column and geochemical profiles for Well USGS-80. The left-side plot shows the data available to Helm-Clark et al. (2005). The right-side plot shows the combined data from Helm-Clark et al. (2005) and this study.

B-1.4 Stratigraphy of Corehole MIDDLE-2050A and INTEC

Deep corehole MIDDLE-2050A was drilled to 1,427 ft bls and completed with a Westbay casing. The location of MIDDLE-2050A is shown on Figure B-5. The stratigraphic column for MIDDLE-2050A is shown in Figure B-6.

The location for MIDDLE-2050A is in the middle of a box with corners at USGS-39, USGS-43, USGS-66, and USGS-84. Wells USGS-66 and USGS-84 display stratigraphy that is correlated to the subsurface at RTC (Helm-Clark et al. 2005). Wells USGS-39 and USGS-43 display stratigraphy correlated to the subsurface under the southern two-thirds of INTEC. These four wells represent the narrowest gap between RTC and INTEC style stratigraphies.

The stratigraphic mismatch between RTC and INTEC is shown in Figure B-7 which shows the vertical discrepancy between units of similar ages. As already noted, the units with ages approximately equal to 460 ka have statistically distinct geochemical profiles but units with ages of approximately 640 ka cannot be distinguished geochemically.^d Geochemical profiling shows that MIDDLE-2050A has a stratigraphic column similar to those of USGS-121 and -123 (see Figure B-8). The similarity of these three wells argues that MIDDLE-2050A shares stratigraphy with most of the INTEC subsurface: this narrows the data gap between INTEC and RTC stratigraphy to less than 1,000 ft.

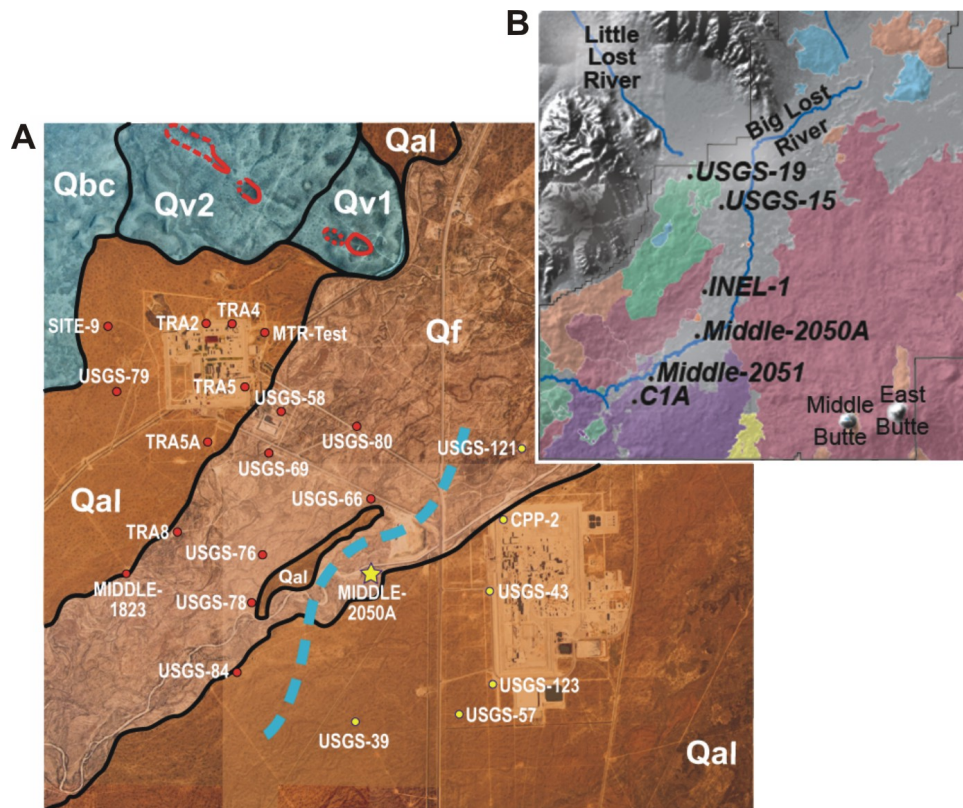


Figure B-5. (A) Surficial geology of the RTC-INTEC area showing selected well locations, and (B) larger domain showing additional selected well locations.

d. Miller, M., C. M. Helm-Clark, and T. McLing, unpublished data, 2005.

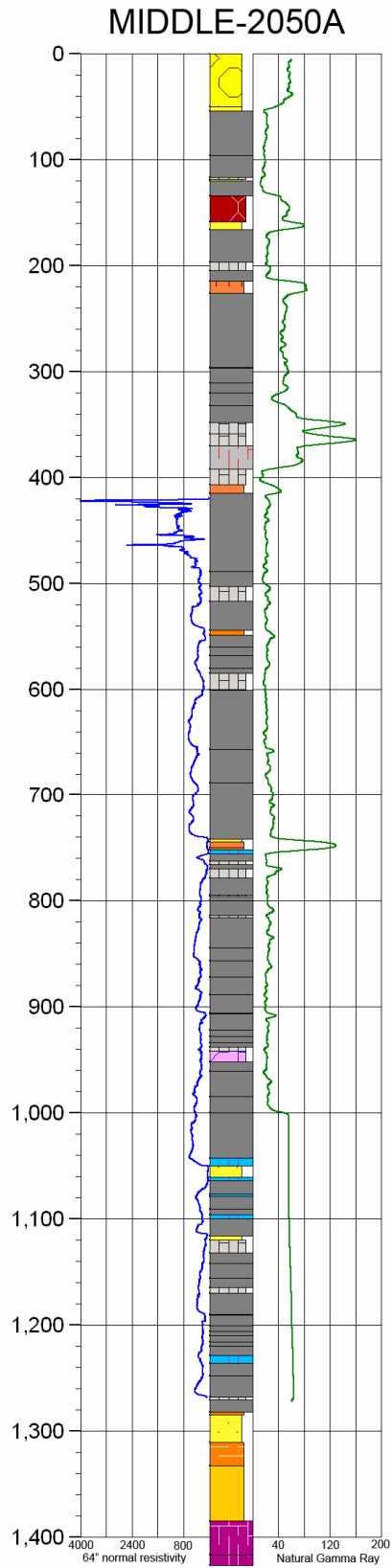


Figure B-6. Stratigraphic column for MIDDLE-2050A. Lithological units are the same as shown in the legend for Figure B-2.

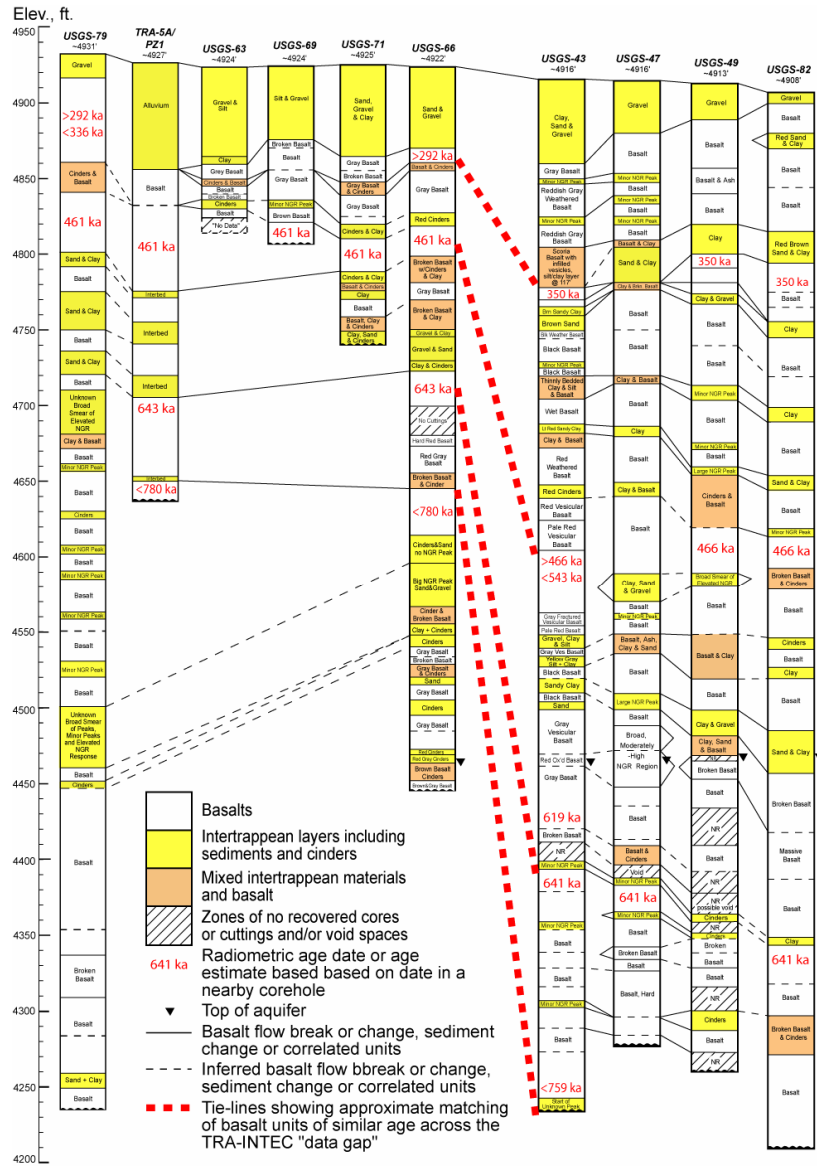
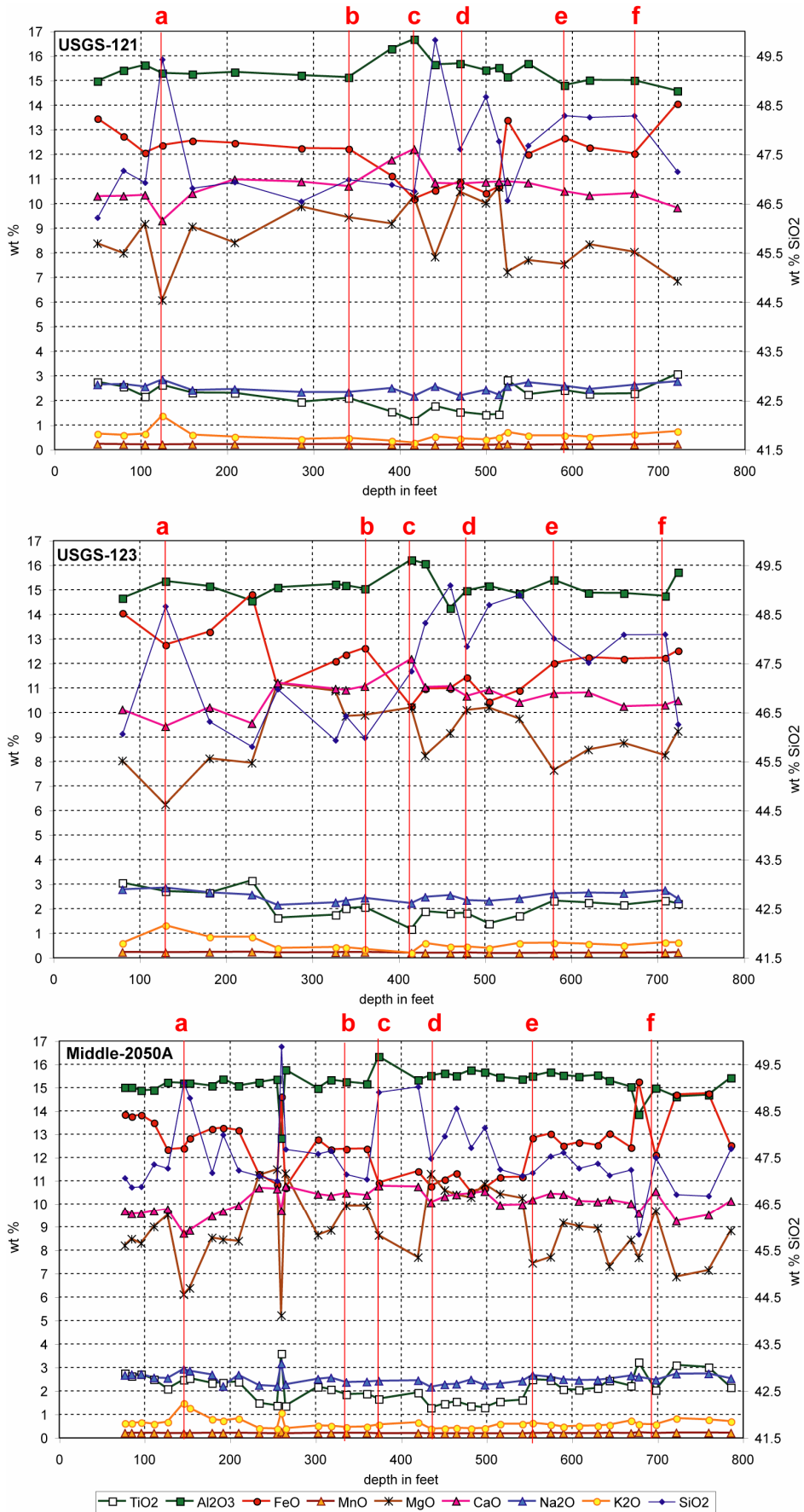


Figure. B-7. Fence diagram across the TRA-INTEC data gap showing the vertical discrepancies between basalts of similar ages.

Figure B-8. Geochemical profiles for Coreholes MIDDLE-2050A, USGS-121, and USGS-123. Selected correlation intervals shared by all three coreholes are denoted by letters.



B-1.5 Stratigraphy between RWMC and Materials and Fuels Complex (MFC) in the Vicinity of U.S. Route 20

During FY 2006, several well records were located that previously were believed to have been lost. Some of these data were found by mining some of the oldest literature written about the INL in the 1950s. One record, for Well ARA-3, was discovered through inquiries to the original drilling company, Casperson's Drilling of Blackfoot, ID. The assemblage of these well records resulted in the cross section shown in Figure B-9. East of Auxiliary Reactor Area (ARA), the stratigraphic columns for these wells show the sediment-poor subsurface with increased near-vent facies expected for boreholes this close to the volcanically productive Axial Volcanic High. West of ARA, the stratigraphic sequence is characterized by many thin sediment and cinder layers in the upper half of these boreholes.

Unit Qal is Quaternary alluvium. Qbc is Quaternary basalt that is younger than 337 ka but older than 292 ka. Qv1 is the Quaternary vent at AEC Butte, dated at 626 ka. Qv2 is an unnamed vent dated at 367 ka. Qf is the Quaternary floodplain of the Big Lost River. All age dates are from the compilation of Hall-Mark et al. (2005). Wells that display RTC style stratigraphy are shown with red symbols. Wells that display INTEC stratigraphy are shown with yellow symbols. The location of MIDDLE-2050A is denoted by a yellow star. The estimated division between RTC and INTEC style stratigraphies is shown as a dashed blue line.

The stratigraphic cross section in Figure B-9 contains two intermediate-composition volcanic sills, one at ~4,250 ft elevation underneath and east of the ARA and one at ~3,800 ft elevation halfway between INL Gate 1 and the Naval Reactors Facility (NRF) site. It also contains two thick clay-rich sediment layers at ~4,200 ft elevation and ~4,000 ft elevation between ARA and CFA.

B-2. DEEP SEDIMENTS SOUTH OF HOWE

Because of the preferential flow paths that are indicated by groundwater chemistry and temperatures, the NRF tablelands were reevaluated for potential causes of lowered hydraulic conductivity. Two features may account for the low groundwater velocities in this area. The first has already been discussed, namely the AEC Butte volcanic rift zone. The second is a combination of features. Six km northwest of NRF is a volcanic vent in a kipuka. This vent is older than 780 ka since it has reversed-polarity paleomagnetic remanence. Another vent is located in a kipuka 5 km northwest of RTC. A third volcanic vent, the 529 ka (Kuntz et al. 1994) State Butte, is located a short distance to the northeast of NRF. These volcanic vents are indicative of buried volcanic vents under the Big Lost River floodplain and in the subsurface of the NRF tablelands.

The occurrence of significant thicknesses of sediments in the aquifer south of Howe may impact hydraulic conductivity. A negative gravity anomaly exists under the north end of the NRF tableland, indicative of a block of lower density materials in comparison to surrounding rocks. The kipuka-hosted vent northwest of NRF and five wells encircle this gravity anomaly. The stratigraphic evidence from these five wells shows that a >100-ft thick south-dipping package of either pluvial or fluvial sediment intersects and passes through the aquifer (see Figure B-10). Several thin layers of near-vent materials like cinders occur above the thick sediment package.

This south-dipping package of fine-grained sediments within the area of the sinks of the Little Lost River likely decreases hydraulic conductivity. This combination of near-vent facies and fine-grained sediments on the north edge of the NRF tableland provides a plausible explanation for preferential groundwater flow paths to the east toward the West Axial Slope and away from the NRF and Crater Butte tablelands.

Figure B-9. Stratigraphic cross section from Well STF-PIE-A-001 to USGS-002. Lithological units are the same as shown in the legend for Figure B-8. This cross section runs approximately along U.S. Route 20 shows the two deep clayey, presumed-lacustrine units between 3,900 and 4,200 ft elevation. The shallower of the two intermediate-composition elevation; the deeper sill is at ~3,900 ft elevation.

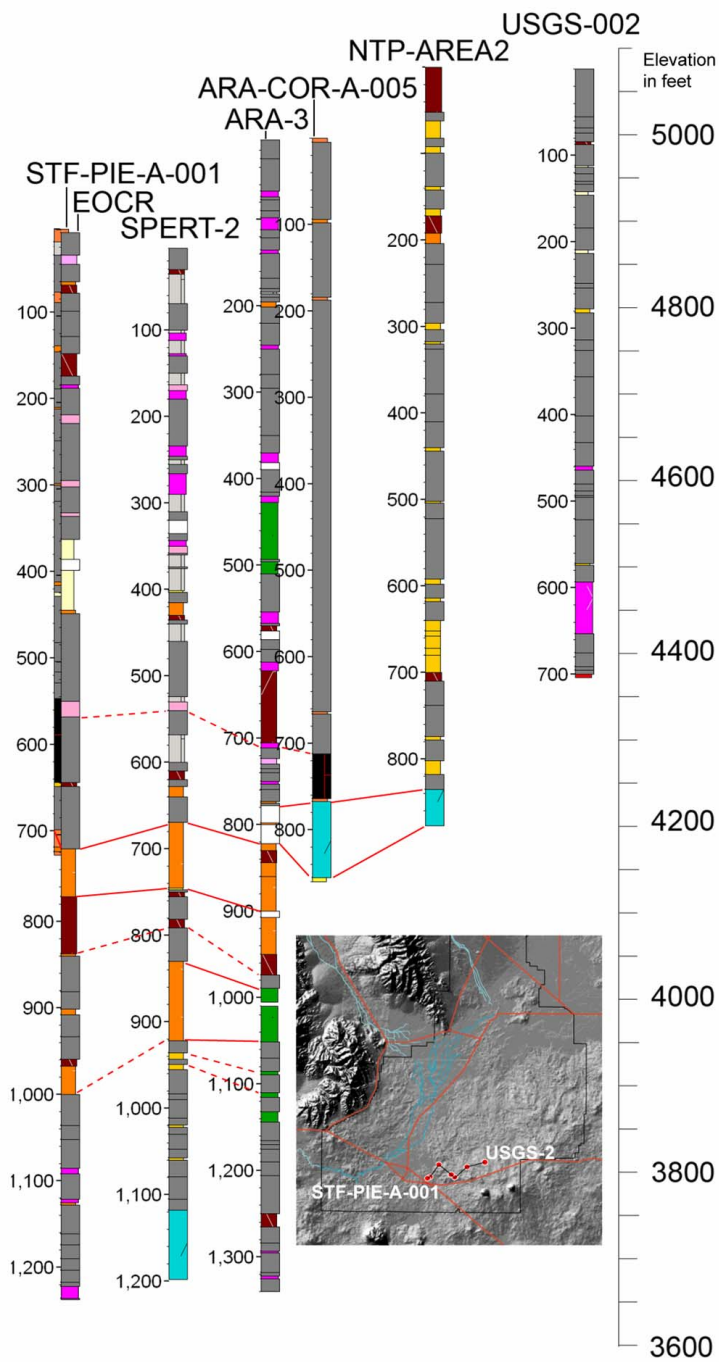


Figure B-9. Stratigraphic cross section from Well STF-PIE-A-001 to USGS-002. Lithological units are the same as shown in the legend for Figure B-8. This cross section running north of and approximately along U.S. Route 20 shows the two deep clayey, presumed-lacustrine units between 3,900 and 4,200 ft elevation. The shallower of the two intermediate-composition sills is at ~800 ft elevation; the deeper sill is at ~3,900 ft elevation.

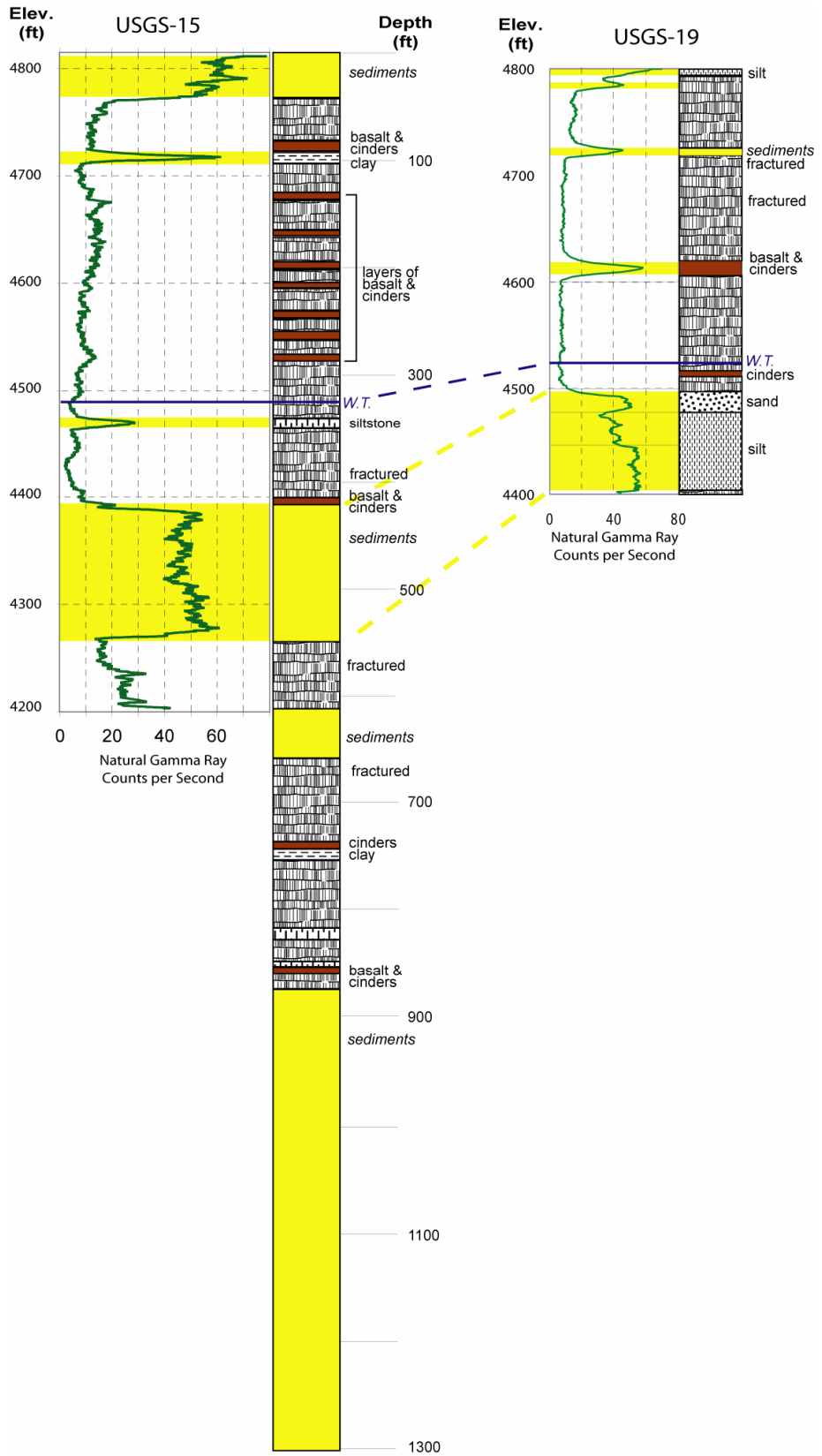


Figure B-10. Fence diagram between USGS-19 to the northwest and USGS-15 to the southeast. These two boreholes are located 3 and 2 miles southeast of Howe, respectively. The top of the thick, south-dipping sediment layer is at 4,500 ft elevation in USGS-19 and 4,400 ft elevation in USGS-15. Groundwater flowlines out of the Howe area toward the eastern Snake River Plain are parallel to a line drawn between USGS-19 and USGS-15. The SRPA is less than 200 ft thick at USGS-19, so it is likely that flow velocity retardation and refraction occur through the thick sediment unit between these two boreholes.

Several hundred feet of sediment was logged in the bottom half of USGS-15, below 4,000 ft elevation. Based on thickness, depth and intercalation of basalt, the current working hypothesis is that these sediments are Plio-Pleistocene in age. Based on gravity (Mankinen et al. 2004; Bruhn, Wu, and Lee 1992) and seismic data (Payne and Oldow 2005) the deep sediments in Well USGS-15 are possibly down-dropped by an unrecognized step fault.

B-3. INTEC-RTC DATA GAP AND SUBSURFACE STRUCTURES WEST OF THE BIG LOST RIVER

Basalt age dates from coreholes indicate that a stratigraphic offset occurs between INTEC and RTC. The exact location of this offset has not been identified. The area between offset coreholes is known as the INTEC-RTC data gap. The purpose of this section is to present the hypotheses that the stratigraphic offset may represent an inactive step fault of limited displacement or a buried NE-trending volcanic rift feature aligned along the current floodplain of the Big Lost River. Regional and local scale information supports these hypotheses and suggests that as many as two distinct stratigraphic blocks occur west of the river, one with a stratigraphic sequence that is characteristic of the RTC subsurface and one with a stratigraphic sequence characteristic of the NRF subsurface that includes a local basement of down-dropped sediments underneath >780,000-year old basalts south of Howe.

The hypothesized subsurface structure presented here provides ample explanation for the differences in stratigraphy, heat flux, gravity and aeromagnetic anomalies, groundwater flow and groundwater chemistry observed for the basalt tablelands west of the Big Lost River when compared to the rest of the INL Site. A concentration of analytical effort regarding this area is justified by the simple happenstance that the majority of facilities of the south central INL are located on or adjacent to this area.

Several studies have mapped step faults, i.e., sets of normal faults stepping down into the plain from the basin and range, trending NE-SW parallel to the eastern Snake River Plain-basin and range boundary. Zentner (1989) compiled a map of all known NE-trending normal faults along the NW and SE boundaries of the eastern Snake River Plain which included 76 normal faults younger than 10 Ma east of a north-south line through Twin Falls. Included in these 76 faults are eight sets of step faults of three or more faults. Most are mapped in basin and range rocks, though two sets of step faults are mapped on the eastern Snake River Plain proper. Zentner (1989) also mapped in detail the step fault set in Heise Volcanic Field tuffs in and around Lidy Hot Springs. These mostly-normal faults form a gridwork with NE and NW trends. Displacements are modest, in the tens to hundreds of meters for individual faults. Based on the ages of unbroken overlying units, fault activity is no younger than 2 Ma.

The Bruhn, Wu, and Lee (1992) study of the Lemhi Fault complex shows a similar though smaller set of step faults, three mapped and one inferred, in the rocks at the southern terminus of the Lemhi Range near Howe. Timing the activity on these faults is poorly constrained^e between the emplacement of the 6 Ma Blue Creek tuffs that these faults cut (Morgan and McIntosh 2005; Kuntz et al. 2003) and the last motion on the Lemhi range front fault at ~20 ka (Bruhn, Wu, and Lee 1992). More recent mapping shows that one of these faults displaces Late Quaternary talus (Kuntz et al. 2003). The exact number and placement of the Lemhi terminal step fault set varies between different studies: e.g., while Kuntz et al. (2003) has three at ~2 km spacings, Kuntz et al. (1994) shows eight in that same interval, some of which are inferred. Kuntz et al. (1994) also maps several widely spaced step faults at the terminal end of the Beaverhead Range (see Figure B-11), three sets of four step faults in the Arco Hills closest to Butte City, plus one set of three and an adjacent set of eight (some inferred) in the Arco Hills next to where the old stage road intersects Route 22 (Figure B-12).

e. Rodgers, D., ISU, personal communication, August 30, 2006.

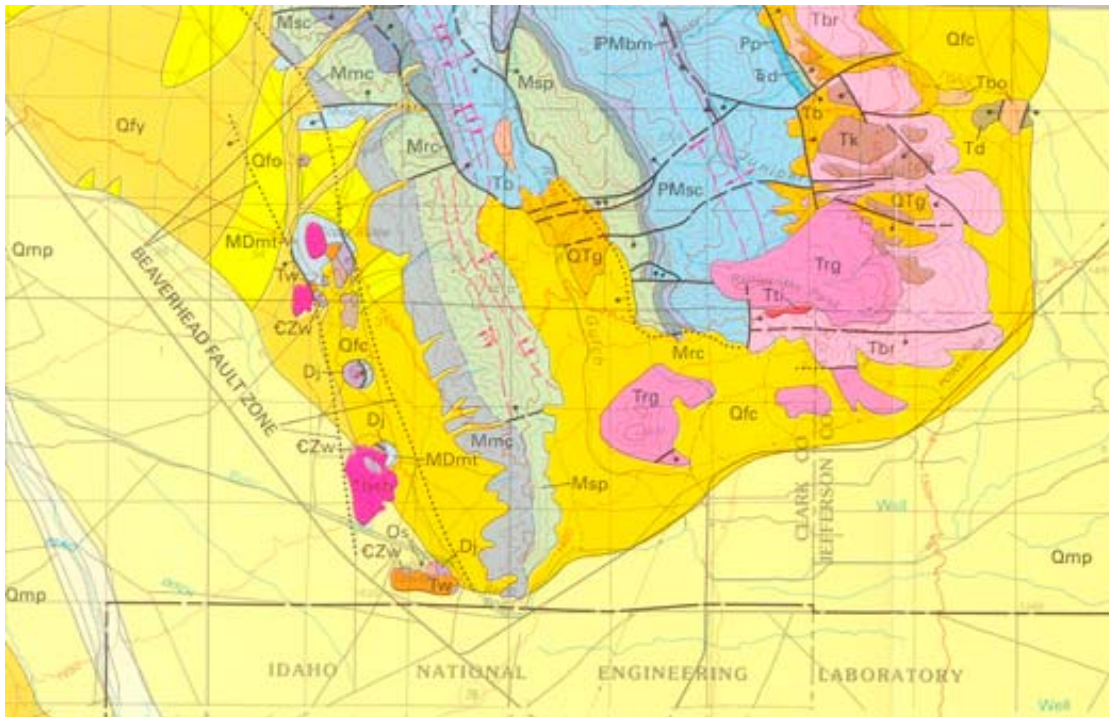


Figure B-11. Surficial geology of faults at the end of the Beaverhead Range, north of the INL. Adapted from Kuntz et al. (1994). Grid based on 1-mile square Jeffersonian section.

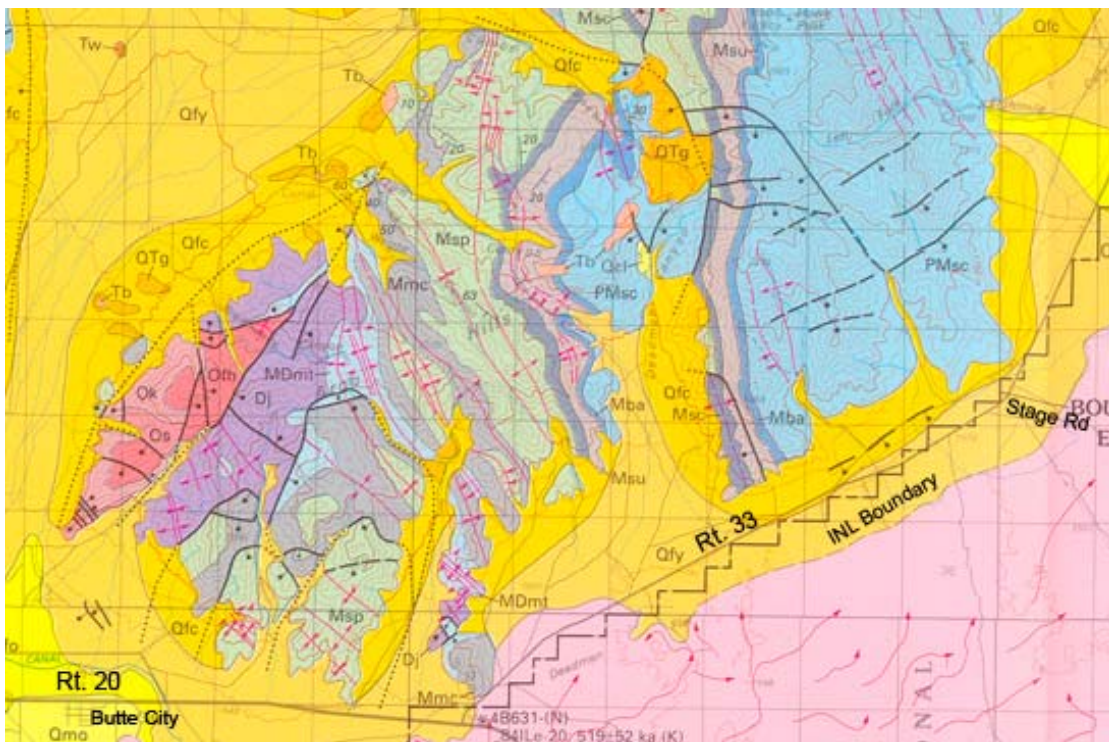


Figure B-12. Surficial geology of the Arco Hills adjacent to Route 22 south of Howe. Adapted from Kuntz et al. (1994). Grid based on 1-mile square Jeffersonian section.

The continuing discussion as to whether NE-SW trending faults occur along the boundary of the eastern Snake River Plain and the basin and range is not new (e.g., Stearns, Crandall, and Stewart 1938). The evidence against such faults is clear. Most fault and fissure features on the eastern Snake River Plain are aligned perpendicular, not parallel, to the long axis of the plain and physical evidence is lacking—such as scarps and vents to support the existence of NE-SW trending boundary faults. Kuntz, Covington, and Schorr (1992) dismissed the mapped faults of Zentner (Rodgers and Zentner 1989; Zentner 1989) as evidence for boundary faults because these were older inactive faults which were discontinuous and were not on the eastern Snake River Plain proper but in the basin and range. Kuntz, Covington, and Schorr (1992) noted that phenomena including eruptions along such boundary faults were not observed though they would be expected and indeed have been observed in true rift valleys. It is the lack, however, of visible and mapable features associated with boundary faults that is most convincing.

The evidence for NE-SW trending step faults along the boundary of the basin and range and eastern Snake River Plain is almost entirely indirect, i.e., not directly observable or mapable. The indirect evidence that comes from geophysical investigations can be summed up as follows. At least three seismic studies have identified fault-like features that are 1.8 and 5 km inboard and 3 km outboard of the eastern Snake River Plain boundary, the former two having ~1 and ~2 km vertical displacement respectively. One gravity survey was interpreted to place a faulted graben in the shallow subsurface at the end of the Lemhi Range and another mapped the location of step faults 3 and 5 km inboard of the plain boundary north of Pocatello. The steep gravity gradient along the south and southeast flanks of the Arco Hills has been interpreted in several studies as evidence of a boundary fault (e.g., Morris et al. 1964). The elevated heat flow at the boundary between eastern Snake River Plain and basin and range indicates that there is some sort of deep conduit through which geothermal fluids can travel to the surface.

The INTEC stratigraphy in MIDDLE-2050A narrows the data gap with the nearest well with RTC-stratigraphy, USGS-66, to approximately 1,600 ft (see Figure B-5). The dashed blue line in Figure B-5 is interpolated at halfway between the wells that now define the known extents of the RTC and INTEC stratigraphic blocks. The perpendicular distance from MIDDLE-2050A to this line is less than 1,000 ft. There are few ways to explain such a complete change in stratigraphy over such a short distance other than a steep fold, a fault, or volcanic rift zone with NE-SW orientation. As there is a continuum between steep folds and faults, for convenience, we will include the former with the latter for the rest of the discussion.

Placement of a NE-trending fault between the blocks of INTEC and RTC stratigraphy is not unreasonable given the geophysical evidence of buried step faults inboard of the eastern Snake River Plain-basin and range boundary. In the 1964 geophysical data, a steep gravity gradient consistent with a fault was aligned with the NE trend of the Big Lost River floodplain. The difference in the basalt of ~460 ka age coupled with the statistically indistinct basalts of ~640 ka age argues for a fault that was active around a half a million years ago but has been quiescent since then.^f The displacement of ~100 m between units of ~640 ka age is similar to the step fault displacements documented by Zentner (1989).

There are problems with placing a fault between RTC and INTEC. First, Pankratz and Ackermann (1982) found a 1 km step only 1.8 km from the boundary of the plain; this feature does not coincide with the location of the RTC-INTEC data gap. Next, the data gap is 12 km inboard from the eastern Snake River Plain boundary, which is further into the plain than any of the geophysically mapped step faults reviewed here. Also, no one has recognized any fault gouge in the many boreholes drilling in the vicinity of the data gap.

f. Miller, M., C. M. Helm-Clark, and T. McLing, unpublished data, 2005.

Kuntz, Covington, and Schorr (1992) objected to boundary faults, in part because no evidence existed of the leaky volcanism expected of such faults. Considering the abundant near-vent facies seen in RTC stratigraphy (Helm-Clark et al. 2005) and under the Tank Farm at INTEC, this is not an objection that would apply to a hypothesized fault in the RTC-INTEC data gap.

The AEC Butte rift zone acts as a stratigraphic divide between the Crater Butte and NRF volcanic tablelands (Helm-Clark et al. 2005). Given the evidence of near-vent facies in wells along the data gap, it is possible that the data gap is derived from a NE-trending volcanic rift zone or cluster of volcanic centers forming as a similar stratigraphic divide. A series of vents along or near the Big Lost River does exist, including a vent where the Big Lost River makes its left turn to head northeast from Box Canyon; a suspected vent near USGS-38 discussed by Anderson, Kuntz, and Davis (1999); the proposed scoria cone under the INTEC Tank Farm; the near-vent facies in the Fire Station Well (Helm-Clark et al. 2005); and State Butte next to NRF. Such a NE-trending set of volcanic vents already exists on the eastern Snake River Plain immediately north of Quaking Aspen Butte, a trend that is 25 km inboard of the boundary of the plain.

B-4. REFERENCES

- Anderson, S. R., and R. C. Bartholomay, 1995, "Use of natural-gamma logs and cores for determining stratigraphic relations of basalt and sediment at the Radioactive Waste Management Complex, Idaho National Engineering Laboratory, Idaho," *Journal of the Idaho Academy of Science*, Vol. 31 (1), pp. 1–10.
- Anderson, S. R., D. J. Ackerman, M. J. Liszewski, and R. M. Freiburger, 1996, *Stratigraphic Data for Wells at and near the Idaho National Engineering Laboratory, Idaho*, DOE/ID-22127, Rev. 0, U.S. Geological Survey Open-File Report 96-248, May 1996.
- Anderson, S. R., M. A. Kuntz, and L. C. Davis, 1999, *Geologic Controls of Hydraulic Conductivity in the Snake River Plain Aquifer at and near the Idaho National Engineering and Environmental Laboratory, Idaho*, U.S. Geological Survey Water Resources Investigation Report 99-4033.
- Bates, David, L., 1999, *The In Situ Chemical Fractionation of an Eastern Snake River Plain Basalt Flow: Implications for Heterogeneous Chemical Interaction with Groundwater Contaminants*, 146 p., 2 plates.
- Bruhn, R. L., D. Wu, and J. J. Lee, 1992, *Final Report on the Structure of the Southern Lemhi and Arco Fault Zone, Idaho*, EGG-NPR-10680, EG&G Idaho, Inc.
- Chadwick, C. G., 2004, *Petrogenesis of an evolved olivine tholeiite and chemical stratigraphy of Cores USGS 127, 128, and 129 Idaho National Engineering and Environmental Laboratory*, M. S. Thesis: Idaho State University, Pocatello, Idaho.
- Champion, D. E., M. A. Lanphere, S. R. Anderson, and M. A. Kuntz, 2002, "Accumulation and subsidence of Late Pleistocene basaltic lava flows of the eastern Snake River Plain, Idaho," in Link, P. K., and L. L. Mink, eds., *Geology, Hydrogeology, and Environmental Remediation, Idaho National Engineering and Environmental Laboratory, Eastern Snake River Plain*, Geological Society of America Special Paper 353, pp. 175–192.
- DOE-ID, 2004, *Idaho National Engineering and Environmental Laboratory Operable Unit 10-08 Sitewide Groundwater Model Work Plan*, DOE/NE-ID-11188, Rev. 0, U.S. Department of Energy Idaho Operations Office, December 2004.

- Fishel, M. L., 1993, *The geology of uplifted rocks on Big Southern Butte, implications for the stratigraphy and geochemistry of the eastern Snake River plain, Idaho*, M. S. Thesis: Idaho State University, Pocatello, Idaho.
- Helm-Clark, C. M., and P. K. Link, 2006, "Sediment-Basalt Architecture, Pliocene and Pleistocene Eastern and Central Snake River Plain," *Eos Transactions, American Geophysical Union*, 87(52), Fall Meeting Suppl., Abs. V51D-1709.
- Helm-Clark, C. M., and D. W. Rodgers, 2004, "New 40AR/39AR data from Pleistocene basalts on the East Snake River Plain, Idaho, and their implications for the subsurface structure of the Big Lost Trough," *Abstracts with Programs – Geol. Soc. of America, Rocky Mountain/Cordillera Joint Section*, April 2004, Vol. 36, Issue 4, pp. 98.
- Helm-Clark, C. M., S. L. Ansley, T. McLing, and T. R. Wood, 2005, *Borehole and Well Middle-1823 and Its Relationship to the Stratigraphy of the South-Central Idaho National Laboratory*, ICP/EXT-05-00790, U.S. Department of Energy, Idaho Completion Project, March 2005, 96 pp.
- Hughes, S. S., M. McCurry, and D. J. Geist, 2002, "Geochemical correlations and implications for the magmatic evolution of basalt flow groups at the Idaho National Engineering and Environmental Laboratory," Link, P. K., and L. L. Mink, (eds.), *Geology, Hydrogeology, and Environmental Remediation, Idaho National Engineering and Environmental Laboratory, Eastern Snake River Plain*, Geological Society of America Special Paper 353, pp. 151–173.
- Kuntz, M. A., G. B. Dalrymple, D. E. Champion, and D. J. Doherty, 1980, *An evaluation of potential volcanic hazards of the Radioactive Waste Management Complex, Idaho National Engineering Laboratory, Idaho* (includes Petrography and paleomagnetism of volcanic rocks at the Radioactive Waste Management Complex, Idaho National Engineering Laboratory, Idaho, with an evaluation of potential volcanic hazards): U.S. Geological Survey Open-File Report 80-388, 68 p.
- Kuntz, M. A., H. R. Covington, and L. J. Schorr, 1992, "An overview of basaltic volcanism on the eastern Snake River Plain, Idaho," in Link, P. K., M. A. Kuntz, and P. L. Platt, eds., *Regional Geology of Eastern Idaho and Western Wyoming*, Geological Society of America Memoir 179, pp. 227–267.
- Kuntz, M. A., B. Skipp, M. A. Lanphere, W. B. Scott, K. L. Pierce, G. B. Dalrymple, D. E. Champion, G. F. Embree, W. R. Page, L. A. Morgan, R. P. Smith, W. R. Hackett, and D. W. Rodgers, 1994, "Geological map of the Idaho National Engineering Laboratory and adjoining areas, eastern Idaho," United States Geological Survey Miscellaneous Investigations Series Map I-2330, scale 1:100,000.
- Kuntz, M. A., P. L. Link, D. L. Boyack, J. K. Geslin, L. E. Mark, M. K. V. Hodges, M. E. Kauffman, D. E. Champion, M. R. Lanphere, D. W. Rodgers, and M. H. Anders, 2003, "Geologic Map of the Northern and Central Parts of the Idaho National Engineering and Environmental Laboratory, Eastern Idaho," Idaho Geological Survey, Geologic Map 35.
- Kuntz, M. A., D. E. Owen, D. E. Champion, P. B. Gans, S. C. Smith, and C. Brossy, 2004, "Geology of the Craters of the Moon 30' X 60' map area and new perspectives on basaltic volcanism of the eastern Snake River plain, Idaho," in Haller, D. M., and S. H. Wood, eds., *Geological field trips in southern Idaho, eastern Oregon, and northern Nevada*, Geological Society of America Field Guide, pp. 136-155.

- Mankinen, E. A., T. G. Hildenbrand, M. L. Zientek, S. E. Box, A. B. Bookstrom, M. H. Carlson, and J. C. Larsen, 2004, *Guide to Geophysical Data for the Northern Rocky Mountains and adjacent areas, Idaho, Montana, Washington, Oregon, and Wyoming*, U.S. Geological Survey Open-File Report 2004-1413.
- Mazurec, J., 2004, *Genetic controls on basalt alteration within the Eastern Snake River Plain Aquifer System, Idaho*, M. S. Thesis: Idaho State University, Pocatello, Idaho.
- Morgan, L. A., and W. C. McIntosh, 2005, "Timing and development of the Heise volcanic field, Snake River Plain, Idaho, western USA," *GSA Bulletin*; Vol. 117, pp. 288–306.
- Morris, D. A., J. T. Barraclough, G. H. Chase, W. E. Teasdale, and R. G. Jensen, 1964, *Hydrology of subsurface waste disposal, National Reactor Testing Station, Idaho, annual progress report, 1964*, U.S. Atomic Energy Commission, Idaho Operations Office Publication, IDO-22047, 186 pp.
- Pankratz, L. W., and H. D. Ackermann, 1982, *Structure Along the Northwest Edge of the Snake River Plain Interpreted from Seismic Refraction*, *J. Geophys. Res.*, Vol. 84, pp. 2676–2682.
- Payne, S. J., and J. Oldow, 2005, *Longitudinal displacement transfer system linking basin and range faults and volcanic rift zones across the northwestern boundary of the eastern Snake River Plain, Idaho*, Geological Society of America Abstracts with Programs, Vol. 37, No. 7.
- Reed, M. F., R. C. Bartholomay, and S. S. Hughes, 1997, "Geochemistry and stratigraphic correlation of basalt lavas beneath the Idaho Chemical Processing Plant, Idaho National Engineering Laboratory," *Environmental Geology*, Vol. 30 (1/2), pp. 108–118.
- Rodgers, D. W., and N. C. Zentner, 1989, *Fault Geometries Along the Northern Margin of the Eastern Snake River Plain, Idaho*, Geol. Soc. of America Abstracts with Programs, 20, pp. 465–466.
- Scarberry, K. C., 2003, *Volcanology, Geochemistry, and Stratigraphy of the F Basalt Flow Group, Eastern Snake River Plain, Idaho*, M. S. Thesis: Idaho State University, Pocatello, Idaho.
- Smith, R. B., L. W. Braile, M. M. Schilly, J. Ansorge, C. Prodehl, M. Baker, J. H. Healey, S. Mueller, and R. Greensfelder, 1982, "The Yellowstone- eastern Snake River Plain seismic profiling experiment: Crustal structure of Yellowstone," *J. Geophys. Res.*, Vol. 84, pp. 2583–2596.
- Spear, D., 1979, *The geology and volcanic history of the Big Southern Butte-East Butte area, eastern Snake River Plain, Idaho*, Ph.D. Dissertation: State University of New York at Buffalo.
- Stearns, H. T., L. Crandall, and W. G. Stewart, 1938, *Geology and ground-water resources of the Snake River Plain in southeastern Idaho*, U.S. Geological Survey Water-Supply Paper 774, 268 p.
- Tauxe, L., C. Luskin, P. Selkin, P. Gans, and A. Calvert, 2004, "Paleomagnetic results from the Snake River Plain: Contribution to the time-averaged field global database," *Geochem. Geophys. Geosystems* 5, No. 8.
- Wood, T. R., C. M. Helm-Clark, H. Huang, S. Magnuson, T. McLing, B. Orr, M. Roddy, M. J. Rohe, M. A. Plummer, and R. Podgorney, 2005, *Operable Unit 10-08 Summary Report on the Subregional-scale Two-dimensional Aquifer Model*, ICP/EXT-05-00979, Rev. 1, Idaho Cleanup Project, October 2005.

Zentner, N. C., 1989, *Neogene normal faults related to the structural origin of the eastern Snake River plain*, M. S. Thesis: Idaho State University, Pocatello, Idaho.

Zohdy, A. A. R., and W. D. Stanley, 1973, *Preliminary interpretation of electrical sounding curves obtained across the Snake River Plain from Blackfoot to Arco, Idaho*, U.S. Geological Survey Open-File Report, 3 p.

Appendix C

The Treatment of Volcanic Rifts and Geophysical Data in the Conceptual Model

Appendix C

The Treatment of Volcanic Rifts and Geophysical Data in the Conceptual Model

There is no doubt that some volcanic rift features on the eastern Snake River Plain have affected groundwater flow on local scales (Anderson, Kuntz, and Davis 1999; Kuntz et al. 2002). Regardless of this recognition, there is no current consensus on the number and exact character of volcanic rifts on the eastern Snake River Plain. Volcanic rifts in active volcanic provinces are traditionally recognized by extensional tectonics; elevated heat flux and geothermal features; and linear trends with volcanic vents, faults and cracks associated with the motion and emplacement of volcanic dikes. Volcanic dikes can cause the formation of grabens bounded by non-eruptive fissures, accompanied by a central eruptive fissure if the dike reaches the surface (Rubin 1992). While this pattern of fissure-and-graben formation has been observed in many volcanically active areas (Rubin and Pollard 1988), it is not universal. Though it may be just an issue of vocabulary, the occurrence of one isolated dike and its associated features may not be sufficient to warrant a label as a volcanic rift. In this report, the term *volcanic rift* is used as defined in Kuntz, Covington, and Schorr (1992), which is to denote linear arrays of volcanic landforms and structures, including non-eruptive fissures, faults and grabens. By this definition, the Axial Volcanic High is not a rift *per se*. It shares many of the characteristics of eastern Snake River Plain rifts; however, it is an elevated volcanic constructional ridge associated with higher heat flux and a concentration of eruptive features. In the conceptual model, it is treated as a rift regardless of its NE-SW orientation. See Figure 2-1 in the main report for locations of geologic and geographic features discussed in this appendix.

A prevailing paradigm for volcanic rifts on the eastern Snake River Plain asserts that rifts form along trends parallel to the trends of nearby basin and range block faults, perpendicular to the long axis of the plain (Kuntz, Covington, and Schorr 1992). The intrusion of dikes in these rifts is a proposed mechanism to accommodate the calculated NE-SW extension of the eastern Snake River Plain aseismically (Parsons, Thompson, and Smith 1998; Smith, Jackson, and Hackett 1996). Eastern Snake River Plain rifts therefore should consist of NW-SE-trending linear rift features with multiple dikes in the subsurface aligned perpendicular to the axis of the plain, where these dikes may or may not reach the surface. The grabens of the Spencer-High Point Rift and the grabens at the northwest end of the Arco Rift may be good examples of this pattern, although in the latter case, it has also been argued that the Arco Rift grabens are related to basin and range faulting and not to dike-induced strain (Kuntz et al. 2002; c.f., Kuntz, Covington, and Schorr 1992).

The number of dikes required to veneer the plain with basalt can be estimated by various schemes, but usually by calculating the eruptive volume required to match post-Yellowstone Hot Spot strain rates and dividing by the volume of an average eastern Snake River Plain lava flow. For example, using such an approach, over a 4.5 Ma time interval and for the portion of the eastern Snake River Plain between Hell's Half Acre and the Great Rift, Parsons, Thompson, and Smith (1998) calculated that upwards of 11,700 1- to 2-m dikes were required if the eastern Snake River Plain were extending at the same rate as the neighboring basin and range province. When spread over the lifetime of the eastern Snake River Plain, emplacing one 1- to 6-m-wide dike every 1,000 years is sufficient to match total number of dikes required and the strain rates of the eastern Snake River Plain (Parsons, Thompson, and Smith 1998; Kuntz, Covington, and Schorr 1992).^a

a. Rodgers, D., ISU, personal communication, December 14, 2006.

The common conjunction of these rift hypotheses for the eastern Snake River Plain is not without problems. First, while the fissure-and-graben pattern is observed along parts of the Great Rift of Idaho, the northernmost Arco Rift, and northwest of the elongated vent of the Hells Half Acre flow, this pattern is not observed elsewhere on the eastern Snake River Plain. The paired New Butte and Minidoka crack sets of the Great Rift lack both central fissures and grabens. The fissure-fed North and South Robbers flows in the Arco Rift and the fissure-and-vent combination of Dick's Fissure and Tea Kettle Butte appear to be examples of eruptive fissures without flanking non-eruptive fissures or grabens. Second, not all linear trends involving volcanic features are rifts. In Laidlow Park at Craters of the Moon, Ant Butte, Big Blowout Butte, Hollow Top, Snowdrift Crater, and North Laidlaw Butte are aligned, but this alignment of shield volcano vents, eruptive craters and cinder cones does not constitute a volcanic rift: the linearity is coincidental. There are no other NE-SW trending features whatsoever in Laidlow Park; several of these buttes have vents elongated in the NW-SE direction, and belong to distinct NW-SE trends of aligned vents, faults, and fissures. Third, estimates of the number of dikes required for extension in the theoretical rift scenarios are also problematic. Most of the rift models use an assumption that one dike equals one eruption event and one eruptive fissure. Evidence exists, however, that some eruptive fissures are the source of more than one flow, e.g., Big Cinder Butte at Craters of the Moon. Other rift-associated volcanic centers can be the site of renewed volcanic activity after a hiatus of hundreds to thousands of years, e.g., the 519 ka Crater Butte with its 292 ka flank vent at the southwest corner of the INL. The assumption of one fissure, one dike, one eruption is not universally true. Fourth, the number of dikes that do not reach the surface is unknown. Fifth, no practical or unambivalent geophysical means are available to image these hypothesized subsurface dikes, because they have no magnetic or density contrast with the basalts through which they intrude. Sixth, while many NW-SE trending volcanic features occur on the eastern Snake River Plain, others are oriented with near N-S trends, like Lava Ridge and the Menan Buttes, or are oriented NNE-SSW like Wapi Park. Last, it is unclear how many dikes are required to make up one volcanic rift on the eastern Snake River Plain and how closely spaced they must be. What is observable on the eastern Snake River Plain is that dikes occur in swarms, much like those at Craters of the Moon, and other dikes occur alone, such as the feeder dike that fed the eruption of the Taber Butte shield volcano.

More questions can be posed about volcanic rifts, but one that is most relevant to the conceptual model is posed as follows: if indeed, hundreds to thousands of basalt dikes occur in the subsurface of the eastern Snake River Plain, then it is not unreasonable to ask where they are located. Because basalts of the eastern Snake River Plain are young, most dikes are still buried. The direct physical evidence of feeder dikes on the eastern Snake River Plain proper is limited to the drained central fissure at King's Bowl (Greeley 1982) and the poorly preserved remains of a dike at the base of the uplifted basalt sequence exposed on Big Southern Butte (Spear 1979). Two uplifted and eroded basalt flows with intact feeder dikes can be seen just outboard of the eastern Snake River Plain boundary at the toe of the Beaverhead Range (Price et al. 1999). Assuming the 11,700 m of dike emplacement of Parsons, Thompson, and Smith (1998) is a reasonable number, then within their 75-km-long box between Hell's Half Acre and the Great Rift, 75,000 m of extruded basalt include 11,700 m of dikes; this implies that there is 1 m of dike every 6.4 m somewhere in the subsurface. It must be noted that this is a model scenario using the assumption common to almost all eastern Snake River Plain rift models, namely that dikes take up the entire width of the plain. In these rift models, the Axial Volcanic High is not accounted for since it does not contribute to the eastern Snake River Plain.

Assuming that the boreholes on the plain penetrate sufficiently deep and that the Parsons estimate is reasonable, the probability of intersecting a basalt dike while drilling on the eastern Snake River Plain is approximately 1 to 6.4. This implies that approximately one-seventh of the boreholes drilled on the plain should have intersected a dike—yet the abundant documentation on drilling in the Big Lost Trough shows no such information. If the Parsons, Thompson, and Smith (1998) strain rate is used and we limit the assessment to young (last million years) and shallow basalts, then the odds of intersecting a dike in a

borehole are 1 to 29. Those are still remarkable odds. Regardless, the fact remains that despite the hundreds of boreholes drilled in the Big Lost Trough and its environs, no dike has ever been identified by drilling in the subsurface. It is one of the main reasons that the arguments for a many-dikes model presented in studies like Anderson, Kuntz, and Davis (1999) and Kuntz et al. (2002) can be questioned.

It can be argued that there are significant impediments to identifying dikes in the subsurface and that this diminishes the validity of questioning why there are no observed dikes. The contention that dikes cannot be identified is based on the following: (1) a sole basalt feeder dike will have no geophysical contrast with surrounding basalt flows; and (2) since most boreholes are not cored, the paucity of core decreases our ability to recognize dikes by direct inspection. The latter case has less impact than it first appears. First, for the last two decades almost all new deep boreholes in the Big Lost Trough have been cored. A disproportionate number of these are located in the southern portion of the INL Site. These new boreholes should actually optimize the probability of observing a dike in core since the southern INL is a vent-rich area. On the Site, volcanic vents and fissures are concentrated in the AEC Butte and Arco Rifts and along the Axial Volcanic High east of Central Facilities Area. If the number of vent corridors in the southern half of the INL is as great as suggested by the scenarios of Anderson, Kuntz, and Davis (1999) and Kuntz et al. (2002), then the likelihood of coring a dike will be even greater since these models insert numerous hypothesized dikes between the AEC Butte and Arco Rifts.

Core is not the only means for potentially observing dike lithology. While most of the pre-1980 wells on the INL Site were not cored, many of them were not cased. The USGS has collected copious video logs of these older uncased wells which again increases the likelihood of identifying a dike through direct observation. Dikes in the subsurface will have a number of features that would aid in their identifications, namely horizontal cooling joints; little to no vesicularity; aphanitic texture; the appearance of being a thick, massive flow *that cannot be correlated* with local stratigraphy; vertical baked contacts; and vertical visible and magnetic flow textures. Last, it is possible that observable dikes in the subsurface go unrecognized because no one is looking for them.

It is also not true that feeder dikes would have no contrast with surrounding basalt flows. A lone dike will have no contrast on gravity, surface magnetic and aeromagnetic surveys, but it could be distinguished by the right combination of wireline logs. Assuming that a borehole intersected more than 2 m of a dike—the average minimum required to avoid resistivity inversion effects—the dike could be distinguished by a combination of resistivity ratios, high magnetic susceptibility due to lack of oxidized or glassy contacts (Helm-Clark, Rodgers, and Smith 2004), very low sonic travel time, high neutron flux, low gamma-gamma flux and no increase or decrease in the caliper log. *The first two logging results are necessary* and without them, the rest are not sufficient to identify a dike. Unfortunately, resistivity, velocity, and magnetic susceptibility are seldom collected in boreholes on the eastern Snake River Plain. Resistivity and sonic logs require the presence of water or a drilling fluid in the borehole but most INL boreholes are drilled using air rotary and usually do not penetrate into the aquifer more than ~30 m. Magnetic susceptibility is rarely used on the eastern Snake River Plain due to unfamiliarity and the difficulty of interpreting its results in basalt (Helm-Clark, Rodgers, and Smith 2004). So, while it is not really true that a buried dike lacks geophysical contrast, it is rare that the suite of data needed to identify a dike is collected. Intervals in a borehole that appear to be hydrogen poor (high neutron flux), dense (low gamma-gamma flux), and competent (no increase in caliper log), and which lack correlation with any units in neighboring wells should be examined for the lithological characteristics of a dike if core and/or video logs are available.

The 1 in 29 probability of drilling through a dike can be refined by simply constraining extension and dike intrusions to four known rift features between Hell's Half Acre and the Great Rift: the AEC Butte rift, the Arco Rift, the Quaking Aspen Butte Rift and the Great Rift of Idaho. The rift areas in question occupy approximately one third of the area between Hell's Half Acre and the Great Rift.

Assuming all dikes are intruded in the rift areas and no dikes are intruded elsewhere, then the probability of drilling through a default 1 m dike drops to approximately 1 in 10. Considering the large number of cored and video-logged INL boreholes in the Arco and AEC Butte Rifts, the lack of observed subsurface dikes cannot be dismissed outright on the grounds that they cannot be observed.

The derivative hypothesis of these studies, that the numerous subsurface dikes have a large influence on hydraulic conductivity, suffers from the additional impediment that while it may be sufficient, it is by no means necessary. There are certainly viable means to explain the lower than average hydraulic conductivities observed for some wells in the study area. Mechanisms for lowering hydraulic conductivity include fine-grained sediment infiltration into fissures, a process that can be observed today on the surface of the Arco Rift at Dick's Fissure and has been documented in core from Well BG-77-1 (Helm-Clark, Rodgers, and Smith 2004). It also has been observed that some wells with low transmissivity effects have been completed with screened intervals placed against fine-grained sediments and cinders, both of which can clog screens. Juxtaposing screens and fine-grained materials may further compromise transmissivity, especially since well development is uncommon in the highly transmissive basalts of the INL. The presence of abundant fine-grained sediment in interflow zones, in discrete sedimentary interbeds^b and in infiltrated fractures (Helm-Clark, Rodgers, and Smith 2004) are other conditions that can lower hydraulic conductivity.

If a volcanic rift zone is formed by the coalescence of parallel basalt dikes feeding a number of eruptive fissures and vents and causing the surface formation of grabens, faults, and non-eruptive fissures, then such a complex should be a significant vertical feature in the subsurface, yet there are only a handful of places on the eastern Snake River Plain where there is a convincing correlation between groundwater flow and volcanic rifts. It is possible that a 1-to-2-m dike experiences enough post-emplacment fracturing that it poses no impediment to groundwater flow, or that most dikes never reach the relatively shallow crustal depths of the aquifer, or both.

Given the questions regarding volcanic rifts and feeder dikes, the geologic conceptual model restricts itself to rift features whose existence are beyond doubt, or rift features that are known or suspected to have an influence on groundwater flow. Rifts could represent barriers to flow by emplacing a dike swarm of coalescent adjacent dikes along a rift, by clogging of non-eruptive fissures through sediment infiltration, by concentrating relatively low-permeability clay-altered near-vent rocks like cinder and ash, or by any combination of these. A few isolated dikes are likely insufficient barriers to groundwater flow by themselves. The several different physical mechanisms associated with dike swarms in rifts may provide barriers to flow. Other rift features may instead represent increased permeability for groundwater flow, particularly through the creation of open fractures, faults, and non-eruptive fissures (Welhan et al. 2002).

Within the study area, rift features can be divided into active and older, inactive rifts. Active volcanic rifts on the eastern Snake River Plain share several distinguishing features: elevated topography relative to surrounding volcanic tablelands; aligned vents, fissures, faults and grabens whose surface expression can be mapped; and surface evidence of Holocene and late Pleistocene volcanism (<20,000 years). Several of the rifts identified here as active features are also associated with geothermal phenomenon, particularly at the north end of the Great Rift at Craters of the Moon, the north end of the Arco Rift, and between Middle and East Buttes along the Axial Volcanic High. Older inactive rifts are similar to active ones with the following differences: there are no known Holocene or Latest Pleistocene features, there is a lack of elevated heat flow or geothermal features; and (in many cases) the formerly elevated rift flanks and crest are wholly or partially buried by younger basalts and sediments. In terms of

b. Welhan, J., ISU, personal communication, December 14, 2006.

hydraulic behavior, there should be little to no difference between active and inactive rifts. The functional difference is that inactive rifts are difficult to locate if they are buried by younger rocks.

Positive magnetic anomalies have been proposed in earlier studies as a characteristic of volcanic rifts on the eastern Snake River Plain (Mabey 1978), but the applicability of this correlation is limited since not all identified rifts have this association and there are many positive anomalies similar to those associated with the north ends of the Great and Arco Rifts that cannot be correlated with known and mapped volcanic rifts. The hypothesis that many rift features are connected, like the Lava Ridge rift and the Hell's Half Acre fissures, is not supported by the aeromagnetic data if indeed positive anomalies are associated with rift features.

The volume of basalt in the dikes of a volcanic rift might control whether a positive magnetic anomaly is present. Magnetic contrast is several orders of magnitude greater for changes in lithology than for changes due to structure. While a thin isolated basalt feeder dike has negligible signal and no imageable magnetic contrast with surrounding basalt flows, a dike swarm in a rift zone may form an appreciable magnetic anomaly by concentrating a mass of basalt lacking the sedimentary and rhyolitic rocks typically intercalated with extruded basalt flows on the eastern Snake River Plain.

Gravity and aeromagnetic evaluation of the study area utilized the newly published (Mankinen et al. 2004) USGS Geophysical Data for the Northern Rocky Mountains, the Western Cordillera gravity analysis of Eaton et al. (1978), and the original USGS aeromagnetic and gravity data collected at the INL (Morris et al. 1964). The bulk of this evaluation relies on the Geophysical Data for the Northern Rocky Mountains with the data sets of Eaton et al. (1978) and Morris et al. (1964) used to clarify specific characteristics of the geophysical data.

C-1. GRAVITY DATA

The Geophysical Data for the Northern Rocky Mountains gravity data set was compiled from the measurements of multiple geophysical campaigns using many generations of instrumentation and covering different areas with highly variable data collection densities. Figure C-1 shows the data density for gravity measurements for the Geophysical Data for the Northern Rocky Mountains data set. In the study area, the Big Lost Trough was well sampled. The three tributary basins through which the Big and Little Lost Rivers and Birch Creek flow appear to have moderately good coverage, though the mountain ranges between the basins are poorly sampled. The northernmost eastern Snake River Plain above 44° N latitude and the central to southern eastern Snake River Plain west of the Arco-Minidoka Road, including the entirety of the Great Rift, are also poorly sampled. Not surprisingly, the heaviest data sampling in data-poor areas is concentrated along roadways; the lines of data collection along the Arco-Minidoka road, Rt. 26, US 93 and Interstates 15 and 86 are all clearly visible in Figure C-1. The patterns of measurement for aeromagnetic surveys are similar.

The complete Bouguer gravity anomaly map from the Geophysical Data for the Northern Rocky Mountains is based on the 1-km gridded data set of Hildenbrand et al. (2000). Corrections were applied to remove: the attraction of the reference ellipsoid; the effect of elevation with respect to the geoid, i.e., the free-air correction; the attraction of material between the elevation of a measurement and the geoid, i.e., the Bouguer correction, using a uniformly thick slab with a density of 2.67 gm/cm³; and the effects of additional mass due to localized variations of terrain around a measurement point out to a radial distance of 166.7 km (Mankinen 2004). The residual gravity anomaly without the terrain corrections is known as the Simple Bouguer Anomaly and with the terrain corrections is the Complete Bouguer Anomaly.

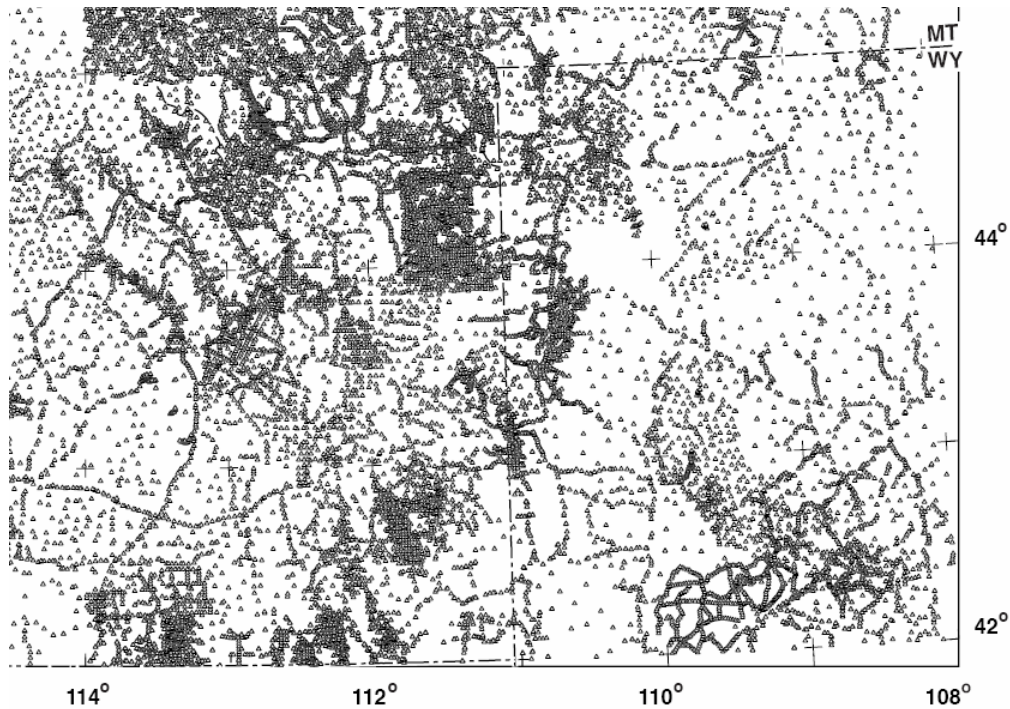


Figure C-1. Gravity data collection locations for the Geophysical Data for the Northern Rocky Mountains data set, modified from Mankinen et al. (2004).

Figure C-2 shows a 1:1,000,000 scale portion of the Geophysical Data for the Northern Rocky Mountains Complete Bouguer gravity anomaly for the study area plus neighboring portions of the eastern Snake River Plain and the Basin and Range Province. Outlines of latest Pleistocene and Holocene lava flows from the 1974 King and Beikman geologic map of the United States (Schruben, Arndt, and Bawiec 1997) plus faults from the USGS Quaternary fault database (Machette et al. 2003) are superimposed on the figure as an aid for locating geological features. Not surprisingly, the figure shows that the volcanic rocks of the eastern Snake River Plain have less negative Bouguer anomalies (indicating greater overall density) than the block-faulted and sediment-dominated Basin and Range rocks.

The compilers of the Geophysical Data for the Northern Rocky Mountains noted a strong inverse correlation at the sub-continental and regional scales between the Complete Bouguer anomaly and elevation throughout the Northern Rockies (Mankinen et al. 2004). At the subregional scale of the study area, this correlation is not apparent because the correlation is due to very long wavelength phenomenon on sub-continental and regional scales. The regional Bouguer-to-elevation inverse correlation is apparent on the Simple Bouguer map of Eaton et al. (1978), which is shown on Figure C-3. On this figure, the labeled regional gravity low is due to the regional uplift, lithospheric thinning, and upwelling of hot asthenosphere beneath the Basin and Range Province and its environs to the north. The correlation is especially strong in south to central Idaho. Since elevation-related effects have been removed from the Bouguer anomaly, this suggests that both the observed regional anomalies (lows over mountain roots/deepened crust - highs over shallow mantle) are due to isostatic compensation. At equivalent regional elevations, however, gravity values in the Great Basin are more negative by approximately 30 mGal (Eaton et al. 1978), suggesting that southern to central Idaho, Yellowstone, and surrounding mountains are compensated at a relatively shallow depth in the crust.

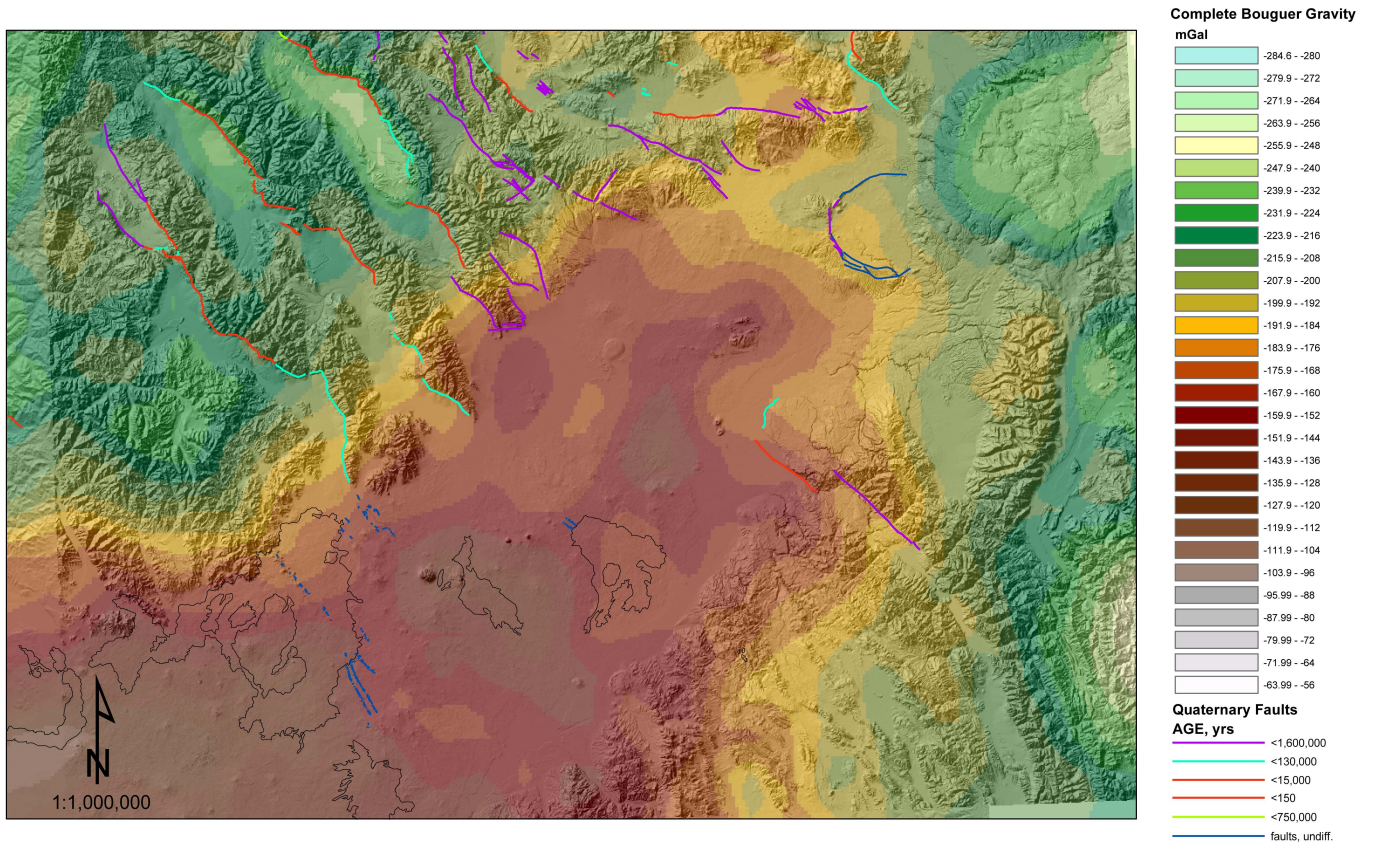


Figure C-2. Complete Bouguer gravity of a portion of southeastern Idaho.

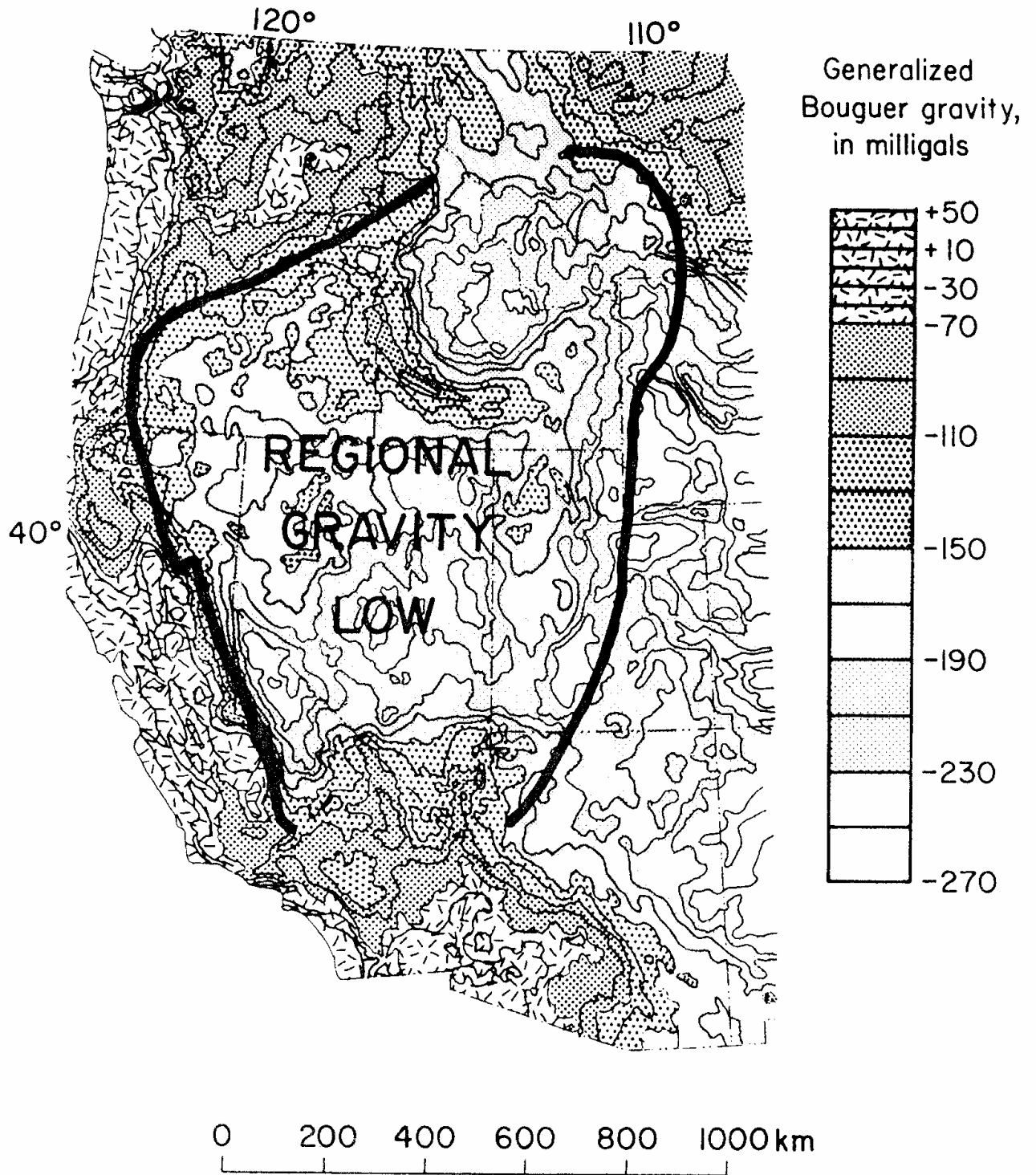


Figure C-3. Simple Bouguer gravity map of the Western United States from Eaton et al. (1978).

The long wavelength gravity effects from isostatic compensation can mask regional and subregional gravity anomalies. Mankinen et al. (2004) applied an isostatic correction to remove these anomalies from the Geophysical Data for the Northern Rocky Mountains Complete Bouguer gravity field assuming a modified-Airy isostatic compensation model with a crustal depth of 25 km, a crustal density of 2.67 gm/cm^3 and a density contrast between the mantle and crust of 0.4 gm/cm^3 (Mankinen et al. 2004). Since the Moho under the eastern Snake River Plain is approximately 40 km based on seismic criteria (Peng and Humphreys 1998), using a 25-km-thick crust may result in under-compensation for the eastern Snake River Plain, which could be the cause (in part) for the positive residual anomaly over the eastern Snake River Plain when compared to the neutral to slightly negative anomalies over the Basin and Range Province north of the plain as seen in Figure C-4.

The vertical derivative of the Isostatic Residual anomaly is supposed to emphasize shorter wavelength features and boundaries between blocks of contrasting rocks (Figure C-5) but the comparison between the whole Isostatic Residual anomaly, its vertical derivative and the long-wavelength portion of the Isostatic Residual anomaly (Figure C-6) shows very little difference between the three. The implication of this comparison is that there are large, persistent mid- to upper-crustal features that pass under the study area and cross the entirety of the eastern Snake River Plain. One band of lower density material (with respect to the rest of the eastern Snake River Plain) starts midway between Arco and the Craters of the Moon and extends to American Falls. Another band of lower density material starts just south of Howe and extends through Hell's Half Acre to the town of Shelley. This leaves positive gravity anomalies centered over the Cerro Grande lava flow, at the end of the Beaverhead Range east of Birch Creek and along the Axial Volcanic High from north of Idaho Falls, and immediately northeast of Juniper Buttes. These anomaly patterns have been interpreted to support both the location of caldera rims and volcanic rifts zones (e.g., Morgan, Doherty, and Leeman 1984); the one feature these large mid-crustal anomalies do not appear to support is the presence of a continuous and pervasive mid-crustal sill under the eastern Snake River Plain, variations of which have been proposed by several researchers including Sparlin, Braile, and Smith (1982); Peng and Humphreys (1998); and McQuarrie and Rodgers (1998), based on either seismic or structural interpretations.

The intermediate-wavelength content of the Isostatic Residual anomaly is shown in Figure C-7. The correlation between range-bound valleys and negative anomalies is suggestive that this wavelength spectrum of the gravity data is sensitive to the deposition of sediments in basins. In the center of the eastern Snake River Plain, where traditional depositional basins do not exist in the basalt-and-rhyolite stratigraphy of the upper crust, the negative anomalies may be due to a variety of causes; these include structural and lithologic differences, such as localized extensive interfingering and intercalation of volcanic rocks with sediments like those documented by Houser (1992) for the Pleistocene American Falls Lake and Raft River formations. It is obvious that there is no discernable correlation between the intermediate wavelength Isostatic Residual gravity field and the Late Pleistocene and Holocene volcanic rift systems.

Figure C-8 shows the simple Bouguer anomaly map from Morris et al. (1964). Overall, the patterns of gravity highs and lows are similar despite differences in data sampling density and data processing techniques (Mankinen et al. 2004; Morris et al. 1963; Morris et al. 1964). A tongue of lower density material appears to extend southward and then southwestward from the valley of the Little Lost River onto the eastern Snake River Plain in both data sets. The same gravity low extending southwestward from the Mud Lake area also appears in both data sets as does the gravity high over the Cerro Grande flow. The pronounced gravity high south of the Beaverhead Range is not as prominent and is displaced to the west in the Morris et al. (1964) simple Bouguer data compared to the intermediate wavelength Isostatic Residual data (Mankinen et al. 2004). Considering that these two data sets are very different in terms of measurement density, processing, and applied gravimetric corrections, the match of features between them is remarkable and argues that the anomalies revealed represent significant differences of density in the mid- to upper-crust.

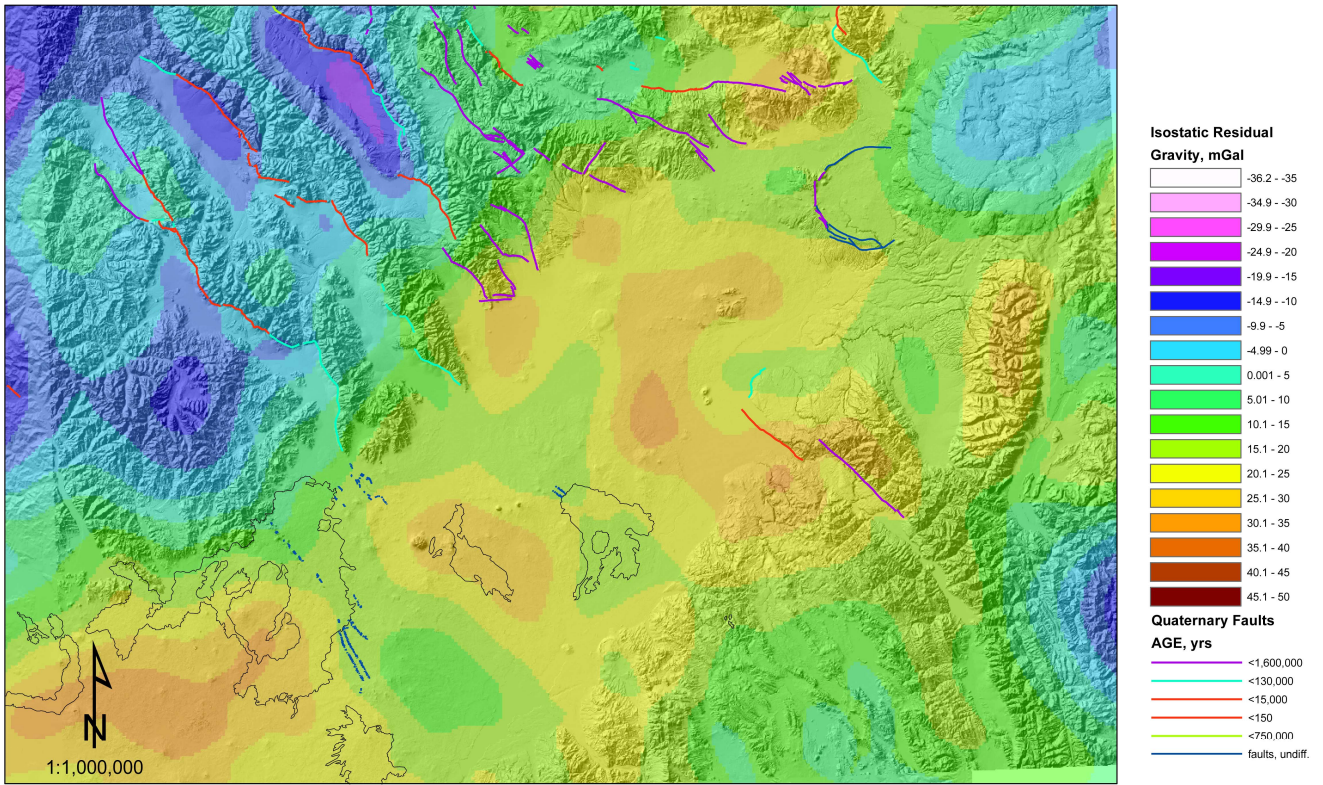


Figure C-4. Isostatic residual gravity for a portion of Southeastern Idaho.

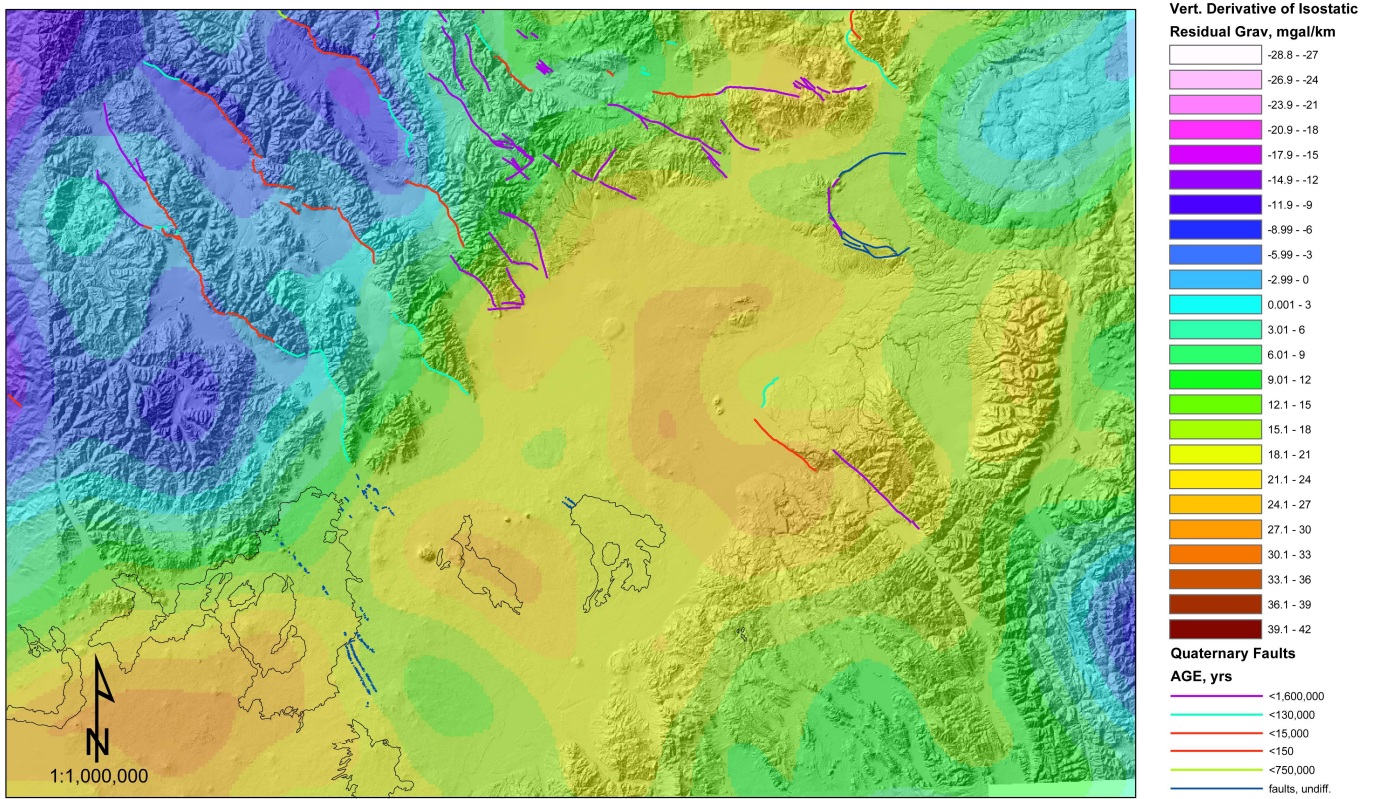


Figure C-5. Vertical derivative of isostatic residual gravity for a portion of southeastern Idaho.

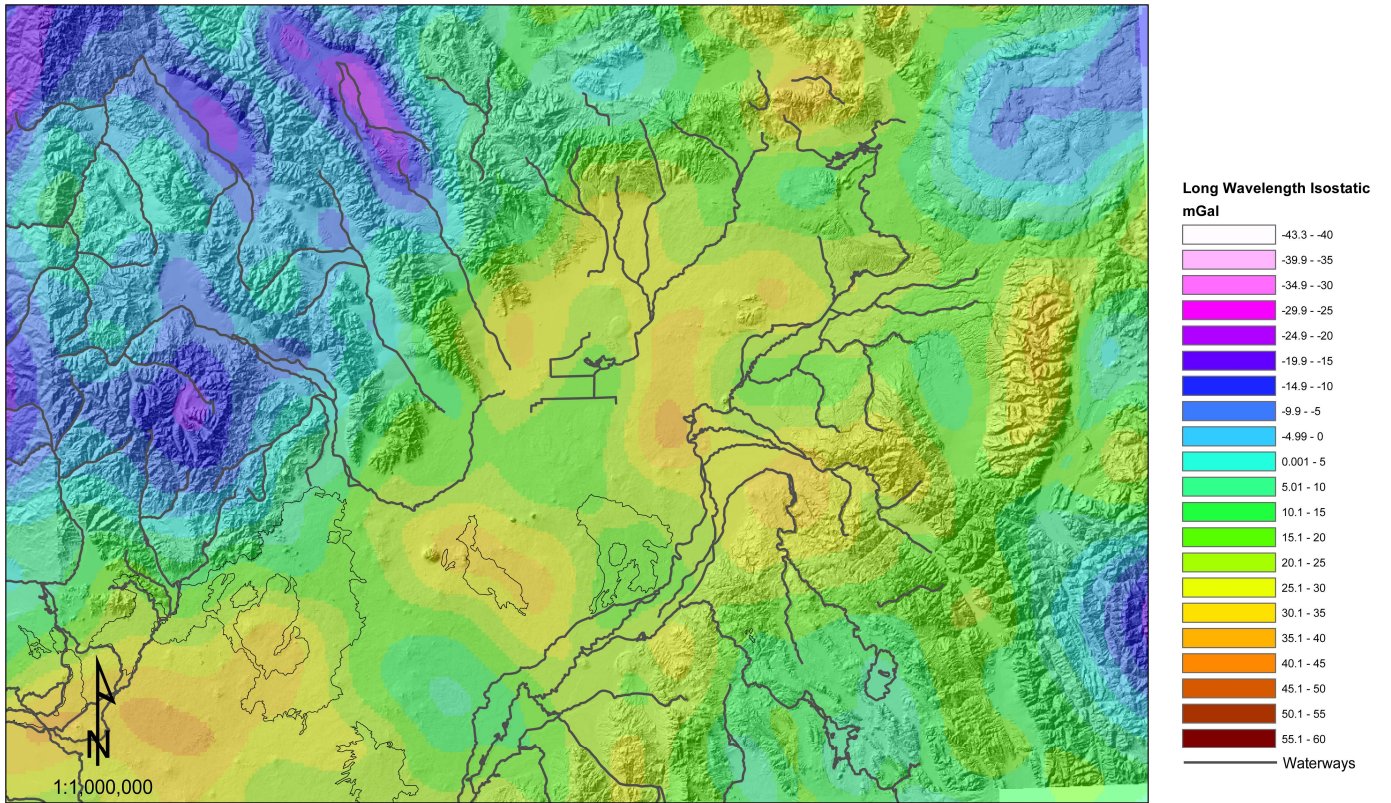


Figure C-6. Long wavelength isostatic residual gravity for a portion of southeast Idaho.

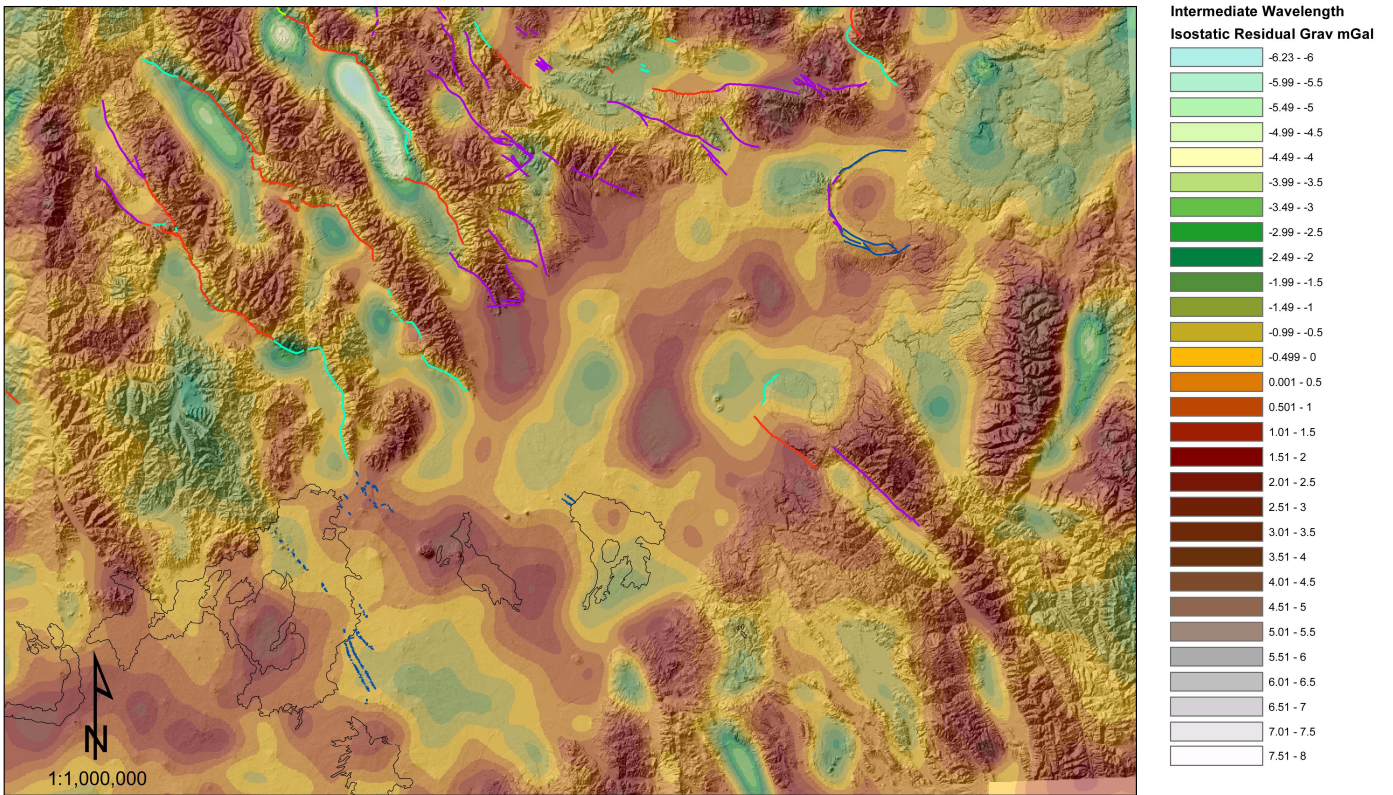


Figure C-7. Intermediate wavelength isostatic residual gravity for a portion of southeast Idaho.

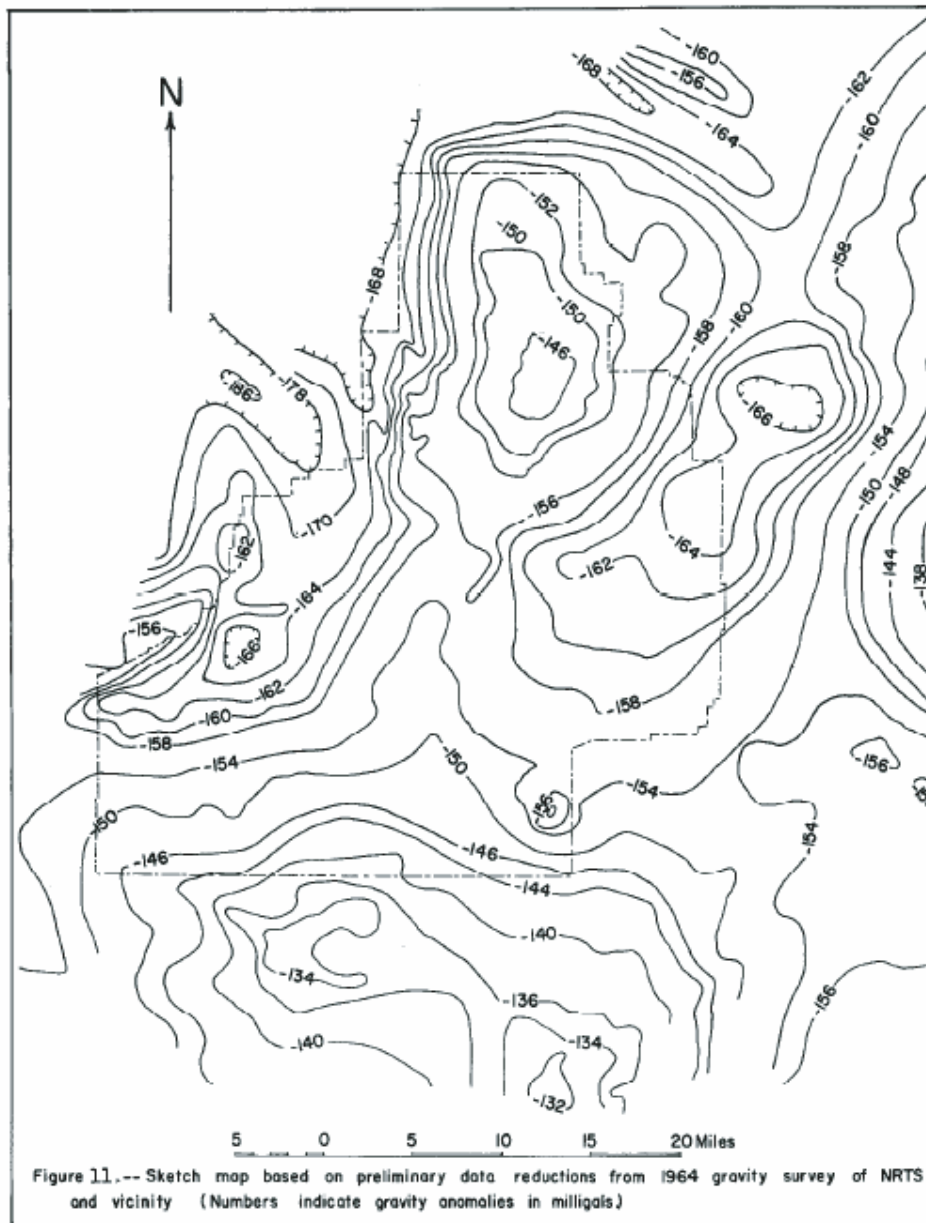


Figure C-8. Simple Bouguer gravity map of the INL from Morris et al. (1964).

Hadley and Cavit collected seismic and gravity data at the INL in 1984. Bruhn, Wu, and Lee (1992) combined these data with data collected for the New Production Reactor program to evaluate fault structures at the southern ends of the Lemhi and Lost River Ranges, a portion of which is shown in Figure C-9. The interpretation of this data argued that there is a down-dropped block of Lemhi Range material south of a third normal fault in a ENE trending set that slices the terminus of the Range. The 1984 Haley and Cavit data are the only gravity data set to show this feature. Unfortunately, this detailed data set may be lost.^c

c. Payne, S., INL, personal communication, September 1, 2006.

A similar local gravity study was made by Bush (1980) of the Tyhee area north of Pocatello. The result of that gravity study which is germane to the OU 10-08 conceptual model is the delineation of shallow and short step faults on the edge of the eastern Snake River Plain's southeast boundary, 3 and 5 km inboard of the edge of the plain.

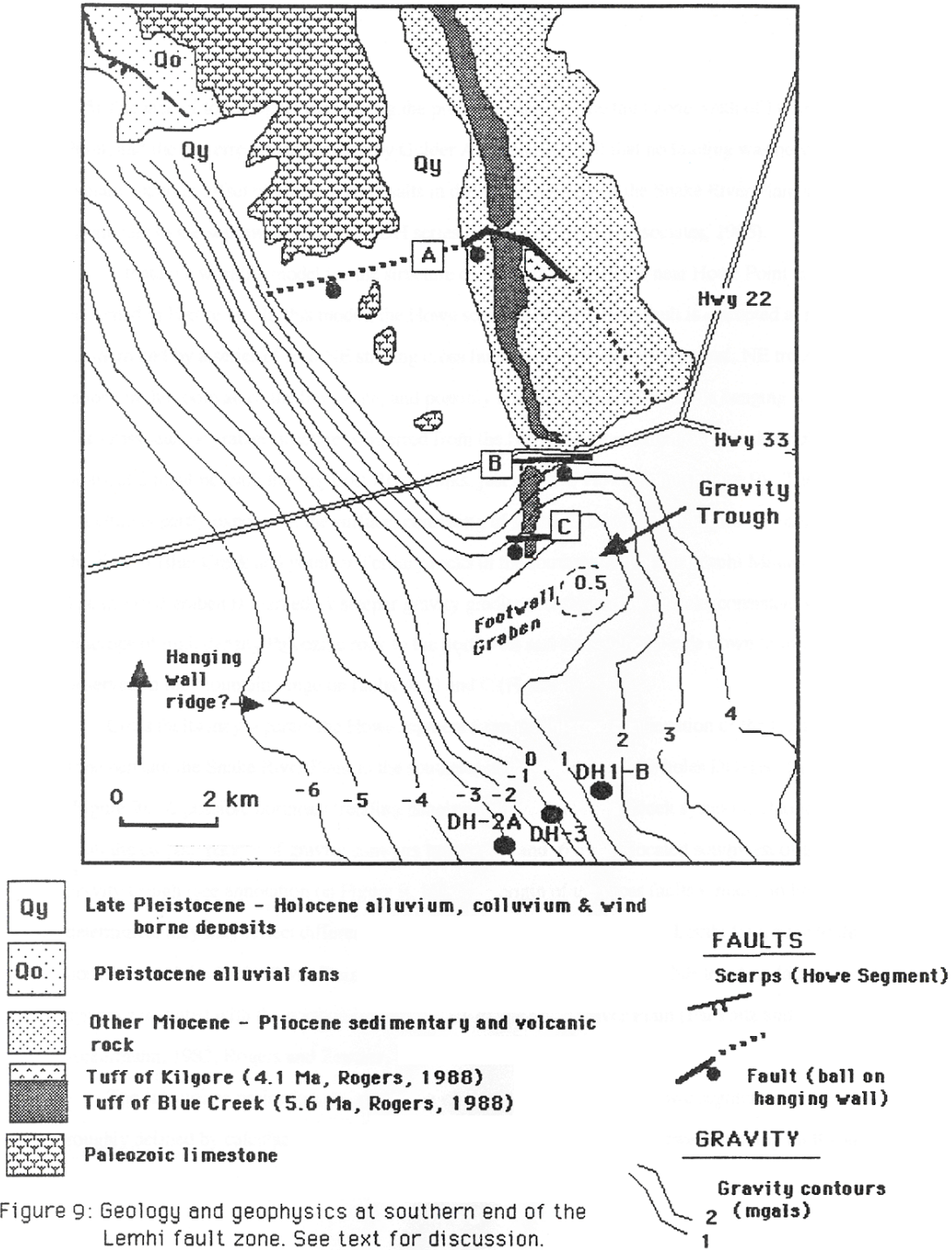


Figure 9: Geology and geophysics at southern end of the Lemhi fault zone. See text for discussion.

Figure C-9. The Bruhn, Wu, and Lee (1992) interpreted map of the 1984 Haley and Cavit gravity data.

C-2. REGIONAL MAGNETIC DATA

Figures C-10 through C-13 show magnetic data from the Geophysical Data for the Northern Rocky Mountains compilation (Mankinen et al. 2004). These data were extracted from the USGS North American magnetic anomaly database (NAMAG 2002). Very long wavelengths of the Earth's geomagnetic field have been removed plus the data have been corrected to a datum 305 m above terrain and gridded to 1 km. The data have been re-projected to an Albers equal-area projection for the Geophysical Data for the Northern Rocky Mountains compilation (Mankinen et al. 2004). All magnetic intensity values are reported relative to the International Geomagnetic Reference Field (IGRF 1992). In the following analysis, the Geophysical Data for the Northern Rocky Mountains data are supplemented by the Morris et al. data (1964) collected by the USGS in 1963–1964 where applicable.

In areas like Idaho where the inclination of the Earth's magnetic field is greater than 60° , the total intensity of magnetic data are approximately equivalent to the vertical component of the magnetic field. Substituting the vertical component for the total field greatly simplifies the interpretation of magnetic anomalies. A general rule for interpreting vertical-component aeromagnetic data is that positive anomalies represent cool iron-rich rocks carrying magnetite (Dobrin 1976). Negative anomalies represent (a) iron-poor rocks (Dobrin 1976), (b) rocks at elevated temperatures close to the Curie or magnetic unblocking temperatures of their magnetic minerals (Butler 1992; Dobrin 1976), or (c) both. In almost all cases, this general rule will be applicable for most regional aeromagnetic analyses. Interpretation can be complicated, however, when the field is perturbed by localized polarity effects since all magnetized objects are dipoles. For example, a magnetized dike with a vertical orientation will make a symmetrical positive anomaly in a magnetic field when seen in plan view (Figure C-14a). In contrast, when that dike is at an angle, the anomaly it makes will be a positive bump with a smaller negative depression next to it (Figure C-14b).

Other phenomena that can result in positive-negative anomaly patterns include the terminal edges of magnetized sills; faulted horizontal layers; inclined magnetized slabs, volcanic stocks or necks; and bodies with significant remanent magnetization that is reversed with respect to the induced field, to name a few examples. In general, anomaly intensity is more sensitive to changes in lithology than to subsurface structure. Anomalies due to lithology, even for deep sources, will usually be more than 1 to 2 orders of magnitude greater than structural effects on the measured magnetic field (see Figure C-15).

Figure C-10 shows the total intensity aeromagnetic data set from the Geophysical Data for the Northern Rocky Mountains at a scale of 1:2,000,000. Several regional features stand out in the aeromagnetic data at this scale. The eastern Snake River Plain and the graben of the western Snake River Plain are mostly positive magnetic anomalies due to the strong magnetic signature of magnetite-rich basalts in the uppermost crust. The Henry's Fork (Island Park) and Yellowstone Calderas are notable negative anomalies due to the predominance of weakly magnetized surface and near-surface rhyolitic rocks, a shallow depth-to-curve-point, or both. The intermediate-to-silicic Idaho Batholith forms a large neutral-to-negative magnetic anomaly in the upper left of the figure, intruded by positive anomaly Challis volcanic rocks north of the eastern Snake River Plain. The Late Pleistocene Blackfoot Volcanic Field is the small positive anomaly to the right. The extremely-high positive magnetic anomalies along the left edge of the figure are the easternmost Columbia River Plateau flood basalts. The two extremely-high magnetic anomalies on the right side of the figure east of Yellowstone are the signatures of the cores of the Absaroka and Wind River Mountains.

Figure C-11 is a map of Geophysical Data for the Northern Rocky Mountains magnetic residuals. Residuals were calculated by upward-continuing observed anomalies and subtracting these from the total field magnetic intensity. This process removes the effect of deep sources and emphasizes surface and near surface sources (Mankinen et al. 2004).

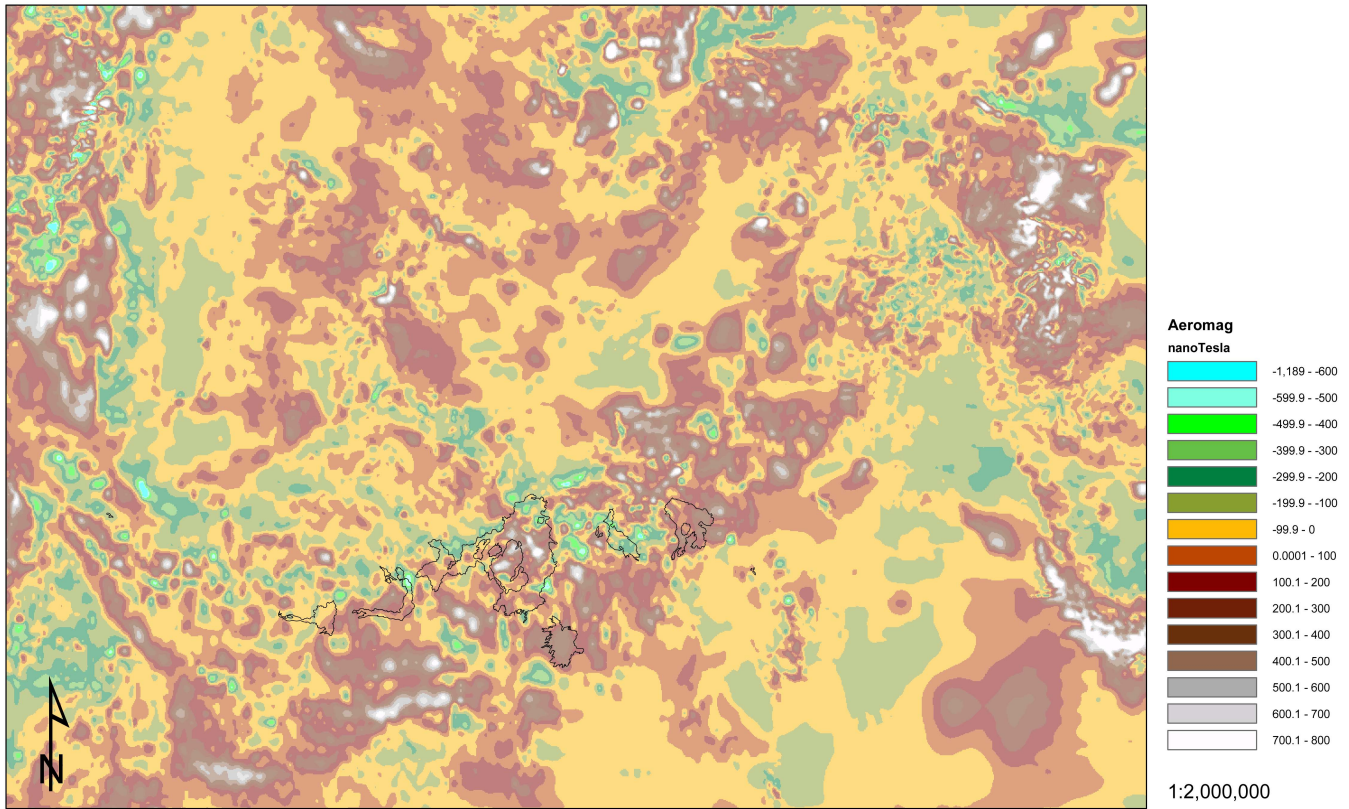


Figure C-10. Aeromagnetic data for a portion of southeast Idaho.

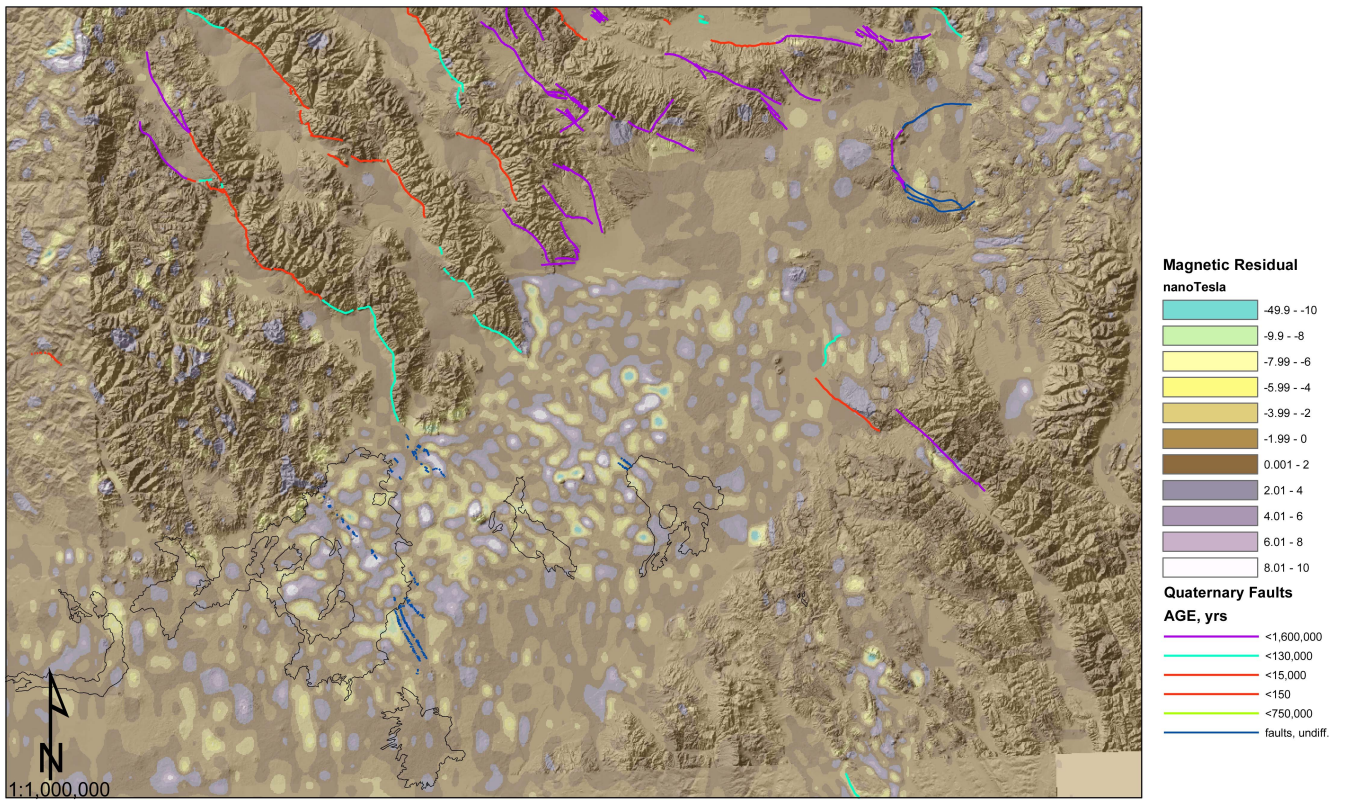


Figure C-11. Magnetic residual data for a portion of southeast Idaho.

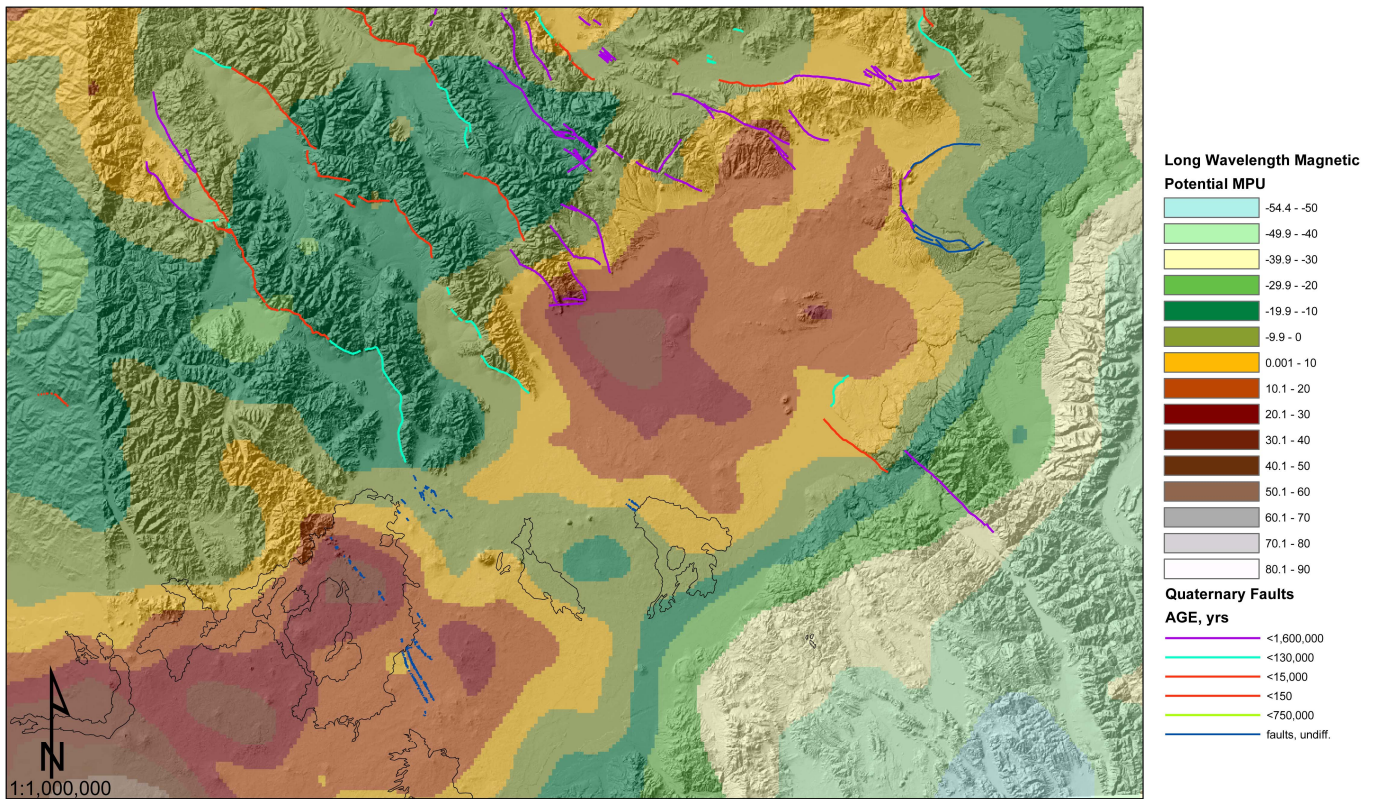


Figure C-12. Long wavelength magnetic potential.

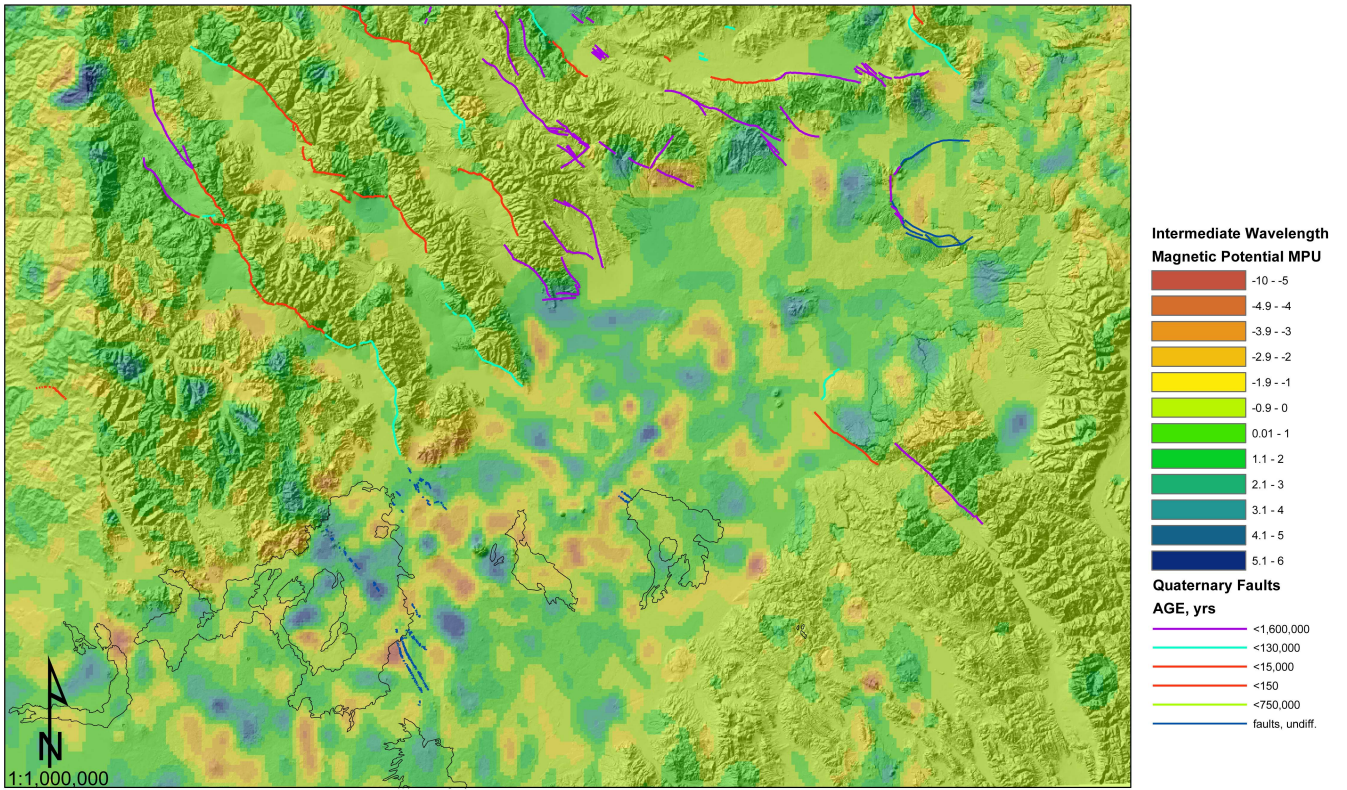


Figure C-13. Intermediate wavelength magnetic potential for a portion of southeast Idaho.

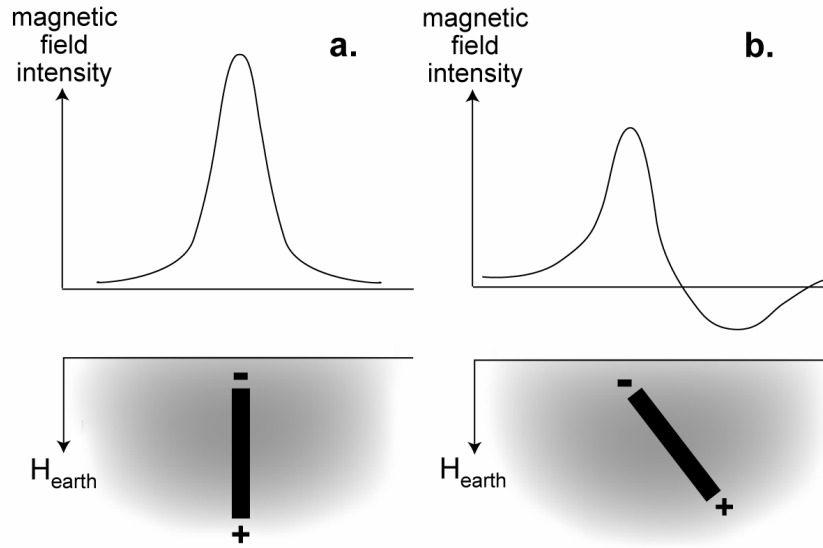


Figure C-14. The affect of intrusive dike orientation on aeromagnetic data (modified from Burger, Sheehan, and Jones [2006]).

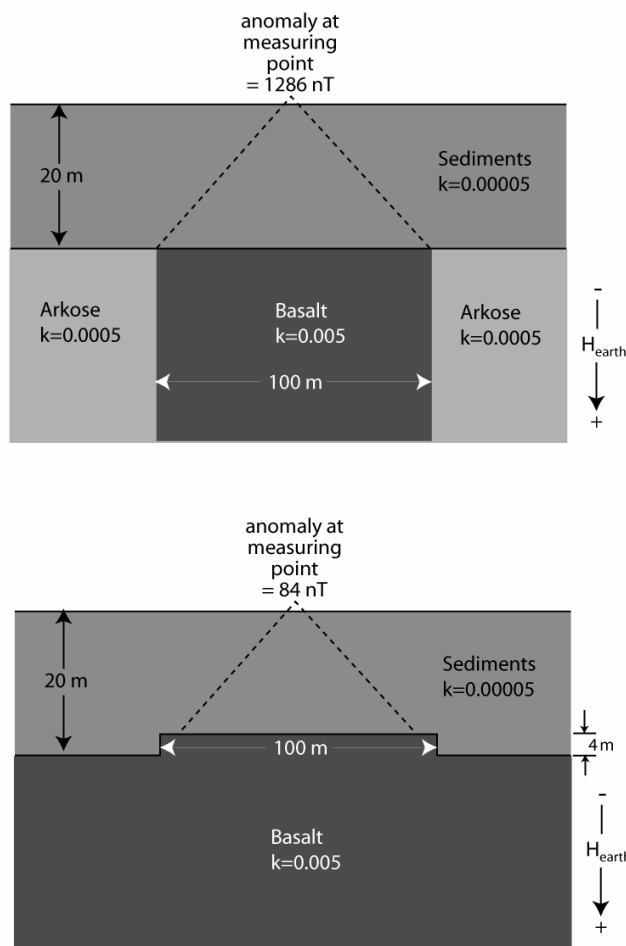


Figure C-15. Measured magnetic field anomalies due to lithology and geologic structure (modified from Burger, Sheehan, and Jones [2006]).

Notable features in the pattern of residuals include the almost-uniform, slightly-positive magnetic residual signature of the Basin and Range Province both north and south of the eastern Snake River Plain. The north end of the eastern Snake River Plain, including the Henry's Fork (Island Park) Caldera, is also characterized by a similar almost-uniform, slightly-positive magnetic residual signature with far less residual anomalies compared to the eastern Snake River Plain to the south of this area or compared to Yellowstone. This is most likely a data artifact. The central portion of the eastern Snake River Plain and Yellowstone are both areas with very dense data collection, whereas the northern portion of the eastern Snake River Plain north of 44° N latitude and west of Island Park is an area with extremely sparse data collection (c.f., Figure C-1). This is not too great a concern for this study since the northern boundary of the INL is only ~1.5 km north of 44° N latitude.

The northern half of the study area around the INL and the southern end around Craters of the Moon both display a residual pattern that is mottled, including areas of very high and very low values. North of the lines defined by the Great Rift and Axial Volcanic High, the lines and blebs of the mottling pattern display preferential alignments that are oriented NE and SW, perpendicular and parallel to the Axial Volcanic High and major rift zones. Several features such as the Axial Volcanic High between East and Kettle Buttes, the fissure system associated with Hell's Half Acre, the entire Great Rift, and the portion of the Arco Rift between Railroad Graben and Coyote Butte are all associated with high magnetic residual values. In contrast, there is a very strong negative residual pattern centered on the rhyolitic Middle and East Buttes although not on Big Southern Butte.

Comparison of the magnetic residual map with the 1964 aeromagnetic survey of the Site (Morris et al. 1964) shows many similarities and some differences (see Figure C-16). The magnetic high associated with the Axial Volcanic High, the high that extends from Materials and Fuels Complex (MFC) toward Howe, and the high east of Test Area North (TAN) are all present in both data sets though the residual high that parallels the trend of the fissure system of Hell's Half Acre is not present in the 1964 data. The low that trends ENE from the Arco Hills and onto the plain south of Howe is present in both data sets as are the lows associated with East and Middle Buttes and associated with the area immediately north of Big Southern Butte, although differences in relative magnitude of these anomalies are apparent, especially for the low at East and Middle Buttes.

The total magnetic intensity and magnetic residual data sets show that there is obviously a range of short to long wavelengths in the data. Since the magnetic field is the spatial derivative of magnetic potential, a traditional method of analyzing such data is to transform the total magnetic field data to magnetic potential data. This greatly simplifies both wavelength-dependent analyses and the identification of magnetic anomalies (Dobrin 1976). The field-to-potential transform, also known as a pseudogravity transform, has the effect of suppressing short wavelength noise from shallow sources. Figures C-12 and C-13 show the long and intermediate wavelength portions of the magnetic potential in dimensionless magnetic pseudogravity units.

Long wavelength magnetic potential data typically sample the mid-crustal sources above the Curie Isotherm, which is typically 20 to 25 km deep except in areas of high heat flow like Yellowstone and the eastern Snake River Plain. Strongly-magnetic shallow sources of large area extent can also contribute to the long wavelength potential, though this is uncommon. In the case of the eastern Snake River Plain, however, magnetic highs associated with the plain are likely due to the substantial surface veneer of basalt that caps the rhyolitic upper crust.

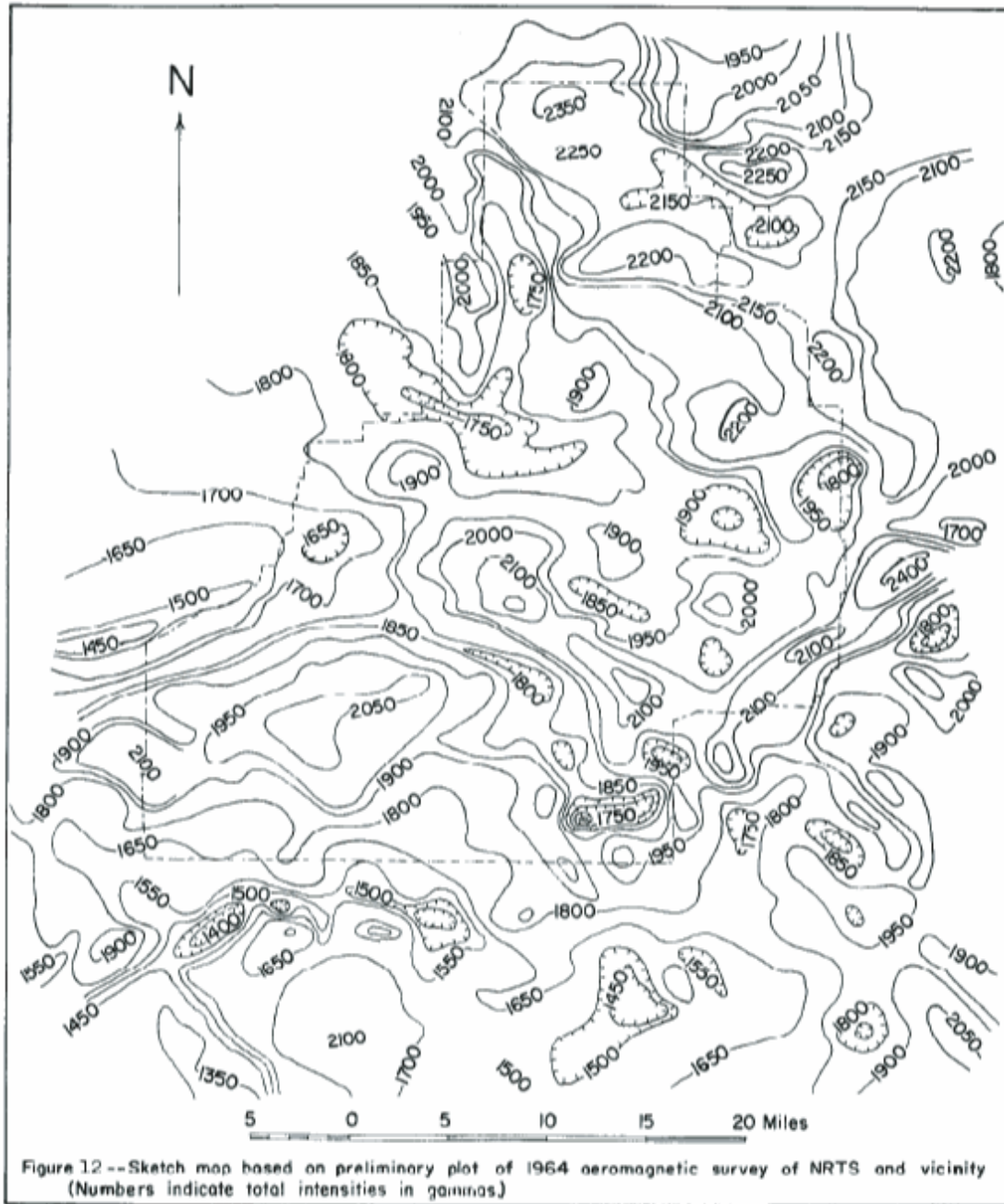


Figure C-16. Aeromagnetic map of the INL (from Morris et al. [1964]).

The long wavelength data in Figure C-12 show two broad areas of positive magnetic anomaly centered on the eastern Snake River Plain surrounded by broad negative anomalies over rocks of the Basin and Range to the north and south. The positive anomalies over the eastern Snake River Plain are likely due to the basalt veneer mentioned immediately above. A band of negative magnetic anomaly separates the two positive anomalies of the plain. This feature is sub-parallel to the Arco Rift with a local negative minima just east of the Cerro Grande flow and south of East and Middle Buttes. It is also roughly aligned with the gravity high centered immediately east of the Cerro Grande flow seen in the long wavelength Isostatic Residual data shown in Figure C-6. This phenomenon is unusual in that high-density

gravity anomalies are commonly associated with magnetic lows in an area with known accumulations of basalt. Though mid-crustal features seen in the gravity and magnetic anomalies for the plain have small bearing on the geology of the much-shallower Snake River Plain Aquifer (SRPA), one possible explanation for the magnetic low is thermal upwelling causing a shallow Curie point depth, more shallow than the depth of the long-wavelength presumed-deep gravity anomalies seen in Figure C-6; this is an untested hypothesis, though it is not incongruent with the geothermal warm spot observed in the SRPA around Well CH-1.

Intermediate-wavelength magnetic potential data sample sources in the mid- to upper-crust with the advantage of eliminating the short wavelength noise, which is a common undesirable feature of magnetic residual data. The intermediate wavelength data on Figure C-13 presents a similar though less complicated anomaly distribution compared to the magnetic residual data in Figure C-11. Comparison of the Geophysical Data for the Northern Rocky Mountains intermediate wavelength data to the 1964 USGS local magnetic data set (Morris et al. 1964) (see Figure C-16) shows that the 1964 data set resembles the magnetic residual data set more closely than the intermediate wavelength data. This implies that the 1964 data set samples more-shallow shorter-wavelength phenomena than the intermediate wavelength magnetic potential shown in Figure C-13. Despite the age and processing-limitations of the 1964 data set, the near-surface information content of these data underscore that data collection at this scale can reveal details not easily discerned from well data.

The positive anomalies from the magnetic residual data of the Axial Volcanic High between Table Legs and Kettle Buttes, the northern and southern eruptive portions of the Great Rift, and the northern end of the Arco Rift are also present in the intermediate wavelength data set and are actually more clearly defined. The Laidlaw Ridge, the southern extension of the Arco Rift at the North and South Robbers flows, plus Quaking Aspen Butte and Split Top Butte are also associated with positive anomalies. Also notable is a broad positive anomaly which extends eastward from Crater Butte to AEC Butte and the bend in the Big Lost River at the unmanned aerial vehicle landing strip north of INTEC. An additional positive anomaly stretches from NW to SE from State Butte to MFC. North of the former and west of the latter anomalies, there is a negative anomaly south of Howe which is fenced-in clockwise by Wells USGS-19, USGS-15, USGS-12, SITE-17, and USGS-23. The other prominent negative anomaly in the study is centered on Lava Ridge whose basalts have reverse-polarity remnant magnetization.

The Lava Ridge anomaly underscores the limitation of using regionally gridded composite data sets of aeromagnetic data and the steeply inclined magnetization assumption for analysis of anomalies. The Lava Ridge anomaly also calls into question the hypothesis that volcanic rift zones on the eastern Snake River Plain and positive magnetic anomalies correlate (Mabey 1978). Lava Ridge is a large block of reverse-polarity basalts exposed at the surface. In an area where so much of the magnetic signal originates in near-surface basalts with well-characterized normal and reversed remnant magnetization, and where higher-than-usual magnetic data already exist or are being added to^d, a rigorous modern magnetic analysis like that performed recently for Yellowstone by Finn and Morgan (2002) might resolve questions about the signal-to-noise content of near-surface magnetic sources in the 1964 and Geophysical Data for the Northern Rocky Mountains magnetic residual data sets and refine subsurface details in areas where dense well data is lacking. Since detailed geothermal data and modeling exist for the eastern Snake River Plain and its environs, a detailed depth-to-Curie point analysis of the INL area similar to that of Bhattacharyya and Leu (1975) for Yellowstone would also contribute to the analysis of unexpected anomalies like that of Lava Ridge. These suggested analyses will not be performed for the OU 10-08 model development project.

d. Payne, S., INL, personal communication, August 23, 2006.

C-3. SEISMIC DATA

In general, traditional seismic studies are not useful in layered basalts like those of the eastern Snake River Plain. The signal of reflected seismic energy, and in many cases refracted seismic energy, traveling through the thinly layered intercalated basalt sequence is lost quickly due to both basalt-channeled overtones and to attenuation by low-velocity interflow zones (e.g., Fuller 1987; Morris et al. 1964; c.f. Pankratz and Ackermann 1982; c.f. Braile et al. 1982). These phenomena prevent the development of high signal-to-noise details on the internal structure of the basalt sequence using traditional seismic gathering and migration techniques.

Some seismic studies have been able to illuminate the general velocity structure of the basin and range to eastern Snake River Plain transition where there is high-velocity contrast between the basalt sequence, underlying rhyolitic tuffs and porphyries, and basin and range sedimentary strata. Figure C-17 shows the location and Figure C-18 shows the results of Payne's interpretation of an Amoco processed seismic section at the transition between basin and range and the eastern Snake River Plain near Howe.^e At the point where eastern Snake River Plain basalts have reached their furthest extent northward, interfingering with the basin fill sediments, the seismic section shows displacement and diffraction patterns, which suggest a small graben downdropped right at the transition between the two provinces. This graben is north and west of the graben interpreted by Bruhn, Wu, and Lee (1992) from the 1984 Haley and Cavit gravity data.

High-energy refraction studies on the eastern Snake River Plain have resolved the structure of the lithosphere and uppermost asthenosphere, especially the studies that used the data from the 1978 Yellowstone and eastern Snake River Plain deep refraction project (Braile et al. 1982; Sparlin et al. 1982). Within the last decade, several seismic P-wave inversion and tomography studies have been published, adding to our knowledge of the lithospheric and asthenospheric structure of the eastern Snake River Plain. The most notable of these studies include Humphreys et al. (2000), Dueker and Yuan (2004), and Yuan and Dueker (2005).

A down-dropped graben occurs where eastern Snake River Plain basalt flows end their interfingering to the north into the basin fill sediments northeast of Howe. Note that the southern two normal faults dip away from the Snake River Plain in a manner similar to some of the faults mapped by Zentner (1989).^f

Significant among non-tomographic seismic studies are the refraction studies of Pankratz and Ackermann (1982) and Elbring (1984). Elbring collected seismic data along a line that followed the Carey-Kimama Rd., across the top of the western half of Craters of the Moon (Figure C-19). Elbring's interpretation of his data included a steeply dipping step-like discontinuity approximately 5 km inboard of the edge of the eastern Snake River Plain (Figure C-20). The vertical displacement on this structure is approximately 2 km.

Similar to the Elbring study, Pankratz and Ackermann (1982) collected several lines of seismic data, one of which followed the old stage coach road that crosses the southwest portion of the INL (Figure C-21). Their structural interpretation of this line is shown in Figure C-22, where a steeply dipping discontinuity has approximately 1 km of downthrown at 1.8 km inboard of the edge of the plain. Assuming that these features are faults, they have not been active within the last 300,000 years.^g

e. Payne, S., INL, unpublished data, 2004.

f. This figure was drafted by S. Payne and used with permission.

g. Payne, S., INL, personal communication, September 1, 2006.

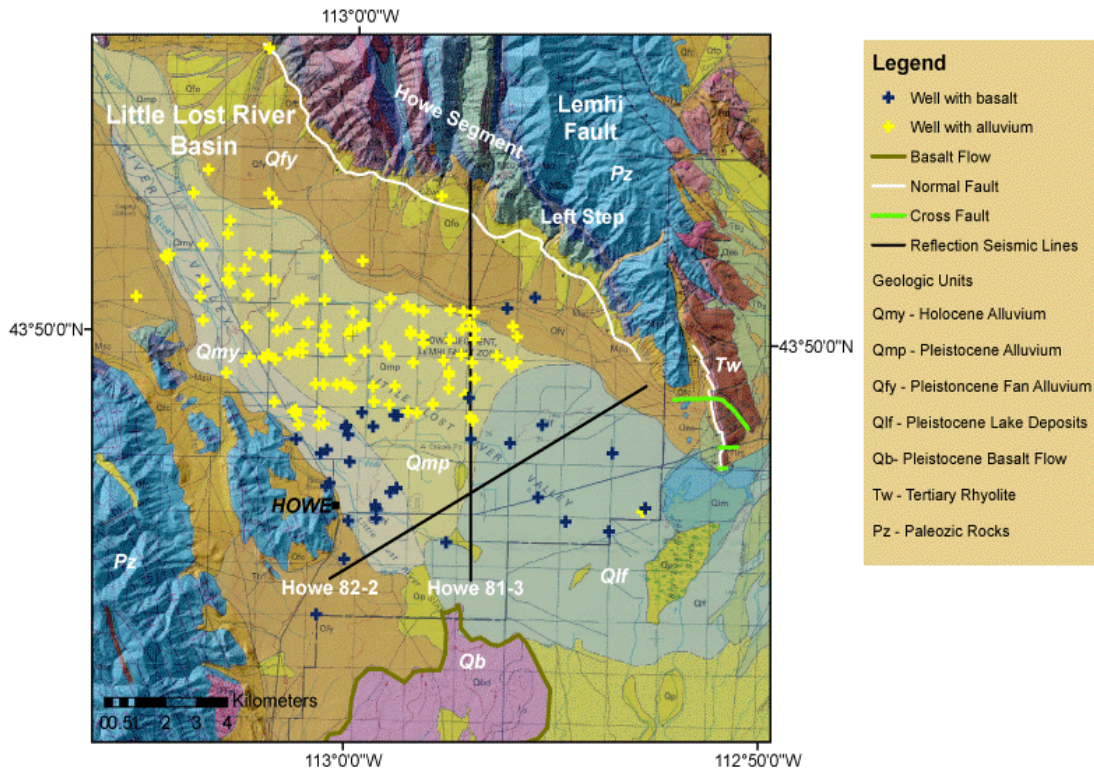


Figure C-17. Location map for Amoco seismic line Howe 81-3. Blue crosses are the locations of wells that intersect basalt. Yellow crosses represent wells that intersect no basalt. The map base is from Kuntz et al. (1994). Note the step faults in green at the end of the Lemhi Range—these are the same faults shown in Figure C-9.^h

h. This figure was drafted by S. Payne and used with permission.

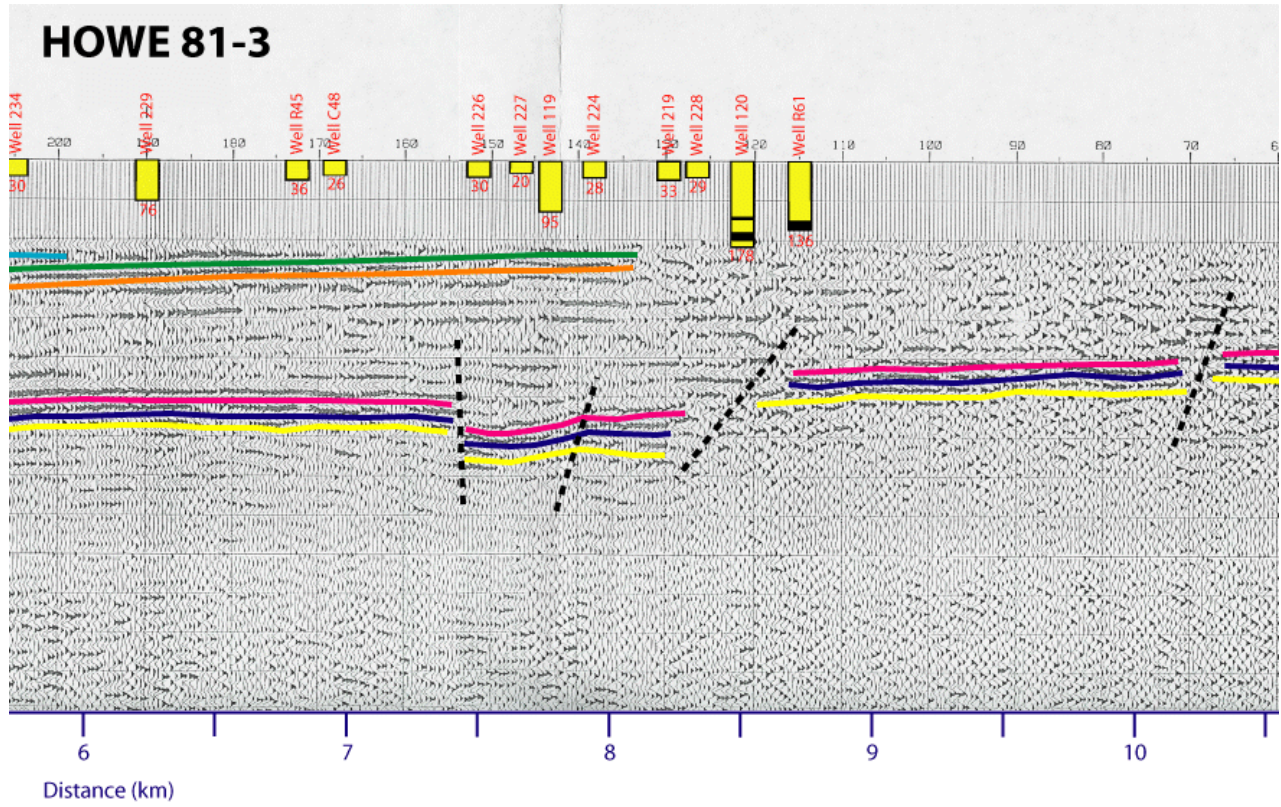


Figure C-18. Amoco seismic line Howe 81-3 as interpreted by S. Payne (see discussion).

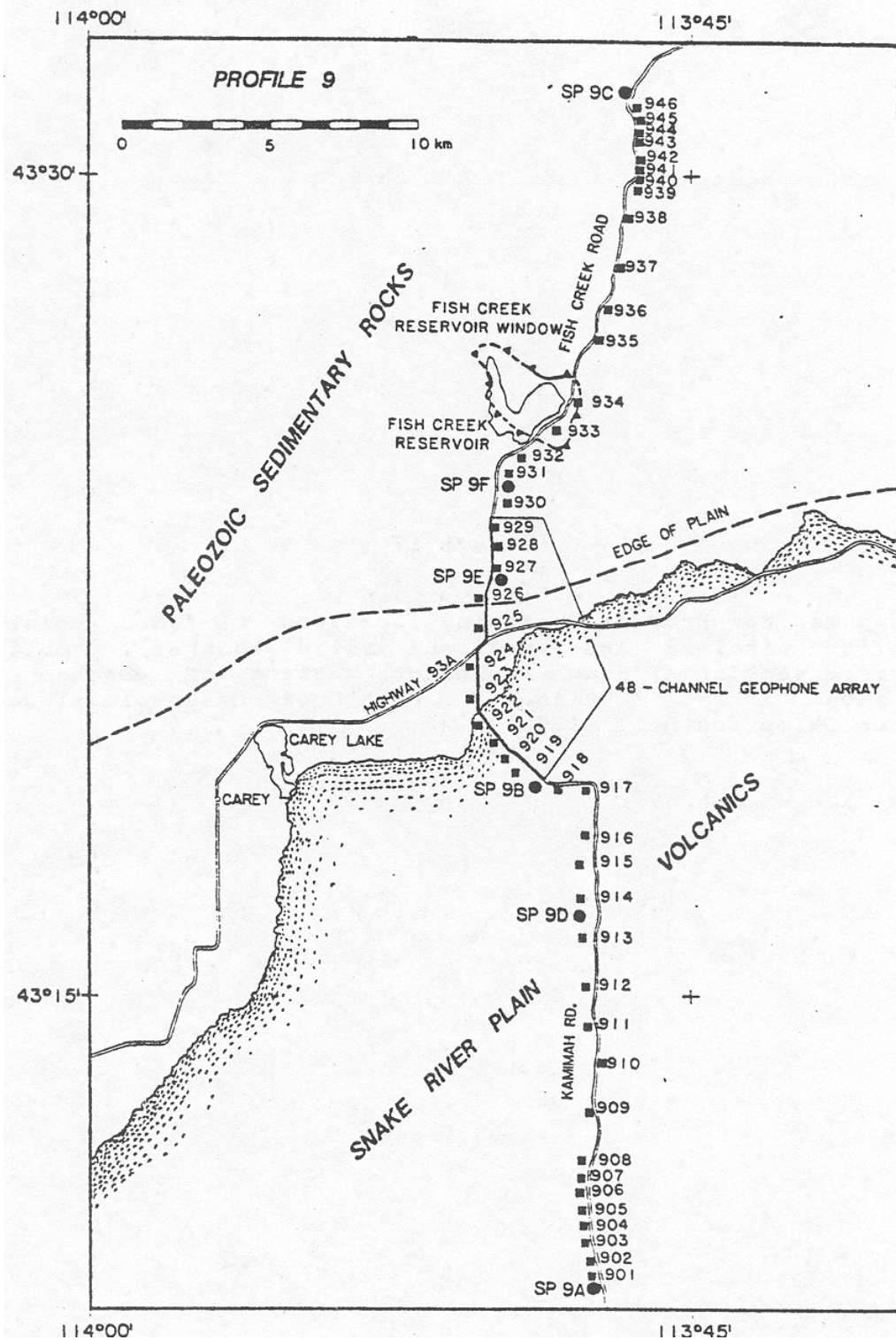


Figure C-19. Seismic line data collection locations on the west side of the Craters of the Moon lava field for the refraction study of Elbring (1984).

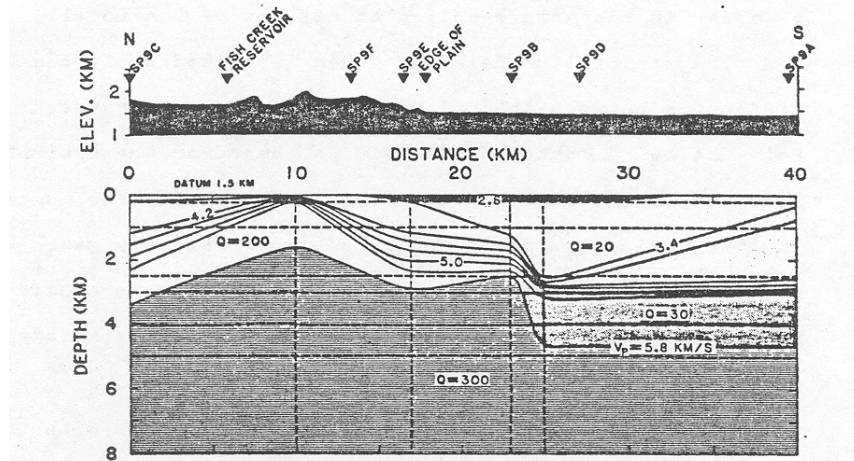


Figure 18

Final velocity model obtained from inversion of Profile 9 data. Shaded areas represent regions of constant Q values. Velocity contours at 0.4 km/s. Vertical exaggeration of 2.0x.

Figure C-20. Interpreted velocity structure for the Elbring (1984) seismic line shown in Figure C-19.

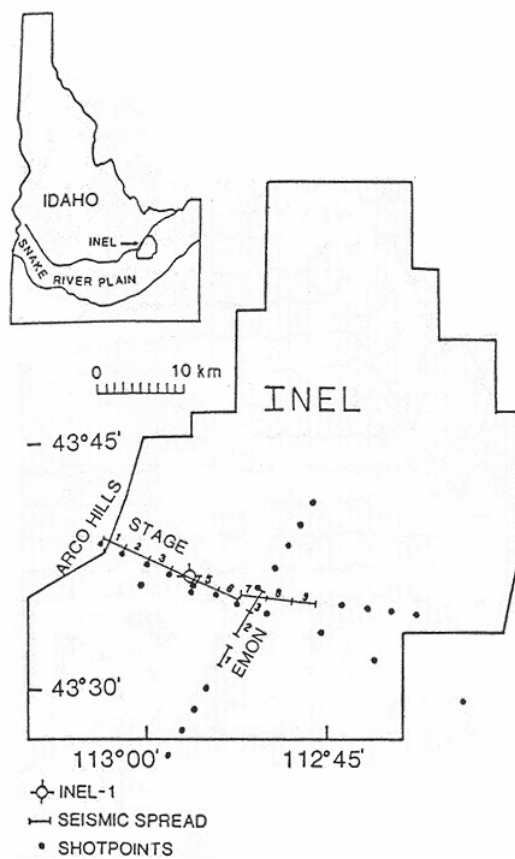


Figure C-21. Map showing the location of the seismic line along the old stage road that runs to the north of RTC for the seismic refraction study of Pankratz and Ackermann (1982). The location of geothermal exploration well INEL-1 is accurately portrayed.

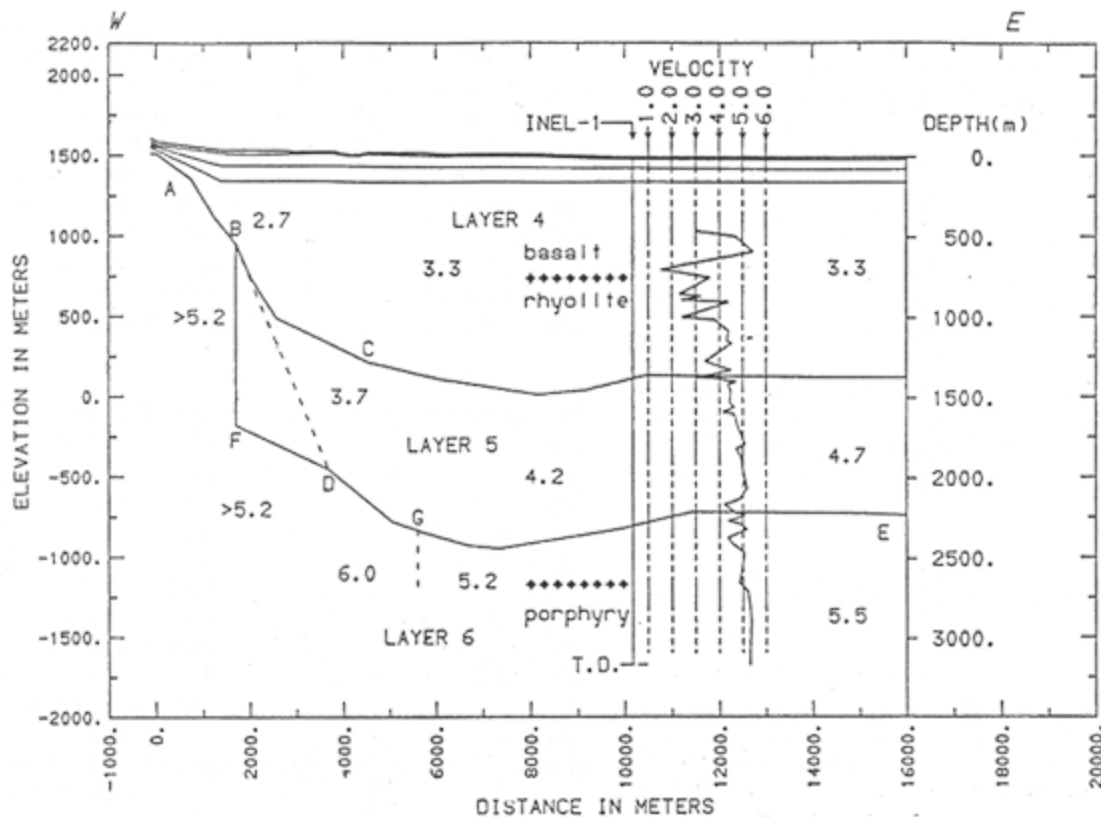


Figure C-22. Interpreted velocity structure for the Pankratz and Ackermann (1982) seismic line.

C-4. REFERENCES

- Anderson, S. R., M. A. Kuntz, and L. C. Davis, 1999, *Geologic Controls of Hydraulic Conductivity in the Snake River Plain Aquifer at and near the Idaho National Engineering and Environmental Laboratory, Idaho*, U.S. Geological Survey Water Resources Investigation Report 99-4033.
- Bhattacharyya, B. K., and L. Leu, 1975, "Analysis of magnetic anomalies over Yellowstone National Park: mapping of Curie point isothermal surface for geothermal reconnaissance," *J. Geophys. Res.*, Vol. 80, pp. 4461-4465.
- Braile, L. W., R. B. Smith, J. Ansorge, M. R. Baker, M. A. Sparlin, C. Prodehl, M. M. Schilly, J. H. Healy, S. Mueller, and K. H. Olsen, 1982, "The Yellowstone-Snake River Plain seismic profiling experiment: crustal structure of the Eastern Snake River Plain," *J. Geophys. Res.*, Vol. 87, pp. 2597-2609.
- Bruhn, R. L., D. Wu, and J. J. Lee, 1992, *Final Report on the Structure of the Southern Lemhi and Arco Fault Zone, Idaho*, EGG-NPR-10680, EG&G Idaho, Inc.
- Burger, H. R., A. F. Sheehan, and C. H. Jones, 2006, *Introduction to Applied Geophysics*, W. W. Norton & Co., New York, 600 pp.

- Bush, R. R., 1980, *Gravity survey of Tyhee area, Bannock County, Idaho*, M. S. Thesis: Idaho State University, Pocatello, Idaho.
- Butler, R. F., 1992, *Paleomagnetism*, Boston: Blackwell Scientific Publications, 319 pp.
- Dobrin, M. B., 1976, *Introduction to Geophysical Propecting (3rd Edition)*, New York: McGraw-Hill, Inc., 630 pp.
- Dueker, K., and H. Yuan, 2004, "Upper mantle P-wave velocity structure from PASSCAL teleseismic transects across Idaho, Wyoming and Colorado," *Geophys. Res. Lett.*, Vol. 31, L08603, doi:10.1029/2004GL019476, 2004.
- Eaton, G. P., R. R. Wahl, H. J. Prostka, D. R. Mabey, and M. D. Kleinkopf, 1978, "Regional gravity and tectonic patterns: Their relation to late Cenozoic epeirogeny and lateral spreading in the western Cordillera," in Smith, R.B., and G. P Eaton, eds., *Cenozoic tectonics and regional geophysics of the western Cordillera*, Geological Society of America Memoir 152, p. 51–91
- Elbring, G. J., 1984, *A method for inversion of two-dimensional seismic refraction data with applications to the Snake River Plain region of Idaho*, Ph.D. Dissertation, Purdue University.
- Finn, C. A., and L. A. Morgan, 2002 "High-resolution aeromagnetic mapping of volcanic terrain, Yellowstone National Park," *Journal of Volcanology and Geothermal Research*, Vol. 115, pp. 207–231.
- Fuller, B. N., 1987, *Seismic reflection data acquisition problems in the Columbia River Plateau and Snake River plain*, M. S. Thesis: University of Wyoming, Laramie, Wyoming.
- Greeley, R., 1982, "The style of Basaltic Volcanism in the Eastern Snake River Plain, Idaho," in Bonnichsen, B., and R. M. Breckenridge, eds., *Cenozoic Geology of Idaho*, Idaho Bur. Mines Geol. Bull., Vol. 26, pp. 407–421.
- Hadley, D. M., and D. S. Cavit, 1984, *Sierra Geophysics Report: Geophysical Investigations at the Idaho National Engineering Laboratory*, Report No. SGI-R-84-111, EG&G Idaho Inc., Idaho Falls, Idaho, 73 p.
- Helm-Clark, C. M., D. W. Rodgers, and R. P. Smith, 2004, "Borehole geophysical techniques to define stratigraphy, alteration and aquifers in basalt," *Journal of Applied Geophysics*, Vol. 55, pp. 1–38.
- Hildenbrand, T. G., B. Berger, R. C. Jachens, and S. Ludington, 2000, "Regional crustal structures and their relationship to the distribution of ore deposits in the western United States, based on magnetic and gravity data," *Economic Geology*, Vol. 95, pp. 1583–1603.
- Houser, B. B., 1992, "Quaternary stratigraphy of an area northeast of American Falls Reservoir, eastern Snake River Plain, Idaho," in Link, P. K., M. A. Kuntz, and L. B. Pratt, eds., *Regional Geology of Eastern Idaho and Western Wyoming*, Geological Society of America Memoir 179.
- Humphreys, E. D., K. G. Dueker, D. L. Schutt, and R. B. Smith, 2000, "Beneath Yellowstone: Evaluating plume and nonplume models using telesiesmic images of the upper mantle," *GSA Today*, Vol. 10, No. 12, pp. 1–7.

- IAGA, Division V, Working Group 8, 1992, "International geomagnetic reference field, 1991 Revision," in Langel, R. A., Chairman, *Analysis of the main field and secular variation: Geophysics*, Vol. 57, pp. 956–959.
- Kuntz, M. A., H. R. Covington, and L. J. Schorr, 1992, "An overview of basaltic volcanism on the eastern Snake River Plain, Idaho," in Link, P. K., M. A. Kuntz, and P. L. Platt, eds., *Regional Geology of Eastern Idaho and Western Wyoming*, Geological Society of America Memoir 179, pp. 227–267.
- Kuntz, M. A., B. Skipp, M. A. Lanphere, W. B. Scott, K. L. Pierce, G. B. Dalrymple, D. E. Champion, G. F. Embree, W. R. Page, L. A. Morgan, R. P. Smith, W. R. Hackett, and D. W. Rodgers, 1994, "Geological map of the Idaho National Engineering Laboratory and adjoining areas, eastern Idaho," United States Geological Survey Miscellaneous Investigations Series Map I-2330, scale 1:100,000.
- Kuntz, M. A., S. R. Anderson, D. E. Champion, M. A. Lanphere, and D. J. Grunwald, 2002, "Tension Cracks, Eruptive Fissures, Dikes, and Faults Related to Late Pleistocene-Holocene Basaltic Volcanism and Implications for the Distribution of Hydraulic Conductivity in the Eastern Snake River Plain, Idaho," in P. K. Link and L. L. Mink, eds., *Geology, Hydrogeology, and Environmental Remediation: Idaho National Engineering and Environmental Laboratory, Eastern Snake River Plain, Idaho*, Geological Society of America Special Paper 353, pp. 111–133.
- Mabey, D. R., 1978, "Regional gravity and magnetic anomalies in the eastern Snake River plain, Idaho," *Journal of Research of the U.S. Geological Survey*, Vol. 6, Issue 5, pp. 553–562.
- Machette, M. N., K. M. Haller, R. L. Dart, and S. B. Rhea, 2003, *Quaternary fault and fold database of the United States*, U. S. Geological Survey Open File Report 2003-417.
- Mankinen, E. A., T. G. Hildenbrand, M. L. Zientek, S. E. Box, A. B. Bookstrom, M. H. Carlson, and J. C. Larsen, 2004, *Guide to Geophysical Data for the Northern Rocky Mountains and adjacent areas, Idaho, Montana, Washington, Oregon, and Wyoming*, U.S. Geological Survey Open-File Report 2004-1413.
- McQuarrie, N., and D. W. Rodgers, 1998, "Subsidence of a volcanic basin by flexure and lower crustal flow, the eastern Snake River plain, Idaho," *Tectonics*, Vol. 17, pp. 203–220, doi: 10.1029/97TC03762.
- Morgan, L. A., D. J. Doherty, and W. P. Leeman, 1984, "Ignimbrites of the eastern Snake River Plain, Idaho: Evidence for major caldera-forming eruptions," *Journal of Geophysical Research*, Vol. 89, pp. 8665–8678.
- Morris, D. A., J. T. Barraclough, G. M. Hogenson, Eugene Shuter, W. E. Teasdale, D. A. Ralston, and R. G. Jensen, 1963, *Hydrology of subsurface waste disposal, National Reactor Testing Station, Idaho, annual progress report, 1963*, U.S. Atomic Energy Commission, Idaho Operations Office Publication, IDO-22046-USGS, 97 p.
- Morris, D. A., J. T. Barraclough, G. H. Chase, W. E. Teasdale, and R. G. Jensen, 1964, *Hydrology of subsurface waste disposal, National Reactor Testing Station, Idaho, annual progress report, 1964*, U.S. Atomic Energy Commission, Idaho Operations Office Publication, IDO-22047, 186 p.
- NAMAG, 2002, *North American Magnetic Anomaly Group*, USGS Open-File Report 02-414.

- Pankratz, L. W., and H. D. Ackermann, 1982, "Structure Along the Northwest Edge of the Snake River Plain Interpreted from Seismic Refraction," *J. Geophys. Res.*, Vol. 84, pp. 2676–2682.
- Parsons, T., G. A. Thompson, and R. P. Smith, 1998, "More than one way to stretch: a tectonic model for extension along the plume track of the Yellowstone hotspot and adjacent Basin and Range Province," *Tectonics*, Vol. 17, pp. 221–234.
- Peng, X., and E. D. Humphreys, 1998, "Crustal velocity structure across the eastern Snake River Plain and the Yellowstone swell," *Journal of Geophysical Research*, Vol. 103, pp. 7171–7186.
- Price, K. B., G. Embree, R. Hoggan, and S. Hansen, 1999, "Field guide along the northern edge of the eastern Snake River Plain, and the Lemhi and Beaverhead mountain ranges bordering Birch Creek Valley, Idaho," in Hughes, S. S., and G. D. Thackray, eds., *Guidebook to the Geology of Eastern Idaho*, Idaho Museum of Natural History, pp. 335–342.
- Rubin, A. M., and D. D. Pollard, 1988, "Dike-Induced Faulting in Rift Zones of Iceland and Afar," *Geology*, Vol. 16, pp. 413–417.
- Rubin, A. M., 1992, "Dike-Induced Faulting and Graben Subsidence in Volcanic Rift Zones," *J. Geophys. Res.*, Vol. 97, pp. 1839–1858.
- Schruben, P. G., R. E. Arndt, and W. J. Bawiec, 1977, *Geology of the Conterminous United States at 1:2,500,000 Scale—A Digital Representation of the 1974 P. B. King and H. M. Beikman Map*, U.S. Geological Survey Digital Data Series DDS.11, Release 2.
- Smith, R. P., S. M. Jackson, and W. R. Hackett, 1996, "Paleoseismology and Seismic Hazards Evaluations in Extensional Volcanic Terrains," *J. Geophys. Res.*, Vol. 101, pp. 6277–6292.
- Sparlin, M. A., L. W. Braile, and R. B. Smith, 1982, "Crustal Structure of the eastern Snake River Plain determined from ray-tracing modeling of seismic refraction data," *Journal of Geophysics*, Vol. 87, pp. 2619–2633.
- Spear, D., 1979, *The geology and volcanic history of the Big Southern Butte-East Butte area, eastern Snake River Plain, Idaho*; Ph.D. Dissertation: State University of New York at Buffalo.
- Welhan, J. A., C. M. Johannesen, K. S. Reeves, T. M. Clemo, J. A. Glover, and K. W. Bosworth, 2002, "Morphology of inflated pahoehoe lavas and spatial architecture of their porous and permeable zones, eastern Snake River Plain, Idaho," in Link, P. K., and L. L. Mink, eds. *Geology, hydrogeology, and environmental remediation, Idaho National Engineering and Environmental Laboratory, Eastern Snake River Plain, Idaho*, GSA Special Paper 353, pp. 135-150.
- Yuan, H., and K. Dueker, 2005, "Teleseismic P-wave tomogram of the Yellowstone plume," *Geophys. Res. Lett.*, 32, L07304, doi:10.1029/2004GL022056.
- Zentner, N. C., 1989, *Neogene normal faults related to the structural origin of the eastern Snake River plain*, M. S. Thesis: Idaho State University, Pocatello, Idaho.

Appendix D

Heat-Flow Implementation Details

Appendix D

Heat-Flow Implementation Details

Calculation of the source terms and first-order decay rates for implementation of heat flow in the Groundwater Modeling System (GMS) involved several steps:

Constants needed for the calculations:

Porosity	$\theta := 0.3$	
Saturation	$S_w := 0.1$	
Densities:		
Water	$\rho_w := 1000 \text{ kg}\cdot\text{m}^{-3}$	
Solid	$\rho_s := 2750 \text{ kg}\cdot\text{m}^{-3}$	
Bulk density	$\rho_{\text{bulk}} := (1 - \theta) \cdot \rho_s$	
Specific heats:		
Water	$c_w := 1 \cdot \text{cal}\cdot(\text{gm}\cdot\text{K})^{-1}$	$c_w = 4.187 \times 10^3 \frac{1}{\text{K}\cdot\text{kg}} \text{ J}$
Solid	$c_s := 0.2 \cdot \text{kcal}\cdot(\text{kg}\cdot\text{K})^{-1}$	$c_s = 837.36 \frac{1}{\text{K}\cdot\text{kg}} \text{ J}$
Heat capacities:		
Water	$C_w := \rho_w \cdot c_w$	$C_w = 4.187 \times 10^6 \frac{1}{\text{m}^3 \cdot \text{K}} \text{ J}$
Solid	$C_s := \rho_s \cdot c_s$	$C_s = 2.303 \times 10^6 \frac{1}{\text{m}^3 \cdot \text{K}} \text{ J}$
Effective	$C_{\text{eff}} := S \cdot \theta \cdot C_w + (1 - \theta) \cdot C_s$	$C_{\text{eff}} = 1.738 \times 10^6 \frac{1}{\text{m}^3 \cdot \text{K}} \text{ J}$
Mean air temperature	$T_{\text{air}} := 5.5 \cdot \text{K}$	
T_{ground} offset from T_{air}	$T_{\text{offset}} := 4 \cdot \text{K}$	
Thermal conductivity:		
Basalt/sediments	$\kappa := 2 \cdot \frac{\text{watt}}{\text{m}\cdot\text{K}}$	$\kappa = 1.728 \times 10^5 \frac{1}{\text{m}\cdot\text{K}} \frac{\text{joule}}{\text{day}}$
Sorption term for MT3DMS	$K_d := \frac{(1 - \theta) \cdot C_s}{\rho_{\text{bulk}} \cdot C_w}$	$K_d = 2 \times 10^{-4} \frac{\text{m}^3}{\text{kg}}$

Example data, to demonstrate fluxes for "average" cells:

Cell area	$A_{\text{cell}} := 149625 \text{ m}^2$
Thicknesses:	
Vadose zone	$b_{\text{vz}} := 100 \text{ m}$
Cell	$b_{\text{cell}} := 70 \text{ m}$

Heat flux calculations for MT3DMS (Specified for input units of m and days)

Note that for concentration to be consistent with concentration as MT3DMS understands it, we establish a measure of mass for temperature that is counts joules per cubic meter in terms of Cw units. That is one mg equals Cw joules.

$$\text{massunit} := C_w \cdot m^3 \cdot K \cdot \frac{1}{\text{mg}} \quad \text{massunit} = 4.187 \times 10^6 \frac{\text{J}}{\text{mg}}$$

Calculation of the geothermal heat flux source term as a mass loading rate (type 15 - no water flux) requires

1. Geothermal heat flux (joule/day/m²)
2. Cell area

Calculate geothermal heat flux term:

Calculate the terms that are not cell-dependent (all but conversion to 'mass' units):

$$J_{\text{geothermal}} := 0.11 \cdot \frac{\text{watt}}{\text{m}^2}$$

$$J_{\text{geothermal}} = 9.504 \times 10^3 \frac{1}{\text{m}^2} \frac{\text{J}}{\text{day}}$$

For cell of average area:

$$\frac{J_{\text{geothermal}} \cdot A_{\text{cell}}}{\text{massunit}} = 339.647 \frac{\text{mg}}{\text{day}}$$

Calculate heat flux through vadose zone:

This is broken up into two terms:

- 1) A mass loading rate representing the heat flux from the surface to the groundwater
- 2) A first order reaction loss rate, representing the loss of heat when the groundwater is warmer than the ground

$$\text{GainLoss} = -\kappa \cdot \frac{T_{\text{gw}} - T_{\text{land}}}{b_{\text{vz}}}$$

$$\text{GainLoss} = \frac{-\kappa}{b_{\text{vz}}} \cdot T_{\text{gw}} + \frac{\kappa}{b_{\text{vz}}} \cdot T_{\text{land}}$$

Heat flux from the surface to the groundwater

Calculation of the vadose zone heat flux source term as a mass loading rate (type 15 - no water flux) requires

1. Mean air temperature
2. Ground temperature offset from air temperature
3. Thermal conductivity of the vadose zone
4. Cell area

Calculate the terms that are not cell-dependent (all but conversion to 'mass' units):

$$R1 := \frac{\kappa}{b_{vz}} \qquad R1 = 1.728 \times 10^3 \frac{1}{m^2 \cdot K} \frac{joule}{day}$$

With average cell area, and average temperature at surface, the value of the vadose zone heat flux source term will be approximately

$$Source := \frac{R1 \cdot (T_{air} + T_{offset}) \cdot A_{cell}}{massunit} \qquad Source = 586.664 \frac{mg}{day}$$

Decay term, per cubic meter of aquifer :

Calculation of the first order rate constant representing heat flux to the ground surface requires

1. Thermal conductivity of the vadose zone
2. Vadose zone thickness
3. Thickness of the cell of the uppermost layer of the aquifer
4. Porosity of the uppermost layer of the aquifer

$$\lambda_a := \frac{\kappa}{b_{vz}} \qquad \lambda_a = 1.728 \times 10^3 \frac{1}{m^2 \cdot K} \frac{J}{day}$$

The decay term is applied to each cubic meter of aquifer. It therefore has to be corrected (divided by) for aquifer thickness. The decay rate is calculated according to **concentration**, which is T, so the concentration has to also represent temperature, accomplished by specifying mass units that make Joules per unit meter equivalent to temperature:

$$\lambda_b := \frac{\lambda_a}{b_{cell} \cdot C_w} \qquad \lambda_b = 5.896 \times 10^{-6} \frac{1}{day}$$

The decay term is most easily applied to a single phase, so here we apply it only to the dissolved phase. As that constitutes only ϕ of the total volume, the retardation rate has to be corrected by $1/\phi$.

$$\lambda_{final} := \frac{\lambda_b}{\theta} \qquad \lambda_{final} = 1.965 \times 10^{-5} \frac{1}{day}$$

At 12 C, the losses, per square meter of aquifer, from fluid and solid phases would be:

$$b_{cell} \cdot A_{cell} \cdot \lambda_{final} \cdot \theta \cdot (12 \cdot K \cdot C_w) = 3.103 \times 10^9 \frac{J}{day}$$

When the gw is the same temperature as the land surface, the decay rate should equal the source term:

$$R1 \cdot (12 \cdot K) \cdot A_{cell} = 3.103 \times 10^9 \frac{J}{day}$$

Calculation of the mass-loading rates for specification of heat-flow boundaries in MT3DMS was performed in a MATLAB script, after importing the necessary data to a MATLAB workspace. The necessary inputs include

1. The entire model grid, with variables identifying
 - a. Whether a cell is inactive or active
 - b. Whether a cell represents the bottom of the domain
2. Cell area
3. Vadose zone thickness.

Item 1 was exported from GMS in the default linear indexing format (i.e., $J + (I-1)I_{max} + (K-1)K_{max}$), read into TECPLOT to provide a visual display of the data and for calculation of the flag indicating whether or not a cell represents the bottom of the domain. The data were then exported from TECPLOT in J,I,K,Data-indexed form. Item 2 was exported from the GMS spreadsheet utility in its default I,J,K, - indexed format and read directly into MATLAB. Item 3 was exported from the GMS two-dimensional grid dataset in its default linear indexing format, read into TECPLOT and exported to a text file in J,I,Datavalue – indexed format. The MATLAB script that calculates the necessary mass loading terms and writes MT3DMS-formatted output text follows.

MAKESM_v5.m

```
%Clear the temporary array used for manipulation of the input data
clear tempfull temp out;

jmax=271;
imax=197;
kmax=6;
ijmax=imax*jmax
NSScells = 2*length(find(Ibundbtm(:,4)==1 & Ibundbtm(:,3)==1)) -
length(find(Ibundbtm(:,5)==1 & Ibundbtm(:,3)==1))

%Consistent with GMS output (&IbundBtm array), the columns of the temporary data file
will be
  %J, I, K, ICbund, Ibtm, Area(m^2), VZfluxbase,FinalSSMterm
  %Sorted by K, then I, then J, so J is changing fastest
tempfull = Ibundbtm;
%tempfull(:,1:3)=int16(tempfull(:,1:3)); %Convert the first 3 columns to integers

%Fill in the col 6 of the temp dataset with the CELL AREA values (provided for 1
layer)
%The columns of the exported Area array are I, J, Area
%For each row of the Area array, calculate the corresponding linear index for the full
%grid cell (I-1)*jmax+J
indexset=(Area(:,1)-1)*jmax + Area(:,2);
for n = 0:5;
  tempfull(n*ijmax + indexset,6) = Area(:,3);
end

%Modify the Ibundbtm array by adding column 7 to it.
  %Col 7 is the SSM data for layer 1 that represents vadose zone heat flux.
  %Cols of the ssm array (exported from Tecplot) are J,I,dataval (sorted
  %by I then J)
tempfull(1:ijmax,7) = SSMperUnitArea(:,3);

%Copy the data to a new temp array, but only cells that are
```

```

%active (col 4=1), AND
%bottom-most (col 5=1) OR in layer 1 (col 3 = 1)
temp = tempfull(find(tempfull(:,4)==1 & (tempfull(:,5)==1 | tempfull(:,3)==1)),:);

%Create a new column and enter in it the geothermal heat flux term to the
%bottom cells plus the vadose heat flux and multiply both by the cell area
HeatFlux = 9504; %(Joules / m^2)
Cw = 4.187e6;
temp(:,8) = (temp(:,7) + HeatFlux) /Cw .* temp(:,6);

%Reorganize the columns to the k,i,j (layer, row, column) format needed
%in the .ssm file and write to new array
out(:,1:6)=[temp(:,3),temp(:,2),temp(:,1),temp(:,8),15.*ones(size(temp(:,1))),temp(:,8)
)];

%Convert the first 3 & 5th columns to integers
out(:,1:3)=int16(out(:,1:3));
out(:,5)=int8(out(:,5));

%Write the appropriately formatted data to an output file
fid = fopen('SSM-all-v5test.txt','w');
fprintf(fid, '%10i%10i%10i%10.3f%10i%10.3f\n', out');
status = fclose(fid);
clear status fid

```


Appendix E

Error Statistics for Head Mismatches (Simulated – Observed) for Four Base Case Models

Table E-1. Error statistics for head mismatches (simulated – observed) for four base case models with facility summaries.

	Number of Wells	Mean Error				Mean Absolute Error				Root Mean Squared Error			
		Model 1	Model 2	Model 3	Model 4	Model 1	Model 2	Model 3	Model 4	Model 1	Model 2	Model 3	Model 4
<i>Model Totals</i>	225	-0.047	0.007	0.003	-0.057	0.490	0.497	0.442	0.490	0.713	0.722	0.656	0.697
<i>Facility Totals</i>													
CFA	14	-0.556	-0.524	-0.446	-0.454	0.713	0.699	0.640	0.662	0.798	0.779	0.713	0.733
INTEC	37	0.149	0.156	0.149	0.121	0.217	0.223	0.212	0.194	0.246	0.252	0.243	0.223
RTC	8	0.221	0.247	0.287	0.292	0.421	0.435	0.453	0.453	0.519	0.531	0.550	0.542
RWMC	18	-0.135	-0.113	-0.036	-0.136	0.338	0.319	0.298	0.328	0.449	0.430	0.401	0.435
TAN	60	-0.131	-0.011	-0.088	-0.205	0.355	0.340	0.332	0.365	0.547	0.520	0.511	0.546
Others	88	0.003	0.044	0.058	0.017	0.698	0.730	0.611	0.710	0.951	0.981	0.869	0.931

Table E-2. Error statistics for head mismatches (simulated – observed) for four base case models (wells listed alphabetically by name).

Well Name or Identifier	Facility (for Table E-1)	Elevation		Observed	Residuals (computed - observed) (m)			
		Top Screen (m MSL)	Bottom Screen (m MSL)	Head (m MSL)	Model 1	Model 2	Model 3	Model 4
30607-2515601		1339.32	1332.91	1341.32	-0.89	-1.01	-0.82	-0.86
30836-3143401		1252.16	1244.54	1253.31	-0.06	0.07	0.05	0.04
30930-2505701		1340.27	1317.36	1342.27	0.48	0.44	0.52	0.58
31929-2421701		1343.86	1322.85	1345.86	0.10	0.07	0.10	0.30
31946-3161401		1259.47	1255.14	1261.47	0.00	0.00	-0.03	-0.04
33759-2225401		1370.43	1366.44	1372.43	-0.21	-0.16	0.01	-0.33
34447-2133401		1378.76	1371.90	1380.76	-0.09	-0.05	-0.03	-0.09
34751-2571801		1419.17	1417.64	1425.49	-0.13	0.15	-0.11	-0.16
34756-2212101		1377.55	1371.31	1379.55	-0.16	-0.03	-0.06	-0.13
35134-2335501		1397.13	1265.85	1399.13	-0.41	-0.27	-0.06	-0.33
ANL-MON-A-013		1361.82	1358.93	1363.82	0.17	0.23	0.14	0.29
ANP-04	TAN	1391.38	1363.24	1393.38	0.19	0.34	0.23	0.11
ANP-06	TAN	1392.13	1384.38	1394.13	-1.08	-0.90	-0.91	-1.04
ANP-07		1391.75	1372.90	1393.75	0.68	0.88	0.60	0.72
ANP-08	TAN	1388.86	1366.96	1392.64	0.34	0.44	0.38	0.25
ANP-09	TAN	1386.79	1363.26	1388.67	1.74	1.79	1.69	1.56
ARA-MON-A-001		1345.50	1339.40	1353.21	-0.63	-0.63	-0.40	-0.61
ARA-MON-A-002		1352.54	1346.44	1353.07	-0.53	-0.53	-0.31	-0.50
ARA-MON-A-004		1353.21	1347.11	1353.71	-0.94	-0.97	-0.71	-0.91
ARA-MON-A-03A		1349.09	1343.00	1353.69	-0.64	-0.74	-0.52	-0.56
ARBOR-TEST		1362.12	1351.34	1364.12	-0.14	-0.14	-0.05	-0.17
CFA-MON-A-001	CFA	1352.24	1346.76	1354.24	-0.55	-0.49	-0.40	-0.35
CFA-MON-A-002	CFA	1352.04	1345.48	1354.04	-0.35	-0.29	-0.22	-0.16
CFA-MON-A-003	CFA	1353.15	1347.05	1353.56	0.13	0.19	0.26	0.33
DH-1B		1344.89	1338.80	1373.84	1.12	0.96	0.84	0.99

E-4

Table E-2. (continued).

Well Name or Identifier	Facility (for Table E-1)	Elevation		Observed	Residuals (computed - observed) (m)			
		Top Screen (m MSL)	Bottom Screen (m MSL)	Head (m MSL)	Model 1	Model 2	Model 3	Model 4
FET-3	TAN	1391.36	1368.02	1393.36	-0.26	-0.10	-0.14	-0.26
GIN-01	TAN	1390.51	1345.38	1392.51	0.37	0.47	0.41	0.29
GIN-02	TAN	1390.61	1336.38	1392.61	0.29	0.39	0.33	0.21
GIN-03_2	TAN	1390.66	1341.31	1392.66	0.21	0.31	0.26	0.13
GIN-04	TAN	1390.78	1365.71	1392.78	0.12	0.22	0.16	0.05
HIGHWAY-2		1364.06	1350.34	1366.10	-1.00	-1.52	-0.23	-1.40
ICPP-1782	INTEC	1355.70	1343.51	1355.78	0.31	0.31	0.30	0.26
ICPP-1783	INTEC	1355.31	1343.12	1355.85	0.26	0.27	0.26	0.22
ICPP-1800	INTEC	1355.05	1342.86	1355.82	0.33	0.33	0.32	0.28
ICPP-1829	INTEC	1354.82	1342.63	1355.83	0.33	0.33	0.33	0.28
ICPP-1831	INTEC	1353.92	1343.78	1355.92	0.14	0.15	0.14	0.10
ICPP-MON-A-019_3	INTEC	1354.51	1352.36	1356.51	0.06	0.08	0.05	0.01
ICPP-MON-A-022	INTEC	1346.35	1340.25	1356.34	0.33	0.36	0.33	0.28
ICPP-MON-A -164B		1353.81	1345.91	1355.81	-0.77	-0.73	-0.62	-0.66
ICPP-MON-A -164C		1353.84	1348.72	1355.84	-1.10	-1.05	-0.91	-0.98
ICPP-MON-A -166		1353.73	1349.98	1355.73	-1.40	-1.36	-1.16	-1.27
LF2-08	CFA	1355.38	1352.33	1355.83	-0.91	-0.89	-0.82	-0.86
LF2-09	CFA	1353.80	1351.87	1355.80	-0.89	-0.87	-0.80	-0.83
LF2-10	CFA	1282.46	1270.26	1355.19	-0.28	-0.27	-0.19	-0.25
LF2-11	CFA	1353.88	1350.09	1355.88	-0.61	-0.60	-0.55	-0.60
LF3-08	CFA	1353.40	1350.35	1355.90	-1.19	-1.17	-1.06	-1.10
LF3-09	CFA	1353.86	1353.66	1355.86	-1.19	-1.17	-1.06	-1.09
LF3-10	CFA	1353.85	1353.87	1355.85	-1.15	-1.12	-1.01	-1.05
M1SA	RWMC	1342.08	1332.93	1347.82	-0.08	-0.03	0.07	-0.07
M3S	RWMC	1345.21	1336.06	1347.93	0.18	0.22	0.27	0.16

Table E-2. (continued).

Well Name or Identifier	Facility (for Table E-1)	Elevation		Observed	Residuals (computed - observed) (m)			
		Top Screen (m MSL)	Bottom Screen (m MSL)	Head (m MSL)	Model 1	Model 2	Model 3	Model 4
M4D	RWMC	1287.65	1278.51	1348.26	-0.70	-0.67	-0.55	-0.68
M6S	RWMC	1345.77	1340.45	1347.77	-0.24	-0.22	-0.18	-0.23
M7S	RWMC	1343.22	1334.08	1348.16	0.43	0.45	0.48	0.39
MIDDLE-2050A_1o	INTEC	1354.61	1338.77	1356.61	-0.40	-0.39	-0.40	-0.37
MIDDLE-2050A_2o	INTEC	1306.40	1288.57	1356.52	-0.32	-0.32	-0.33	-0.30
MIDDLE-2050A_3o	INTEC	1262.21	1256.84	1355.70	0.50	0.49	0.45	0.51
MIDDLE-2050A_4o	INTEC	1197.99	1185.64	1356.09	0.08	0.06	0.01	0.08
MIDDLE-2050A_5o	INTEC	1142.75	1128.89	1355.94	0.21	0.20	0.16	0.21
MIDDLE-2051_1o		1350.25	1338.26	1352.30	-1.56	-1.78	-1.71	-1.68
MIDDLE-2051_2o		1296.93	1289.10	1350.26	0.52	0.36	0.39	0.39
MIDDLE-2051_3o		1271.75	1256.91	1350.20	0.66	0.52	0.57	0.52
MTR-TEST	RTC	1354.27	1319.54	1356.27	0.99	1.02	1.06	1.03
NO-NAME-01	TAN	1377.58	1290.71	1392.75	0.03	0.18	0.16	0.05
NPR-TEST		1350.02	1341.49	1360.20	-1.80	-1.61	-1.66	-1.43
NTP-AREA_2		1337.03	1315.10	1356.72	-0.89	-0.87	-0.76	-0.85
OWSLEY-2		1382.25	1366.40	1388.39	-0.41	-0.24	-0.34	-0.44
P&W-1		1391.38	1378.84	1393.38	0.03	0.28	0.30	0.22
P&W-2		1391.31	1374.10	1393.31	0.21	0.45	0.45	0.39
P&W-3		1390.82	1366.76	1393.50	1.46	1.55	0.98	1.24
PBF-MON-A-001		1357.03	1347.89	1358.45	-2.14	-2.10	-1.99	-2.11
PBF-MON-A-003		1345.49	1336.35	1352.47	0.63	0.61	0.63	0.67
PBF-MON-A-004		1346.52	1340.42	1353.62	1.14	1.14	1.16	1.24
PSTF-TEST	TAN	1390.92	1362.63	1392.92	-0.36	-0.24	-0.27	-0.38
RWMC-MON-A-013	RWMC	1345.16	1339.25	1347.16	0.09	0.11	0.15	0.11
RWMC-MON-A-065	RWMC	1346.81	1231.89	1348.55	-1.14	-1.12	-1.00	-1.12

Table E-2. (continued).

Well Name or Identifier	Facility (for Table E-1)	Elevation		Observed	Residuals (computed - observed) (m)			
		Top Screen (m MSL)	Bottom Screen (m MSL)	Head (m MSL)	Model 1	Model 2	Model 3	Model 4
SITE-01A_3		1320.35	1313.95	1333.41	0.01	0.10	0.11	-0.03
SITE-14		1298.13	1242.76	1375.35	-3.07	-3.19	-2.82	-2.77
SITE-15		1373.01	1353.12	1375.01	0.03	0.13	-0.02	0.07
SITE-17		1361.54	1304.72	1363.54	-0.62	-0.69	-0.43	-0.69
SOUTH-MON-A-001_2	RWMC	1338.15	1332.05	1349.06	0.60	0.51	0.57	0.54
SOUTH-MON-A-002_2		1349.45	1343.36	1351.96	-0.04	-0.19	0.09	-0.13
SOUTH-MON-A-003_2		1342.28	1336.18	1348.12	1.63	1.56	1.63	1.57
SOUTH-MON-A-004_2	RWMC	1343.53	1340.48	1348.25	0.43	0.44	0.50	0.41
SOUTH-MON-A-009	RWMC	1346.99	1340.89	1347.87	-0.05	-0.03	0.02	-0.05
SOUTH-MON-A-010	RWMC	1346.28	1338.50	1348.28	-0.01	0.02	0.06	-0.03
STF-MON-A-003		1349.24	1342.21	1351.24	1.99	2.05	1.90	1.93
STF-MON-A-004		1349.51	1342.77	1351.51	1.53	1.61	1.41	1.48
STF-MON-A-01A		1342.17	1336.08	1352.49	0.74	0.81	0.65	0.68
STF-MON-A-02A		1349.46	1343.36	1352.27	1.41	1.46	1.39	1.32
TAN-04	TAN	1391.30	1388.78	1393.30	-0.06	0.07	-0.02	-0.13
TAN-05	TAN	1377.82	1371.26	1393.26	-0.02	0.10	0.02	-0.10
TAN-06	TAN	1387.43	1381.33	1393.21	0.08	0.20	0.10	-0.02
TAN-07	TAN	1368.28	1362.19	1393.18	0.11	0.22	0.13	0.01
TAN-08	TAN	1390.44	1383.92	1392.99	0.11	0.23	0.16	0.04
TAN-09	TAN	1365.62	1358.92	1393.34	-0.17	-0.04	-0.12	-0.23
TAN-10	TAN	1391.95	1382.31	1393.35	-0.20	-0.07	-0.15	-0.26
TAN-10A	TAN	1391.22	1381.13	1393.31	-0.16	-0.03	-0.10	-0.22
TAN-11	TAN	1368.72	1362.62	1393.36	-0.21	-0.09	-0.16	-0.27
TAN-12	TAN	1346.58	1340.72	1393.39	-0.25	-0.12	-0.19	-0.31
TAN-13A	TAN	1391.30	1385.20	1393.01	0.06	0.19	0.12	0.01

Table E-2. (continued).

Well Name or Identifier	Facility (for Table E-1)	Elevation		Observed Head (m MSL)	Residuals (computed - observed) (m)			
		Top Screen (m MSL)	Bottom Screen (m MSL)		Model 1	Model 2	Model 3	Model 4
TAN-14	TAN	1342.63	1336.54	1392.81	0.26	0.38	0.32	0.20
TAN-15	TAN	1388.36	1382.26	1392.98	0.19	0.30	0.21	0.10
TAN-16	TAN	1367.01	1360.91	1393.13	0.03	0.15	0.06	-0.06
TAN-17	TAN	1362.35	1356.25	1393.09	0.01	0.13	0.06	-0.06
TAN-18	TAN	1312.78	1306.68	1393.10	0.11	0.23	0.15	0.04
TAN-19	TAN	1343.39	1337.29	1393.27	-0.06	0.07	-0.02	-0.13
TAN-20	TAN	1350.05	1343.95	1393.33	-0.26	-0.13	-0.19	-0.31
TAN-21	TAN	1327.82	1321.72	1392.82	0.17	0.27	0.21	0.10
TAN-22A	TAN	1303.37	1297.27	1393.09	0.06	0.17	0.09	-0.03
TAN-23A	TAN	1326.55	1320.46	1393.12	0.03	0.14	0.06	-0.06
TAN-24A	TAN	1391.15	1387.05	1393.21	-0.33	-0.23	-0.29	-0.42
TAN-CH2MON2	TAN	1311.75	1308.70	1392.70	0.40	0.51	0.44	0.33
TAN-CH2MON2_2	TAN	1131.09	1128.04	1395.12	-2.15	-2.03	-2.10	-2.23
TANT-INJ-A-003	TAN	1381.62	1381.32	1393.19	-0.03	0.10	0.03	-0.09
TANT-MON-A-004	TAN	1391.46	1381.40	1394.22	-1.04	-0.90	-0.96	-1.08
TANT-MON-A-007	TAN	1392.08	1328.99	1394.24	-1.03	-0.90	-0.98	-1.10
TANT-MON-A-008	TAN	1391.93	1330.53	1393.93	-0.75	-0.62	-0.70	-0.81
TANT-MON-A-009	TAN	1391.94	1330.32	1393.94	-0.76	-0.63	-0.71	-0.82
TANT-MON-A-010	TAN	1391.95	1326.82	1393.95	-0.76	-0.64	-0.72	-0.84
TANT-MON-A-011	TAN	1391.58	1329.34	1393.58	-0.41	-0.29	-0.36	-0.48
TANT-MON-A-015	TAN	1387.00	1324.51	1393.68	-0.49	-0.36	-0.44	-0.56
TANT-MON-A-016	TAN	1391.75	1330.18	1393.75	-0.56	-0.43	-0.51	-0.62
TANT-MON-A-017	TAN	1391.68	1328.75	1393.68	-0.49	-0.36	-0.44	-0.56
TANT-MON-A-018	TAN	1391.52	1329.02	1393.52	-0.33	-0.20	-0.28	-0.40
TANT-MON-A-019	TAN	1391.76	1327.47	1393.76	-0.57	-0.44	-0.52	-0.64

Table E-2. (continued).

Well Name or Identifier	Facility (for Table E-1)	Elevation		Observed	Residuals (computed - observed) (m)			
		Top Screen (m MSL)	Bottom Screen (m MSL)	Head (m MSL)	Model 1	Model 2	Model 3	Model 4
TANT-MON-A-020	TAN	1349.50	1337.30	1393.28	-0.10	0.03	-0.05	-0.17
TANT-MON-A-025	TAN	1345.23	1333.04	1393.24	-0.08	0.05	-0.02	-0.14
TANT-MON-A-027	TAN	1389.92	1380.78	1393.32	-0.16	-0.03	-0.11	-0.22
TANT-MON-A-028	TAN	1390.33	1378.14	1393.25	-0.08	0.05	-0.02	-0.14
TANT-MON-A-029	TAN	1389.58	1377.39	1393.29	-0.11	0.02	-0.06	-0.17
TANT-MON-A-030A	TAN	1365.96	1359.87	1393.28	-0.11	0.02	-0.06	-0.17
TANT-MON-A-048	TAN	1391.78	1389.81	1393.78	-0.57	-0.44	-0.53	-0.64
TANT-MON-A-050	TAN	1391.27	1323.90	1393.27	0.01	0.13	0.04	-0.08
TANT-MON-A-051	TAN	1391.25	1323.39	1393.25	-0.11	0.00	-0.08	-0.19
TANT-MON-A-052	TAN	1390.56	1315.33	1392.56	0.49	0.59	0.52	0.40
TANW-MON-A-MW2	TAN	1391.22	1386.65	1393.22	-0.35	-0.25	-0.31	-0.43
TCH-1	TAN	1338.09	1336.57	1393.35	-0.17	-0.04	-0.11	-0.23
TRA-06	RTC	1340.86	1331.72	1356.03	0.37	0.40	0.43	0.45
TRA-07	RTC	1354.44	1352.89	1356.44	-0.13	-0.10	-0.05	-0.05
TRA-08	RTC	1353.94	1351.33	1355.94	0.07	0.10	0.15	0.18
USGS-001		1348.06	1338.91	1349.91	-0.35	-0.22	-0.10	-0.44
USGS-002		1356.68	1350.28	1358.89	0.56	0.73	0.46	0.66
USGS-004		1373.54	1291.86	1376.56	1.17	1.22	1.18	1.12
USGS-006		1355.50	1348.49	1364.28	0.37	0.47	0.31	0.79
USGS-006_2		1331.11	1304.29	1364.28	0.37	0.47	0.31	0.78
USGS-008		1345.32	1336.14	1347.88	-0.23	-0.45	0.12	-0.34
USGS-009		1344.71	1335.56	1346.46	0.36	0.37	0.38	0.32
USGS-011		1339.52	1329.97	1343.97	-0.46	-0.42	-0.26	-0.24
USGS-012		1290.11	1258.10	1365.54	-0.55	-0.66	-0.34	-0.38
USGS-013		1316.51	1281.51	1336.18	-0.14	-0.15	-0.07	-0.02

Table E-2. (continued).

Well Name or Identifier	Facility (for Table E-1)	Elevation		Observed	Residuals (computed - observed) (m)			
		Top Screen (m MSL)	Bottom Screen (m MSL)	Head (m MSL)	Model 1	Model 2	Model 3	Model 4
USGS-014		1342.81	1337.42	1344.81	-0.26	-0.12	-0.01	-0.13
USGS-017		1339.98	1337.85	1362.38	1.68	1.89	1.37	1.70
USGS-017_2		1322.31	1321.63	1362.38	1.68	1.88	1.37	1.70
USGS-018		1373.39	1365.77	1378.96	1.22	1.41	1.28	1.24
USGS-019		1376.42	1370.02	1377.10	-0.07	-0.03	-0.01	-0.19
USGS-020	CFA	1353.41	1330.27	1355.41	0.70	0.71	0.77	0.70
USGS-021		1365.21	1351.34	1370.65	-0.10	-0.20	0.02	-0.13
USGS-022		1350.20	1339.23	1350.78	0.00	0.27	-0.09	0.23
USGS-023		1361.71	1357.80	1363.71	-1.10	-1.12	-0.71	-1.10
USGS-025		1391.26	1380.59	1393.31	0.21	0.43	0.39	0.32
USGS-026	TAN	1389.15	1378.64	1393.35	1.31	1.38	0.97	0.94
USGS-027		1382.28	1364.61	1387.14	-1.37	-1.13	-0.88	-1.37
USGS-029		1373.23	1357.33	1375.23	-0.96	-0.92	-0.87	-1.00
USGS-030A		1242.79	1232.88	1379.60	-2.51	-2.46	-2.56	-2.56
USGS-030B		1341.85	1340.33	1375.61	1.46	1.52	1.43	1.43
USGS-030C		1373.09	1370.04	1375.62	1.45	1.51	1.42	1.42
USGS-031		1376.59	1328.43	1378.65	-0.01	0.06	-0.16	-0.07
USGS-032		1373.66	1347.45	1374.99	0.07	0.16	0.15	0.23
USGS-034	INTEC	1350.03	1326.26	1355.89	-0.05	-0.05	-0.04	-0.08
USGS-035	INTEC	1353.89	1326.24	1355.89	-0.03	-0.02	-0.02	-0.05
USGS-036	INTEC	1353.98	1329.58	1355.98	-0.16	-0.15	-0.15	-0.18
USGS-037	INTEC	1347.96	1328.30	1355.90	-0.10	-0.09	-0.08	-0.12
USGS-038	INTEC	1295.91	1280.37	1355.91	-0.10	-0.12	-0.09	-0.13
USGS-040	INTEC	1354.19	1291.56	1356.19	0.25	0.27	0.24	0.22
USGS-041	INTEC	1354.17	1293.13	1356.17	0.23	0.24	0.22	0.19

Table E-2. (continued).

Well Name or Identifier	Facility (for Table E-1)	Elevation		Observed	Residuals (computed - observed) (m)			
		Top Screen (m MSL)	Bottom Screen (m MSL)	Head (m MSL)	Model 1	Model 2	Model 3	Model 4
USGS-042	INTEC	1354.18	1292.21	1356.18	0.16	0.17	0.16	0.13
USGS-043	INTEC	1354.18	1292.44	1356.18	0.29	0.31	0.28	0.27
USGS-044	INTEC	1354.16	1300.88	1356.16	0.21	0.22	0.20	0.18
USGS-045	INTEC	1353.96	1300.62	1355.96	0.35	0.36	0.34	0.32
USGS-046	INTEC	1354.19	1300.98	1356.19	0.18	0.19	0.17	0.15
USGS-048	INTEC	1354.16	1270.08	1356.16	0.20	0.21	0.20	0.17
USGS-051	INTEC	1354.41	1298.38	1356.20	0.04	0.05	0.05	0.00
USGS-052	INTEC	1354.14	1298.33	1356.14	0.43	0.46	0.43	0.40
USGS-057	INTEC	1353.83	1277.28	1355.83	0.26	0.26	0.26	0.23
USGS-058_2	RTC	1354.97	1345.82	1356.21	0.67	0.70	0.72	0.73
USGS-059	INTEC	1354.13	1297.38	1356.13	0.23	0.25	0.24	0.19
USGS-065_2	RTC	1355.09	1349.37	1357.09	-0.67	-0.65	-0.61	-0.60
USGS-076	RTC	1353.98	1283.74	1355.98	0.26	0.28	0.28	0.33
USGS-077	INTEC	1353.82	1321.56	1355.82	0.15	0.16	0.18	0.12
USGS-079	RTC	1354.08	1289.04	1356.08	0.20	0.23	0.31	0.27
USGS-083	CFA	1348.94	1277.00	1352.51	0.27	0.34	0.32	0.43
USGS-086		1345.74	1336.88	1347.74	-0.52	-0.53	-0.20	-0.48
USGS-087	RWMC	1346.31	1324.18	1348.31	-0.23	-0.19	-0.12	-0.24
USGS-088	RWMC	1346.37	1336.95	1348.37	-0.79	-0.75	-0.65	-0.78
USGS-089	RWMC	1346.07	1336.22	1348.07	-0.28	-0.23	-0.10	-0.26
USGS-097		1359.87	1325.58	1361.87	0.39	0.49	0.25	0.32
USGS-098_2		1347.32	1334.52	1361.56	-0.58	-0.49	-0.42	-0.67
USGS-099		1359.66	1347.95	1361.66	-0.51	-0.37	-0.48	-0.44
USGS-100		1361.32	1343.73	1363.32	0.32	0.49	0.15	0.48
USGS-101		1361.28	1337.05	1363.28	-0.37	-0.23	-0.32	-0.55

Table E-2. (continued).

Well Name or Identifier	Facility (for Table E-1)	Elevation		Observed	Residuals (computed - observed) (m)			
		Top Screen (m MSL)	Bottom Screen (m MSL)	Head (m MSL)	Model 1	Model 2	Model 3	Model 4
USGS-103		1345.13	1294.63	1347.13	1.14	1.04	0.98	0.82
USGS-104		1347.53	1307.20	1349.53	0.37	0.23	0.04	-0.27
USGS-105		1345.12	1309.16	1347.12	-0.26	-0.27	-0.34	-0.28
USGS-106		1345.78	1297.05	1347.78	2.20	2.19	2.24	2.04
USGS-107		1348.84	1288.56	1350.84	-0.03	0.00	-0.28	-0.11
USGS-108		1345.06	1301.93	1347.06	0.29	0.24	0.21	0.19
USGS-109		1344.46	1293.47	1346.46	0.26	0.27	0.19	0.23
USGS-110		1347.18	1286.22	1349.99	-0.59	-0.57	-0.49	-0.62
USGS-111_2	INTEC	1353.84	1316.90	1355.84	0.26	0.26	0.27	0.22
USGS-112_2	INTEC	1353.90	1330.42	1355.90	-0.10	-0.09	-0.07	-0.12
USGS-113	INTEC	1353.86	1330.25	1355.86	0.02	0.03	0.04	-0.01
USGS-114	INTEC	1353.86	1328.97	1355.86	0.21	0.22	0.24	0.18
USGS-115	INTEC	1353.80	1322.49	1355.80	0.33	0.33	0.36	0.30
USGS-116_2	INTEC	1354.09	1324.08	1356.09	0.16	0.17	0.19	0.12
USGS-117	RWMC	1345.91	1328.86	1347.91	-0.16	-0.12	-0.03	-0.16
USGS-118	RWMC	1346.17	1342.48	1348.17	-0.47	-0.43	-0.36	-0.46
USGS-119	RWMC	1338.98	1318.86	1347.79	-0.12	-0.09	-0.01	-0.12
USGS-120	RWMC	1341.89	1321.50	1347.31	0.10	0.12	0.24	0.12
USGS-122	INTEC	1354.08	1352.98	1356.08	0.26	0.28	0.27	0.22
USGS-127	CFA	1352.83	1329.56	1354.83	-1.16	-1.11	-0.98	-0.96
USGS-128	CFA	1353.89	1316.73	1355.89	-0.61	-0.60	-0.53	-0.57
USGS-OBS-A-124		1326.61	1311.37	1345.70	0.01	0.08	0.20	0.25
USGS-OBS-A-125		1344.26	1303.56	1346.26	0.16	0.16	-0.03	0.04
USGS-OBS-A-126A		1330.37	1323.06	1393.34	0.30	0.54	0.55	0.50
USGS-OBS-A-126B		1391.34	1382.97	1393.34	0.30	0.54	0.55	0.50